

Separation Media Based on Defined Hydrogel Systems

PhD Thesis
by

M.Sc. Christoph Pfeifer

Institute for Chemical Technology and Polymer Chemistry

supervisor: Prof. Dr. Manfred Wilhelm
co-supervisor: Prof. Dr. Patrick Theato

Nov. 2015 - April 2020



This document is licensed under a Creative Commons Attribution-ShareAlike 4.0 International License (CC BY-SA 4.0): <https://creativecommons.org/licenses/by-sa/4.0/deed.en>

Hydrogele als Separationsmedien auf Basis definierter Porengrößen

Zur Erlangung des akademischen Grades eines
DOKTORS DER NATURWISSENSCHAFTEN (Dr. rer. nat.)
von der KIT-Fakultät für Chemie und Biowissenschaften des Karlsruher
Instituts für Technologie (KIT) genehmigte
DISSERTATION

von

M.Sc. Christoph Pfeifer

1. Referent: Prof. Dr. Manfred Wilhelm
2. Referent: Prof. Dr. Patrick Theato
Tag der mündl. Prüfung: 21.04.2020

Institut für Technische Chemie und Polymerchemie

Nov. 2015 - April 2020

Declaration

Hereby, I declare that the current thesis was written independently and without unauthorized foreign help and using no other than the specified sources and aids.

Karlsruhe, 11.03.2020

Christoph Pfeifer

Abstract

Polyelectrolyte networks, which consist of a three dimensional assembly of charged polymer chains, such as poly(sodium acrylate) (PSA) and poly(sodium methacrylate) (PSMA), provide a high ability to incorporate water. Such materials can swell up to 1000 times of their original size in water and thus, are referred to as superabsorbent polymers (SAP). These are widely utilized in daily necessities, such as diapers, with a yearly world production of 3.2 Mt. In addition, the desalination of saltwater has been proposed as a new potential application of SAPs.

In an ideal case, a polymer network is represented by a grid in which the distance between the junctions is uniform. However, in industrial samples, the chain length between two junction points is not uniform but reveals a broad distribution. Moreover, the presence of defects, such as unreacted moieties and loops, increase the irregularity of the network. These structural defects affect the macroscopic behavior of the networks in terms of mechanical stability and swellability. Nowadays, the major challenges are the development of synthetic strategies for a homogeneous polymer network and the verification of the regular structure to maximize the application potential, e.g. in desalination.

Different synthetic pathways have been chosen to obtain defined polymer networks based on methacrylic and acrylic acid. The cross-link density (DC) of the networks, as the dominating factor of the macroscopic properties, is usually varied in the range of 0.3 to 5.0 mol%. For the purpose of comparison, undefined free radical polymerized PSA and PSMA networks were synthesized. For defined polymer networks, anionic co-polymerization of the monomer tert-butyl methacrylate (t BuMA) and a bifunctional linker was utilized. Additionally, telechelic polymers of t BuMA were produced by anionic polymerization, which were subsequently connected into polymer networks by addition of a bifunctional monomer, or by an azide-alkyne Huisgen ligation. These organogels have been hydrolyzed and charged into the respective PSMA networks. Furthermore, reversible addition-fragmentation transfer (RAFT) co-polymerization of acrylic acid and N,N' -methylene bisacrylamide was investigated as an independent living radical polymerization procedure. All polymer networks have been characterized by high-field ^1H -NMR to confirm their chemical composition.

Time-domain nuclear magnetic resonance (NMR) was utilized to acquire an in-depth understanding of the polymer network structure by using techniques sensitive to the local mobility of the chain segments, namely ^1H -NMR relaxometry (T_2) and ^1H double quantum coherence (DQ-NMR). The T_2 -relaxation revealed more constraints in the polymer network by higher DC , which lead to a lower mobility and to higher T_2 -relaxation rates. The PSMA samples revealed, independent of the synthetic procedure, comparably widths of relaxation rates indicating similar network heterogeneities. The comparison of the PSA samples obtained by RAFT polymerization exhibits broader distributions by increasing the contents of RAFT agent. These could be assigned to higher amounts of dangling ends, which are likely arising from lower effective chain lengths for higher RAFT contents.

DQ-NMR has proven that for all samples the amount of defects is decreasing with DC . After subtraction of the contribution of defects, all networks of the same monomer show

a similar width of the mobility distributions implying a similar level of network homogeneity.

The inverse size exclusion chromatography (iSEC) was adapted to probe the pore size distribution low cross-linked PSMA. It can be confirmed that a higher degree of cross-linking results in smaller pores. This trend was correlated to the chain segment mobility, as obtained by T_2 -relaxation measurements, which is validating that the alternations in mobility are in fact representing a change in the pore sizes.

According to dielectric spectroscopy, there is a reduction of the direct current (dc) conductivity (κ) of PSMA networks with increasing DC. Furthermore, κ was reduced by the network to $\approx 33\%$ of the potential conductivity of a pure sodium ion solution indicating a reduction in the diffusivity of ions.

As potential application, the desalination of saltwater was tested, whose efficiency is governed by the salt partitioning between hydrogel and supernatant phase. The synthetic procedure of the PSMA networks had no significant influence on the salt repulsion. The charge distribution between the hydrogel and surrounding solution could be qualitatively described by the Donnan model. Although, only presumed much lower charge densities in the Donnan model of $\sim 30\text{ mol}\%$ shows a good agreement with the experimental data.

Contents

1	Introduction and Motivation	1
2	Fundamentals and Theoretical Description of Polymer Networks	5
2.1	Polymer Networks	5
2.2	Polyelectrolytes and Superabsorbent Polymers	9
2.3	Theoretical Description of Polymer Chains and Networks	11
2.3.1	Single Polymer Chain	11
2.3.2	Polymer Solutions	13
2.3.3	Elastic Deformation	16
2.3.4	Equilibrium Swelling	21
2.4	Ionic Interaction	24
2.4.1	Poisson-Boltzmann	24
2.4.2	Debye-Hückel Theory	24
2.5	Swelling of Polyelectrolyte networks	26
2.5.1	Donnan Equilibrium	26
2.5.2	Flory-Rehner Theory	27
2.6	Basics of Nuclear Magnetic Resonance Spectroscopy	29
2.7	Basics of Size-Exclusion Chromatography	35
3	Synthesis of Defined Polyelectrolyte Hydrogels	39
3.1	Methacrylic Acid	41
3.1.1	Free Radical Polymerization, (Type A)	41
3.1.2	Considerations Regarding the Anionic Polymerization	44
3.1.3	Anionic Polymerization of Polymer Networks in a Single Step, (Type A)	46
3.1.4	Anionic Polymerization of Quasi-Model Polymer Networks (Type B)	47
3.1.5	Model Networks by Anionic Polymerization with Subsequent Cross-Linking via Azide-Alkyne Huisgen Ligation (Type C)	49
3.2	Acrylic acid	55
3.2.1	Free Radical Polymerization	55
3.2.2	Reversible Addition Fragmentation Transfer Polymerization	56
4	Determination of Network Heterogeneity	59
4.1	Swelling Experiments	61
4.2	Low-Field Nuclear Magnetic Resonance Spectroscopy	64

4.2.1	$^1\text{H-NMR}$ Transverse Relaxation, T_2	64
4.2.2	Residual Dipolar Coupling Measured by Double Quantum Coherence	82
4.3	Inverse Size-Exclusion Chromatography	95
4.3.1	Introduction	95
4.3.2	Results of the Inverse Size-Exclusion Chromatography	99
4.4	Dielectric Spectroscopy	103
4.4.1	Introduction to Dielectric Spectroscopy	103
4.4.2	Determination of the Direct Current Conductivity	106
4.5	Salt Rejection	108
5	Conclusion and Outlook	113
	Bibliography	119
A	Experimental	129
A.1	Materials	129
A.2	Free Radical Polymerization of Methacrylic Acid	130
A.3	Anionic Polymerization of Poly(Sodium Acrylate)	131
A.3.1	Anionic Polymerization of Polymethacrylate Networks in a Single Step	131
A.3.2	Anionic Polymerization of Quasi-Model Polymer Networks	132
A.3.3	Model Networks by Anionic Polymerization with subsequent Cross-linking by Azide-Alkyne Huisgen Ligation	133
A.4	Free Radical Polymerization of Acrylic acid	136
A.5	Reversible Addition Fragmentation Transfer Polymerization of Acrylic acid	136
B	Experimental Characterization Procedures	139
B.1	Swelling experiments	139
B.2	Fourier-Transform Infrared Spectroscopy	139
B.3	Nuclear Magnetic Resonance Spectroscopy	140
B.3.1	High-Field NMR-Spectroscopy	140
B.3.2	$^1\text{H-NMR}$ T_2 -relaxation	140
B.3.3	Residual Dipolar Coupling Measurements	141
B.4	Size-Exclusion Chromatography	143
B.4.1	Conventional Size-Exclusion Chromatography (SEC)	143
B.4.2	Coupled Fourier-Transform Infrared Spectroscopy Size-Exclusion Chromatography	144
B.5	Inverse Size-Exclusion Chromatography	144
B.6	Dielectric Spectroscopy	145
C	Figures	146
D	List of Variables	149
	List of Tables	153
	List of Figures	154

Chapter 1

Introduction and Motivation

Polymer networks are a three-dimensional assembly of polymer chains, which are connected physically or by chemical bonds. [1–3] Usually, these networks have a high affinity for solvents, which are incorporated into their structure, while the cross-links prevent dissolution of the material. [4] Their ability to incorporate solvents is called swelling, which is mainly determined by the chemistry of the polymer backbone. [5] Hydrogels, for example, are networks able to swell in water due to the presence of hydrophilic groups on the polymer chain. [6] Their water absorbency is substantially enhanced if permanent charges are introduced within the network microstructure [7,8] forming so-called polyelectrolyte gels. They often exhibit high uptake of water or aqueous solutions that can exceed several hundred times of their own weight. Thus, the material is often referred to as superabsorber (superabsorbent polymer, SAP) and is found in many applications. [9] The strong affinity of SAPs to water opens the door for a broad range of large scale applications like personal hygiene products, [10] as soil conditioners in agriculture, [11] or waste water treatment. [12] New promising applications were recently proposed, such as separation agents for the desalination of salt water, [13–15] or the recovery of energy in an osmotic engine. [16] The production of SAPs reached 3.2 Mt/year in 2015, [17] with poly(sodium acrylate) (PSA) covering 65 % of the market share. [18]

On a large scale, polymer networks are often synthesized via conventional free radical polymerization (FRP), [19] which allows only a poor control over the network microstructure leading to hydrogels with an undefined pore size distribution and cross-linking density. [1] Beside the chemical composition, this network microstructure plays an important role for the achievement of, for example, a more homogeneous network topology to improve mechanical strength and swelling ability. [20] It was shown that structural defects, such as loops (polymer chain is cross-linked to itself), negatively affect the elasticity of the network, [21,22] while single bound chains, i.e. dangling ends and unreacted moieties, increase the width of the pore size distribution and thus, the swelling ability. [23] Materials

with a defined network structure could be applied as model systems to answer the crucial point how the nanoscopic network structure affects the bulk properties and therefore the application performance. If the molecular structure-macroscopic performance relationship is well understood, it paves the way for better designed materials for each application. Although the presence of defects is currently still inevitable during the cross-linking process, [24] recent research focuses on the development of new synthetic methods to limit their formation. In order to avoid primary loops, i.e. the chain is coupled to itself, two types of macro-monomers can be combined with either tetrahedral structure, [25] or a mixture of tetrahedral and linear chains. [26] Additionally, the utilization of efficient ligation methods, such as azid-alkyne Huisgen ligation, is proposed as a beneficial tool for efficient cross-linking processes leading structures with few unreacted moieties and limited dangling ends. [27] Starting from the pioneering work of Fukuda, [28,29] controlled radical polymerization methods have been employed for the synthesis of more defined structures by avoiding undesired side reactions. [30,31] Anionic polymerization provides good control over the chain formation [32] and is consequently also used for the preparation of hydrogel networks. [33–35] Nevertheless, recent reports disputed the homogeneity of networks obtained via “living” polymerizations. [36,37] At the same time, the expansion of analytical tools to detect the presence of defects and to investigate their impact on the final properties of the gel plays a key role in recent research. [38,39]

In the present thesis, various synthetic procedures were employed with the objective to validate if a homogeneous network topology could be created. Here, sophisticated anionic polymerization and controlled radical polymerization techniques, with and without azide-alkyne Huisgen ligation, have been used in order to minimize the formation of undesired network defects. The challenge on the way towards more defined systems arises not only from the synthetic procedure but also from the demanding characterization of polymer networks. The difficulties are associated with the insolubility of the analyte as well as the complexity of the network microstructure. [20,40] Existing methods should be adapted and developed further for the usage on polymer hydrogels. For example, the analysis of the network structure via low-field proton nuclear magnetic resonance ($^1\text{H-NMR}$) techniques, such as T_2 -relaxation and double quantum $^1\text{H-NMR}$ (DQ-NMR), was recently introduced as a powerful tool for the determination of network structures in polyelectrolytes. [41] In polymer networks, some structural elements show distinct mobilities, for instance cross-linking points are rigid, while dangling ends move freely. These differences in mobility can be correlated to structural inhomogeneities. [42,43] The other main characterization method is based on the diffusion of non-charged polymers into the network structure. These are evaluated via the development of a specific inverse size-exclusion chromatography (iSEC) [44] and allow for the measurement of pore sizes and the distributions thereof.

Several steps are necessary for the synthesis, characterization and the testing of the polyelectrolyte hydrogels. This thesis is structured as follows: In Chapter 2, theoretical models for charged polymer networks are presented to explain how molecular parameters affect the macroscopic properties. In addition, the basics of the employed main characterization methods are described.

In Chapter 3, the synthesis of the diverse network topologies is explained, starting from simple randomly cross-linked hydrogels as a reference system to more complex topologies. It is shown how the different architectures can be achieved and which synthetic parameters are varied. More sophisticated anionic polymerization methods and controlled radical polymerizations are utilized to for a better control over the polymerization process. The networks are made of either poly(sodium acrylate) (PSA) or poly(sodium methacrylate) (PSMA).

The synthesized networks are characterized in Chapter 4. After a short introduction of the basics behind the applied methods, the influence of the synthetic parameters on the network structure is discussed. The water absorbency of the hydrogels is studied, as this is a critical performance properties for most applications. Furthermore, $^1\text{H-NMR}$ relaxometry, DQ-NMR and iSEC are employed to gain information about the network dynamics and structure. In a last step, the ion mobility and the salt rejection are quantified as important network parameters for SAP applications, such as desalination.

The concluding Chapter 5 presents a summary of the main findings of this thesis and an outlook to the future, where further possible developments are discussed.

Chapter 2

Fundamentals and Theoretical Description of Polymer Networks

The following chapter provides an introduction into polymer networks including the main challenges for the synthesis of defined structures as well as the main theoretical approaches for the description of these networks. For detailed information the reader is referred to the books of Lechner [45], Tieke [46], Young [47] and Flory [4], on which this chapter is based on.

2.1 Polymer Networks

Polymers consist of long chains of covalent coupled small molecules, the so-called monomers. [45, 46] By linking the monomers together, increasingly complex topologies, such as linear chains, rings, branched or cross-linked architectures can be achieved as fundamental structural units, as displayed in **Figure 2.1**. The physical properties of polymers are mainly driven by the chemical nature of the monomer, the molecular weight – and its distribution – as well as the mentioned topology of the polymer [47]. Therefore, structurally non-linear polymers provide distinct properties from their linear counterparts.

Polymer networks, as the main focus of the current work, have three-dimensional structures, which consist of single chains that are bonded to other chains via different junction points. Consequently, the macroscopic sample is ideally composed of a single molecule. The physical behavior of these cross-linked polymers is mainly defined by the number of junctions ν_e per volume V_0 . The degree of cross-linking, also called cross-link density, can be defined as the number of junction points along a polymer chain, which are often normalized to the number of monomer units resulting in a dimensionless number $n_{\text{cross-linking}}/n_{\text{monomer}}$ in mol%, see **Figure 2.2**. [47] The individual chains in the network are anchored by the interconnections, which lead to a reduction in the flexibility of the

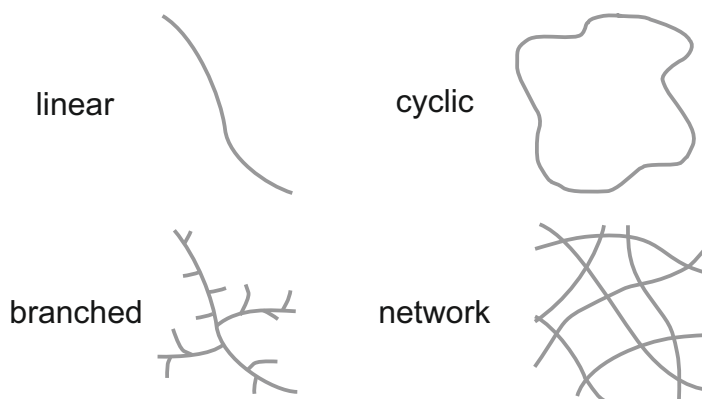


Figure 2.1: Schematic representation of different polymer topologies. The most prominent cases are linear, cyclic, and branched polymers, as well as polymers, which are coupled into networks via physical or chemical bonds, adapted from [47].

chain. Thus, the polymer is a predominantly elastic material at low degrees of cross-linking (~ 1 mol%, above the glass transition temperature T_g), which becomes more rigid upon increasing the number of junctions (≥ 5 mol%) leading to thermosetting plastics. In contrast to idealized polymer networks, real networks have a variety of defects, as displayed in **Figure 2.2**. They exhibit the already mentioned physical entanglements, which add additional rigidity to the material. If such an entanglement is set between two cross-links, it becomes permanent since it cannot dissolve. Furthermore, the same junction point can be linked by multiple chains to another junction point creating highly rigid connections. Additionally, real polymers have dangling ends in form of unbound chain ends and loops if a chain is interconnected to itself. These defects do not contribute to the mechanical strength of the material. Finally uncoupled chains, the sol, can be found within the network polymer likewise linker which are bonded to only one chain, as can be seen in **Figure 2.2**. [47]

The individual polymer chains of networks cannot be melted or dissolved, in contrast to relatively mobile single polymer chains, due to the restrictions caused by the interconnections. Rather than dissolve, the network exclusively expands upon contact with solvents by incorporation of solvent molecules into its architecture. The junction points in a network can be divided into temporary physical and permanent chemical bonds. Physical cross-links can consist of entanglements and of electrostatic or dipolar interactions between different chains. These physical interconnections can readily move along a polymer chain and are continuously formed and dissolved. In contrast, chemical bonds are fixed linkages between two molecules, which are unable to migrate. In case of cross-linked ma-

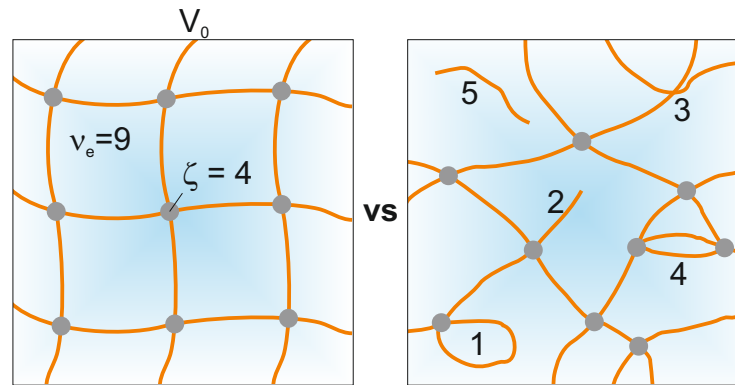


Figure 2.2: Comparison between an ideal network polymer (left) and a real network polymer (right), both with 9 junction points (ν_e). In addition, the unit volume V_0 and the functionality ζ of the cross-link are presented, i.e. the number of coupled chains per junction. The synthesized networks feature defects like (1) loops, (2) dangling ends, (3) entanglements, (4) multiple coupled and (5) unbound chains (sol).

terials, entanglements cannot be dissolved but move freely between two junction points. These entanglements are permanent and contribute to the overall cross-link density of the network.

Synthesis of polymer networks involves additional challenges compared to linear chains. Since cross-linked polymers are not melt- and solvable, all products have to be either shaped *in situ* in the form of their application or mechanically re-treated. Commonly used polymerization methods include free-radical, ionic, controlled radical and catalyzed polymerization. They are conducted in bulk, emulsion, suspension and solution. [45, 46] The preparation of polymers networks can be further classified into two approaches.

On the one hand, the simultaneous incorporation of a multifunctional linker during the polymerization can be applied. Here, a molecule with two or more double bonds is employed to combine different growing polymer chains. This approach leads to rather broadly distributed networks. Their mesh size depends on the co-polymerization parameters, the activity of the additional double bonds of the linker and other effects. The benefit of the approach lies in the simplicity of the procedure. The network formation can be conducted in a single step, since no further cross-linking is required. [45–47].

On the other hand, single polymer chains can be synthesized followed by a cross-linking step. A possible realization of the approach includes formation of unsaturated polymers. Prominent examples are natural rubber and co-polymers with butadiene. Those unsaturated polymers are cross-linked in a second reaction step or in parallel, either by

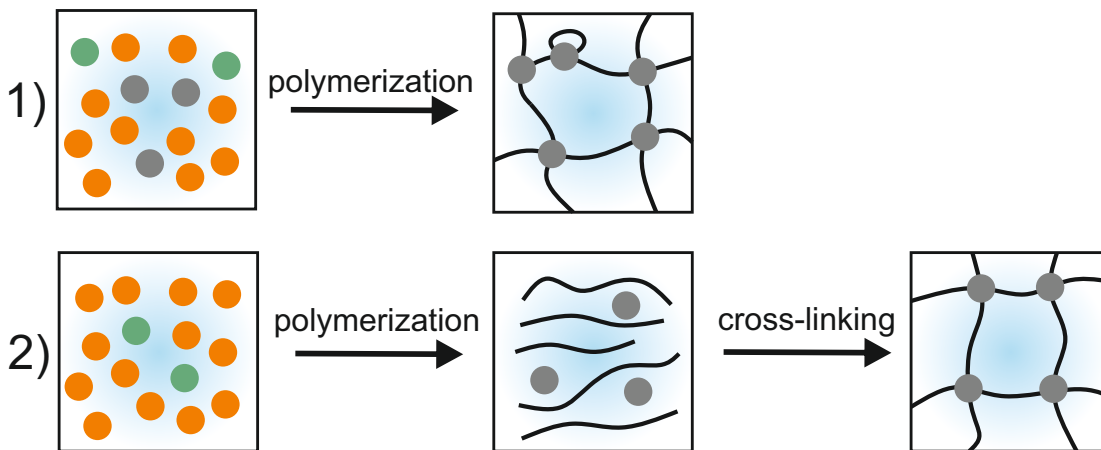


Figure 2.3: Depiction of the general approaches for polymer network synthesis using an initiator (green) and the monomer (orange) yielding the polymer (black). 1) The network formation can be conducted in a single step by in situ copolymerization of a multifunctional linker (gray). 2) In the second approach, the polymer chain is formed first, which is cross-linked in a subsequent step.

insertion of a linker into the double bonds of two neighboring chains, e.g. sulfur during the vulcanization, or by subsequent polymerization of an added new monomer and the incorporation of the pre-polymers into the growing chains, e.g. with styrene for the curing of glass-fiber reinforced composites. Another possible realization requires first the build-up of the polymer chain and subsequently the functionalization on both ends, so-called telechelic polymers. These telechelic polymer chains are then combined with a defined linker via controlled reactions mechanism, the 'click' reactions, such as the azide-alkyne Huisgen ligation. The procedure provides control over the synthesis of the single chain, if anionic or controlled radical polymerization approaches are employed. Thereby, neat distributions of mesh sizes with few network defects should be achievable. [27] An outline of possible polymerization techniques and utilized procedures will be provided in **Chapter 3, p. 39**

2.2 Polyelectrolytes and Superabsorbent Polymers

Polyelectrolytes are polymers, which releases a counterion during dissolving. [48] Due to their particular microstructure, cross-linked polyelectrolytes are insoluble, so that in contact with solvent they swell rather than dissolve. The driving forces of the incorporation are the energy gained from the reduction of electrostatic repulsion of the ions and the release of the osmotic pressure. The swelling ability mainly depends on the affinity of the network for the solvent, which in turn is determined by the chemistry of the polymer backbone. Networks, which swell in water due to the presence of hydrophilic

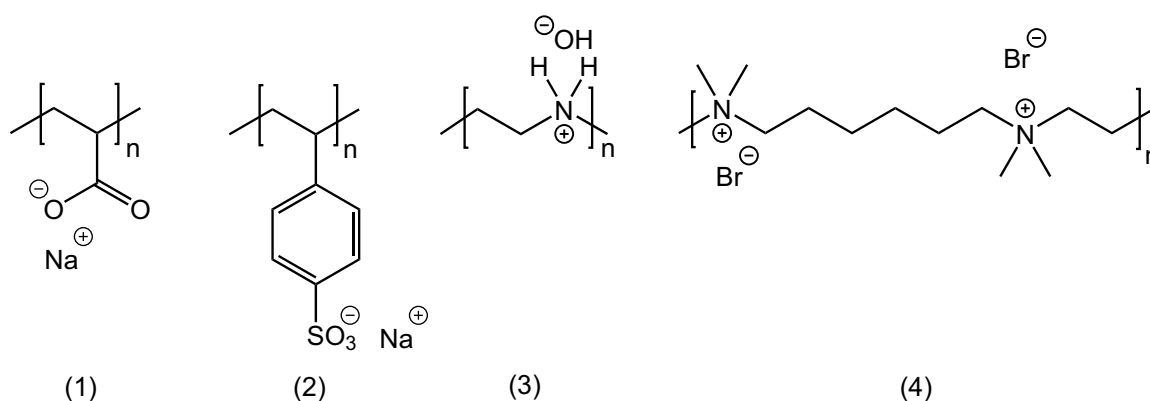


Figure 2.4: Examples of (1) weak, e.g. poly(sodium acrylate) and (2) strong anionic polyelectrolytes, e.g. poly(sodium styrene sulfonate), as well as (3) weak, e.g. polyethylenimine (generates in aqueous solutions in-situ a polyelectrolyte by proton abstraction), and (4) strong cationic polyelectrolytes, e.g. poly(hexadimethrine bromide). The strong polyelectrolytes can be used under basic and acidic conditions, while weak acids, such as polyacrylic acid are limited to neutral or basic media. The weak basic polymers, like polyethylenimine, can be employed in neutral or acidic conditions to ensure dissociation into the ions.

groups on the polymer chains are called hydrogels. Polyelectrolytes are subdivided into polycations, which carry positive charges on the backbone and polyanions, which bear a negative charge on the backbone. Strong electrolytes readily dissociate in solution, while in case of weak electrolytes the dissociation depends on the pH value. Related to the application requirements and the pH value at usage, weak (e.g. polyacrylic acid) and strong acids (e.g. polystyrene sulfonate) and weak (e.g. polyethylenimine) and strong basic (e.g. trimethylammonium) materials are employed to create the polyelectrolytes, as shown in **Figure 2.4**. The ionic group can be attached to the backbone directly,

or can be part of a side-group or side-chain. [48] Some examples of polymer networks with cross-link densities below 1 mol% can incorporate more than 100 times of their own weight in water and are called superabsorbent polymers (SAP). Poly(meth)acrylic acid, polyacrylamides, polyvinyl alcohol, carboxymethylcellulose and polyethylene oxides are commonly used SAP examples, as depicted in **Figure 2.5**. [48]

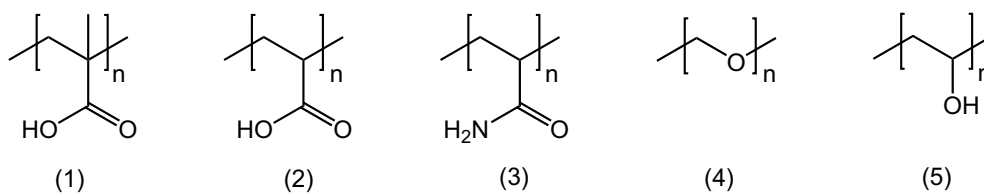


Figure 2.5: Various examples of polymers commonly employed in superabsorbents, either directly or as co-polymers. (1) polymethacrylic acid, (2) polyacrylic acid, (3) polyacrylamide, (4) polyethylene oxide and (5) polyvinyl alcohol.

As already mentioned, their production reached 3.2 Mt/year in 2015, [17] with poly(sodium acrylate) (PSA) covering 65 % of the market share. [18] The strong affinity of SAPs to water opens the door for a broad range of large scale applications like personal hygiene products (e.g. diapers), [10] as soil conditioners in agriculture, [11] or waste water treatment. [12] Superabsorbents can also be found in artificial snow, [49] in additives for oil-drilling fluids [50] or within concrete [51] and specifically designed coatings for underwater-cable sealings. [52] Contrary to the water, ions present in solution are partially excluded due to the electrostatic repulsion of the polyelectrolyte and concentration effects of the ions. Based on this concept a new promising procedure for the desalination of salt water has been developed. [13–15] SAP consisting of PSA are employed in consecutive swelling and squeezing cycles. The dry network is swollen in salt water and subsequently the supernatant phase, which is now enriched in salt, is removed. Water with a lower salinity is recovered by squeezing of the particles, which are re-used for a new cycle. In another process, consecutive swelling and deswelling of gels with solutions of different salinity can be used to recover energy in an osmotic engine. [16] To extend the fields of possible applications, the focus in recent research was laid on the development of double network structures for ultra-tough hydrogels [53] and on self-healing hydrogels for fast curing. [54] Another important field of interest are stimuli responsive polymers,

which react upon irradiation, [55] or changes in pH, [56] or temperature [57] enabling new applications, such as drug delivery systems in medicine [58], actuators for nanorobots [59], or sensors in aqueous environments. [60]

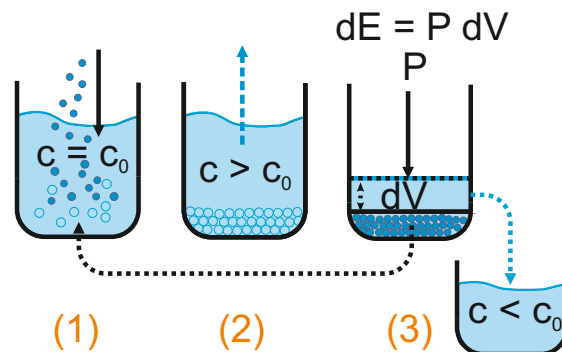


Figure 2.6: Illustration of the desalination procedure based on poly(sodium acrylate) hydrogels. (1) Mixing of dry polymer network with brine; (2) Removal of the supernatant phase enriched in salt; (3) Release of desalinated water from the gel interior via external pressure. The energy consumption of the process ΔE can be estimated by the required pressure P and the change in volume dV using $dE = P dV$.

2.3 Theoretical Description of Polymer Chains and Networks

2.3.1 Single Polymer Chain

For a theoretical description of the behavior of a non-charged polymer network, it is convenient to start from the building blocks it consist of, the polymer chain. These chains are interconnected by cross-linking points. Each chain folds in random conformations between two junction points, which leads to distinct end-to-end distances. The polymer chains stretch and unfold if mechanical forces are applied, which leads to a loss of entropy. The required force and energy can be estimated from the change in entropy. In detail, the entropy is derived from the probability per volume $P(x, y, z)$ to find the end of a free polymer chain at a certain point (x, y, z) , while the other chain end is set as the origin. The two ends have the distance r from each other, as can be seen in **Figure 2.7**. The distance r can be described by the vector $\vec{r}(x, y, z)$, with $r = |\vec{r}|$ [45]. Under the assumption of a Gaussian distribution of the end-to-end vectors the probability can be expressed by

$$P(r) = \left(\frac{\beta}{\pi^{1/2}} \right)^3 \exp(-\beta^2 r^2) \quad (2.1)$$

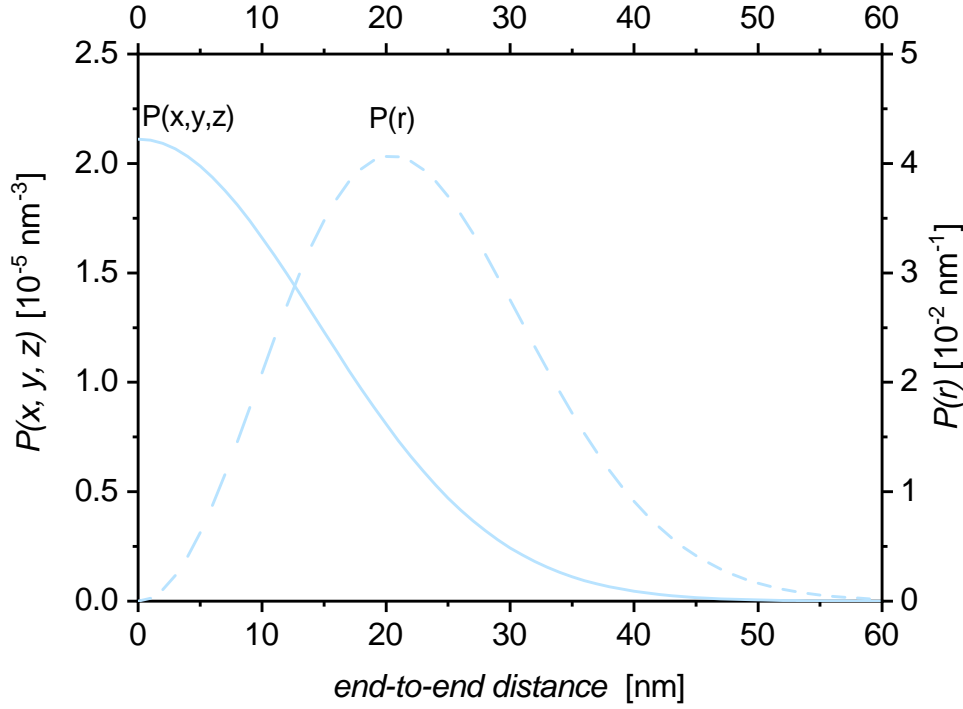


Figure 2.7: Arithmetic example of distribution functions $P(x, y, z)$ and $P(r)$ calculated for a polymer chain with 10,000 repeating units and an efficient link length of 0.25 nm (\approx one monomer).

with the parameter $\beta = (3 / (2nl^2))^{1/2}$, where n is the number of links of length l . [47,61] The parameter β is basically the inverse of a standard deviation $\beta \propto 1 / \langle r^2 \rangle$ and a characteristic specification for the individual chain, which is closely related to the Gaussian or ideal chain. [62] For a ideal non-charged chain with vanishing excluded volume interaction the end-to-end vector r is given by

$$\langle r^2 \rangle = n l^2 \quad (2.2)$$

while n and l are fit parameters, which are optimized for the polymer.

Within thermodynamics, the Boltzmann equation, **Equation 2.3**, quantifies the entropy S as [46]

$$S = k_B \ln \left(\frac{\Omega}{\Omega_0} \right) \quad (2.3)$$

with the Boltzmann constant $k_B = 1.38 \cdot 10^{-23} \text{ J/K}$ and the number of possible conformations of the chain Ω can be employed to calculate the entropy. For small r , the probability

distribution $P(r)$ becomes large, since many conformations are possible. Whereas for large r the number of achievable conformations and thus, $P(r)$ decreases. Consequently, it is a justifiable assumption that Ω is proportional to $P(r)$, leading to

$$S = C - k_B \beta^2 r^2 \quad (2.4)$$

with the constant C . The entropy of a single chain can be calculated using **Equation 2.4**, if the number of segments and their length is known. [47, 61, 62]

2.3.2 Polymer Solutions

Flory and Huggins developed a mathematical description of the evolving of the entropy and the energy during a mixing process of a non-charged system. [63, 64] The whole system is subjugated to a couple of assumptions. First, it is presumed that the overall volume remains unchanged during the mixing and that the volume of the mixture equals the sum of the individual volumes of the components. Secondly, it is assumed that each molecule requires the same space. Based on these premises the entropy of mixing is derived from the number of possible states of each particle. The number of states is estimated by dividing the available space into unit cells. Each cell should be occupied by a particle with the extend of the cell. The number of possible conformations allows to calculate the entropy. Main considerations are mentioned in the caption of **Figure 2.8** using the example of a basic two-dimensional lattice model.

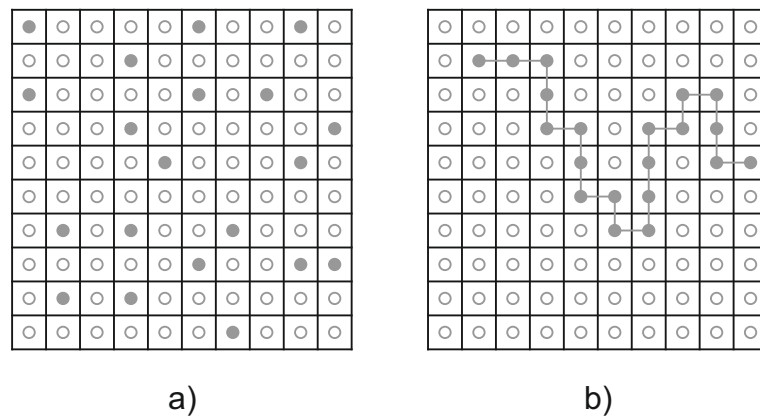


Figure 2.8: Difference in entropy of mixing of **a)** two low molecular species with the same size and **b)** of a polymer in a solvent. While **a)** provides $N = N_1 + N_2$ atom sites for each particle and therefore the same number N of states, **b)** has more parameters, since the polymer segments can move freely and adopt many conformations. The polymer chains exhibit the additional constrain of the connection between their sub-units, adapted from literature. [65]

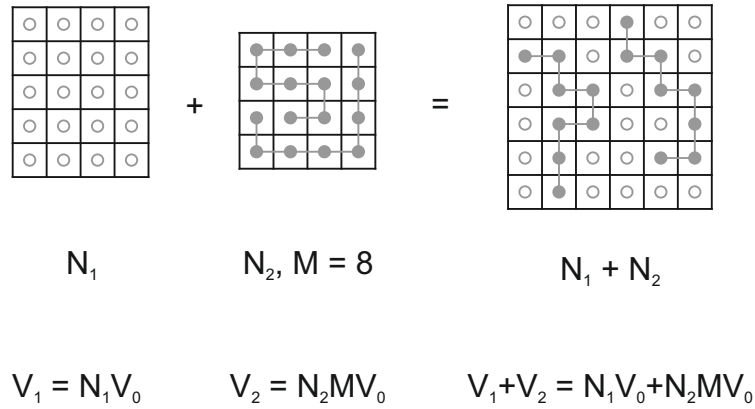


Figure 2.9: Partial volume V_1 and V_2 and mixing volume $V_1 + V_2$ of a polymer solution, adapted from [65].

Based on the described lattice model the entropy of mixing of an ideal mixture of two molecules of equal size (e.g. mixing of two solvents) can be calculated by [65]

$$\Delta S = -k_B [n_1 \ln(x_1) + n_2 \ln(x_2)] \quad (2.5)$$

where n_1 and n_2 are the numbers of component 1 and 2, x_1 is the mole fraction of component 1 and x_2 is the mole fraction of component 2, see **Figure 2.8 a**. The probability to find a particle of type 1 or 2 in a specific volume is defined by the mole fraction x . If the particles exhibit equal sizes the mole fraction can be directly assigned to the volume fraction of each component. In case of polymer solutions, this approach of an ideal solution cannot be employed due to the very distinct extensions of polymers compared to solvent molecules. Nevertheless, the entropy of mixing of a polymer can be approximated using the lattice model with respect to the volume fraction, as shown in **Figure 2.9**. In the following approach, the polymer is subdivided into interconnected sub-units with the same size as the solvent molecules. In the simplest assumption, the spatial extension of an unit cell equals to a monomer. Consequently, the volume fraction describes the probability of finding the polymer in a unit cell with higher precision in comparison to the mole fraction, since it takes the number of connected sub-units per polymer chain M into account. The volume available is split into unit cells with the size of a solvent molecule V_1 similar to the model of ideal mixing. All unit cells are either occupied by a solvent molecule or a polymer sub-unit. Here, the populated space of the polymer V_2 is given by $V_2 = M V_1$. Employing N_1 as the number of solvent molecules and N_2 as the number of polymers, the volume fraction of solvent ϕ_1 and polymer ϕ_2 can be calculated by [65]

$$\phi_1 = \frac{V_1}{V_1 + V_2} = \frac{N_1}{N_1 + M N_2} \quad \text{and} \quad \phi_2 = \frac{M N_2}{N_1 + M N_2} \quad (2.6)$$

In ideal polymer solutions, the probability to find a molecule in a volume segment is defined by its volume fraction. Thus, the entropy of a polymer solution can be expressed by the so-called Flory-Huggins equation, **Equation 2.7**, using a modified version of **Equation 2.5** [65]

$$\Delta S = -k_B [N_1 \ln(\phi_1) + N_2 \ln(\phi_2)] \quad (2.7)$$

Contrary to the ideal solution, the entropy of mixing of polymers results in a unsymmetrical entropy curve instead of a mirror-symmetrical distribution, as can be seen in **Figure 2.10**.

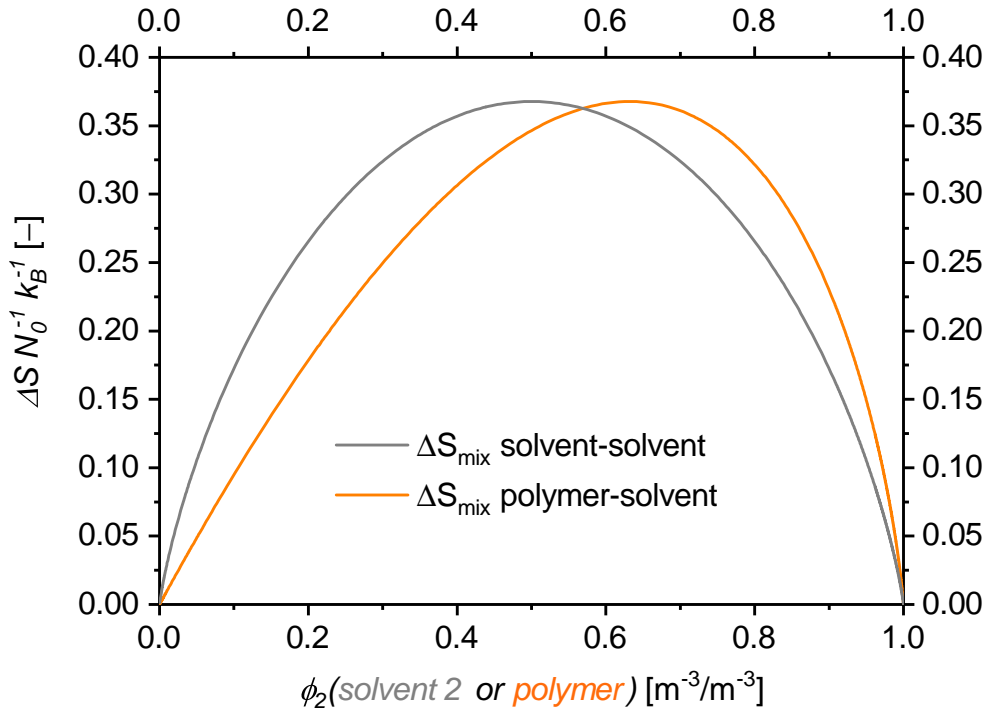


Figure 2.10: Entropy of mixing ΔS_{mix} per monomer unit normalized to k_B as a function of the volume fraction of polymer ϕ_2 with the number of sub-units (\equiv monomers) in a polymer chain $M = 500$ and the total number of unit cells $N_0 = N_1 + M N_2$, adapted from [65]. Please note that at polymer chain lengths above $M = 500$ the mixing term becomes independent of M . [66]

Consecutively, the enthalpy of mixing ΔH_{mix} is calculated applying a modified equation of ideal mixtures. Here, $N_1 + M N_2$ is employed for the total number of particles and the volume fraction ϕ_2 instead of the mole fraction, giving [46]

$$\Delta H_{\text{mix}} = N_1 \phi_2 \chi k_B T \quad (2.8)$$

with χ as the Flory-Huggins parameter of solutions. The parameter χ is normalized to the energy $k_B T$ and describes the polymer-solvent interaction, while:

$$\begin{aligned} \chi \gg 0 & \text{ is a weak solvent-polymer interaction with a tendency towards segregation} \\ \chi \leq 0 & \text{ relates to a good solvent.} \end{aligned} \quad (2.9)$$

Consequently, the tendency of the solution to decompose increases with growing Flory-Huggins parameter χ , since the mixing enthalpy ΔH_{mix} becomes larger than the entropy of mixing $-T\Delta S$. Combining the expressions of the entropy of mixing, **Equation 2.7**, and of the enthalpy of mixing, **Equation 2.8**, the free enthalpy ΔG_{mix} can be computed leading to

$$\Delta G_{mix} = \Delta H_{mix} - T\Delta S = k_B T [N_1 \ln(\phi_1) + N_2 \ln(\phi_2) + \chi \ln(\phi_2)] \quad (2.10)$$

It can be concluded that the presented Flory-Huggins model results in well-arranged qualitative statements considering mixing enthalpy, despite using general assumptions. [47, 61–65, 67]

2.3.3 Elastic Deformation

2.3.3.1 Affine Model

The change in entropy of a complete network can be estimated from the change of the entropy of a individual chain. Based on the assumption that the junction points are fixed within the chain, while the cross-links fluctuate around a constant mean position, **Equation 2.4** can be employed, regardless if the material is strained or relaxed. In addition, the chain segments between cross-links are supposed to be free in their movement enabling all conformations. These assumptions are reasonable for mobile polymer networks above T_g and low degrees of cross-linking, which exhibit long polymer chains between two junctions points with many possible conformations. Additionally, it is presumed that the volume remains unchanged during the deformation and that the displacement of each chain is proportional to the deformation of the entire material, which means the polymer network deforms affine, see **Figure 2.11**.

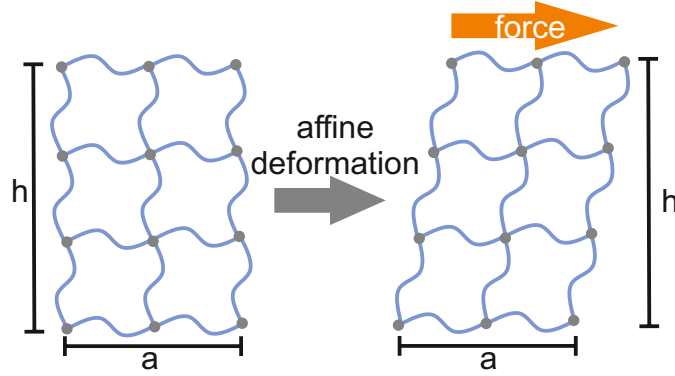


Figure 2.11: Schematic representation of a network deformation under affine conditions, i.e. the local displacement is proportional to the overall displacement.

The displacement under stress is modeled starting from a single chain segment between two intersections. One junction point is fixed in the origin $(0, 0, 0)$, while the other junction point will be shifted from (x, y, z) to (x', y', z') , as is shown in **Figure 2.12** [47]. Using affine networks, the deformation of the chain can be described by extension ratios λ and the distance r giving

$$\begin{aligned} x' &= \lambda_x x, & y' &= \lambda_y y, & z' &= \lambda_z z \\ r^2 &= (x^2 + y^2 + z^2) \end{aligned} \quad (2.11)$$

which leads to the following expressions employing **Equation 2.4**

$$\begin{aligned} S &= C - k_B \beta^2 (x^2 + y^2 + z^2) && \text{(before deformation)} \\ S' &= C - k_B \beta^2 (\lambda_x^2 x^2 + \lambda_y^2 y^2 + \lambda_z^2 z^2) && \text{(after deformation)} \end{aligned} \quad (2.12)$$

Consequently, the change in entropy of a single chain, which was deformed from (x, y, z) to (x', y', z') is given by

$$\Delta S_i = S' - S = -k_B \beta^2 [(\lambda_x^2 - 1)x^2 + (\lambda_y^2 - 1)y^2 + (\lambda_z^2 - 1)z^2] \quad (2.13)$$

A polymer network consists of many individual chains. Hence, going from the single chain to a network the number of polymer chains between junction points per unit volume N has to be taken into account. The amount of chains dN , which have their ends in the volume $dx dy dz$ at (x, y, z) can be derived from the distribution function, **Equation 2.1**, as

$$dN = N P(x, y, z) dx dy dz \quad (2.14)$$

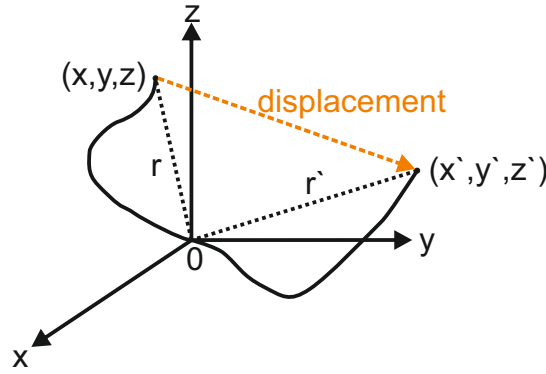


Figure 2.12: Schematic representation of the displacement of a cross-link in a polymer network from (x, y, z) to (x', y', z') under strain, adapted from [47].

which leads to

$$dN = N \left(\frac{\beta}{\pi^{1/2}} \right)^3 \exp [-\beta^2 (x^2 + y^2 + z^2)] \, dx dy dz \quad (2.15)$$

The change in entropy of single polymer chains upon deformation is given by ΔS_i and thus, the overall change in entropy ΔS is given by the integral over the individual entropy changes of all chains as

$$\Delta S = \int \Delta S_i \, dN \quad (2.16)$$

which leads to the following expression

$$\Delta S = \iiint_{-\infty}^{\infty} -\frac{Nk_B\beta^5}{\pi^{3/2}} [(\lambda_x^2 - 1)x^2 + (\lambda_y^2 - 1)y^2 + (\lambda_z^2 - 1)z^2] \exp [-\beta^2 (x^2 + y^2 + z^2)] \, dx dy dz \quad (2.17)$$

Equation 2.18 can be derived employing the standard solutions of the exponential functions with [46]

$$\int_{-\infty}^{\infty} \exp(-\beta^2 x^2) x^2 \, dx = \frac{\pi^{1/2}}{2\beta^3} \quad \text{and} \quad \int_{-\infty}^{\infty} \exp(-\beta^2 x^2) \, dx = \frac{\pi^{1/2}}{\beta} \quad (2.18)$$

Therefore, the overall entropy change is described by

$$\Delta S = -\frac{1}{2} Nk_B (\lambda_x^2 + \lambda_y^2 + \lambda_z^2 - 3) \quad (2.19)$$

Equation 2.19 is based on the assumption of an incompressibility of the material (constant volume), an uniaxial deformation, and a constant Poisson ratio (i.e. the contraction perpendicular to the stress is uniform). [47] It assigns the change in entropy to the number of polymer chains between two junction points per unit volume and the extension ratios. Consequently, the Helmholtz free enthalpy per unit volume ΔG is given by **Equation 2.20**, since the pressure and the enthalpy H remain unchanged at isothermal deformations.

$$\Delta G = -T\Delta S = \frac{1}{2}Nk_B T (\lambda_x^2 + \lambda_y^2 + \lambda_z^2 - 3) \quad (2.20)$$

The isothermal reversible work of the deformation per unit volume W is received using [47]

$$W = \frac{1}{2}Nk_B (\lambda_x^2 + \lambda_y^2 + \lambda_z^2 - 3) \quad (2.21)$$

The value of N is governed by the amount of physical and chemical junction points in the polymer. If defects are neglected and the molecular weight of the polymer M_n is much larger than that of the polymer between two junction points M_c ($M_n \gg M_c$) the influence of chain ends can be disregarded. Thus, the network can be treated as if all chains are coupled to the network on both ends and the density of the polymer ρ is obtained by the following approximation

$$\rho = \frac{NM_c}{N_A} \quad \text{or} \quad N = \frac{\rho N_A}{M_c} = \frac{\rho R}{M_c k_B} \quad \text{or} \quad N = \frac{V_0 R}{\nu_e k_B} \quad (2.22)$$

with V_0 as the volume of the undeformed polymer network, ν_e as the effective number of chains in a network, R as the gas constant and N_A as the Avogadro constant. Hence, N is given by $N = (\rho N_A) / M_c$ which leads to the following expression employing

$$W = \frac{\rho R}{2M_c} (\lambda_x^2 + \lambda_y^2 + \lambda_z^2 - 3) \quad (2.23)$$

The quality of predictions made by the affine model of network deformation is mainly governed by the quality of the assumed distribution function. The presumption of an ideal chain with no excluded volume interaction, which would lead to a Gaussian distribution function, is only applicable for low cross-linked networks. Additionally, ideal networks with little to no defects fail to describe real synthesized polymer networks. [47, 62, 63]

2.3.3.2 Phantom Model

The theory of phantom network assumes that chains are Gaussian and can be described by the distribution $P(r)$ of the end-to-end vector, compare **Equation 2.1**. [68] These chains only interact at junction points. As a consequence, chains can move freely through one another like 'phantoms' giving the theory its name. [1] Hereby, excluded volume effects and chain entanglements are excluded. In analogy to the affine model, it is assumed

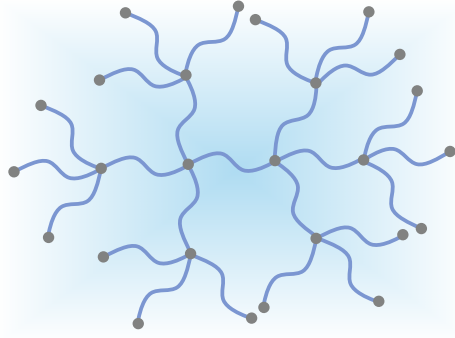


Figure 2.13: Visualization of the mathematical approach for the description of the phantom model. The network is considered as a patchwork of consecutive layers of connected, e.g. tetrafunctional, cross-links (with functionality $\zeta = 4$) having a tree-like topology. The last tier of cross-links fixes the network on the surface of the volume element. The network is unimodal, symmetrically grown, adapted from [1].

that all junctions at the surface of the network are fixed and deform affinely under a macroscopic strain, while all junctions and chains inside the bulk of the network fluctuate around their mean positions. [69]

For an infinitely large network with a symmetrical tree-like topology, as schematically depicted in **Figure 2.13**, the mean-square fluctuations of junctions $\langle(\Delta R)^2\rangle$ and correlations between fluctuations of two junctions i and j $\langle R_i \cdot R_j \rangle$ is described by the following matrix

$$\begin{bmatrix} \langle(\Delta R_i)^2\rangle & \langle\Delta R_i \cdot \Delta R_j\rangle \\ \langle\Delta R_j \cdot \Delta R_i\rangle & \langle(\Delta R_j)^2\rangle \end{bmatrix} = \frac{3}{2} \langle r^2 \rangle_0 \begin{bmatrix} \frac{\zeta-1}{\zeta(\zeta-2)} & \frac{1}{\zeta(\zeta-2)(\zeta-1)^m} \\ \frac{1}{\zeta(\zeta-2)(\zeta-1)^m} & \frac{\zeta-1}{\zeta(\zeta-2)} \end{bmatrix} \quad (2.24)$$

where ζ is the functionality of the junction point (e.g. $\zeta = 4$, see **Figure 2.2**) and m is the number of separating junctions in between i and j . The mean-square fluctuations of the distance $|r_{ij}| = |R_i - R_j|$ between the junctions i and j with the origin vectors R_i and R_j are given by

$$\langle(\Delta r_{ij})^2\rangle = \langle(\Delta R_i - \Delta R_j)^2\rangle = \frac{2 [(\zeta - 1)^{m+1} - 1]}{\zeta (\zeta - 2) (\zeta - 1)^m} \langle r^2 \rangle_0 \quad (2.25)$$

For the special case of mean-square fluctuations of the end-to-end vector r with $m = 0$ **Equation 2.25** simplifies to

$$\langle(\Delta r)^2\rangle = \frac{2}{\zeta} \langle r^2 \rangle_0 \quad (2.26)$$

The vector r_{ij} between junctions i and j is described by

$$r_{ij} = \bar{r}_{ij} + \Delta r_{ij} \quad (2.27)$$

where Δr_{ij} is the spontaneous fluctuation of r_{ij} and \bar{r}_{ij} is the time average of r_{ij} . Instantaneous fluctuations and mean values are uncorrelated. Consequently, squaring both sides of **Equation 2.27** and taking the ensemble average leads to

$$\langle r_{ij}^2 \rangle = \langle \bar{r}_{ij}^2 \rangle + \langle (\Delta r_{ij})^2 \rangle \quad (2.28)$$

Combining **Equation 2.26** and **Equation 2.28** results in

$$\langle \bar{r}_{ij}^2 \rangle = \left(1 - \frac{2}{\zeta}\right) \langle r^2 \rangle_0 \quad (2.29)$$

Like in the affine model, the mean positions of junctions transform affinely under macroscopic strain, while the fluctuations are independent of strain, hence

$$\langle r^2 \rangle = \left[\left(1 - \frac{2}{\zeta}\right) \frac{\lambda_x^2 + \lambda_y^2 + \lambda_z^2}{3} + \frac{2}{\zeta} \right] \langle r^2 \rangle_0 \quad (2.30)$$

Thus, the following expression for the free energy of the phantom network is obtained

$$\Delta A = \frac{1}{2} \left(1 - \frac{2}{\zeta}\right) N k_B T (\lambda_x^2 + \lambda_y^2 + \lambda_z^2 - 3) \quad (2.31)$$

The resulting **Equation 2.31** is very similar to **Equation 2.20** for the affine network. The only difference is the functionality ζ of the cross-link, which is taken into account in the phantom model. [8]

2.3.4 Equilibrium Swelling

Non-charged, cross-linked polymers are unable to formally dissolve but absorb solvent molecules by incorporating them into the network. This ability is one of the main features in superabsorbent polymers for their application. The swelling behavior of a polymeric network is described based on a simplified unit cubes, which consists of N polymer chains per unit volume. The main assumption includes that the increase in volume of the unit cube is proportional to the incorporated volume of the solvent. Here, the swollen material comprises of the volume fraction of liquid Φ_1 and that of the polymer Φ_2 . The swelling ratio Q , also called degree of swelling, is defined as the inverse of Φ_2 ($Q = 1/\Phi_2$). Employing the previously introduced extension ratios λ and assuming an isotropic expansion, the change of the cube in each dimension will be $\lambda_0 = 1/\Phi_2^{1/3}$. This change in entropy due to the swelling consist of two main contributions. On the one hand, the isotropic expansion from the solvent incorporation results in a reduction in entropy in the polymer

chains, since the amount of possible conformations decreases. On the other hand, the deformation of the swollen polymer network leads to further reductions in entropy. [47] The emerging change in entropy $\Delta S'_0$ upon deformation of the swollen network can be described by [47]

$$\Delta S'_0 = -\frac{1}{2}Nk_B (l_1^2 + l_2^2 + l_3^2 - 3) \quad (2.32)$$

with l_1 , l_2 and l_3 as the side length of the unit cell at the unswollen state. The change of entropy induced by the swelling ΔS_0 can be calculated by modifying **Equation 2.19** to [47]

$$\Delta S_0 = -\frac{1}{2}Nk_B (\lambda_1^2 + \lambda_2^2 + \lambda_3^2 - 3) = -\frac{1}{2}Nk_B (3\Phi_2^{-2/3} - 3) \quad (2.33)$$

The overall change of entropy for the swollen network $\Delta S'$ is the difference between the two types of entropy alternations and it yields

$$\Delta S' = \Delta S'_0 - \Delta S_0 = -\frac{1}{2}Nk_B (l_1^2 + l_2^2 + l_3^2 - 3\Phi_2^{-2/3}) \quad (2.34)$$

The extension ratios λ_1 , λ_2 and λ_3 are defined in relation to the undeformed swollen network with $l_1 = \lambda_1\lambda_0 = \lambda_1\Phi_2^{-1/3}$, $l_2 = \lambda_2\lambda_0 = \lambda_2\Phi_2^{-1/3}$, and $l_3 = \lambda_3\lambda_0 = \lambda_3\Phi_2^{-1/3}$. Therefore, **Equation 2.34** can be transformed into

$$\Delta S'_u = -\frac{1}{2}Nk_B\Phi_2^{-2/3} (\lambda_1^2 + \lambda_2^2 + \lambda_3^2 - 3) \quad (2.35)$$

which gives the entropy per unit volume of the unswollen network $\Delta S'_u$. For the swollen network the entropy per unit volume ΔS is calculated by

$$\Delta S = \Phi_2\Delta S'_u = -\frac{1}{2}Nk_B\Phi_2^{1/3} (\lambda_1^2 + \lambda_2^2 + \lambda_3^2 - 3) \quad (2.36)$$

Consequently, the isothermal reversible work per unit volume W is estimated by

$$W = -T\Delta S = \frac{1}{2}Nk_B T (3\Phi_2^{-2/3} - 3) \quad (2.37)$$

The **Equation 2.37** should be valid for non-charged, ideal polymer networks at any degree of swelling of the polymer. In practice, the swelling will reach an temperature-dependent equilibrium, if provided enough time. The Flory-Huggins approach for the solvent-polymer interaction, [4] together with the entropy change of the polymer, leads to the total free energy ΔG using

$$\Delta G = \Delta G_m + \Delta G_e \quad (2.38)$$

with ΔG_m as the free energy of mixing for an uncross-linked polymer network with the solvent and ΔG_e as the free energy of the network expansion. Taking **Equation 2.22**

into account and presuming that the network expands isotropically, results in $\lambda_1 = \lambda_2 = \lambda_3 = \Phi_2^{-1/3}$. **Equation 2.37** reduced to

$$W = \frac{3\rho RT}{2M_c} \left(\Phi_2^{-2/3} - 1 \right) \quad (2.39)$$

The change in free energy is given by dW/dn_1 , with n_1 as the number of solvent molecules, which expand the network. The relationship between Φ_2 and n_1 can be described by

$$\Phi_2 = \frac{n_2 V_2}{n_1 V_1 + n_2 V_2} \quad \text{or} \quad \frac{1}{\Phi_2} = 1 + n_1 V_1 \quad (2.40)$$

where V_1 and V_2 are the molar volume of the solvent and the polymer, respectively, while n_2 denotes the number of polymer molecules. By inserting **Equation 2.40** into **Equation 2.37** and subsequent differentiation one can receive

$$\Delta G_e = \frac{dW}{dn_1} = \frac{\rho RT}{M_c} V_1 \Phi_2^{1/3} \quad (2.41)$$

Combining the free energy of mixing ΔG_m from the Flory-Huggins solution theory, as displayed in **Equation 2.10**, with the free energy of expansion ΔG_e given by **Equation 2.41** leads to

$$\Delta G = RT \left[\ln(1 - \Phi_2) + \left(1 - \frac{1}{x_p} \right) \Phi_2 + \chi \Phi_2^2 + \frac{\rho V_1}{M_c} \Phi_2^{1/3} \right] \quad (2.42)$$

where χ is the Flory-Huggins parameter for the solvent-polymer interaction and x_p is the degree of polymerization. At the swelling equilibrium, the free energy $\Delta G = 0$. For high degree of polymerization, **Equation 2.42** can be simplified to the Flory-Rehner equation:

$$\Delta G = 0 = \ln(1 - \Phi_2) + \Phi_2 + X \Phi_2^2 + \frac{\rho V_1}{M_c} \Phi_2^{1/3} \quad (2.43)$$

The logarithmic is subjugated to a Taylor series expansion and stopped after the second term leading to

$$0 \approx \left(\chi - \frac{1}{2} \right) \Phi_2^2 + \frac{\rho V_1}{M_c} \Phi_2^{1/3} \quad \text{or} \quad \Phi_2^{5/3} \approx \left(\frac{1}{2} - \chi \right) \frac{M_c}{\rho V_1} \quad (2.44)$$

The degree of swelling $Q \equiv 1/\Phi_2$ can be modified according to **Equation 2.44** to

$$Q^{5/3} = M_c \frac{\frac{1}{2} - \chi}{\rho V_1^2} \quad (2.45)$$

with M_c as the molecular weight between two junction points. Since the degree of cross-linking ν_e/V_0 is inverse proportional to M_c rearranging **Equation 2.45** gives

$$Q = \left[M_c \frac{\frac{1}{2} - \chi}{\rho V_1^2} \right]^{3/5} \sim \left(\frac{\nu_e}{V_0} \right)^{-3/5} \quad (2.46)$$

Thus, Q increases for low cross-linked networks with a power law dependency and an exponent of -0.6. The degree of swelling is also affected by the quality of the solvent towards the polymer χ , as shown in **Equation 2.45**. For applying these simplified concepts on polyelectrolytes one should notice that all mentioned predictions above were made for the uncharged polymers. [3, 47, 62, 70]

2.4 Ionic Interaction

2.4.1 Poisson-Boltzmann

The theoretical description of polyelectrolyte networks can be evolved starting from charge distributions of single ions in solution. Ions can be considered as point charges with a negligible extent. The solvent is treated as a continuum, which is mainly characterized by its relative electric permittivity ϵ_r . Here, the distribution of the charged particles is mainly governed by the electrostatic repulsion and the thermodynamic motions. A single ion forms a Coulomb electrical field potential of spherical symmetry, which can be described by the Poisson equation, [8] as

$$\nabla^2 \phi(r) = \frac{1}{r^2} \frac{d}{dr} \left(r^2 \frac{d}{dr} \right) \phi(r) = -\frac{\rho(r)}{\epsilon_0 \epsilon_r} \quad (2.47)$$

with ∇ as the nabla operator, r as the distance between two ions and ϵ_0 as the dielectric constant. The charge density $\rho(r)$ can be described by the concentration of the individual ions c_j with the charge z_j and the elementary charge e giving

$$\rho(r) = e \sum_j z_j c_j(r) \quad (2.48)$$

Based on the assumption that the concentration of ions c_j follows a Boltzmann distribution of the energies, the potential $\phi(r)$ can be given by the Poisson-Boltzmann equation, [45] as

$$\nabla^2 \langle \phi(r) \rangle = -\frac{e}{\epsilon_0 \epsilon_r} \sum_j z_j c_j^0 \exp \left(-\frac{z_j e \langle \phi(r) \rangle}{k_B T} \right) \quad (2.49)$$

where k_B is the Boltzmann constant. However, the Poisson-Boltzmann differential cannot be analytically solved, since the potential ϕ is unknown. [62, 71]

2.4.2 Debye-Hückel Theory

A possibility to analytically solve the potential Φ is provided by the Debye-Hückel theory. The case of dilute solutions of ions is considered, in which the mean distance between two charges is large. Therefore, the electric repulsion becomes weak in comparison to the thermic energy, i.e. $|z_j e \Phi(r)| \ll k_B T$. In a next step, the exponential terms of the potential Φ are approximated by expansion in a Taylor series to the first term. The estimation is consequently limited to low concentrations, e.g. $\leq 10^{-3}$ mol/l for single charged ions $z_j = 1$. For higher charged ions the range of validity is even smaller. Based on these approximations the Debye length λ_D as a characteristic parameter for the definition

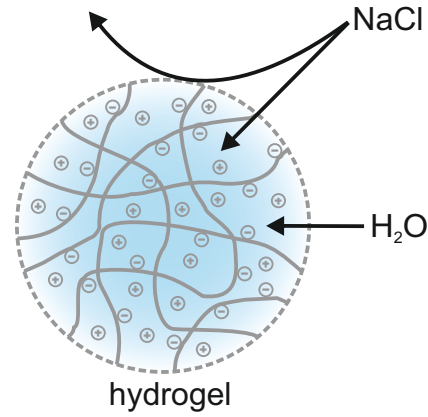


Figure 2.14: Polyelectrolyte particles in a salt solution partially repel ions from solution during swelling, whereby the surrounding solution is enriched in salt content.

the range of the electrostatic interaction of an ion can be introduced giving [8]

$$\begin{aligned}\nabla^2 \langle \Phi(r) \rangle &= \frac{e^2 \sum_j z_j^2 c_j^0}{\epsilon_0 \epsilon_r k_B T} \langle \Phi(r) \rangle \\ &= \frac{1}{\lambda_D^2} \langle \Phi(r) \rangle\end{aligned}\quad (2.50)$$

Consequently, the Debye length can be calculated by

$$\lambda_D = \frac{\epsilon_0 \epsilon_r k_B T}{2e^2 I} \quad \text{with} \quad I = \frac{1}{2} \sum_j z_j^2 n_j^0 \quad (2.51)$$

with I as the ionic strength of a dissolved ion. Since the Debye-Hückel theory is limited to the description of diluted ions in solution it struggles to characterize polyelectrolytes, which bear many ions on the backbone. In addition, polyelectrolytes have a considerable size in solution, which contradicts the assumption of a point charge. Nevertheless, the Debye-Hückel theory provides a guideline for the general behavior of charged single molecules. Furthermore, it explains qualitatively the repulsion of ions in solution, as is shown in **Figure 2.14**. The presented term of the ionic strength will be re-used in the following chapter. [62, 71] Another quantity that can be derived from the Debye-Hückel theory is the Bjerrum length λ_B , which describes the point where the electrostatic repulsion equals the thermal energy $k_B T$. At larger distances the counter-ions will diffuse away and at smaller a large share will stay bound to the ion. This counterion condensation takes place in polyelectrolytes with high charge density and is called Manning condensation. [72]

The Bjerrum length λ_B can be computed using [62]

$$\lambda_B = \frac{e^2}{4\pi\epsilon_0\epsilon_r k_B T} \quad (2.52)$$

and yields $\approx 7 \text{ \AA}$ at $T = 298 \text{ K}$ in water.

2.5 Swelling of Polyelectrolyte networks

2.5.1 Donnan Equilibrium

A polyelectrolyte network features immobilized ions, e.g. the COO^- attached to the backbone and its counter-ions, e.g. Na^+ . The free ions from the polyelectrolyte gel generate an osmotic pressure alike all other ions in solution and an electrostatic repulsion. The ions cannot leave the network, since they are attached to the backbone by electrostatic interactions. As a consequence, the gel can be treated as a concentrated solution of ions, which is separated by a semi-permeable membrane from the external medium, as schematically depicted in **Figure 2.15**. Ions and solvent molecules can interchange between the polymer matrix and the solution. The established distribution depends on the difference in chemical potential $\Delta\mu$ between the gel and the external medium, which can be described by

$$\Delta\mu_{1,sg} = \Delta\mu_{1,s,ion} - \Delta\mu_{1,g,ion} \quad (2.53)$$

with $\Delta\mu_{1,s,ion}$ as the chemical potential of the solution and $\Delta\mu_{1,g,ion}$ as the chemical potential of the gel. Generally, the chemical potential $\Delta\mu_1$ of a species 1 with respect to the osmotic pressure is given by

$$\Delta\mu_1 = \mu_1 - \mu_1^0 = gRT \ln(x_1) \quad (2.54)$$

where μ_1 is the chemical potential of species 1, μ_1^0 the chemical potential of species 1 at the ground state, g the osmotic coefficient and x_1 the mole fraction of species 1 in the solvent. The absolute temperature of the solution is denoted by T and the gas constant by R . In case of dilute systems, $g \approx 1$ and $x_1 \approx -V_1 \sum_j c_j$, which leads to

$$\Delta\mu_1 = -RT V_1 \sum_j c_j \quad (2.55)$$

with c_j as the concentration of species j in solution. Inserting the chemical potential of species 1 in **Equation 2.53** results in

$$\Delta\mu_{1,sg} = -RT V_1 \sum_j (c_{j,s} - c_{j,g}) \quad (2.56)$$

Here, the concentrations of species j outside the gel $c_{j,s}$ and inside the gel $c_{j,g}$ are required. [62, 63, 67]

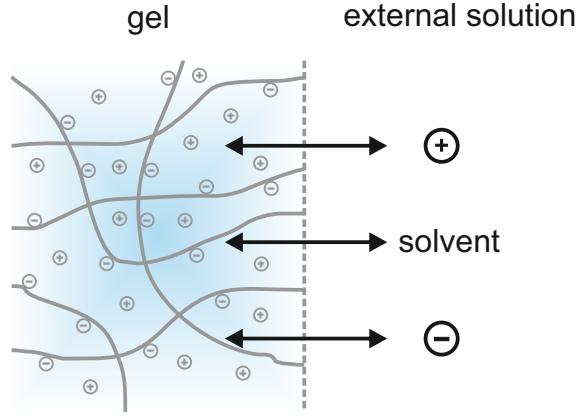


Figure 2.15: Figure of swollen ionic gel in equilibrium with external electrolyte solution. Adapted from [4].

2.5.2 Flory-Rehner Theory

The change in the chemical potential by swelling the network polymer is separated into three terms, the mixing of the polymer and the solvent $\Delta\mu_{1, ps}$, the mixing of the polymer with the mobile ions of the external solution $\Delta\mu_{1, i}$ and the elastic deformation of the network $\Delta\mu_{1, el}$

$$\mu_1 - \mu_1^0 = \Delta\mu_{1, ps} + \Delta\mu_{1, i} + \Delta\mu_{1, el} \quad (2.57)$$

Since the ions in the polymer cause an osmotic pressure Π and the solvent enters the polymer due to the osmotic pressure derived from the chemical potential, it is justifiable to express **Equation 2.57** in terms of [65]

$$\Pi_1 = \frac{\Delta\mu_1}{V_1} = \Pi_{1, ps} + \Pi_{1, i} + \Pi_{1, el} \quad (2.58)$$

It can be assumed that the external solution yields a strong electrolyte in the form $A^+ B^-$, while the ions in the gel are immobilized. A part of the mobile ions $A^+ B^-$ will enter the network. The concentration gradient causes the osmotic pressure. Therefore, the osmotic pressure is given by

$$\Pi = RT \sum_j \Delta c_j = RT [i c_2 - (c_{j, s} - c_{j, g})] \quad (2.59)$$

in diluted systems, where interactions between the different components can be neglected. The parameter i denotes the ionization degree of the monomers. The concentration of free ions due to dissolving of the polyelectrolyte is $i c_2$, $c_{j, s}$ is the concentration of the

external electrolyte and $c_{j, g}$ the concentration of the electrolyte which entered the gel. The parameter c_2 can be substituted by the polymer volume fraction per volume in the swollen state ϕ_2/V_2 . The quantity of $c_{j, s} - c_{j, g}$ is not predictable by theory and it has to be evaluated by experiments. For small concentrations of ions in the external solution $c_{j, s} \ll ic_2$ the second term of **Equation 2.59** might be neglected. Furthermore, it can be assumed that the swelling reached its equilibrium. Therefore, $\Pi = \Pi_p = 0$ and since $d\mu = (dG/dn)$, Π can be derived from ΔG . Extracting Π from **Equation 2.44** and equating with **Equation 2.59** yields

$$\frac{i\phi_2}{V_2} = \frac{1}{V_1} \left[\left(\chi - \frac{1}{2} \right) \Phi_2^2 + \frac{\rho V_1}{M_c} \Phi_2^{1/3} \right] \quad (2.60)$$

For low salt concentrations the swelling might be high causing ϕ_2 to become small. If the number of junctions ν_e per unit volume V_0 with $\rho/M_c \approx V_0/\nu_e$ is employed and the solvent polymer interactions are weak, then the second term can be neglected simplifying **Equation 2.60** to

$$Q^{2/3} \approx \frac{i V_0}{V_2 \nu_e} \quad (2.61)$$

where Q is the degree of swelling with $Q = 1/\phi_2$. In the opposite case, if the external salt concentration is high $c_{j, s} \gg ic_2$, the concentration difference $c_{j, s} - c_{j, g}$ might be of the same magnitude as ic_2 . Hence, the osmotic pressure is given by

$$\Pi \approx RT \frac{(ic_2)^2}{4I} \quad (2.62)$$

where I is the ionic strength of the Debye-Hückel theory. Combining **Equation 2.62** with **Equation 2.44** gives

$$Q^{5/3} \approx \left[\left(\frac{i}{2V_2 I^{1/2}} \right)^2 + \frac{\frac{1}{2} - X_1}{V_1} \right] \frac{V_0}{\nu_e} \quad (2.63)$$

for a diluted polymer. In case of high salt concentrations the effective charge of the polyelectrolyte is shielded by the ions and the network behaves similar as an uncharged polymer. Therefore, **Equation 2.63** becomes **Equation 2.45**. [62, 63, 73, 74] The consequence is that for highly charged polymers again a power law dependency of Q on the cross-link density is to be expected, with an exponent of -0.6.

2.6 Basics of Nuclear Magnetic Resonance Spectroscopy

Nuclear magnetic resonance (NMR) spectroscopy, which was discovered by E. Purcell and F. Bloch in 1946, [75] is a commonly used technique for the investigation of the chemical structure of molecules. In the current thesis NMR was used for two purposes: On the one hand, high-field NMR ($\omega_L/2\pi = 400$ MHz) was utilized as standard characterization method to obtain information about the chemical structure of self-synthesized polymers. Especially quantification of the end-groups and conversion rates of the cross-linking process were analyzed, as is shown in **Chapter 3.1.5**. On the other hand, ^1H -NMR relaxometry was applied at low-fields ($\omega_L/2\pi = 20$ MHz) to investigate the polymer mobility. The synthesized polymer networks consist of rigid components like cross-linking points, restrained polymer chains as bridges between them, as well as flexible dangling ends and sol. Each of these parts relax on a different time scale and thus, information about the network topology are accessible. Defects in the network structure, such as loops, also contribute to the overall relaxation behavior of the network and are simultaneously measured. To provide an overview of the basic principles of NMR and to understand the differences of the applied methods, a short introduction of the technique will be given in this section. For more details, the reader is referred to the literature. [76–79]

All isotopes, without an even number of both neutrons and protons, exhibit a spin (angular momentum) I , which is quantized into $2I + 1$ discrete energy states. In case of the most abundant isotope ^1H of hydrogen, the nuclei have a spin of $I = 1/2$. If a static magnetic field \vec{B}_0 is applied along the z-axis, the spins will undergo precession along the field direction. The precession can be described by its characteristic frequency, the Larmor frequency ω_L , which is proportional to the strength of the magnetic field $B_0 = |\vec{B}_0|$ and is given by

$$\omega_L = \gamma B_0 \quad (2.64)$$

with the gyromagnetic ratio γ , which specifies the magnitude of nuclear magnetic moments of a certain type of nuclei.

NMR spectroscopy allows for a multitude of interactions with the system of nuclei spins present in molecules. Consequently, different quantum mechanic problems, which corresponds to difference structural motives in the analyte, can be solved depending on the employed NMR technique. The sum of all energy exchanges in NMR is given by the Hamiltonian \hat{H} , an mathematical operator corresponding to the kinetic energies and potential energies of the system, which is described by

$$\hat{H} = \hat{H}_{Zeeman} + \hat{H}_{dipol} + \hat{H}_{quadropol} + \hat{H}_J + \hat{H}_{chemical} \quad (2.65)$$

with \hat{H}_{Zeeman} resulting from the Zeeman splitting, while \hat{H}_{dipol} and $\hat{H}_{quadropol}$ represent the dipolar and quadropolar interactions, respectively. The operator \hat{H}_J denotes the so-

called J-coupling, whereas $\hat{H}_{chemical}$ is caused by the chemical environment of the nuclei leading to the so-called chemical shift. In the following, a qualitative overview of these interaction will be provided and how they can be employed in NMR spectroscopy.

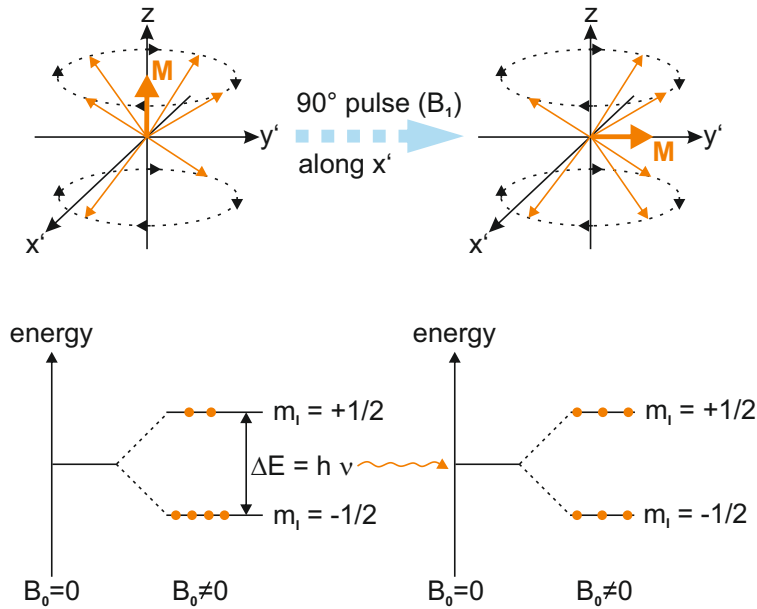


Figure 2.16: Principle scheme of the NMR process. The spins precess after application of an external magnetic field \vec{B}_0 along the z-axis (left), displayed in a rotating frame around z. The population difference between the two separate energy states results in a net magnetization \vec{M} . A pulse B_1 perpendicular to the static field \vec{B}_0 causes the spins to flip. This results in saturation of the energy levels and the net magnetization rotates into the $x'y'$ -plane (right).

Zeeman Effect $\left[\hat{H}_{Zeeman} \right]$

The Zeeman splitting is described by the Hamiltonian [76]

$$\hat{H}_{Zeeman} = -\gamma \hbar \hat{I} \mathbf{1} \hat{B}_0 \quad (2.66)$$

where \hbar is the Planck quantum, \hat{I} the spin vector operator, $\mathbf{1}$ the unit matrix, and \hat{B}_0 the magnetic field operator. The Zeeman interaction, is the strongest effect in most NMR experiments interfering with the spins. [79] By applying the magnetic field \vec{B}_0 , the initially degenerated energy states of the spins split up in two energy levels with Eigenvalues of $m_I = +1/2$ or $m_I = -1/2$, which reassemble parallel and anti-parallel precession around the axis of \vec{B}_0 . The two energetic states differ by the energy ΔE , as shown in **Figure**

2.16 on the left. The population difference of these two states is governed by the energy difference ΔE and is provided by the Boltzmann relationship

$$\frac{N_{+\frac{1}{2}}}{N_{-\frac{1}{2}}} = \exp\left(-\frac{\Delta E}{k_B T}\right) \approx 1 - \frac{\hbar\omega_L}{k_B T} \quad (2.67)$$

where $N_{-1/2}$ is the population in the ground state and $N_{+1/2}$ the population in the excited state. The energy difference ΔE is small compared to the thermal energy and consequently, the population difference is only in the range of 10 to 100 ppm for protons in high field NMR. A macroscopic net magnetization \vec{M} along the magnetic field \vec{B}_0 is resulting from the population difference since more spins are in the ground state, as it is displayed in **Figure 2.16** on the left. The energy exchange is commonly visualized in a coordinate system (x', y', z) that rotates with ω_L around the z-axis and \vec{B}_1 and \vec{M} appear static. In order to transfer spins from the ground state ($m_I = -1/2$) to the excited state ($m_I = +1/2$) energy is required in form of a second, rotating magnetic field \vec{B}_1 perpendicular to the static \vec{B}_0 -field. The \vec{B}_1 -field is emitted from the probe coil, while the pulse length is usually adjusted to bring the full net magnetization into the xy-plane, a so-called 90° pulse in NMR. Resonance occurs if the frequency ν of the second field B_1 matches the Larmor frequency $\omega_L/2\pi$.¹ The transition is called Rabi oscillation. After the 90° pulse, both energy states are saturated and the net magnetization \vec{M} is located in the xy-plane.

Chemical shift $\left[\hat{H}_{chemical}\right]$

As described in **Equation 2.65** further interactions are relevant to NMR spectroscopy. The difference in ω_L between the two spins can be measured in form of the corresponding resonance frequency difference. Here, the protons are shielded by their surrounding electrons, which alters the effective magnetic field that influences the nuclei. The local reduction of the \vec{B}_0 -field reassemble in first approximation the electron density at every point in a molecule and thus, mirrors the chemical environment of each nuclei. Precisely, the Hamilton of the chemical shift is provided by [80]

$$\hat{H}_{chemical} = \gamma \hat{I} \mathbf{b} \hat{B}_0 \quad (2.68)$$

with the shielding tensor \mathbf{b} . Hence, the resonance frequency $\Delta\nu$ are slightly changed by the shielding in the range of ~ 10 ppm for each proton. Thus, the proton resonance signals split up into a NMR-spectrum with distinct peaks, which can be assigned to the chemical groups of the analyzed molecule revealing its structure.

J-couplings $\left[\hat{H}_J\right]$

In addition to the chemical shift, a fine splitting of the peaks in the frequency domain of

¹Since the pulses in NMR are very short, they contain a broad distribution of frequencies around ω_L and therefore excite all spins similarly and simultaneously.

^1H -NMR spectra can be observed. The effect is arising from indirect spin-spin interactions along the chemical bonds, the J-couplings. These can be described using the Hamiltonian [80]

$$\hat{H}_J = 2\pi\hat{I}_i\mathbf{J}\hat{I}_j \quad (2.69)$$

where \mathbf{J} is the J-coupling tensor and \hat{I}_i and \hat{I}_j denote the spin vector operators of the spins i and j , respectively. The J-couplings are mainly dominated by the next neighboring groups of the proton, since the coupling strength strongly decays with each consecutive bond. Depending on the number of next neighbors, a splitting of the peak in multiplets can be observed and thus, the order of neighboring groups assigned and with it the chemical structure of the molecule.

Quadrupolar couplings $[\hat{H}_{quadrupol}]$

The quadrupolar interactions are expressed by the operator [80]

$$\hat{H}_{quadrupol} = \frac{eQ}{[2I(2I-1)\hbar]}\hat{I}\mathbf{Q}\hat{I} \quad (2.70)$$

with the elemental charge e , the proportionality factor Q , and the quadrupolar coupling tensor \mathbf{Q} . The ^1H -nuclei exhibits no quadrupole moment. Consequently, the quadrupolar interactions can be neglected in ^1H -NMR spectroscopy.

Dipolar couplings $[\hat{H}_{dipol}]$

The ^1H -nuclei exhibits a magnetic dipole moment, which leads to dipolar interactions that can be described by [80]

$$\hat{H}_{dipol} = -\frac{\mu_0\gamma_i\gamma_j}{4\pi}\hat{I}_i\mathbf{D}\hat{I}_j \quad (2.71)$$

where μ_0 is the magnetic susceptibility, \mathbf{D} denotes the dipolar coupling tensor, while γ_i and γ_j are the gyromagnetic ratios of the spins i and j , respectively. In the standard spectral resolved high field liquid ^1H -NMR the dipolar interactions between spins are averaged by the fast motion of the molecules. If the motion of the molecules (and with it the spins) is restricted, an effective residual dipolar coupling remains. These residual couplings can now be utilized to access information about the network structure. The effect is crucial for the characterization of the polymer structures by low field ^1H -NMR and therefore, will be discussed in detail in **Chapter 4.2.1, p. 64**.

Spectra and relaxation processes

The precessing magnetization \vec{M} induces a corresponding oscillating voltage in the detection coil surrounding the sample. [77] After a certain time-frame, different relaxation

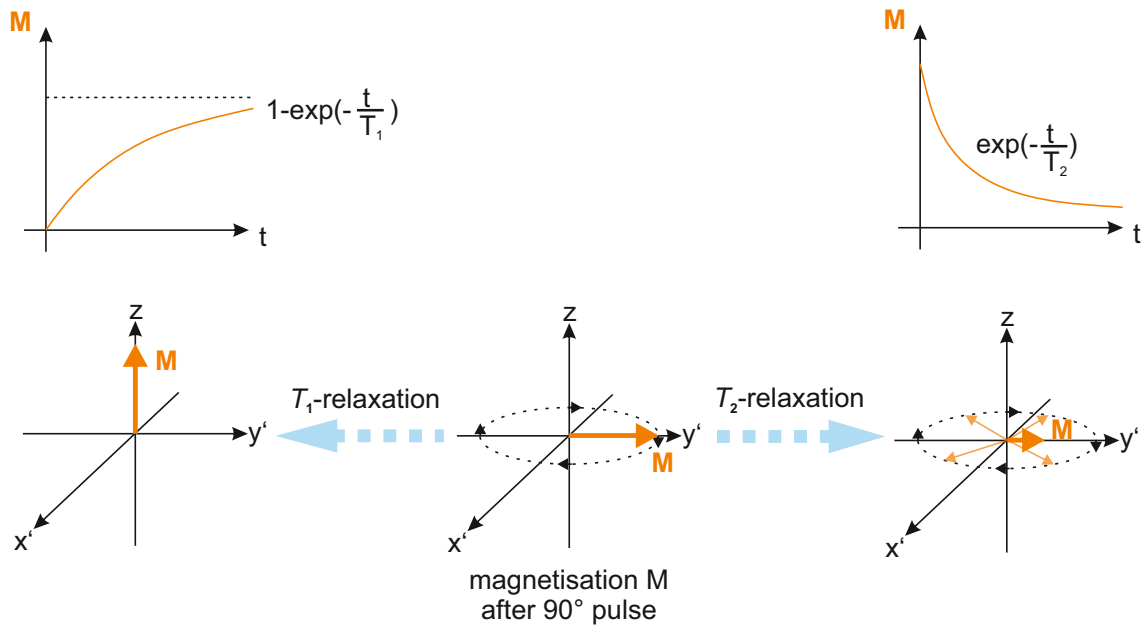


Figure 2.17: After applying a 90° pulse the net magnetization \vec{M} is rotating in the $x'y'$ -plane (middle). Two relaxation mechanisms lead \vec{M} back to its initial state at equilibrium: The longitudinal T_1 -relaxation along the z -axis (left), where the energy is transferred to the surrounding lattice and the spins drop to the ground state. In case of the transversal T_2 -relaxation (right) the spins are dephasing over time, which causes a loss of net magnetization in the $x'y'$ -plane.

mechanisms (T_2 -relaxation), such as dipolar coupling, will dampen the oscillating signal in plane resulting in a so-called free induction decay (FID). In parallel, local fluctuations in the magnetic field induce other relaxation processes, which bring the spin-population back to the initial steady state Boltzmann distribution (T_1 -relaxation), as shown in **Figure 2.17**. Afterwards, a new pulse or scan can be applied to the sample.

NMR can be utilized in two ways to obtain information about the material structure on different length scales. In liquid NMR acquiring of the resonance frequency with its small deviation based on the chemical shift and the fine splitting arising from the J-coupling allows for the determination of the chemical structure of the molecule. Practically, the resonances are not scanned individually. [76] Instead the time dependent FID is recorded, which contains information about all frequencies and transferred via Fourier transformation into the frequency space. Since the energy difference, and with it the population difference, between the energy states depend on the \vec{B}_0 -field, stronger magnetic fields

result in a higher sensitivity of a NMR spectrometer.¹ Consequently, high-field NMR spectrometer are employed whenever spectral resolution is required.

In the second technique, the time dependent relaxation processes are measured instead of acquiring a the full frequency spectrum. Here, the longitudinal relaxation, also referred to as spin lattice relaxation (T_1) and the transverse relaxation (T_2), also termed spin-spin relaxation are obtained, as displayed in **Figure 2.17**. The T_1 -relaxation describes the recovery of the magnetization along the z -axis, while the T_2 -relaxation represents the de-phasing of spins in the $x'y'$ -plane. Examination of the decay of the NMR experiments yield the longitudinal relaxation the characteristic time constant T_1 and for the transverse relaxation T_2 . The relaxation processes of fast moving molecules in liquids can be described using the BPP-theory (named after Bloembergen, Purcell and Pound). The statistical motions of the molecule causes small fluctuation in the magnetic field at the site of the nuclei. These fluctuations lead to transitions of the energetic states, which result in the dissipation of the energy of the excited state. The relaxation process is governed by the spectral density function $J(\omega)$, which is by definition the Fourier transform of the auto-correlation function of the motion. With $J(\omega)$ the characteristic relaxation times T_1 and T_2 can be calculated according to [80]

$$\frac{1}{T_1} = \left(\frac{\mu_0 \hbar}{4\pi} \right)^2 \frac{\gamma^4}{r^6} I(I+1) \frac{3}{2} [J(\omega_L) + J(2\omega_L)] \quad (2.72)$$

$$\frac{1}{T_2} = \left(\frac{\mu_0 \hbar}{4\pi} \right)^2 \frac{\gamma^4}{r^6} I(I+1) \frac{3}{2} \left[\frac{J(\omega=0)}{4} + \frac{5J(\omega_L)}{2} + \frac{J(2\omega_L)}{4} \right] \quad (2.73)$$

Through studies of the relaxation mechanism valuable information about the dynamics of the polymer chains in the network are accessible, which can be employed to draw conclusions about the network topology. The relaxation mechanism are dominated by dipolar couplings and their application to hydrogel networks will be described in detail in the characterization part, **Chapter 4.2.1, p. 64**. This method requires high pulse intensities and is tolerant towards less homogeneous magnetic fields, the measurements can be conducted on a simpler spectrometer at lower fields. In this thesis, a 20 MHz relaxometer was utilized, see **Appendix B.3**. Such instruments are inexpensive (<100,000 €) in the maintenance and were successfully employed to analyze dynamics in polyelectrolyte hydrogels in previous works. [14, 41, 81]

¹with the signal to noise ratio $S/N \sim B_0^2$

2.7 Basics of Size-Exclusion Chromatography

The following section provides an insight into size-exclusion chromatography (SEC) as a characterization technique for polymers. For detailed information the reader is referred to the literature. [82, 83] Most synthetic polymers are heterogeneous in terms of chain length, i.e. molar mass. They reveal a molar mass distribution, which originates from the statistical nature of the polymerization process. Polymers are often characterized by average molar masses, prominently the number average molecular weight M_n and the weight average molecular weight M_w . The M_n expresses the amount of species in terms of number of moles n_i and the weight-average molar mass M_w considers the mass m_i of the species i . The M_n and the M_w can be calculated using the individual molecular weight M_i of species i by **Equation 2.74** and **Equation 2.75**, respectively

$$M_n = \frac{\sum n_i M_i}{n_i} \quad (2.74)$$

$$M_w = \frac{\sum m_i M_i}{m_i} = \frac{\sum n_i^2 M_i}{\sum n_i M_i} \quad (2.75)$$

The dispersity of the obtained molecular weight distribution is commonly described by the dispersity index D with $D = M_w/M_n$.

Size-exclusion chromatography is a commonly employed technique for the separation of polymers with respect to their hydrodynamic volume in solution. Here, a solution of the analyte is passed through a column filled with gel particles at a fixed flow rate. These particles of the stationary phase exhibits pores of a controlled size in the dimension of the desolved polymer. The small polymer molecules will be able to penetrate into these pores, while large molecules remain in the interstitial solution. After some time, the small molecules will diffuse out of the pores and continue to flow down the column until they meet another pore of an adequate size. Consequently, large molecules will elute faster than small molecules since they reside less in the pores, which results in distinct chromatographic bands, as displayed in **Figure 2.18**. A concentration dependent detector located at the end of the column, usually a differential refractive index (DRI) detector, records the eluting peaks.

The distribution of the eluting species between the gel and the interstitial solution in SEC is dependent on both, the pore size distribution of the stationary phase and the size of the polymers. In SEC, the pore size distribution of the gel is taken into account by calibration with polymer standards of a known size. By using their molecular weight dependent elution curve as a reference, the molecular weight distribution of an unknown polymer of the same type, by means of composition and topology, can be determined. The elugram

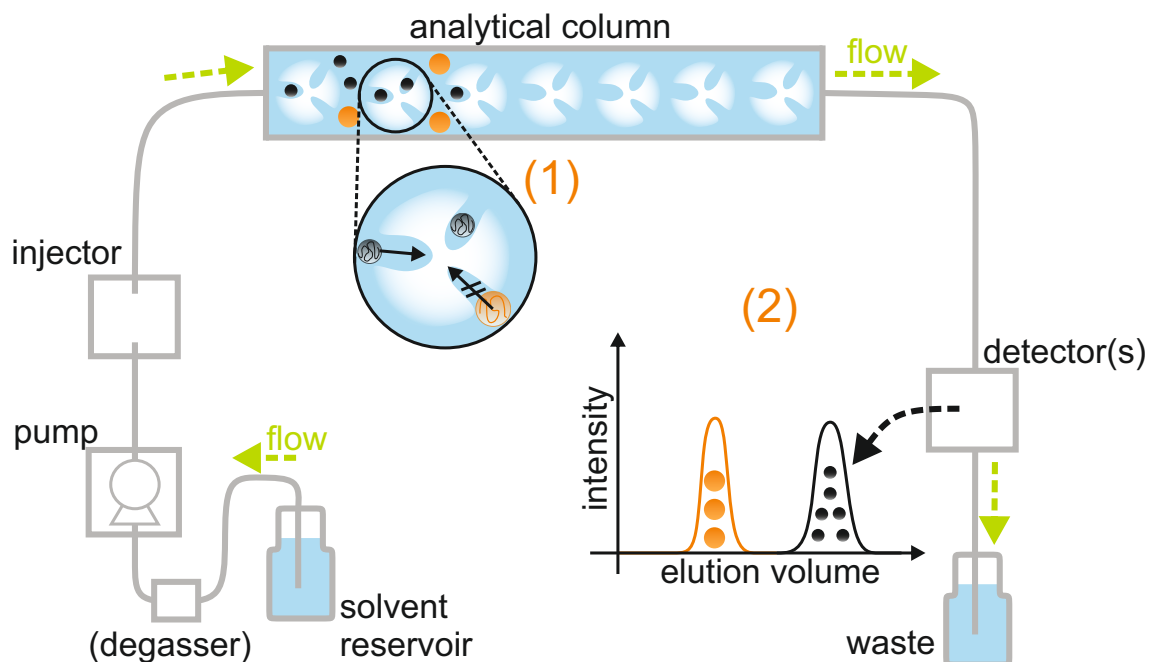


Figure 2.18: Scheme of a size exclusion chromatography set-up with – in flow direction [green] – the solvent reservoir, (optional: a degasser unit for increased baseline stability), the high-pressure pump, an injector with autosampler, the analytical column, the detector(s) and the solvent waste. (1) In the analytical column the polymers are separated according to their size in solution. Small polymer coils [gray] might enter the porous stationary phase, while large coils [orange] find no suitable pores to reside and thus, flow faster down the column. (2) This results in different elution volumes, which can be recorded by the detector(s). Adapted from [82] and [83].

of a column exhibits an upper and lower exclusion limit at which the column shows no separation anymore. At the upper limit the large polymer finds no suitable pore to diffuse in and thus, no separation occurs, while at the lower exclusion limit the analyte is small enough that all pores are available and a further reduction of the polymer size yields no difference, see **Figure 2.19**. The void volume of a column V_0 , i.e. the volume of the interstitial solvent between the particles, is characterized by the upper exclusion limit. Whereas the volume of the pores V_{pore} can be described by the difference of the void volume and the total available volume of the column V_t , which is denoted by the lower exclusion limit, i.e. $V_{\text{pores}} = V_t - V_0$.

The size of the polymers in solution is dependent on the chain length (\sim molecular weight,

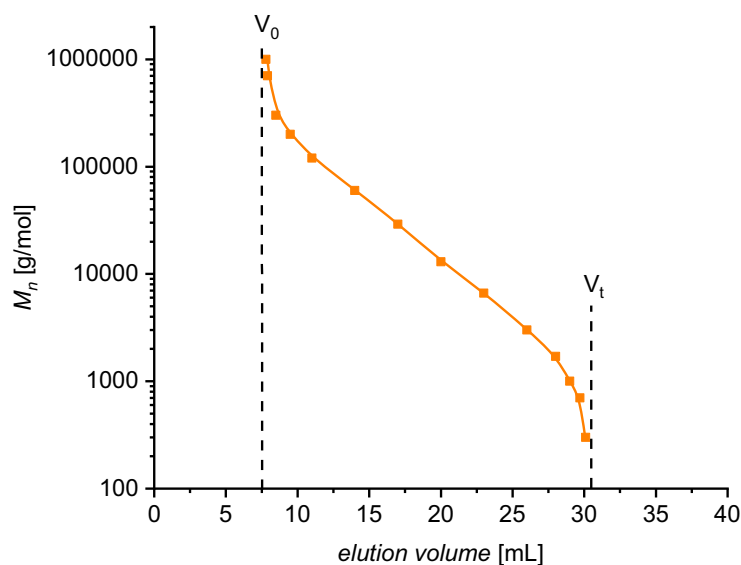


Figure 2.19: Typical SEC calibration curve: The logarithm of the molecular weight is plotted versus the elution volume revealing the upper exclusion limit (\equiv void volume of the column V_0), i.e. the polymer coils are too large for the pores, and the lower exclusion limit (\equiv total available volume $V_t = V_0 + V_{\text{pores}}$), i.e. the polymer is small enough that it fits in all pores. Adapted from [82].

see **Equation 2.2**) and the interaction between the monomer unit and the solvent. Polymer chains fold in solution forming a coil, whose extent can be described by its equivalent radius, the radius of hydration R_h . The molecular weight dependency can be empirically determined by **Equation 2.76**

$$R_h = Q_M M^\alpha \quad (2.76)$$

with q_M and α as polymer-solvent dependent parameters (e.g. $q_M = 0.0145$ and $\alpha = 0.578$ for pullulan in water). [84]

The conditions in SEC are ideally adjusted that no enthalpic interaction between the analyte and the stationary phase take place. Thus, the process is exclusively driven by the entropy S , which is dependent of the number of possible conformations Ω the species in solution can assume, with $S = k_B \ln(\Omega/\Omega_0)$. The resulting equilibrium constant K_{SEC} , which describes the partitioning of the polymers between the pores and the solution, can be described by [82]

$$K_{SEC} = \exp\left(\frac{\Delta S}{R}\right) \quad (2.77)$$

where R is the gas constant.

To ensure, that the technique is driven under purely entropic conditions, the polarity of the solvent and the stationary phase are adapted to each other. The stationary phase consists normally of highly cross-linked polymer beads. Common solvent-gel combinations include tetrahydrofuran as solvent and polystyrene-divinylbenzene columns (SDV) for unpolar polymers, dimethylformamide and polymethylmethacrylate columns for polar polymers and water with polyacrylic acid columns for highly polar polymers.

The most common type of detector is the differential refractive index (DRI) detector. [82] It measures differences in the refractive index between the moving, sample-containing stream and a static reference of the pure eluent by a split optical cell. The detector response is proportional to the concentration of the polymer and requires that the refractive index of the polymer is distinct from the mobile phase in which they are dissolved. Another common type of concentration dependent detector is the ultraviolet (UV) detector, which is sensitive to chemical functionalities, such as aromatic rings and carbonyls. [82] The combination of a concentration dependent detector (e.g DRI) and a detector, which is sensitive to chemical functionalities (e.g UV detector) can enable the determination of the composition of co-polymers. The multi-angle laser light scattering detectors (MALLS or MALS) measure the scattered light at up to 18 different angles. The MALS detector is capable of producing Zimm plots, which allows for the determination of the weight-average molecular weight, radius of gyration, and second virial coefficient of the polymer. With these information different polymer topologies can be distinguished (e.g. linear chains from branched polymers). [82] A relatively new coupled technique relies on the utilization of an on-line coupled Fourier-transform infrared spectrometer (FTIR) as information rich detector. [85,86] Thus, the molecular weight dependent chemical composition can be accessed. To enhance the signal-to-noise ratio in SEC-FTIR further, quantum cascade lasers (QCL) have been introduced as new IR source, which allows even for the on-line determination of single groups in the polymer chain. [87,88]

Chapter 3

Synthesis of Defined Polyelectrolyte Hydrogels

The main goal of this thesis is to understand how the network architecture of polyelectrolyte hydrogels is influenced by different polymerization techniques. Therefore, a variety of different synthetic techniques is employed, which will be described in detail in this chapter. The synthetic parameters of each procedure are systematically adjusted with the aim of achieving more homogeneous network structures, with respect to the mesh size distribution. General considerations are described, on how the different architectures can be accomplished and which synthetic parameters should be altered. First, hydrogels are produced by free radical polymerization (FRP) as a reference system based on poly(sodium acrylate) (PSA), or on poly(sodium methacrylate) (PSMA). These materials were chosen, since they are commonly utilized as hydrogels in industries. [8]

Next, strategies for the formation of networks with more uniform mesh size distributions are presented. In this thesis, reversible addition-fragmentation chain transfer (RAFT) polymerization as well as anionic polymerization based routes will be critically discussed. In the context of anionic polymerization, three independent strategies will be reviewed, as displayed in **Table 3.1**:

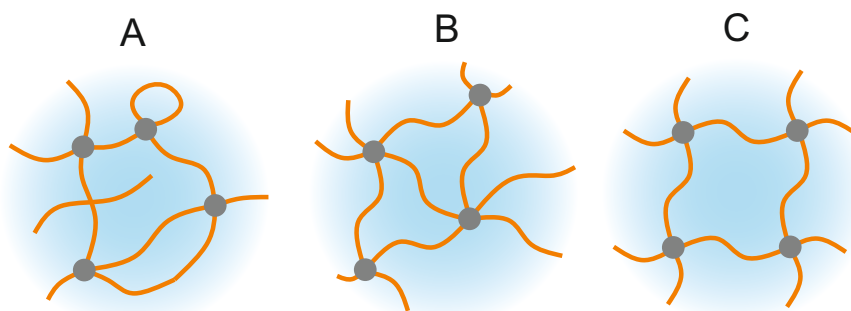
- A) The direct co-polymerization of monomer and cross-linker, while free radical, anionic and RAFT polymerization are used
- B) The sequential co-polymerization of monomer and cross-linker, where first the polymer is created and then the chains are interconnected
- C) The network synthesis by anionic polymerization of the chains and subsequent network formation via azide-alkyne Huisgen ligation

It has to be considered that in FRP the cross-linking reaction depends on the statistical incorporation of a molecule with two or more vinyl functionalities into two growing polymer chains. As a consequence, network defects, such as dangling ends and loops, are inevitable formed. [27] Therefore, a broad range of different chain lengths between two junction points are to be expected, as well as regions in which the polymer concentration

is permanently higher. [89] In case of the direct co-polymerization of monomer and cross-linker similar to the FRP using RAFT polymerization or anionic polymerization a more narrow mesh size distribution might be expected. While exhibiting the same statistical incorporation of the cross-linker, side reactions, such as chain termination, that would lead to additional dangling ends inside the network structure are suppressed and thus, a better control over the polymerization is achieved.

In the sequential approach, the chain lengths between two junction points are uniform. The cross-link functionality remains ill defined, since different amounts of chains might end in the cross-linker micelles.

The sequential approach followed by azide-alkyne Huisgen ligation provides defined chain lengths between two junction points as well as a fixed cross-link functionality. In principle, increasingly homogeneous networks should be achievable by following the described approaches as outlined in the subsequent sections.



	A) randomly cross-linked networks	B) quasi-model networks	C) model networks
elastic chains	broad length distribution	defined length	defined length
cross-link functionality	fixed	not fixed	fixed
polymerization technique	free radical (RAFT/anionic)	anionic	anionic
assumed pore size distribution	broad (middle–broad)	middle	small

Table 3.1: Schematic representation of the polymer networks achievable by the different synthetic procedures including the presumed network heterogeneities.

3.1 Methacrylic Acid

3.1.1 Free Radical Polymerization, (Type A)

In the present work, all samples are self-synthesized to ensure full control over the network parameters. The synthesis was carried out in 1,4-dioxane by free radical co-polymerization of methacrylic acid with an di-functional co-monomer as cross-linker. Here, the in-situ cross-linking was chosen instead of cross-linking of the final polymer chains due to simplicity of the approach. The random co-polymerization of the linker molecule with the monomer yields polymer network samples with an allegedly broad mesh size distribution. [1,23] The spatial heterogeneity originates from the mechanism of the cross-linking co-polymerization and different aspects have to be considered. In the early stage of the polymerization, chain cyclization and local multiple cross-linking are pronounced. This results in the formation of a suspension of nanogels. At higher conversions, these nanogels are loosely interconnected to a continuous polymer network, as displayed in **Figure 3.1**. Therefore, the synthesized hydrogel reveals a heterogeneity on a 10 – 100 nm length scale. [89]

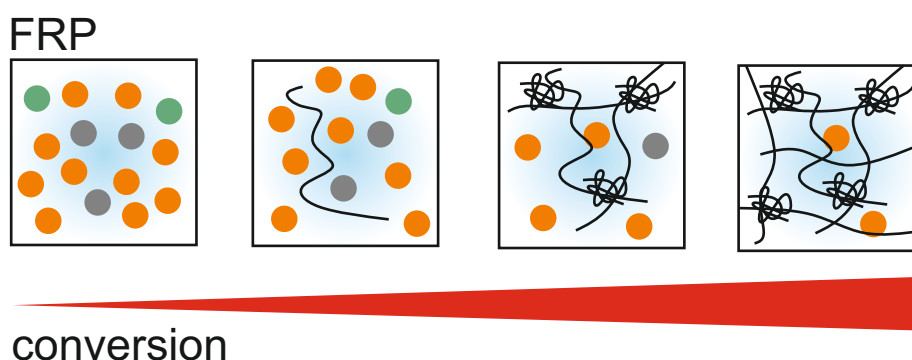


Figure 3.1: Representation of the cross-linking process via FRP polymerization between a mono- (orange) and a bifunctional (gray) monomer, in the presence of the initiator (green). The resulting polymer chains are displayed in black. The overlap between the polymer chains is considered as a junction point, independently of its origin (backbiting reaction, entanglement or cross-linking agent). The FRP polymerization yields high cross-linked nanogels, which are later loosely connected by bridging chains. Figure adapted from [30].

In addition, the free radical polymerization leads via the statistical occurring termination and chain transfer reactions, as shown in **Figure 3.2** to a considerable broad molecular weight distribution in linear polymers with the dispersity \mathcal{D} in the range of 2. The \mathcal{D} , in combination with the statistical incorporation of the cross-linker, causes a broad mesh size distribution, see **Figure A Table 3.1, p. 40**.

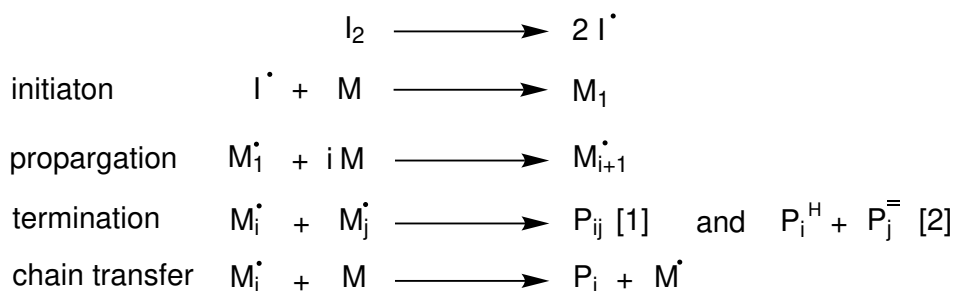


Figure 3.2: The process of free radical polymerization (FRP) includes: 1. the initiation, which generates active radicals by decomposition of the initiator (I); 2. the propagation, where the (macro)radical grows by sequential addition of monomers (M), and 3. the termination ([1] radical recombination or [2] disproportionation) and transfer reactions, where the final polymer chain (P) is obtained.

Nevertheless, the samples obtained by FRP were taken as a starting point to establish the network analysis methods and as comparison for the polymer networks, which were synthesized by more elaborated routes mentioned in the subsequent chapters. As suitable cross-linker ethylene glycol dimethylacrylate (EGDMA) was used as a common cross-linker from industries, [9] which provides co-polymerization parameters close to unity. [90] The cross-linker forms junction points, which connect the individual polymeric chains consisting of poly(methacrylic acid) into a continuous network, which reaches the extension of the macroscopic sample, as it is displayed in the reaction scheme in **Figure 3.3**. The carboxylic acid is transferred into the carboxylate by addition of a strong base, such as sodium hydroxide. The neutralization with sodium hydroxide was conducted post-synthesis to circumvent electrostatic repulsion between the monomer units during synthesis, which might alter the network structure. In addition, other synthetic approaches described later, like the anionic synthesis, necessitate electrically neutral monomers and thus, the comparability of these networks would be otherwise limited.

The polymerization reaction proceeds via a radical chain reaction. Hereby, the C-C double bond of the acrylic acid is transformed into two single bonds adding another monomer unit to the growing chain. The polymerization step releases a large amount of enthalpy,

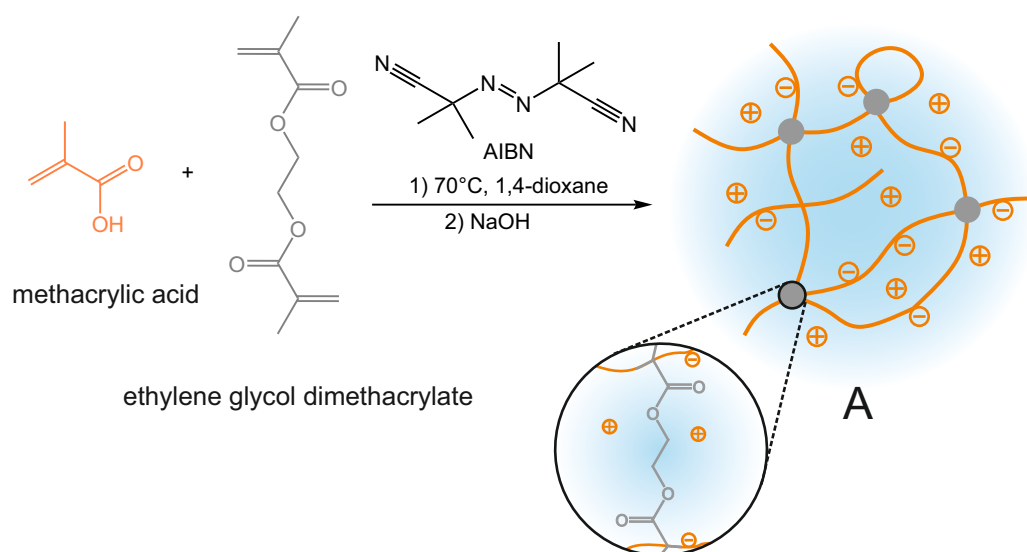


Figure 3.3: Synthesis route for the free radical polymerization of poly(sodium methacrylate) (PSMA). The methacrylic acid (MAA) is co-polymerized with ethylene glycol dimethylacrylate (EGDMA) using azobisisobutyronitrile (AIBN) as initiator. Subsequently, the polymer is neutralized with 0.1 M sodium hydroxid (NaOH).

which drives the process. Consequently, an effective dissipation of the generated heat is required, which is provided by the solvent (1,4-dioxane, bp. 101 °C). The chain carrier is a radical generated by a suitable initiator, which should be readily soluble. Azobisisobutyronitrile (AIBN) as a common initiator from industry fulfills the requirements. It is known to decompose readily at 70 °C and is reported to polymerize a number of methacrylic monomers with high yields ($\geq 98\%$). [91] However, the absence of oxygen is necessary as it inhibits the reaction due to its diradicalic nature and leads to undefined samples and an increased sol content. The exact synthesis route is provided in the **Appendix A.2, p. 130** with the precise quantities and a list of the produced samples. The reaction route outlined above offers several parameters that can be adjusted to alter the obtained hydrogel. All parameters are given with respect to the amount of the methacrylic acid monomer in the mixture. First, the statistical mesh length of the polymer network is given by the amount of cross-linker added. The theoretical degree of cross-linking (DC) is defined as the ratio of the amount of bifunctional cross-linkers n_{linker} to the moles of monomer n_{mon}

$$DC = 100\% \frac{n_{linker}}{n_{mon}} \quad (3.1)$$

and is given in mol%. In case of the poly(methacrylic acid) samples obtained by FRP, the

DC was varied from 0.4 to 20 mol%. Hereby, samples with very distinct properties should be achieved with respect to their swellability, mesh size and mobility of chain segments in the networks. Thus, the underlying dependencies and trends should be accessible as displayed in the following **Chapter 4**.

The addition of base to the polymer results in a conversion of acidic functionalities on the backbone into its ionic form. Thus, the degree of neutralization in mol% (DN) is given as

$$DN = 100\% \frac{n_{base}}{n_{mon}} \quad (3.2)$$

with n_{base} as the amount of base in mol. In the present thesis, only fully charged samples have been employed if not specified otherwise.

The ratio between network structure and amount of solvent during polymerization has to be taken into account, since a higher monomer dilution yields longer primary chains, but also the proportion of inelastic defects increases. Therefore, a reference state is defined in form of a swelling ratio Q_{syn} in mass, as the ratio of all polymer components during synthesis with respect to the solvent. It defines the relaxed state of the meshes in respect to all other connected meshes. In the present thesis, the Q_{syn} parameter was kept constant at 20 wt% monomers to solvent, since its influence on the network structure was thoroughly studied in earlier work. [14] The swelling ratio Q_{syn} is provided by the following equation

$$Q_{syn} = \frac{m_{mon}}{m_{solv}} \quad (3.3)$$

where m_{mon} is the mass of the monomer and m_{solv} the mass of the solvent. A list of the produced samples can be found in the **Experimental** in **Table A.1 p.130**. The specific batch is described in this work by a incorporating of its synthetic parameters. First, the polymer is given (i.e. poly(sodium methacrylate), PSMA, or poly(sodium acrylate), PSA), next the DC in mol%, and at the end the polymerization method is written (e.g. free radical polymerized, FRP). The DN in mol% is only provided if required.

3.1.2 Considerations Regarding the Anionic Polymerization

The anionic polymerization is a convenient technique to prepare linear polymers with a narrow size distribution with a low dispersity ($\mathcal{D} < 1.1$). [32] Similar to the free radical polymerization it is a chain growth reaction exhibiting the same reaction steps: chain initiation, chain propagation and chain termination. In contrast to free radical polymerization the propagating species is a carbanion instead of a radical, which provides several benefits. Hereby, no termination reaction takes place and the growing chain remains active. Due to this ability, anionic polymerization is also called a living polymerization technique. [32] It can be utilized to synthesize high molecular weight polymers with a low

D and enables the functionalization of chain ends in selected cases. Several precautions have to be complied to ensure the living character of the anionic polymerization. All reagents have to be absolutely free of protic molecules, such as acids, alcohols or water, as well as carbon dioxide and oxygen. Generally, electrophile groups have to be absent, which drastically limits the number of available monomers and solvents. [32] All these components can react with the carbanion resulting in an undesired termination. Consequently, the required reactants and solvents have to be dried and degassed prior to application. In addition, high vacuum techniques and usage of inert argon atmospheres are necessary. Since the carbanion would readily react with the acidic group, methacrylic acid cannot be employed directly. Commonly, the tert-butyl ester is utilized as protecting group for carboxylic groups, since it provides a strong kinetic hindrance and can be facile cleaved off subsequently by hydrolysis with strong acids. [92] Moreover, it has to be taken into account that the otherwise not sterically hindered carbonyl group might cause side reactions, which have to be circumvented. [93,94] On the one hand, the initiator could attack the carbonyl functionality lowering the number of growing chains. On the other hand, the growing carbanion could perform an intramolecular backbiting reaction, or an intermolecular 1,2-addition on the carbonyl group could occur, leading to self-termination, as it is displayed in **Figure 3.4**.

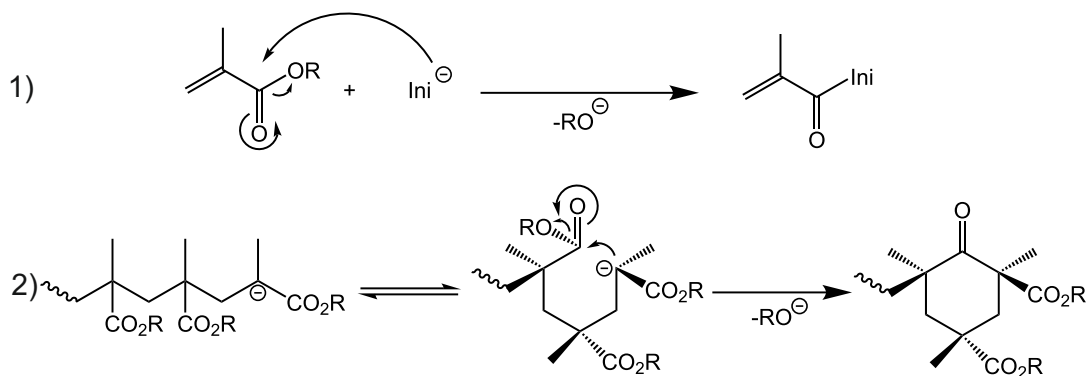


Figure 3.4: Typical side reactions in the anionic polymerization of (meth-)acrylates: 1) 1,2-addition of the initiator Ini (e.g. $s\text{-BuLi}$) onto the carbonyl function, which lowers the amount of growing chains. 2) Intramolecular backbiting reaction of the carbanion onto the carbonyl group, which ends the chain propagation. This attack can also occur intermolecularly resulting in the ligation of two chains.

To ensure that the polymerization maintains its living character, the reaction conditions have to be carefully monitored. [95] The reactivity of the carbanion has to be decreased in THF by lowering the temperature below $-60\text{ }^{\circ}\text{C}$ and by adding lithium salts, which form complexes with the reactive center. [96] The polymerization should be conducted in a polar, non-protic, solvent like tetrahydrofuran (THF), which reduces the aggregation of ions and lowers the probability of backbiting. [93] In addition, sterically demanding groups at the initiator help to reduce undesired attacks on the carbonyl functionality. Methacrylates were favored over acrylates, since the methyl group provides an additional inductive effect (+I-effect), which enhances the stability of the anion. In combination with the sterical hindrance of the methyl group and by replacing the acidic proton next to the carbonyl functionality, the abstraction of a hydrogen atom on the polymeric backbone is prevented. If not controlled by even lower temperatures, the abstraction of protons on the backbone can lead to branched materials.

As cross-linker ethylene glycol dimethacrylate (EGDMA) was utilized to provide similar incorporation probabilities of monomer and cross-linker in the growing polymer chain during polymerization. [90] Otherwise, gradients might occur, which would lead to domains enriched in cross-linker resulting in additional heterogeneities in the network structure.

3.1.3 Anionic Polymerization of Polymer Networks in a Single Step, (Type A)

The basic idea of using direct anionic co-polymerization in the scope of this thesis is to combine the rather simple reaction procedure from FRP with the advantage of a better control over the polymerization provided by the anionic polymerization mechanism. [97] Undesired side reactions as chain termination and chain transfer are avoided by this approach. These would lead to a more heterogeneous topology with many network defects, such as dangling ends. The synthetic route used in this thesis is presented in **Figure 3.5**. The tert-butyl ester of the monomer was required to circumvent that the anions of the initiator and the growing polymer chain might attack the carbonyl group of the monomer unit under formation of a stable side product. Thus, the tert-butyl ester is employed as protecting group, which was cleaved off after polymerization. The counterion sodium was introduced by neutralization with 0.1 M sodium hydroxide (NaOH) solution. The content of linker molecules in the synthesis was systematically varied from 0.3 to 5.0 mol% to illustrate the change in network structure. Regarding the detailed solvent and monomer purification procedures as well as the employed masses the reader is referred to the experimental section. The polymer networks obtained in this chapter will be named single step anionic (SSA) polymerized throughout the thesis.

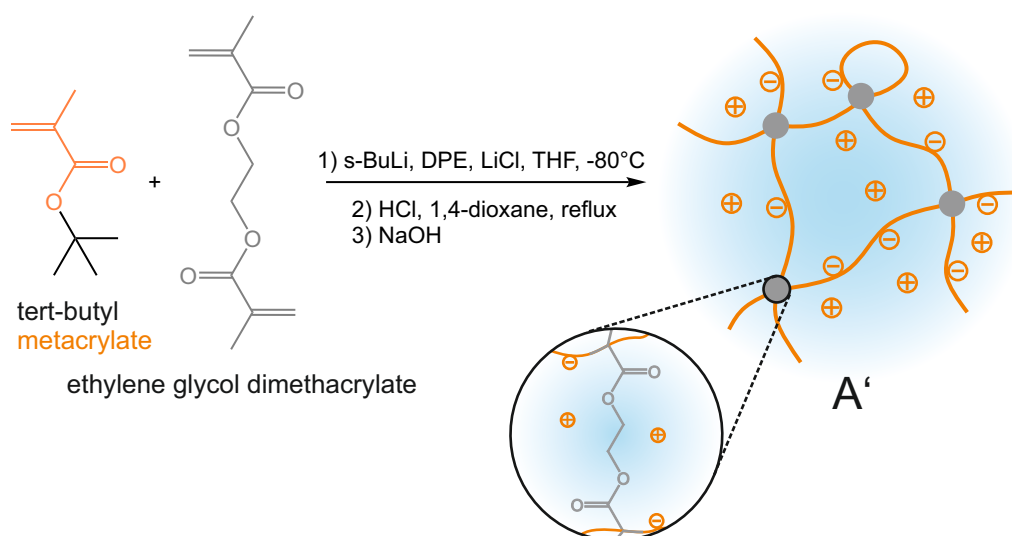


Figure 3.5: Schematic display of the synthesis of poly(sodium methacrylate) in a single polymerization step. The monomer tert-butyl methacrylate (*t*BuMA) is co-polymerized with ethylene glycol dimethylacrylate (EGDMA) by anionic polymerization. Afterwards, the ester is cleaved off and the carboxylic group is transformed into the carboxylate by addition of 0.1 M sodium hydroxide (NaOH).

3.1.4 Anionic Polymerization of Quasi-Model Polymer Networks (Type B)

As already described in beforehand, ideal networks can never be obtained, since defects such as dangling ends, loops, or intermolecular entanglements are always formed during the polymerization mechanism. [27] While structural perfection cannot be achieved, the so called quasi-model systems provide a compromise between structural perfection and the facility of the synthetic procedure. In these systems, the chain length between two junction points is fixed, while the cross-link functionality remains undefined, as displayed in Figure B **Table 3.1, p. 40**. [98] A common way to obtain quasi model systems is the synthesis of amphiphilic triblock co-polymers via a living polymerization technique with an ABA structure. Here, the end block A consists of a hydrophobic polymer, which forms micelles in water that connects the polymer chains physically. The middle block B is made of a hydrophilic monomer, which provides the actual hydrogel. [99–101] Earlier publications focused on non-charged systems, while more recent work also described the utilization of (meth)acrylic acid as monomers for the middle block. [81,102–105]

Another technique evolves from the synthesis of telechelic polymer chains by a living polymerization technique, followed by the addition of a multifunctional cross-linker. Telechelic

polymers are end-functional polymers, where both ends possess the same functionality. In this case that is the carbanion, which can facile react with the provided linkers under formation of high cross-linked micelles. In this way, several organogels have been synthesized by anionic polymerization, [27, 106] while Patrickios et al. studied the group transfer polymerization for the synthesis of poly(methacrylic acid) based hydrogels. [98, 107] For reasons of simplicity of the polymerization technique, with fewer reaction steps and simplified working up procedure, the latter approach was chosen for the production of quasi-model systems.

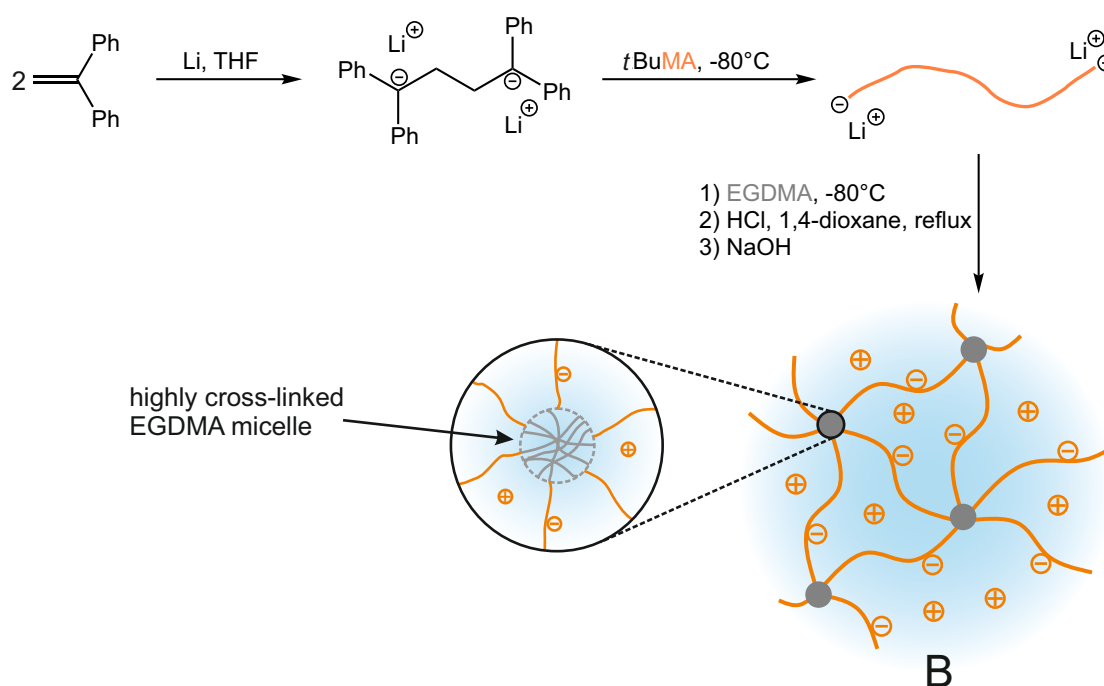


Figure 3.6: Synthesis route of poly(sodium methacrylate) by sequential anionic polymerization. In a first step, the elastic chain is build-up from tert-butyl methacrylate (*t*BuMA) and in a subsequent reaction the cross-linking takes place by addition of ethylene glycol dimethylacrylate (EGDMA). The micelles are resulting from the excess of EDGMA, which is required to ensure network formation. The tert-butyl protecting group is cleaved off with 50/50 vol% HCl/1,4-dioxane and subsequently the polymer neutralized by addition of 0.1 M sodium hydroxide (NaOH).

In this approach, a difunctional initiator based on diphenyl ethylene (DPE) is used, which is dimerized in polar solvents in the presence of lithium. [108] The method is especially suitable for poly(alkyl methacrylate) co-polymers, since the high steric hindrance of the

initiator prevents side reactions. In this way, the polymer chain is synthesized first, while samples were taken prior to the cross-linking to confirm the linear growth of the polymer chains. Polymers with molecular weights of 3.1 to 46.3 kg/mol were obtained with a dispersity of $D \leq 1.3$, as displayed in **Table A.3, p.133** in the experimental section. Then, the cross-linker is added, which reacts with the two living ends on both sides of the chain to create the network, see **Figure 3.6**. The cross-linker is employed in a eight-fold excess to ensure that the cross-linking occurs regardless of the repelling charges at the end of the chains. This approach features the disadvantage that cross-linker micelles are formed. These remain ill defined, since an unknown number of cross-linker molecules contribute to each micelle and an unknown amount of chains enters. Arens et al. reported the synthesis of quasi-model networks based on phase separated ABA-type block-co-polymers. They obtained over 45 chains per micelle as confirmed by small-angle X-ray scattering. [81] Although the synthesis procedures are not directly comparable, it illustrated the point that the formation of these micelles, and with it the number of chains per micelle, remain unpredictable. After the network formation, the protecting group was cleaved off. The chain lengths between two cross-link points have been adjusted corresponding to a cross-link density (in the FRP case) of 5.0 to 0.3 mol% and are accordingly labeled. These quasi-model polymer networks will be abbreviated with quasi-model (QM) in the following chapters.

3.1.5 Model Networks by Anionic Polymerization with Subsequent Cross-Linking via Azide-Alkyne Huisgen Ligation (Type C)

The synthesis of networks without any defects is not possible, as highlighted in the previous sections. [27] Consequently, the best producible network is a model network, in which the chain lengths between two junction points and the cross-linked functionality are well defined, as displayed in **Figure C Table 3.1, p.40**. These systems are more challenging to synthesize, since the combination of a living polymerization technique followed by a fast ligation ('click'-type) coupling reaction is required.

The preparation of PEG-hydrogels is well established, [109] while fewer publications have been focused on charged systems due to the limited synthetic control. [110] Wegner et al. reported the synthesis of well defined poly(tert-butyl)methacrylate star precursor polymers exhibiting an anthryl group at the end of each arm. These groups were dimerized upon irradiation under formation of the network with the subsequent transformation to poly(methacrylic acid) by hydrolysis. [111] Other examples included the utilization of thiols, [112] Diels-Alder cycloadditions, [113] or the copper catalyzed azide-alkyne Huisgen reaction. [114] In this thesis, the azide-alkyne approach was employed due to the high con-

versions and fast reaction, which can be achieved with this technique. [115] In addition, it is insensitive to other functional groups in the utilized polymer. [115]

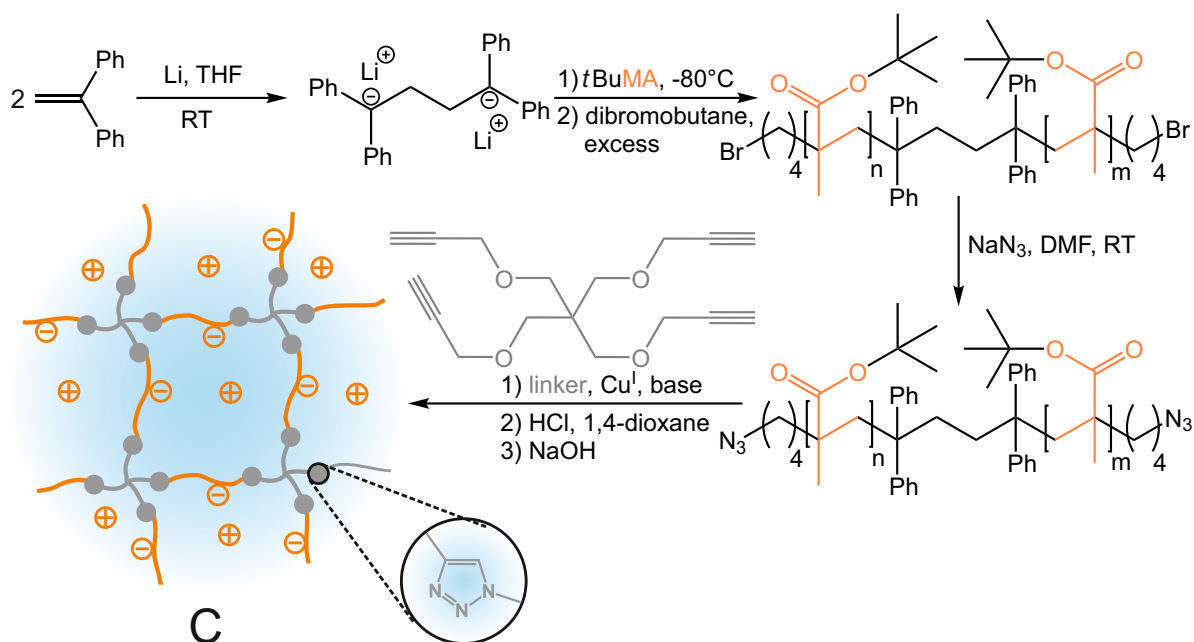


Figure 3.7: Synthesis of model hydrogels by anionic polymerization of the tert-butyl methacrylate (*t*BuMA). The chains are end-capped with bromide functionalities, which are transformed into the azide end groups by a S_N-reactions. Afterwards, the polymer network is formed by azide-alkyne Huisgen ligation and the protecting groups are removed to enable the neutralization with 0.1 M sodium hydroxide (NaOH).

Anionic Polymerization and End-Capping

In the current thesis, an anionic build up of the polymer chain was chosen in combination with the azide-alkyne Huisgen ligation for the formation of the polymer network, as shown in **Figure 3.7**. A detailed reaction procedure is described in the experimental section. The difunctional initiator was formed from diphenyl ethylene using elemental lithium. The initiator provides the benefit of a high sterical hindrance and does not attack on the carbonyl bond of the monomer. To obtain a telechelic polymer with bromide end groups on both sides the reaction was quenched with an excess of dibromobutane after the polymerization was finished. The linear propagation of the polymer chain was validated by SEC analysis. Molecular weights of 4.0 kg/mol to 35.7 kg/mol were obtained with dispersities \mathcal{D} of ≤ 1.3 , compare **Table A.4, p. 134** in the experimental section. The functionalization step could lead to the formation of elongated chains as side reaction, since a reactive bromide group is introduced, where the living end group of another chain

could attack. In SEC analysis, this attack would lead to the appearance of peaks at multiple times the molecular weight of the main signal. However, the peak in SEC at double the molecular weight accounted in each case for less than 1 % of the total intensity and thus, inter-molecular chain elongation could be excluded as major side reaction.

In high field NMR, the end group conversion Y in % was additionally quantified by a comparison of the integral ratios of the phenyl protons I_{ini} (initiator), with a multiplet ranging from $\delta = 7.05$ to 7.35 ppm, to the protons neighboring the bromide end group I_{end} ($-CH_2 - Br$), with a triplet at 3.38 ppm, by

$$Y = 100\% \frac{I_{end}}{I_{ini}} \quad (3.4)$$

while each intensity was normalized to the respective number of protons. The obtained conversion rates are shown in **Table A.4, p. 134** in the experimental chapter and disclose values of 92 to 100 % for Y validating the successful end-linking. In return, side reaction, such as ring formation, termination, or chain extensions accounted for ≤ 8 %.

Based of these results, the bromide was converted into the respective azide by a simple S_N reaction, as displayed in **Figure 3.7**. After working up by precipitation from water and subsequent drying, NMR spectra and FTIR spectra of the polymer were recorded. The shift of the triplet from $\delta = 3.38$ to 3.22 ppm in the NMR spectra affirmed the change of the bromide into the azide functionality, as shown exemplary in **Figure 3.10** on the left. Appearance of a signal at $\nu = 2090 \text{ cm}^{-1}$ in the infrared spectrum, which could be assigned to vibration modes of the azide group, [116] validated the conversion of the end group. However, first trials with commercial three-armed alkyne cross-linkers resulted in no network formation. Measurements of the polymer with online coupled SEC-FTIR gave the elugram displayed in **Figure 3.8** on the left. A signal at $\nu = 2130 \text{ cm}^{-1}$, associated to NaN_3 was eluting at the same time as the system peak, shown as a negative signal at $\nu = 1726 \text{ cm}^{-1}$. This indicates the presence of impurities of dissolved sodium azide, which were co-precipitated together with the polymer during the working up procedure. Introduction of two additional precipitation steps gave exemplary the elugram in **Figure 3.8** on the right. A polymer, with a signal at $\nu = 1726 \text{ cm}^{-1}$ in the IR spectrum, was eluting at 55 to 65 min and the azide signal at $\nu = 2094 \text{ cm}^{-1}$ was co-eluting with the polymer. This affirms the presence of the azide group at the end of the polymer chain.

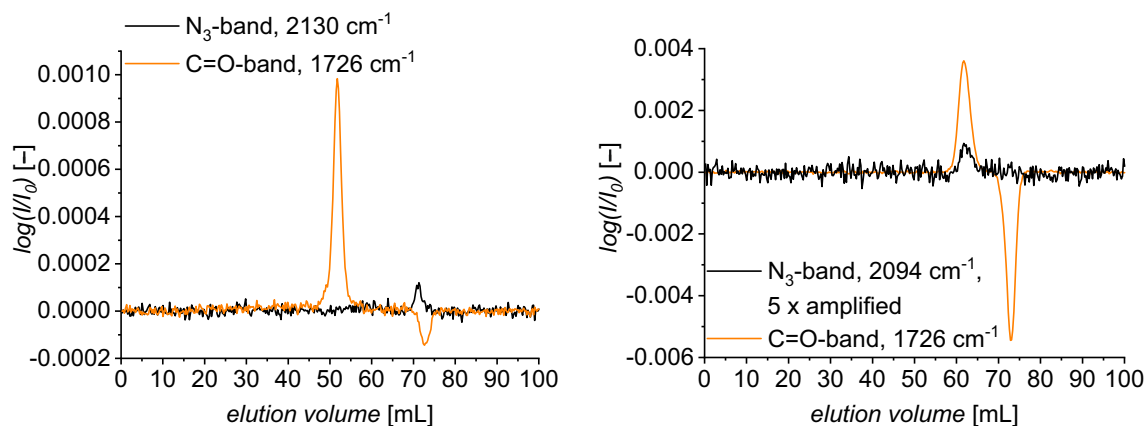


Figure 3.8: Elugrams obtained by size-exclusion chromatography coupled with a Fourier-transform infrared spectrometer (SEC-FTIR). The intensities of the carbonyl vibration (1726 cm^{-1}) and the azide vibration (ca. 2100 cm^{-1}) are displayed. On the left, an example of a insufficient purified polymer is shown, which exhibits residual sodium azide as indicated by the azide signal eluting together with the system peak. On the right hand side, a polymer with an improved working-up procedure is displayed. Here, no dissolved sodium azide is affirmed but an azide signal eluting together with the polymer indicating a successful end-functionalization.

Linker Synthesis

A four-armed alkyne cross-linker was synthesized in parallel from pentaerythritol and propargyl bromide. The cross-linker was chosen to provide a similar tetrahedral environment at each junction point as in the FRP case (compare **Figure 3.3**). The four-armed linker has compared to a tree-armed one the advantage that even if one chain is missing still a junction point exists. Going towards higher numbers of arms might bring the disadvantage of a considerable sterical hindrance, which might limit the cross-linking efficiency. [117] After reaction the base was removed by extraction with water and the crude product was purified by chromatography over silica. Mass spectrometry and ^1H -NMR spectroscopy confirmed the achievement of the desired product, as shown in the **Table A.5, p. 135**.

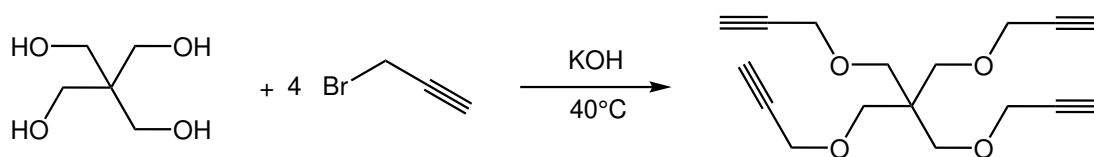


Figure 3.9: Synthesis of the four armed alkyne linker tetrapropargyl pentaerythritol from pentaerythritol and propargyl bromide at elevated temperature in presence of potassium hydroxide.

Azide-Alkyne Huisgen Ligation

Finally, the end-capped polymers were transferred into the network by an azide-alkyne Huisgen ligation, as displayed in **Figure 3.7**, p. 50. The polymer networks were extracted, to remove residual copper catalyst and dried overnight at 60 °C in vacuo. High field $^1\text{H-NMR}$ spectra were taken in the swollen state in d_2 -tetrachloroethane. New peaks were found at 3.75, 4.30 and 7.73 ppm, which could be assigned to the formed triazole, as exemplary displayed in **Figure 3.10** on the right.

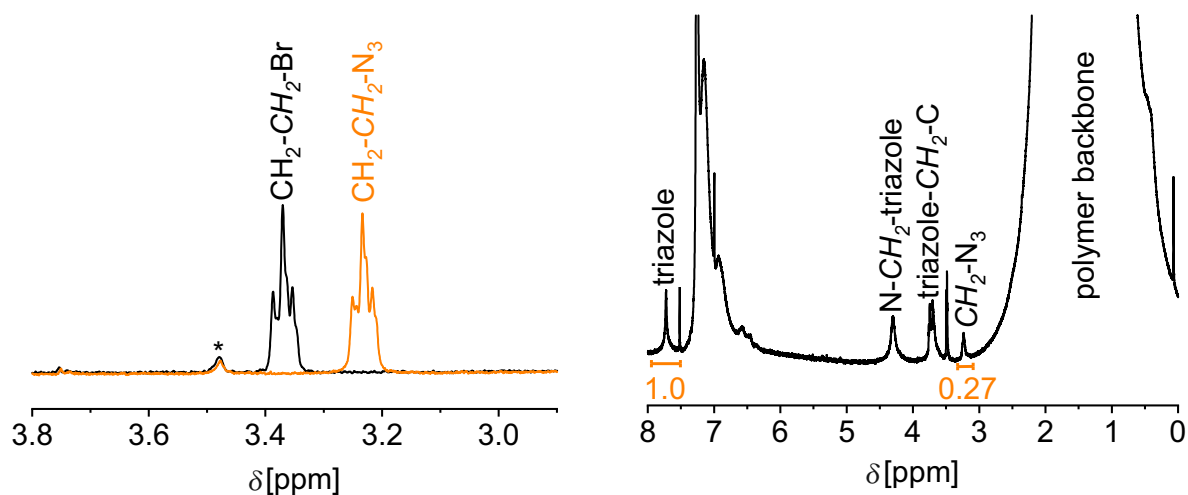


Figure 3.10: End group analysis of the telechelic PSMA polymers by high field $^1\text{H-NMR}$ -spectroscopy. The transformation of the bromide to the azide end-group is shown on the left, while on the right the $^1\text{H-NMR}$ -spectrum of a swollen network (in D_2O) after the cross-linking is displayed. The integrals over the azide and the triazole peaks reveal an insufficient cross-linking, while 21 % of all azides remained unreacted. (1024 scans, RT)

Comparison of the integrals gave the conversion rate Y in % as

$$Y = 100\% \frac{I_{\text{triazole}}}{I_{\text{end}} + I_{\text{triazole}}} \quad (3.5)$$

with I_{end} and I_{triazole} as the integrals of the end group and the triazole at $\delta = 7.73$ ppm, respectively, each normalized to the number of protons. Due to the broadening of the peaks arising from dipolar couplings and different chemical shifts along the polymer chain, the end group signals slightly overlapped with the feet of the signals of the polymer backbone. Thus, a sliding baseline was laid through the spectrum to obtain the end group integrals without distortions. The integral ratios revealed conversion rates of approximately 70 % to the desired triazole as shown in **Table A.5, p.135** in the experimental. It has to be stated that this approach, while being reproducible with a standard deviation of ≤ 2 %, contains sources of systematic error. Since chain ends are more mobile than the cross-linked functionality, [41] they relax on a different timescale and are less affected by the peak broadening in NMR described above. This leads to an overestimation of the azide integral, which is challenging to quantify. Nevertheless, it can be affirmed that a considerable amount of azide functionalities remain unreacted in the network. Unfortunately, all signals arising from the alkyne linker itself show the same chemical shifts as the polymer backbone and are consequently not available for quantification. A second attempt with doubled reaction times of four weeks yielded the same finding. Two main reasons can be given for the non-quantitative conversion: A simple mismatch of the employed end-group to linker ratio, or that the polymer chains are immobilized in the network after gelation occurs and thus, cannot reach each other for reaction. An addition of 30 % of the linker to the polymer networks in a second step leads to the disappearance of the azide signal. However, the characteristic swellability indicated a loss of the control over the network structure, since the swellability did not correlate with the degree of cross-linking, see **Figure C.2, p. 147** in the Appendix. A third attempt with a 10 % higher amount of linker gave the same finding of around 30 % of unreacted azide groups, which contradicts the assumption of a mismatch of functional groups. Neffe et al. also obtained residual azide groups in hydrogels produced via azide-alkyne Huisgen ligation, when using equimolar batches as indicated by the introduction of fluorescent chemical groups. [118] These findings confirm the hypothesis of immobilized functionalities after gelation. Therefore, the polymer networks obtained in a single cross-linking cycle were employed as received without further attempts to optimize the cross-linking efficiencies.

Afterwards, the tert-butyl protecting group was cleaved off using the HCl-1,4-dioxane mixture presented in the previous sections. ^1H -NMR spectroscopy in D_2O revealed the disappearance of the singlet at 1.42 ppm, which confirmed the successful removal of the tert-butyl ester, compare **Figure C.1, p. 146** in the Appendix. The employed chain lengths between cross-links corresponded to a DC of 2.0 to 0.2 mol% in the FRP samples

and are named accordingly. The samples obtained by azide-alkyne Huisgen ligation will be denoted model networks (MN) in this thesis.

3.2 Acrylic acid

3.2.1 Free Radical Polymerization

In the following, the main steps of the preparation of hydrogels based on acrylic acid and the synthetic parameters are described, see **Figure 3.11**. The polymer was prepared in water by free radical co-polymerization of acrylic acid with an di-functional monomer as a linker.¹ To remain consistent with the PSMA samples, in-situ cross-linking was employed. The free radical polymerized (FRP) samples were used as a comparison to the networks obtained by reversible addition-fragmentation chain-transfer (RAFT) polymerization described below. N,N'-methylenebisacrylamide (MBA) was utilized for this FRP, since it is dissolvable in water and has a co-polymerization parameter of close to 0.5. [120] The carboxylic acid is transformed into the carboxylate by adding 0.1 M sodium hydrocarbonate solution as a mild base. The base was chosen to ensure the best comparability with the samples obtained by reversible fragmentation chain-transfer (RAFT) polymerization. Here, a mild base is required to avoid scission of the trithiocarbonate group. Since electrostatic repulsion between the monomer units during synthesis might change the network structure, the sodium ions were introduced afterwards. Furthermore, the anionic synthesis needs electrical neutral monomers and the comparability would be otherwise limited.

A water soluble initiator, 4,4'-Azobis(4-cyanovaleric acid) (V-501) was employed, as it is known to decompose readily and work well with acrylic monomers. [121] Again, the absence of oxygen is required as it inhibits the reaction and induces an increased sol content. The content of cross-linker was systematically varied from 0.3 to 5 mol% to verify the influence of the number of junction points on the network structure. In addition, it acts as a standard for comparison to the samples obtained by RAFT polymerization. Furthermore, the degree of neutralization was altered from 0 to 100 % in case of the FRP PSA networks in order to understand the charge contribution to the network mobility. The synthesis technique was adapted from recent literature, [121] while the exact procedure and weightings are provided in the **Appendix A.5, p. 136** together with **Table A.6, p. 137** of the produced samples.

¹The synthesis of the poly(sodium acrylate) samples was carried out by Federica Cavalli in a cooperation project within the scope of the SFB1176, which is published in a joint paper. [119]

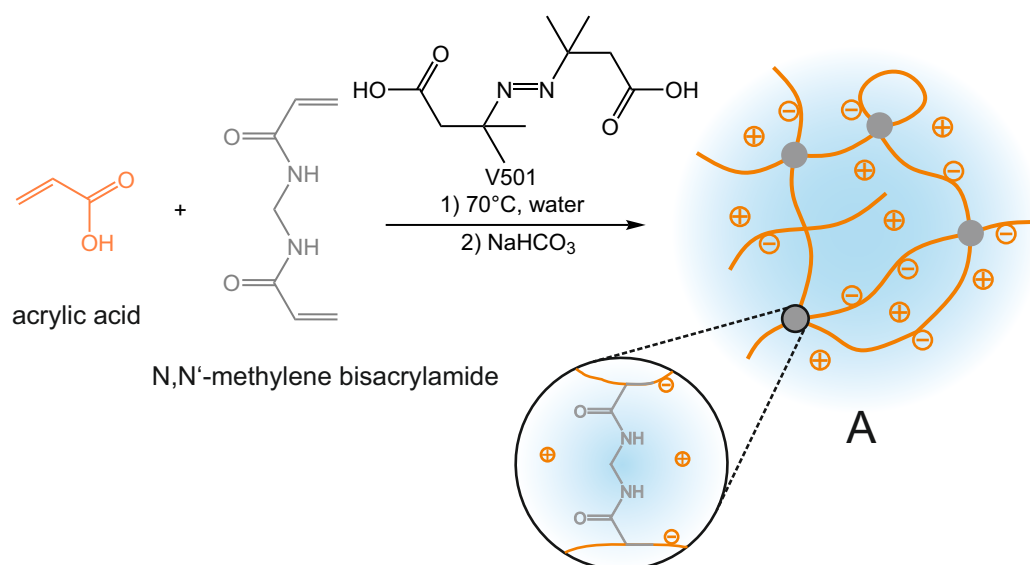


Figure 3.11: Synthesis route of free radical polymerized poly(sodium acrylate) using acrylic acid (AA) and N,N'-methylene bisacrylamide (MBA) followed by a neutralization with 0.1 M sodium hydrogencarbonate (NaHCO₃).

3.2.2 Reversible Addition Fragmentation Transfer Polymerization

Reversible addition-fragmentation chain-transfer (RAFT) polymerization is beneficial for the formation of polymer networks due to the control it exhibits over the synthesis of linear polymers. Here, RAFT agents allow for a linear increase of the molecular weight of the polymer with conversion. In addition, they reduce termination and transfer reactions of the propagating chains. Whereas in FRP, the chains reveal high and broad molecular weight distributions at any stage of the polymerization. For the synthesis of linear chains, the mechanism of the polymerization is well understood, while in case of the cross-linking process the impact of a RAFT agent is still under debate. [36] The proposed mechanism includes the formation of highly cross-linked nanogels in the early stage of FRP. Afterwards, the nanogels react with each other leading to an inhomogeneous network characterized by multiple domains having different degree of cross-linking (see Figure 3.2). [2, 24, 30] However, a RAFT mediated process is expected to grow first small chains, which are later cross-linked into a gel. The second technique should provide a better diffusion of the chains and consequently yielding a more homogeneous pore structure. [30, 122]

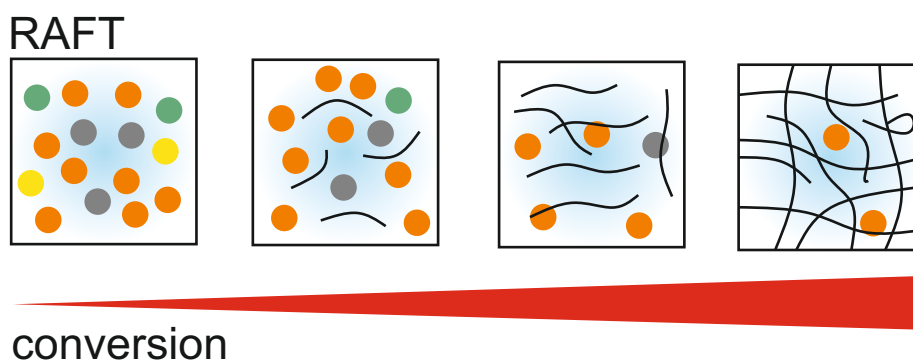


Figure 3.12: Representation of the cross-linking process via RAFT polymerization between a monomer (orange) and a bifunctional linker (gray) using an radical initiator (green). The RAFT agent is depicted by a yellow circle, while the polymer is denoted by the black lines. The overlap between the polymer chains reveals the cross-linking points, which can originate from backbiting reactions, entanglements, or the cross-linking agent. In RAFT polymerization small linear chains are formed, which are cross-linked in a later stage of the polymerization process, compare also **Figure 3.1, p. 41**. The figure is adapted from [30].

Networks with and without RAFT agent were synthesized to validate the claim of more homogeneous network structures by RAFT polymerization. Furthermore, the content of RAFT agent during network formation was varied to illustrate the impact of the RAFT concentration on the process. Samples with varying content of cross-linker were produced to analyze, if the incorporation efficiency of the cross-linker is dependent on the amount of RAFT agent. The detailed reaction procedure, the employed quantities and a list of samples are provided in the **Appendix A.5, p. 136**. The differences between the samples with respect to their network structure were examined by swelling, NMR-relaxation, double quantum coherence experiments, as well as inverse size exclusion chromatography (iSEC), which are described in the following **Chapter 4**.

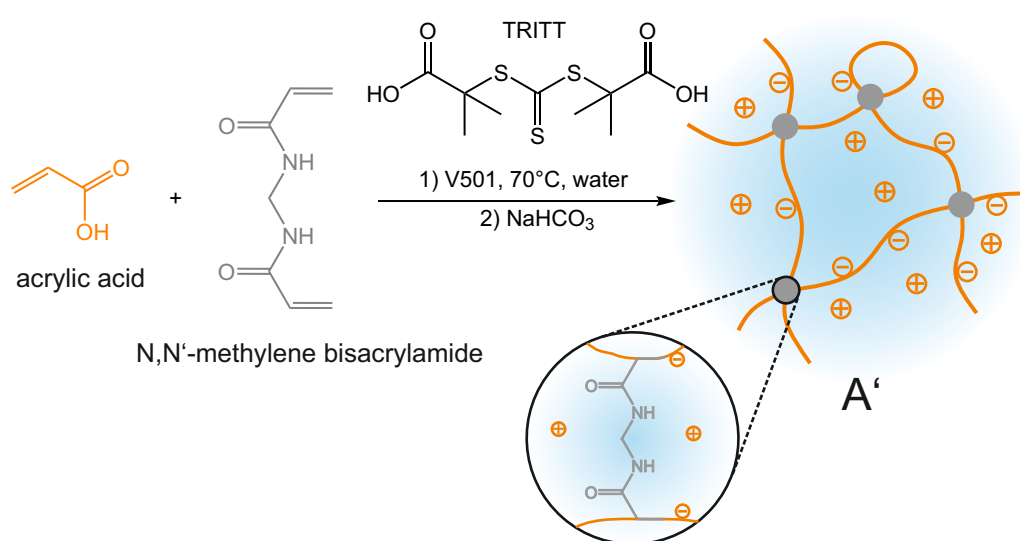


Figure 3.13: Synthesis route towards poly(sodium acrylated) hydrogels based on RAFT polymerization using acrylic acid (AA) as monomer, methylene bisacrylamide (MBA) as cross-linker, and S,S-di((2-methyl)propionic acid) trithiocarbonate (TRITT) as RAFT agent.

Chapter 4

Determination of Network Heterogeneity

Several techniques have been reported for the characterization of polymer networks. [44, 123–125] However, in all cases, the challenges arise from the insolubility of the analyte, as well as the complexity of its microstructure. [20, 40] Cross-linked polymer chains are inaccessible, e.g., for standard liquid nuclear magnetic resonance (NMR) spectroscopy, size-exclusion chromatography (SEC), or mass spectrometry. Since the analyte cannot be dissolved, analytical techniques require either indirect methods, where the interaction of a probing species is observed, or the observation of the material in bulk. The commonly employed characterization techniques for the network structure of polymers can be subdivided concerning the available length scales into three main groups. The first group provides mean values throughout the whole material for the degree of cross-linking, i.e. how many cross-links are present in the structure per unit volume. Swelling experiments, for instance, rely on the varying solvent uptake of networks, [8] while oscillatory shear rheology measures the viscoelastic stress response of the network to derive its average cross-link density. [126] Yet, if the complete picture of the network microstructure should be determined, information have to be gained on different length scales. [20] Thus, the second group of characterization techniques provides an insight into the network structure in the range of 10 nm up to 100 nm by looking at spatially heterogeneous cross-linked domains in the network. [124] These domains can be uncovered by distinct scattering patterns arising from the local density differences. Utilized methods include the usage of light in the dynamic light scattering [125] and neutron beams from nuclear reactors in the small angle neutron scattering. [127] In the length scale below 10 nm, the patterning of the individual meshes can be accessed. [20] The employed methods are often also not spatially resolved, i.e. provide average values for the mesh size in the network structure, but reveal a more complete picture by giving a distribution of the analyzed parameters. In addition, the analytical methods allow for the detection of network defects, such as loops, unreacted moieties, and dangling ends. [39, 128] Concerning the quantification of

unreacted moieties, reported approaches include the usage of a fluorine containing cross-linker, whose conversion is studied by ^{19}F -NMR spectroscopy, [129] or the utilization of a linker, which becomes fluorescent upon reaction. [128] Neffe et al., however, presented the post-functionalization of unreacted linkers with fluorescent marker molecules. [118] Moreover, Johnson and coworkers developed a procedure for the quantification of primary and secondary loops. [21, 39] Here, the gel is disassembled after network formation by a decomposable group in the in the polymer chain. The resolvable group is not placed in the middle of the chain and thus, always a short and a long fragment is produced. The cross-linked fragments are identified via SEC and from the patterning of large and small network fragments the amount of loops can be back-calculated. [21, 39] In addition, the pore size distribution can be determined by evaluating the diffusion of probing species of known size within the network matrix. [123] For instance, the diffusion of magnetic nanoparticles upon application of magnetic fields is monitored. [130] Here, the particles are incorporated into the network matrix during synthesis. Ever larger and larger particles are employed until the particles become too voluminous to be able to jump from mesh to mesh. Thus, a lower and upper limit of the mesh sizes can be back-extrapolated. [131] Another example includes the diffusion of non-charged polymers standards into the structure, which can be evaluated via inverse size-exclusion chromatography (iSEC). [44, 132] In this connection, a SEC column is filled with the porous gel and from the retention times of the employed polymers the underlying pore structure can be back-calculated. [132] Recently, the analysis of the network structure via low-field ^1H -NMR techniques, such as T_2 -relaxation and double quantum ^1H -NMR (DQ-NMR), was discussed in the literature as a powerful tool for correlating differences in mobility to structural inhomogeneity. [42, 123] The concept is based on the fact that the network is composed of structural elements with significant different mobility, such as rigid cross-linking points, or mobile dangling ends and loops. Furthermore, the mobility of an elastic chains between two junction points increases by increasing the length of the chains itself.

In the following, a detailed analysis of the structure of the networks, whose preparation has been introduced in the previous chapter, will be presented. Here, the network structure will be compared among the samples and trends established. In order to conduct a first comparison, swelling experiments are examined. Afterwards, T_2 -relaxation experiments will be shown and correlated to DQ-NMR measurements. These provide information about the mobility of chain segments and thus, a first impression of the network structure. Subsequently, iSEC experiments are described to relate the obtained mobility distributions to the fundamental pore size distributions. Dielectric spectroscopy has been performed to examine the motion of ions in the confined environment of the networks, which could be beneficial for future applications, where the kinetics of ions play a role, e.g. ion conducting

materials. In the last section of this chapter, the salt partitioning of the samples is presented, which shows the potential usage of the employed networks in desalination processes.

4.1 Swelling Experiments

Swelling is a typical process of polymeric networks and one of the most important features used in applications. [133] Through the swelling process, the network structure is expanded as a suitable solvent is incorporated and the previously liquid phase is solidified and immobilized. The determination of the solvent capacity is used extensively for the characterization of gels as it is closely connected to their network topology, as introduced in **Chapter 2**. The degree of swelling of a network is determined by the ratio of solvent, which is taken up, to polymeric material. In the present thesis, the degree of swelling at equilibrium Q_{eq} is provided based on the mass and is defined as

$$Q_{eq} = \frac{m_{water}}{m_{polymer}} = \frac{m_{total} - m_{polymer}}{m_{polymer}} \quad (4.1)$$

where $m_{polymer}$ is the mass of the dry polymer, m_{total} the complete mass in the swollen state, while m_{water} represents the amount of solvent, which was taken up. Only the mass ratios are considered because in this way the densities are not required, which would be challenging to acquire. If a dry polyelectrolyte polymer is brought in contact with a water reservoir it will start to swell. The solvent uptake process is diffusion controlled and therefore the main factors for its swelling rate are particle form and size. [8] Since most applications are conducted in the swollen state, only the equilibrium swelling degree Q_{eq} is measured after all exchange processes have ceased. The parameter Q_{eq} is a thermodynamic property of the gel, which depends on the solvent-polymer interaction, temperature, pressure and the concentration of other dissolved species. The extent of the swellability of poly(meth)acrylates is known to be determined by several synthetic parameters, such as the degree of cross-linking, the degree of neutralization, the Q_{syn} , and the salt concentration in the water reservoir. [9, 134]

The equilibrium values Q_{eq} were measured for a variety of samples of poly(sodium methacrylates) (PSMA) obtained by different polymerization procedures, see **Chapter 3**. The main focus was laid on the influence of the degree of cross-linking (DC) on the swelling capacity. The sample was placed on a custom build rack in a Petri dish, which was filled with water with 1 wt% sodium chloride until the water surface touched the dry hydrogel from below. The Petri dish was sealed and the system equilibrated overnight. The interstitial water was removed and weighted, while the equilibrium degree of swelling Q_{eq} was determined according to **Equation 4.1**. The accuracy of these measurements is typically high with a reproducibility within 1 %. This error is given by the standard deviation

of three independent experiments on the same batch, while the detailed procedure is described in the experimental section.

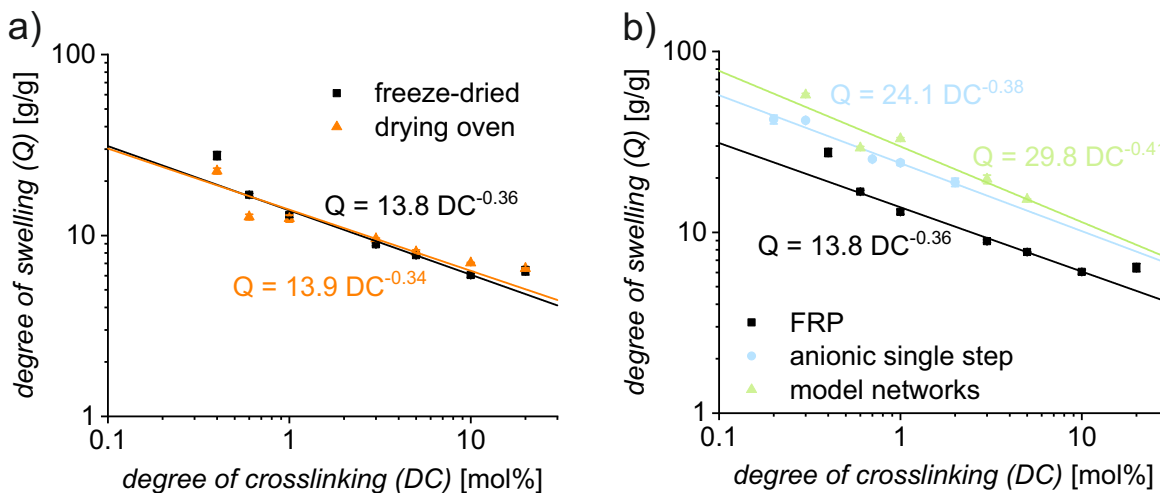


Figure 4.1: a) Determination of the degree of swelling of the FRP PSMA samples with different working-up procedures. b) Swellability of PSMA hydrogels arising from different synthetic procedures. (1 wt% NaCl, overnight)

The investigated polyelectrolyte hydrogels typically showed high solvent capacities with a strong dependence on the sample composition, as displayed in **Figure 4.1 and 4.2**. In each case, a power fit of the form,

$$Q_{eq} = A \cdot DC^B \quad (4.2)$$

which results from the Flory-Rehner theory, compare **Equation 2.61, p. 28**, represented the data well. It was reported that the drying process might have an influence on the final network structure. [135] During freeze-drying (lyophilization) the sample is frozen and the growing ice crystals inside the network might rupture the structure. [136] Whereas by the drying in a oven the elevated temperatures of 70 °C might lead to radical formation by homolysis of chemical bonds, [137] which add by radical-radical recombination further cross-links to the structure. In addition, radical depolymerization of the network might occur. [138] Consequently, in a first set of experiments, free radically polymerized (FRP) PSMA samples with varying DC resulting from the same batch were split in two control groups and subjugated to the different working up procedures. The two data sets overlay almost perfectly, as displayed in **Figure 4.1 a)** on the left. This accordance in the data indicates only a minor influence of the drying process on the network structure and was

therefore neglected in the further course of the thesis. In a next step, the bulk of the poly(methacrylate) samples was analyzed. The FRP samples provided smaller swellabilities than the samples obtained by anionic polymerization, as shown in **Figure 4.1 b**). This indicates a more loose knotted network matrix in case of the anionically polymerized networks. The hydrogels obtained by Huisgen ligation, by FRP and by anionic polymerization in a single step all revealed similar scaling exponents in their power fits, which could imply comparable network structures. The scaling exponent is with approx. -0.4 is lower than the expected -0.6 resulting from the Flory-Rehner theory. This discrepancy could be explained by the methyl group on the backbone of the polymer chain. This functional group adds by sterical hindrance further constrains to the chain and stiffens it. [139] Thus, the assumption of the Flory-Rehner theory of flexible chains might be invalid here leading to the found discrepancy between data and theory.

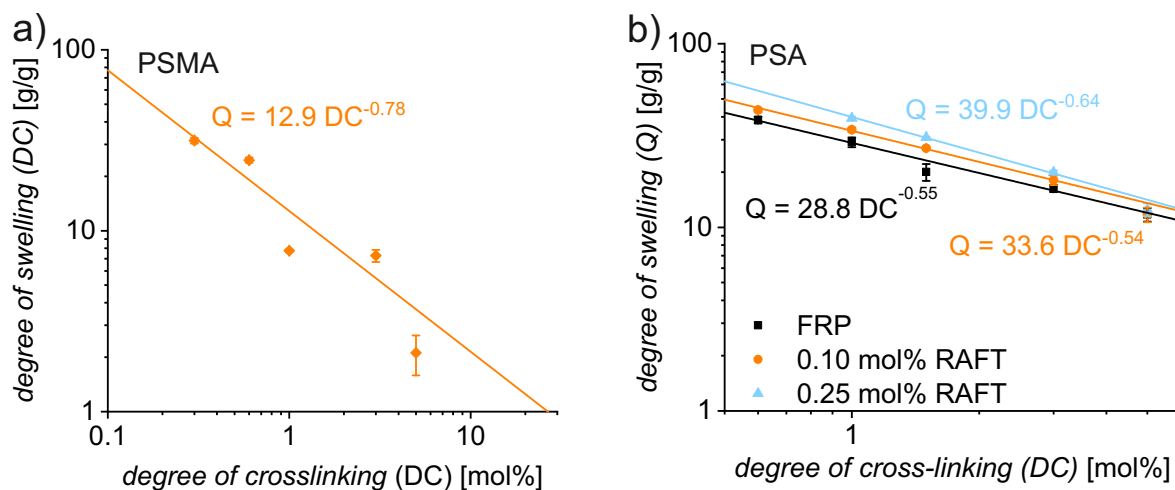


Figure 4.2: a) Depiction of the swelling experiments of the quasi-model PSMA networks. b) The degree of swelling of poly(sodium acrylate) hydrogels with varying RAFT agent contents. (1 wt% NaCl, overnight)

The samples obtained by sequential anionic polymerization showed generally lower Q_{eq} at the same DC with a scaling exponent of ca. -0.8 a stronger dependency on the degree of cross-linking as the other poly(methacrylate) gels, as displayed in **Figure 4.2 a**). The deviations could result from the hydrophobic micelles of cross-linker, which are formed during the network synthesis and thus, change the interaction of the gel and the liquid phase. The same reason explains the difference from the Flory-Rehner approach, since no phase separated gel systems are considered. In addition, the FRP poly(sodium acrylate)

hydrogels and those based on reversible addition-fragmentation transfer (RAFT) polymerization¹ were analyzed by swelling experiments, see **Figure 4.2 b**). They revealed with power exponents of ca. -0.55 a good agreement with the Flory-Rehner theory. Furthermore, a higher pre-factors of the power fit of ca. 30 – 40 was found compared to the pre-factors of ca. 13 to 30 for the poly(methacrylate) hydrogels. These should result from the more hydrophobic nature of the methacrylate based networks caused by the additional methyl group. Finally, a higher degree of swelling was found for the RAFT based polymer networks compared to the FRP, which again implies an effectively less cross-linked network structure.

4.2 Low-Field Nuclear Magnetic Resonance Spectroscopy

4.2.1 ¹H-NMR Transverse Relaxation, T_2

In the following, a brief introduction into the transverse magnetization relaxation process in polymer networks will be given. After proposing the experimental procedure, the results will be discussed in the following chapter.

The transverse or spin-spin relaxation time, T_2 , is related to a loss of the macroscopic magnetization M in the $x'y'$ -plane orthogonal to the applied B_0 field. After application of a 90° pulse, all spins are flipped into the $x'y'$ -plane and precess with the Larmor frequency ω_L around the B_0 field, as displayed in **Chapter 2.6, Figure 2.16, p. 30**. The spins exhibit the same phase directly after excitation by the pulse. A fanning-out of the spins in the rotating frame is observable over time corresponding to an exponential decay of the macroscopic magnetization M in the $x'y'$ -plane. The decay is characterized by the time T_2 , which is defined as the point where $\sim 63\%$ of the magnetization is lost ($\equiv 1/e$ remains). The dominant relaxation mode in the transverse ¹H-NMR relaxation arises from the orientation-dependent homonuclear dipolar couplings \hat{H}_D of neighboring proton spins along a polymer chain. The orientation dependency is characterized by the distance \vec{r} between the spins ($|\vec{r}| = r$) and the angle Θ of the spins to the applied magnetic field B_0 according to [78]

$$D = \frac{\kappa}{r^3} (3 \cos^2 \Theta - 1) \quad (4.3)$$

with the dipolar coupling constant D and the proportionality factor $\kappa = 120 \text{ kHz } \text{\AA}^3$ for ¹H – ¹H spin pairs. [140] The distance of neighboring protons is rather constant (lowest distance = 1.76 \AA tetrahedral groups, such as $-\text{CH}_3$), but the angle Θ can change over time averaging the $3 \cos^2 \Theta - 1$ term to values close to zero. By adding the lowest H-H-distance 1.76 \AA and $\cos^2 \Theta = 1$ to **Equation 4.3**, the highest possible dipolar coupling

¹Many thanks to Federica Cavalli for conducting these swelling experiments

can be estimated as ≈ 44 kHz.

The relaxation behavior can be linked to the orientation autocorrelation function of chain segments as the most relevant description of molecular dynamics. [42, 141] The cross-linking points in networks bring additional constraints into the system and result in a long-time plateau of the autocorrelation function. The amount of residual correlation, which is related to the cross-linking density, can be measured either by a direct analysis of the residual dipolar couplings D_{res} , as described later in the double quantum section, or by analyzing transverse relaxation decays. The transverse relaxation of the magnetization is related to the autocorrelation function of the motion and thus it is mostly affected by slow motions. Consequently, the molecular dynamics of polymer chain segments in a network, as probed by T_2 -NMR, can be linked to the network topology via its hindered dynamics, as displayed in **Figure 4.3**.

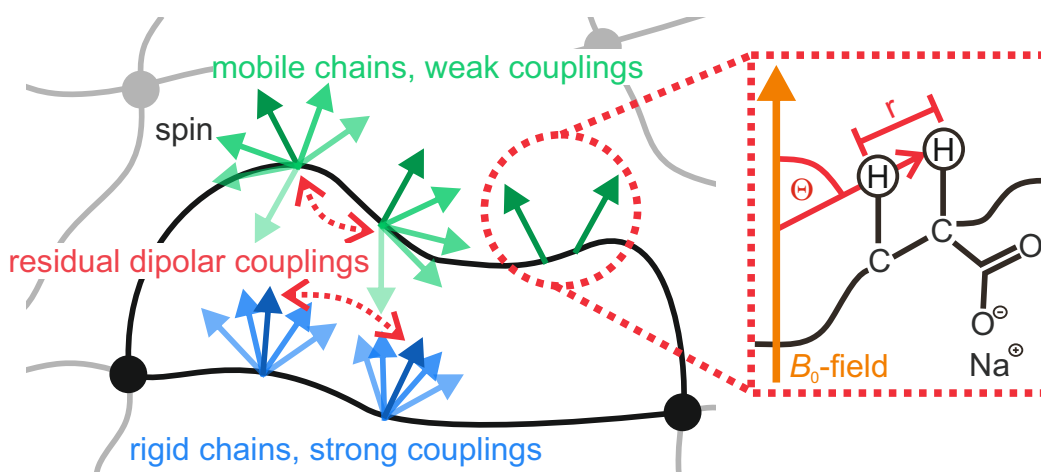


Figure 4.3: Schematical representation of the main principle of the determination of the network structure by T_2 -NMR experiments. The relaxation process is caused by homonuclear dipolar couplings of protons. These are distance r and angular Θ dependent, see **Equation 4.3**. Rigid polymer chains (blue) reveal strong dipolar couplings, since the angle changes comparably slowly causing high residual dipolar couplings. Mobile chains (green) are changing the angle faster and thus, cause weak residual dipolar couplings.

The transverse relaxation process cannot be recorded in the FID directly, since field inhomogeneities result in a faster free induction decay (FID), which would lead to a

shorter apparent relaxation time T_2^* . Thus, spin echo (Hahn-echo) techniques are applied, which refocus the spin magnetization after a 90° with a 180° pulse. The 90° pulse rotates the magnetization into the $x'y'$ -plane, while after the evolution time τ_e the 180° pulse flips all spins in the plane. The spins rephase after the same time delay τ_e forming the T_2 -echo without the T_2^* effects. [142] It was demonstrated in previous work that a single Hahn-echo is not sufficient to cover the whole T_2 -relaxation behavior in hydrogels. [14] Instead a combination of a magic solid echo (MSE) [143] and Carr-Purcell-Meiboom-Gill

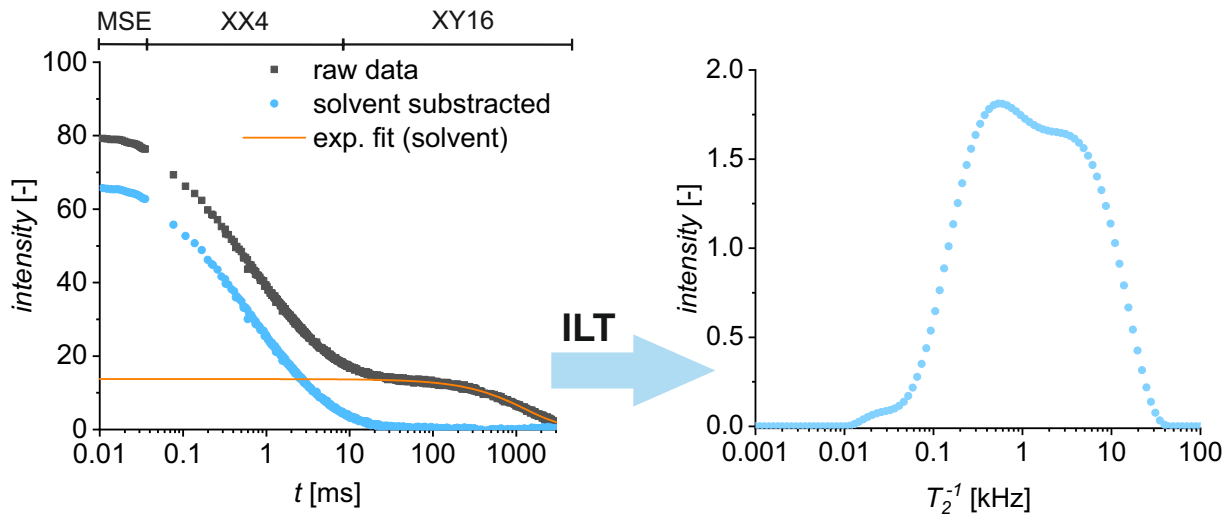


Figure 4.4: (Left) Display of the whole T_2 -relaxation curve for a typical sample (PMA-DC01-FRP) by combining the CPMG/ $XY16$ experiments with three different evolution times τ_e with the early points measured by MSE and $XX4$. In blue: The solvent subtracted data fitted with a single exponential function as described in the text. (Right) The distribution of relaxation rates T_2^{-1} obtained by the inverse Laplace transformation (ILT). [41]

(CPMG) [144, 145] sequences proved to be necessary to cover the full relaxation decay. The Hahn-echo creates a single echo, while the CPMG pulse sequence utilizes a series of echoes to recover larger parts of the relaxation curve at once. [146] Within the CPMG sequence the pulse phases are cycled in the echo train by advanced pulse arrays, such as $XY16$, to avoid spin-lock effects. [144, 145, 180] The whole relaxation curve spans over five decades in time, which requires the application of 3 $XY16$ pulse trains with varying echo delays τ_e . [41] These $XY16$ pulse sequences were recorded individually as displayed in **Figure 4.4**. In addition, the fast initial decay is measured by the MSE to overcome the dead-time of about $10 \mu s$ of the instrument. [147] The MSE was utilized in combination

with a XX4 pulse sequence, which is another derivative of the CPMG pulse train with cycled pulses for a stabilization of the echo. The XX4 sequence is less stable than the XY16 sequence, but requires a shorter pulse train, which enables an earlier acquisition and higher sampling rates. [144, 181] The employed pulse sequences were adapted from previous work and are summarized in the **Experimental B2**. [41]

To remove the relaxation contribution, which is resulting from the protons in the residual water (mainly HDO) content of the hydrogels, a single exponential function was fitted to the long tail of the relaxation curve and subsequently subtracted, as displayed in **Figure 4.4** on the left. [41]

4.2.1.1 T_2 -Relaxation Measurements of Poly(Sodium Methacrylate) Networks

Methodology

The obtained relaxation curves are challenging to interpret, since the relaxation behavior is complex and contains many information. Therefore, two different techniques for the data processing are presented and discussed. As a first approach, an empirical fit function is applied to the data set consisting of a modified version of a stretched exponential function (also called Kohlrausch-Williams-Watts-function). The time dependent signal intensity $I(t)$ is denoted by

$$I(t) = A \exp\left(-\left(\frac{t}{\tau}\right)^\beta\right) \quad (4.4)$$

where t is the time, A the normalization pre-factor, τ the empirical time constant and β the stretch factor. According to Böhmer et al. the empirical stretch factor β is inverse proportional to the width of the relaxation rate distribution in decades. [148, 149] Consequently, β^{-1} can be taken as a measure for the inhomogeneity in the mobility of the network. The factor τ refers to the characteristic relaxation time and provides an insight into the average mobility of the networks. The stretched exponential fit is a good description for the relaxation behavior for networks with a similar structure and in slowly relaxing samples. Here, the time constants and stretch factors can be compared. However, in systems with large differences in the structure, or very steep decays the stretched exponential function fails to predict the relaxation curve. In these cases, the differences from an ideal single-exponential decay (as for small molecules) becomes more pronounced and the distributions in mobility too broad to be represented by a single relaxation time. As a second approach, a set of exponential decay functions is overlaid with the data. These can be deconvoluted employing the inverse Laplace transformation (ILT), as shown in **Figure 4.4** on rate distribution. The equation is given as [150]

$$\mathcal{L}\{f(t)\} = \frac{1}{2\pi i} \int_{-\infty}^{\infty} f(t) \exp(-ts) dt \quad (4.5)$$

with \mathcal{L} being the Laplace transform operator. The Laplace transformation is classed among the 'ill posed' mathematical problems, since it cannot be analytically solved and provides an infinite amount of possible solutions. [150, 151] Consequently, the ILT can only be calculated if prior assumptions are made. The algorithm has been proposed by Ryland et al., which was implemented into the MATLAB software package. [152, 153] The main parameters, which have to be set are the number of time data points (\equiv number of exponential fit functions applied) and the smoothing parameter α , which weights the residuals between the fit and the data. A low number of points and a high α parameter lead to broad logarithmic Gaussian distributions, whereas high number of points in combination with low values of α result regularly in a set of delta functions. Consequently, it is crucial that these parameters were kept constant for all samples throughout this thesis in order to avoid losing comparability. A smoothing parameter of $\alpha = 10$ and a number of 100 points were chosen, which have been reported to match hydrogel data well. [41] If the ILT is applied to noisy or incomplete data sets, the evaluation cannot describe the raw data accurately. It has to be clarified that the intensity scale of the ILT data can only be utilized for relative comparisons, since it mainly depends on the number of points applied in the inversion curves. Additionally, it has been stated that this method can be invalid if non-exponential decays are treated. [154]

In the second approach, the inhomogeneity of the mobility of the network was determined by calculating the standard deviation σ_{log} , as it represents the width of the T_2 -relaxation rate distribution. To ensure that all points have an equal spacing and thus, an equal weight in the calculation of the standard deviation, the x-axis was linearized by taking the logarithm giving the linearized standard deviation σ_{lin} . In this way, the comparison of distributions is enabled, which are different in shape and well separated on the logarithmic scale. Subsequently, the standard deviation σ_{log} was obtained by back-transformation of σ_{lin} by

$$\sigma_{log} = 10^{\sigma_{lin}} \quad (4.6)$$

With these tools the information from the raw data, a comparative study of the synthesized samples was conducted.

Free radical polymerized poly(sodium methacrylate) networks

In a first attempt, free radical polymerized poly(sodium methacrylate) (PSMA) samples with varying content of cross-linker, ranging from 0.4 to 20 mol% with respect to the monomer, were compared. Those hydrogels are taken as standards for other samples from more elaborated synthesis techniques (synthesis, see **Chapter 3.1.1, p. 41**). It was evaluated, if these polymerization methods result in an more homogeneous mobility distribution, which could be an indicator for more homogeneous network structures.

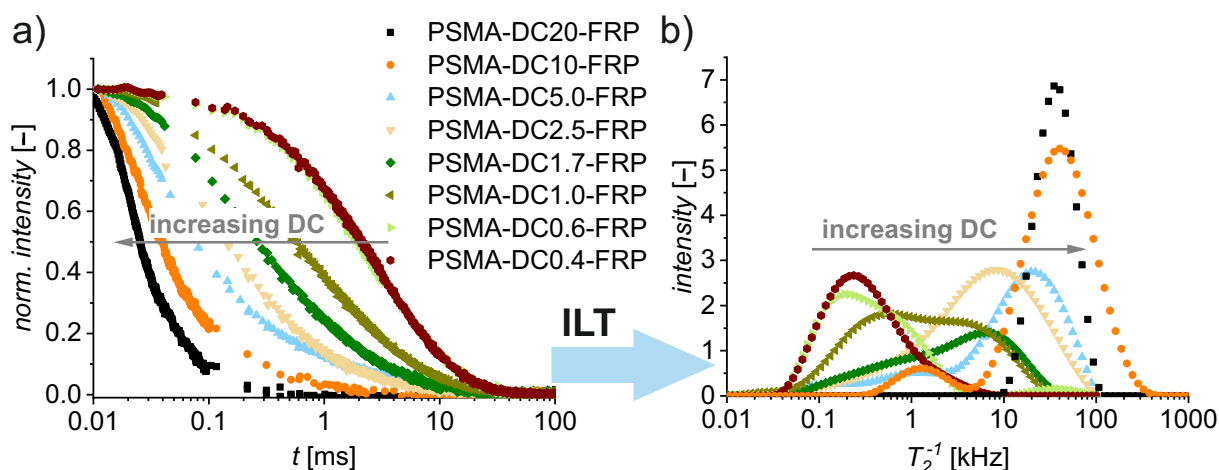


Figure 4.5: a) The ^1H -NMR T_2 -relaxation curves and b) the corresponding relaxation rate (T_2^{-1}) distributions of free radical polymerized (FRP) poly(sodium methacrylate) (PSMA) samples with different degrees of cross-linking (DC in mol%) (1024 scans, 1/6 (g/g) polymer/ D_2O , RT, low-field NMR, pulse sequence see **Appendix B.3.2**, p. 140).

The respective relaxation curves are depicted in **Figure 4.5 a)** and reveal a faster relaxation for a higher degree of cross-linking (DC). This reflects the reduced mobility of the chains due to the additional cross-links. The fastened relaxation behavior is characterized by the relaxation rate distribution resulting from the ILT with increasing relaxation rates, as shown in **Figure 4.5 b)**. In the swelling experiments, same correlation of DC and the effectively achieved density of junctions in the network, which indicates that the loss in mobility is directly reflecting a change in the network structure. For a quantification of this trend, the characteristic relaxation times τ were analyzed, which are provided by the stretched exponential fit, see **Equation 4.4**. They exhibit a power law dependency of the degree of cross-linking, as depicted in **Figure 4.9**, with a scaling exponent of -0.95.

Anionic single step

The samples provided by direct anionic co-polymerization of monomer and linker in a single polymerization step were also tested with different degree of cross-linking, synthetic procedure see **Chapter 3.1.3**, p. 3.1.3. The DC was altered from 0.3 to 5.0 mol%. The T_2 -relaxation curves exhibited higher relaxation rates and faster relaxations with higher DC like the FRP samples, as shown in **Figure 4.6**.

In addition, a clear deviation from the monomodal relaxation behavior is found for the 5.0 and 3.0 mol% cross-linked samples, which are characterized by a very broad T_2 -relaxation

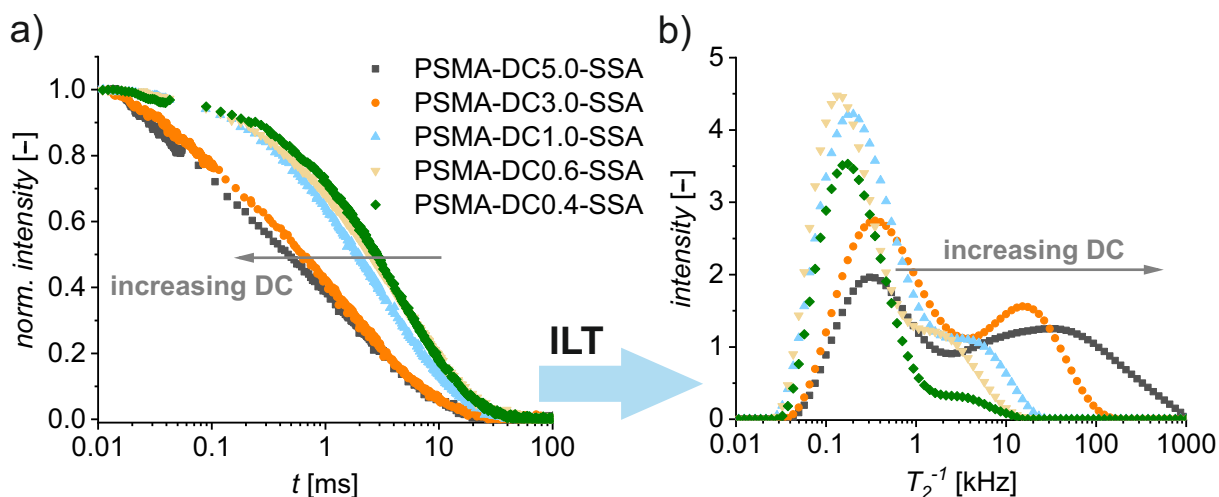


Figure 4.6: a) The ^1H -NMR T_2 -relaxation curves and b) the corresponding relaxation rate distributions of poly(sodium methacrylate) (PSMA) samples obtained by anionic copolymerization in a single step with different degree of cross-linking (DC in mol%). (1024 scans, 1/6 (g/g) polymer/ D_2O , RT, low-field NMR, pulse sequence see **Appendix B.3.2, p. 140**) Please note that relaxation rates higher than 44 kHz are not physically meaningful, see **Equation 4.3, p. 64**. This can be seen as mathematical artifacts resulting from the ILT.

rate distribution. The obtained bimodal distribution could result from a loss of control during the cross-linking process, or parts of the network were destroyed during the deprotection reaction. Contradicting to the assumption of a partial deterioration, no pronounced bimodal distributions were detected in any of the other polymerized samples subjected to the same deprotection technique. The dependency of τ on DC disclosed the same empirical power law as the FRP samples. However, the values of τ are higher and the scaling exponent is smaller, with a value of -0.37, see **Figure 4.9**. These findings imply a less dense linked network through the anionic polymerization process, which is confirmed by the swelling experiments, see **Figure 4.1, p. 62**.

Quasi-model networks

In this case, the hydrogels were fabricated by sequential polymerization, where the polymer chains were polymerized first, followed by the coupling reaction by adding the cross-linker. The linker forms highly cross-linked micelles with an undefined number of coupled chains. The length of the polymer chains between two junctions was adjusted to the (theoretical) length of the chains in the FRP samples. The resulting DC was varied from 0.3 to 5.0 mol%.

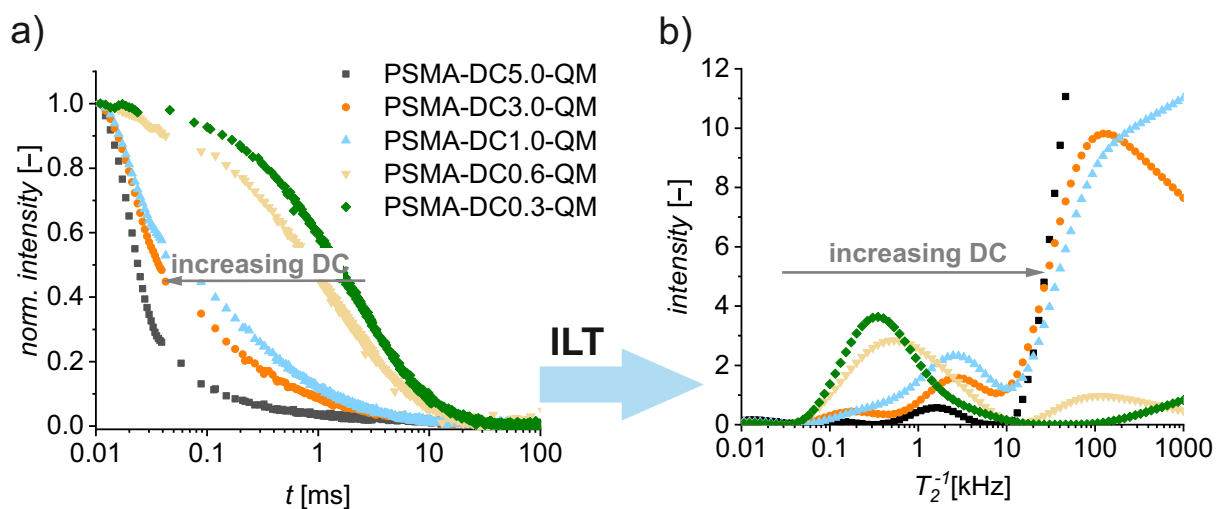


Figure 4.7: a) The ^1H -NMR T_2 -relaxation curves b) and the corresponding relaxation rate distributions of poly(sodium methacrylate) (PSMA) samples obtained through anionic polymerization with subsequent coupling. The respective degree of cross-linking (DC) is provided in the legend in mol%. Please note that relaxation rates faster than 44 kHz are not physically meaningful, see **Equation 4.3**, p. 64 (1024 scans, 1/6 (g/g) polymer/ D_2O , RT, low-field NMR, pulse sequence see **Appendix B.3.2**, p. 140).

Like the FRP and single-step anionic samples, the hydrogels obtained from sequential anionic polymerization revealed a faster relaxation for higher DC , as displayed in **Figure 4.7 a)**. However, the highly cross-linked micelles showed very strong dipolar couplings (majority > 10 kHz), which lead to bimodal distributions of the T_2 -relaxation rates. The relaxation rates of the samples were so high that they couldn't be resolved by ILT, but reached into infinity, as shown in **Figure 4.7 b)**. This trend towards high relaxation rate intensities is caused by the Gaussian decay of the polymer samples, which cannot be treated by the ILT transformation due to a limitation to exponential functions.

Thus, data of those samples were not taken for further analysis and comparison of the T_2 -relaxation rates. With a scaling exponent of -1.4, the parameter τ of those samples indicate a stronger dependency of the DC than that of the FRP samples, due to the immobilizing effect of the hydrophobic micelles. These are through their size and the many entering chains rather immobile, [81] and therefore stiffen the surrounding polymer chains.

Model Networks

In the next step, the polymer networks were analyzed, which were synthesized by anionic polymerization of the chains with subsequent azide-alkyne Huisgen ligation as cross-linking reaction, refer to **Chapter 3.1.5, p. 49**. The chain length between two cross-links was adjusted to the (theoretical) length of the meshes in the FRP samples for an facile comparison. The designed DC was varied from 0.2 to 2.0 mol%. The polymer networks

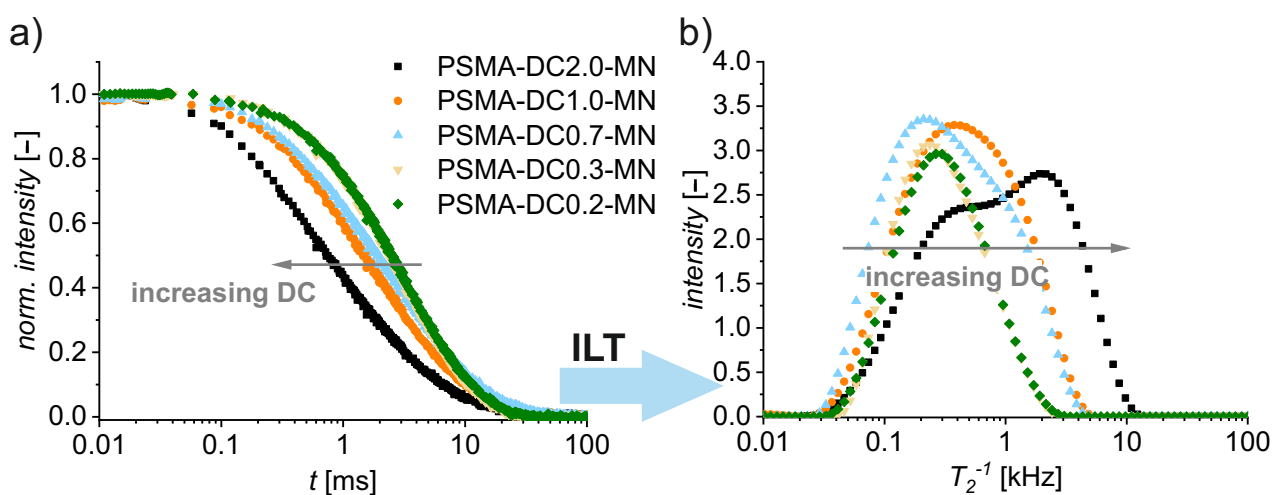


Figure 4.8: a) ^1H -NMR T_2 -relaxation curves and b) the corresponding relaxation rate distributions of poly(sodium methacrylate) (PSMA) samples obtained by anionic polymerization with subsequent cross-linking via azide-alkyne Huisgen ligation with different degree of cross-linking (DC) (1024 scans, 1/6 (g/g) polymer/ D_2O , RT, low-field NMR, pulse sequence see **Appendix B.3.2, p. 140**).

are more mobile than their FRP counterparts, as suggested by the relaxation curves in **Figure 4.8 a)** indicating a lower cross-linked network structure. This reduced cross-link density is confirmed by the higher swelling rates, compare **Figure 4.1 b)**, **p. 62**. The same trend of fast relaxations with higher DC was observed, while the characteristic relaxation time τ revealed the same power dependency as the FRP samples.

The scaling exponent is with a value of -0.49 lower than that of the FRP sample. This indicates that the cross-linking efficiency through the azide-alkyne Huisgen ligation is lower.

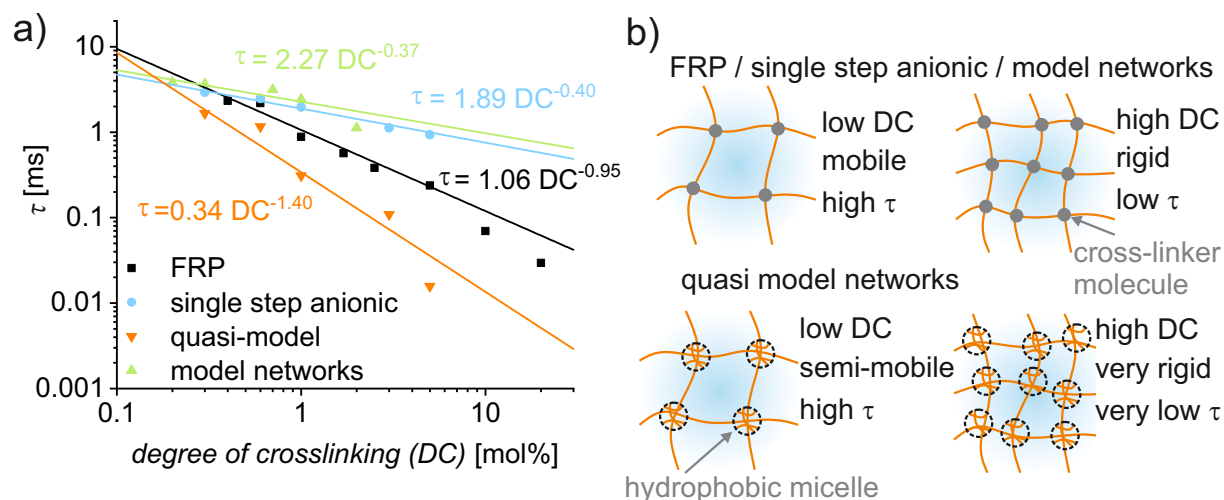


Figure 4.9: a) Comparison of the characteristic T_2 -relaxation times τ as obtained by the stretched exponential fit (Equation 4.4, p. 67). Each data set was fitted employing an empirical power law. The lower slopes and higher prefactors indicate a lower efficiency of the cross-linking process in case of the anionic single step hydrogels and the model networks. b) Schematic representation of the correlation between τ and the network structure. The quasi-model networks provide more rigid polymer network structure, due to the large hydrophobic micelles of EDGMA arising from the synthesis.

Characterization of the network heterogeneity

As explained in the introduction, the heterogeneity of the mobility in the polymer networks can be quantitatively compared using two approaches. The stretched exponential fit function yields β^{-1} as a measure for the width of the relaxation rate distribution, see Equation 4.4, p. 67. [148, 149] The three sets of polymer networks, regardless of the utilized production process, exhibit a similar level of mobility heterogeneity, as displayed in Figure 4.10 a). The apparent heterogeneity, i.e. β^{-1} , increases until a DC of 3.0 mol% and drops afterwards. This behavior can be attributed to the stiffening effect of the cross-links, see Figure 4.11. At low DC, the relaxation behavior is dominated by long polymer chains, whose motion is almost unhindered by the comparably few junction points. In the intermediate case, between $1.0 \leq DC \leq 5.0$ mol% the chains are more and more constrained by the additional junction points. The heterogeneity increases, since both, restricted chain segments close to the cross-links and mobile chain segments in the

middle of the meshes, are equally represented. This leads to the broad distributions in mobility. In case of $DC > 5$ mol%, the chains between two junction points are short and highly restricted in their motion. The whole network becomes rigid, leading to narrow distributions on the NMR timescale.

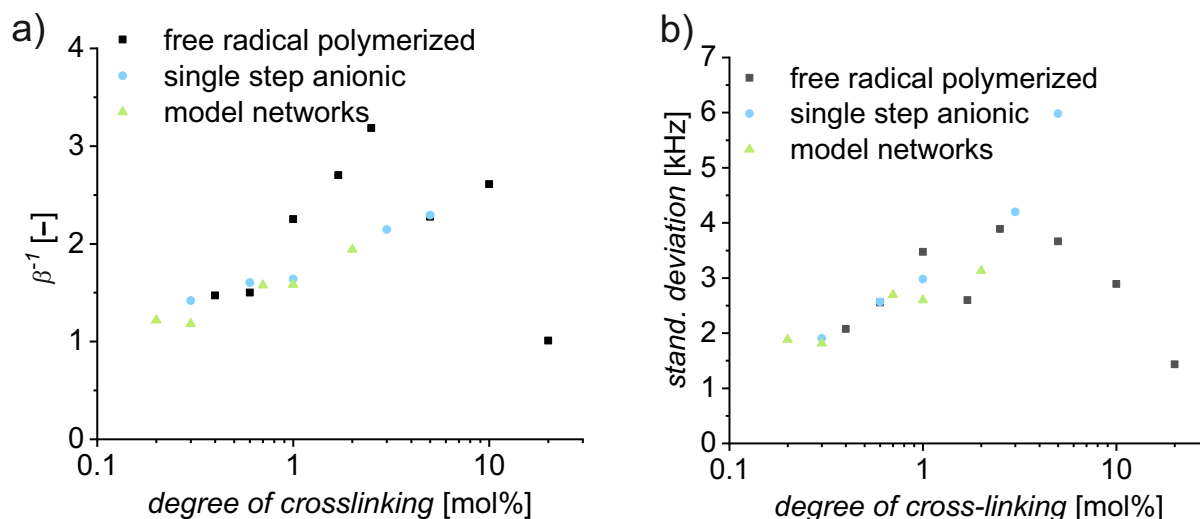


Figure 4.10: Heterogeneity of the mobility of the polymer networks produced with different methods as measured by the T_2 -relaxation behavior. a) Displayed are the width of the distribution, as measured by the stretched exponential fit (**Equation 4.4, p. 67**), b) and the standard deviation of the relaxation rate distributions (**Equation 4.6, p. 68**), as obtained by the inverse Laplace transformation. They reveal similar heterogeneities of the PSMA mobility distributions regardless of the synthetic procedure.

The second approach to quantify the heterogeneity is the determination of the standard deviation on the logarithmic scale σ_{log} of the relaxation rate distribution provided by the ILT. The results are shown in **Figure 4.10 b)**. Both techniques yield the qualitatively the same trends and show that the heterogeneity in the relaxation rates is similar for all types of hydrogels. This implies that the mobilities and with it the mesh size is on a similar level of heterogeneity. In addition, the σ_{log} from the ILT describes the structural behavior better in case of bimodal distributions, see **Figure 4.6, p. 70**. Comparatively, a single β value is not sufficient to describe these broad distributions.

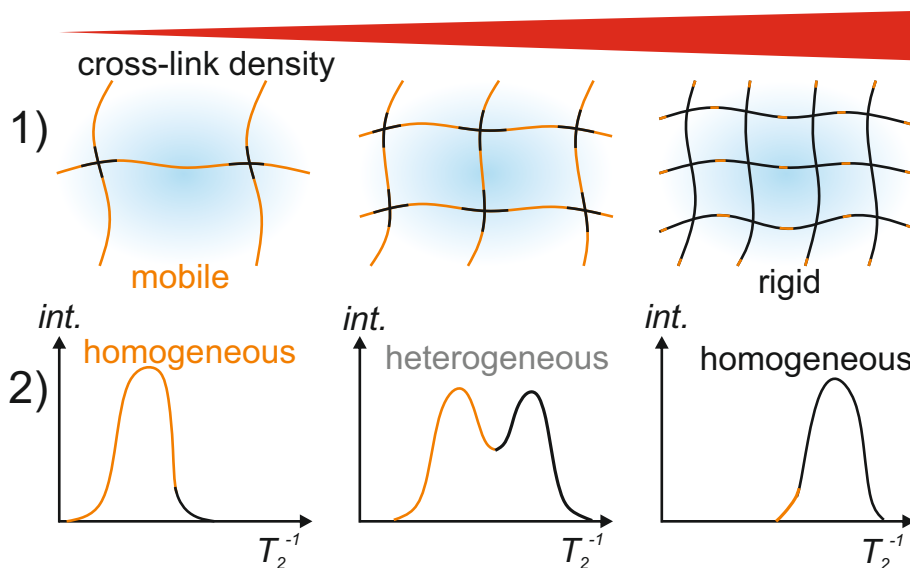


Figure 4.11: 1) Schematic representation of the influence of the cross-link density on 2) the heterogeneity of the T_2 -relaxation rate distributions. Crossing chains denote junction points. With few cross-links the chains in the network are unrestricted in their motion leading to a narrow mobility distribution (T_2^{-1}). In case of many cross-links the short polymer chains are stiffened, which also causes narrow T_2 -relaxation rate distributions (at higher rates). If mobile chain segments and rigid junction points are equally represented in the network broad mobility distributions are obtained.

4.2.1.2 T_2 -relaxation Measurements of Poly(Sodium Acrylate) Networks

A variety of poly(sodium acrylate) (PSA) networks was synthesized in order to illustrate the influence of a reversible addition-fragmentation transfer (RAFT) agent on the growth and the final structure of a polymer network. It is widely accepted that the RAFT polymerization method allows for a high control over the formation of linear polymer chains. [28, 30, 31] If the addition of RAFT agents provides a better control over the formation of polymer networks remains disputed. [36, 37]

Degree of cross-linking

In a first approach, a set of samples with varying degree of cross-linking DC were synthesized with and without the presence of a RAFT agent. Here, the DC was alternated between 0.6 and 5.0 mol%. Similar to the poly(sodium methacrylate) (PSMA) samples the PSA networks exhibited a faster relaxation for higher DC , representing the increasing rigidity of the structures. The addition of 0.1 mol% of RAFT agent to the polymerization

resulted in a softer material with longer relaxation times, as shown in **Figure 4.12 a)**. The differences between RAFT based samples and FRP networks decreased for higher DC and vanished for a $DC = 5$ mol%. The data with 0.25 mol% RAFT agent are displayed in **Figure C.3, p. 148** in the Appendix and reveal the same qualitative behavior.

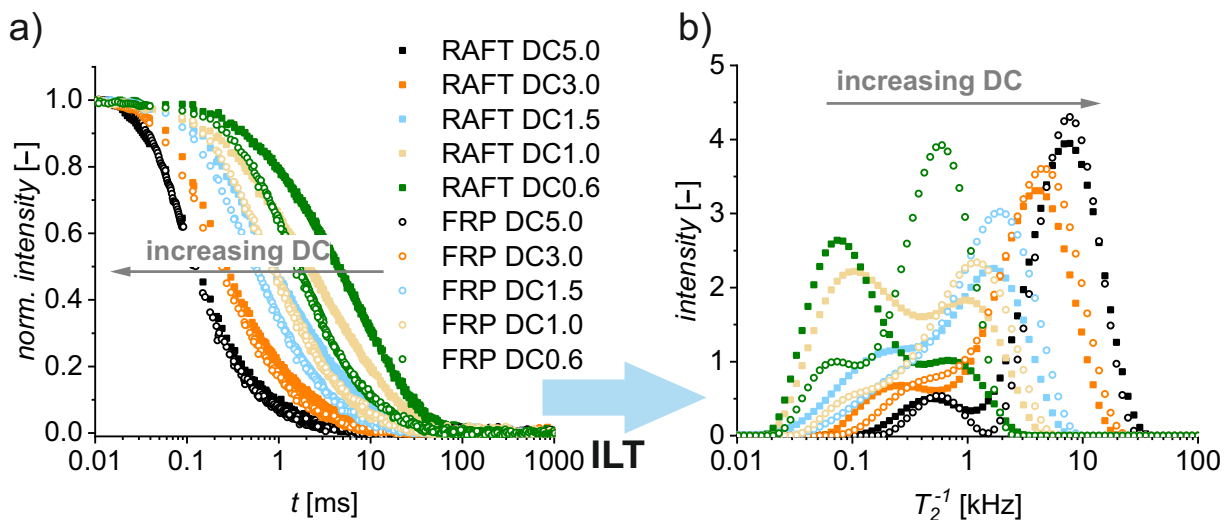


Figure 4.12: a) ^1H -NMR T_2 -relaxation curves of poly(sodiumacrylate) (PSA) hydrogels with a degree of cross-linking DC ranging from 0.6 to 5 mol% synthesized via FRP, empty symbols, or with 0.10 mol% RAFT agent, full symbols. (1024 scans, 1/6 (g/g) polymer/ D_2O , RT, low-field NMR, pulse sequence see **Appendix B.3.2, p. 140**) b) The respective relaxation rate distributions resulting from the inverse Laplace transformation (ILT).

The factor τ , which is extracted from the relaxation curve using a stretched exponential fit (**Equation 4.4, p. 67**), refers to the characteristic relaxation time and provides an insight into the average mobility of the networks. The parameter τ revealed the same empirical power law dependency on the degree of cross-linking as the PSMA samples, which reflects the loss of mobility due to the additional cross-links, as shown in **Figure 4.13 a)**. The parameter β can be taken as a measure for the inhomogeneity in mobility of the network and was found to be in the range of 2.38 to 1.61, independently from the polymerization procedure, as shown in **Figure 4.13 b)**. In case of a more homogeneous network, a narrower distribution of the relaxation time is to be expected.

According to the obtained measurements, most of the RAFT mediated networks have a higher inhomogeneity than the FRP networks, which is likely correlated to a higher heterogeneity of the RAFT network topology.

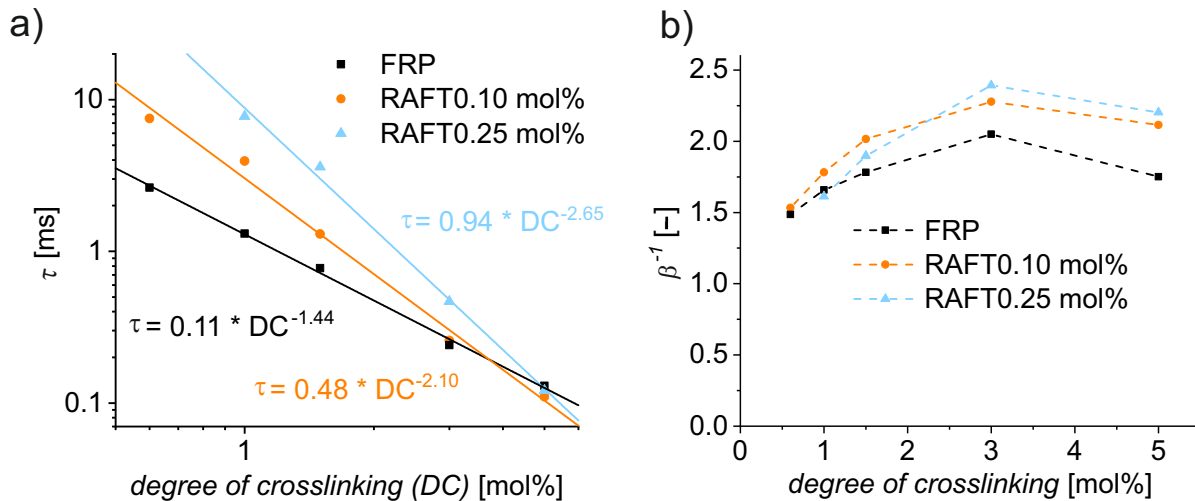


Figure 4.13: a) The dependency of the characteristic relaxation time of the magnetization τ on the degree of cross-linking DC at different RAFT agent contents: 0 (black), 0.10 (orange) and 0.25 mol% (blue). b) The dependency of the heterogeneity on the DC as measured by β^{-1} obtained by fitting of the relaxation data. The respective RAFT agent concentrations in mol% are given in the legend.

RAFT agent content

In a second approach, a set of samples with alternating RAFT agent content were synthesized with the same DC of 1.0 mol%. The RAFT agent content during the polymerization was varied between 0.05 and 0.25 mol%. The T_2 -relaxation measurements revealed a faster relaxation decay with diminishing RAFT content, as shown in **Figure 4.14 a)**. Quantification of this trend with the characteristic relaxation time τ exhibited a linear dependency on the RAFT agent content, as displayed in **Figure 4.15 b)**. It implies that the effective DC is linearly decreasing with increasing RAFT content. In a next step, the parameter β^{-1} was determined, which provided less pronounced differences, with values between 1.61 and 1.82, than the dependency on the DC from the previous section, with changes from 2.38 to 1.61. A weak increase with RAFT content was found with exception of the last data point. This implies that the RAFT based samples are almost equally heterogeneous.

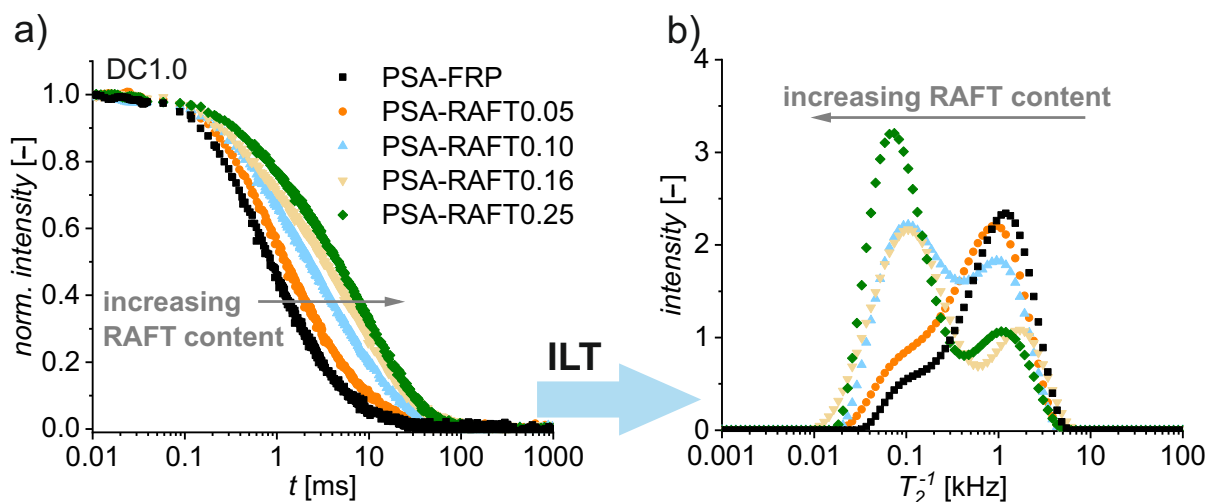


Figure 4.14: a) Normalized decay of the transversal magnetization of poly(acrylic acid) hydrogel samples with a degree of cross-linking of 1.0 mol% and varying RAFT agent contents of 0.05 to 0.25 mol%, as depicted in the legend. b) Inverse Laplace transform of the relaxation decay, revealing the distribution of relaxation rates.

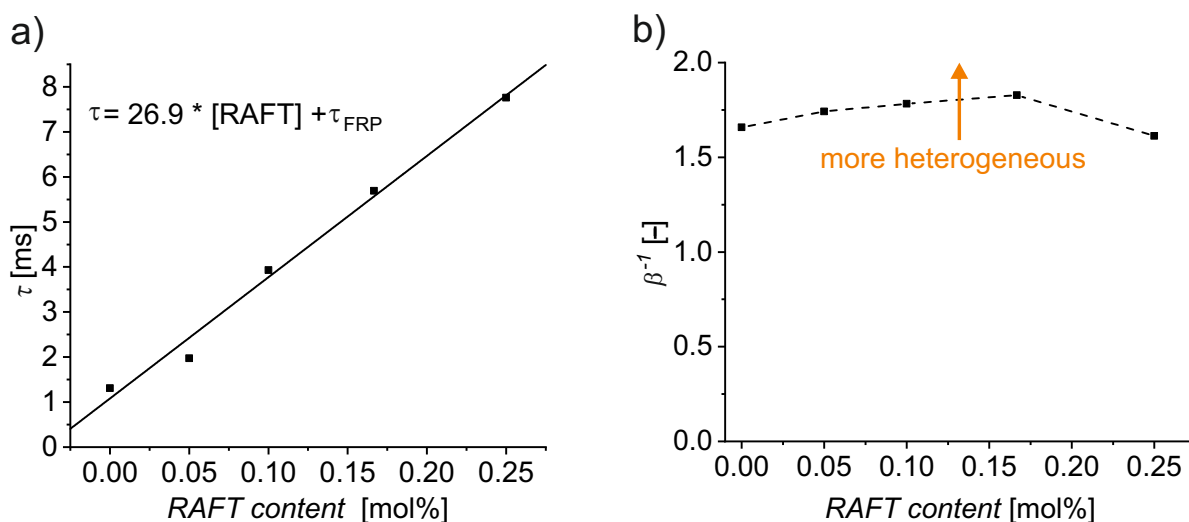


Figure 4.15: a) Depiction of the interconnection between the empirical time constant τ and the RAFT agent content. b) The dependency of the heterogeneity of poly(sodium acrylate) (PSA) networks on the RAFT agent content as measured by β^{-1} obtained by fitting of the relaxation data (**Equation 4.4**, p. 67). The degree of cross-linking DC was kept at 1.0 mol%.

Degree of neutralization

Besides the junction points, another influence on the motion of the network structure might arise from the amount of charges on the backbone. The chain backbone is stiffened, if charges are added due to electrostatic repulsions. [155] The charges increase the incorporation of water due to osmotic effects, which solvate the chains and thus, enhances the mobility. To exclude strong effects of the degree of neutralization (DN) on the relaxation, the samples were prepared starting from the same uncharged material and the degree of neutralization was varied by addition of the respective amount of base. Five different samples targeting 0, 25, 50, 75 and 100 mol% of charges were prepared according to the experimental procedure reported in **Chapter A.4**, p. 136 in the Appendix. A weak restriction of the motion was observed with increasing amount of charges, as shown in **Figure 4.16**. At charge contents above ≈ 50 mol% the influence of more charges is negligible, which is indicated by the plateau of the characteristic relaxation times τ , as displayed in **Figure 4.17 a)**. This can be explained by counterion condensation, also called Manning condensation, see **Chapter 2.4.2**, p. 24, which decreases the effective amount of charges in the network above values of $DN \geq 30$ mol%. (≥ 1 mol/L). [72] The comparison of the heterogeneity of the mobilities as characterized by β^{-1} revealed the

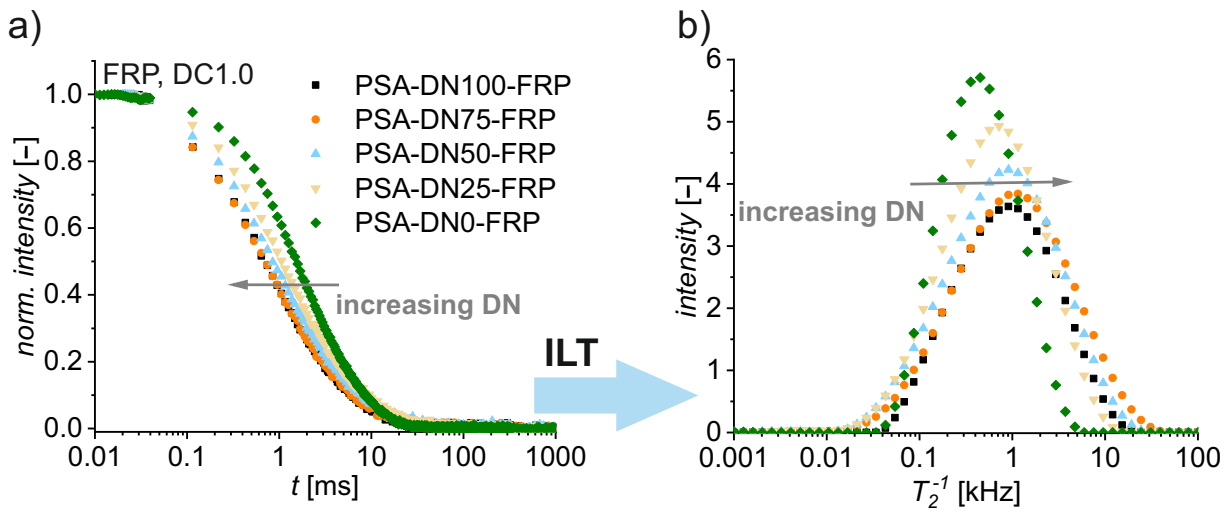


Figure 4.16: a) Normalized decay of the transversal magnetization of poly(acrylic acid) hydrogel samples with varying degree of neutralization (DN) of 0 to 100 mol%, as depicted in the legend. (1024 scans, 1/6 (g/g) polymer/ D_2O , RT, low-field NMR, pulse sequence see **Appendix B.3.2**, p. 140) b) Inverse Laplace transform of the relaxation decay, revealing the distribution of relaxation rates.

same dependency. At $DN \leq 50$ mol% the heterogeneity increases, while above 50 mol% charging β^{-1} leveled off, see **Figure 4.17 b)**. These findings are in good agreement with swelling experiments reported in literature, where also no changes of the swellability were found above DN of approx. 50 mol%. [14] Consequently, the influence of the number of charges in the polyelectrolyte network on the mobility can be neglected preconditioned a $DN \geq 50$ mol%.

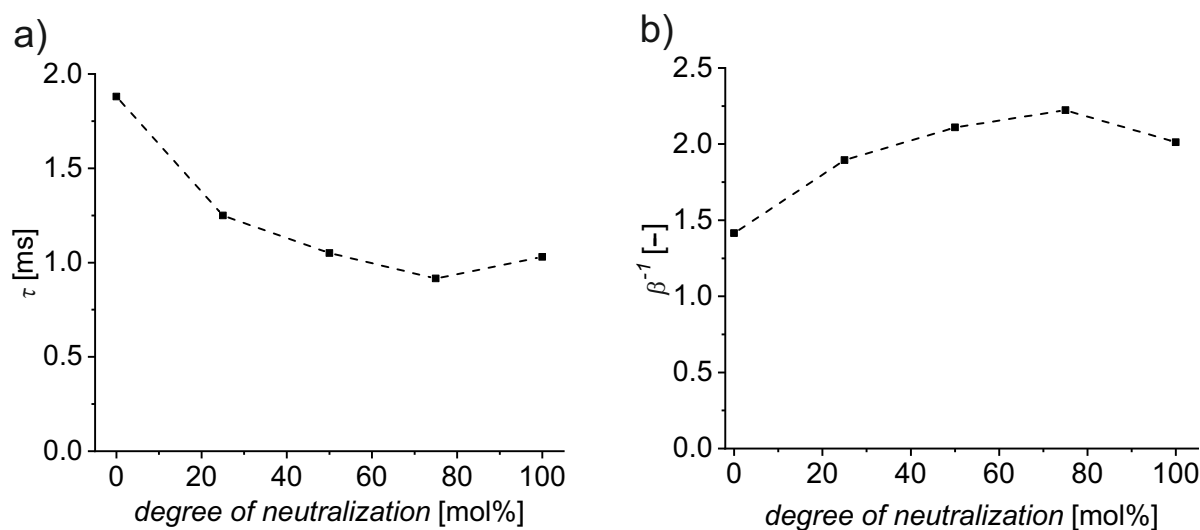


Figure 4.17: a) Depiction of the dependency of the empirical time constant τ on the degree of neutralization DN . b) The interconnection of the heterogeneity and the DN as measured by β^{-1} obtained by fitting of the relaxation data. The degree of cross-linking (DC) was kept at 1.0 mol%. The parameter β^{-1} reveals a plateau formation at $DN \geq 50$ mol%.

Comparison of the mobility heterogeneity

The mobility distribution of the RAFT samples becomes narrower towards extreme DC in both directions, while the for FRP samples the trend is less pronounced, as shown in **Figure 4.18**. The same dependency on the DC was found beforehand for the PSMA networks. An explanation for that effect could be that at the extremes the polymer networks appear more homogeneous, since at a low DC most meshes are long and thus, the chain segments are not much affected by the rigid junction points. However, at high DC most meshes are short and consequently, their chain segments are strongly influenced by the immobile cross-links. This reduces the differences in mobility in the networks and therefore, in the relaxation rates. The findings are also in agreement with those obtained using the stretched exponential approach, where the width of the distribution increases with increasing RAFT content (see **Figure 4.13 b**), p. 77.

The RAFT polymerization based samples are displayed in **Figure 4.18 b**). Here, a more consistent trend towards higher widths of distributions with growing RAFT content was observed than for the β^{-1} (compare **Figure 4.15 b**), p. 79). Since it is assumed that a broader distribution is associated with a less homogeneous network microstructure, the next step is to understand if the heterogeneity arises from a more heterogeneous mesh

size distribution or from a higher content of mobile network defects, such as dangling ends. For this purpose, double quantum measurements were performed, as reported in the following section.

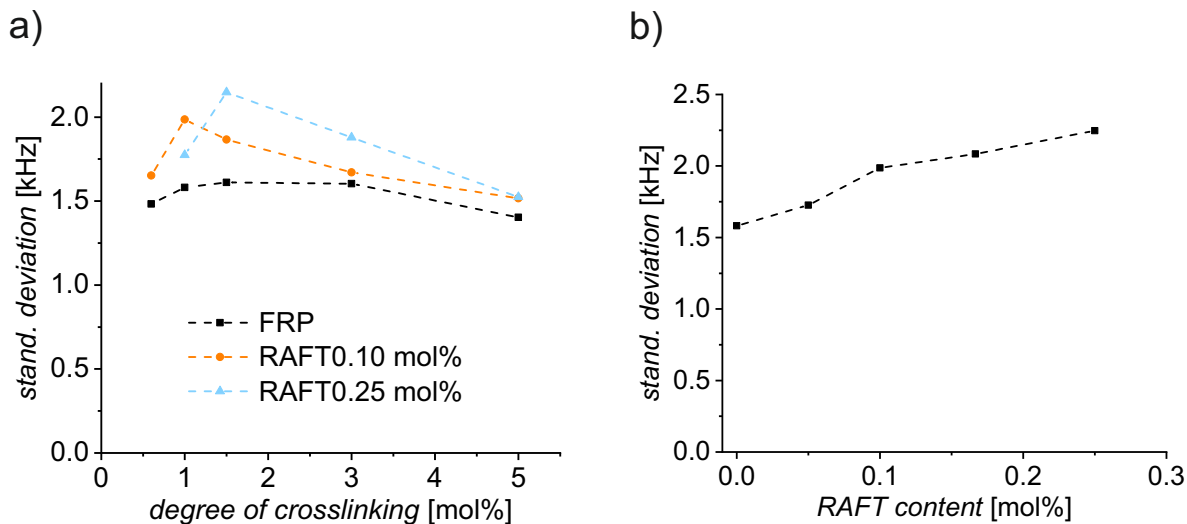


Figure 4.18: a) Width of the T_2 -relaxation rate distributions of poly(sodiumacrylate) with varying degree of cross-linking (DC) and b) RAFT agent contents as obtained by **Equation 4.6, p. 68**.

4.2.2 Residual Dipolar Coupling Measured by Double Quantum Coherence

The measurement of the double quantum (DQ) coherence is a different approach to access the molecular dynamics of polymer chains in a network, compare **Chapter 4.2.1, p. 64**. [156, 157] In a DQ measurement, filter sequences are used instead of echo experiments, which provides more information on the network structure, while sacrificing signal intensity. During these experiments, the residual dipolar coupling is directly obtained. As already explained in the T_2 -relaxation section, the residual dipolar coupling occurs due to an incomplete averaging of spatially anisotropic dipolar couplings, which are angular and distance dependent and can be described using **Equation 4.3**. Thus, the orientation dependent residual dipolar couplings can be related to the dynamics of the network, which is affected by its topology. [156] Fast moving polymer segments, i.e. in solution, average magnetic dipolar interactions to zero, since all accessible conformations are isotropic. Nevertheless, constraints in polymer networks, such as cross-links and entanglements, result in non-isotropic segmental fluctuations and consequently in residual dipolar couplings. These can be quantified by the residual dipolar coupling constant

D_{res} . [157] The experimental realization of the DQ-NMR measurements results in the simultaneous gathering of two sets of data, which can be traced back to either isotropic or non-isotropic effects. In previous work, DQ-NMR experiments were successfully employed to study elastomers [42,154,158] and hydrogels. [38,41,157] For detailed information about DQ-NMR, the reader is referred to the respective literature. [156]

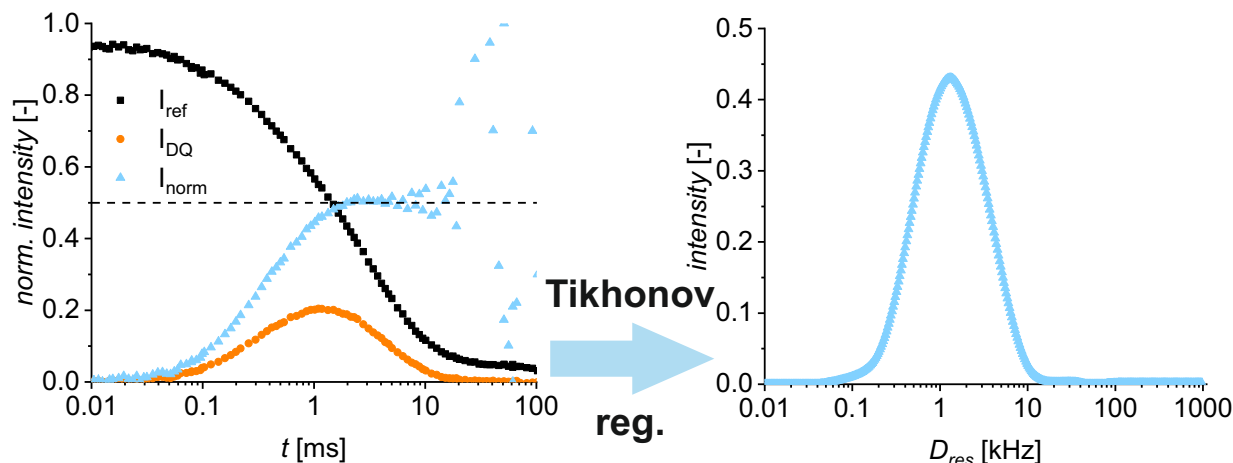


Figure 4.19: Example for a double quantum build-up curve (I_{norm} , left) and the resulting D_{res} distribution from the Tikhonov regularization (right). The build-up curve free from contribution of defects is obtained from the reference signal (I_{ref}) and the double quantum signal (I_{DQ}) by stepwise subtraction of two exponential fits and subsequent normalization, detailed procedure see **Chapter B.3.3, p. 141**. (1024 scans, 1/6 (g/g) polymer/ D_2O , RT, low-field NMR, pulse sequence see **Appendix B.3.3, p. 141**)

The measurement of DQ coherences is accomplished by the complex Baum-Pines pulse sequence, which was further improved and implemented for the minispec by Saalwächter et al. [156,159] Their pulse sequences were adapted, although the change from the old ND series to the NF series of minispec instruments made small changes in the pulse programs necessary due to the newly introduced digital filter. The employed pulse train is displayed in **Figure B.2, p. 142** in the Appendix and comprises of two sequences. The first part is used for the excitation of dipolar couplings between two spins, while the second part reconverts the magnetization back to an observable signal. The 90° pulse at the end discriminates by its relative phase between the DQ intensity I_{DQ} (blue triangles in **Figure 4.19**, left) and all the other intensities I_{ref} (red circles in the same graph). Before evaluating the DQ data, an extensive data treatments is required to obtain the build-up

curve undistorted by relaxation effects. A detailed description of the employed data processing is given in the experimental section, see **Chapter B.3.3, p. B.3.3**. Here, the long-time tail (I_{tail}) of the build-up curve is removed by stepwise fitting and subtraction of two exponential functions. Through this, the contribution of slow relaxing components, such as solvent, sol, loops and dangling ends are eliminated leading to the normalized build-up curve, as displayed in (**Figure 4.19**). [38, 41] Thus, the network structure can be analyzed free from the contribution of those network defects by evaluation of the normalized DQ intensity I_{norm} result from the following expression

$$I_{norm} = \frac{I_{DQ}}{I_{ref} + I_{DQ} - I_{tail}} \quad (4.7)$$

compare **Equation B.2, p. 142** in the Experimental. The obtained build-up curves and the analysis thereof are presented in the following section.

4.2.2.1 Double Quantum Coherence Measurements of Poly(Sodium Methacrylate)

Methodology

The pulse sequence yields the reference signal I_{ref} and the double quantum signal I_{DQ} , as shown in **Figure 4.19** (left). To determine the content of mobile species in the polymer networks, the DQ data can be described by a tri-exponential function according to [160]

$$\frac{S_{ref}(t) - S_{DQ}(t)}{S_{ref}(t=0)} = A_n \exp\left(-\frac{t}{a_n}\right) + B_n \exp\left(-\frac{t}{b_n}\right) + C_n \exp\left(-\frac{t}{c_n}\right) \quad (4.8)$$

where $A_n + B_n + C_n = 1$ and t is the time. The exponential pre-factor A_n represents the contribution of the elastic network to the overall signal, B_n the amount of mobile network fractions, i.e. network defects as loops or dangling ends. The factor C_n provides the content of mobile components, such as solvent, or extractables. The empirical factors a , b and c serve as the characteristic relaxation rates of the fractions A_n , B_n and C_n . The network its defects (B_n) relax faster than the mobile components due to the higher rigidity, which is introduced by the cross-linking points resulting in $a_n < b_n < c_n$. The results from the tri-exponential fit can be used to quantify the contribution of the network defects to the overall relaxation behavior. The content of the very mobile component C_n was not considered for this comparison, since it cannot be separated from the solvent. Moreover, a short recycle delay was employed resulting in a partially relaxed solvent fraction, which cannot be quantified.

Hydrogel networks exhibit not only a single residual dipolar coupling constant D_{res} but a complex distribution, which is resulting from their inhomogeneous structure. Different approaches can be employed to extract the underlying distributions from the build-up curve. The first method is based on fitting the data with a semi-analytical build-up function. This function assumes a Gaussian distribution of D_{res} providing the average

residual dipolar coupling constant \bar{D}_{res} and the width of the distribution σ_{DQ} . [42] The fit function denotes as [159]

$$I_{norm} = 0.5 \left[1 - \exp \left(-\frac{0.4\bar{D}_{res}^2 t^2}{1 + 0.8\sigma_{DQ}^2 t^2} \right) / \sqrt{1 + 0.8\sigma_{DQ}^2 t^2} \right] \quad (4.9)$$

where t is the time.

The second method, utilizes the numerical Tikhonov regularization to extract the distribution of the residual dipolar coupling constants, D_{res} , from the normalized DQ data. The procedure was conducted on the FTIKREG program reported by Chassé et al. [159] Gaussian kernel functions were used for the regularization, which are reported to fit the DQ build-up curves of hydrogels well. [41] A more detailed insight into the employed data processing procedure is provided in the experimental section. The main advantage of the Tikhonov regularization is that the resulting D_{res} distribution is calculated for different error parameters ϵ together with a X^2 -error. The latter parameter defines the deviation between the experimental build-up curve and the fit function from the regularization process. [159] In this way a criterion for the most reliable distribution is defined, which is not the case for the analysis of the T_2 -relaxation curves with the inverse Laplace transformation. The data up to 2 ms could be utilized for the Tikhonov regularization, since the data started to scatter as can be seen exemplary in **Figure 4.19**. In the following, the obtained build up curves are presented together with the D_{res} distributions of the best Tikhonov regularization.

Free radical polymerized

The PSMA networks synthesized by free radical polymerization (FRP) and a varying DC of 0.4 to 5.0 mol% were evaluated. The polymer networks with a higher DC could not be analyzed due to the fast build-up of the double quantum signal, which made the acquiring of the full signal experimentally impossible (i.e. \sim half of the DQ-signal intensity was reached when the first data point was recorded). The measured samples revealed a faster build-up of the normalized DQ curves with increasing DC . This confirms the findings of the previous mentioned T_2 -relaxation measurements of a reduced mobility of the networks with a higher number of junction points. Consequently, the resulting D_{res} distributions are shifting towards higher numbers with growing DC . The normalization process of the DQ data yield information about the network structure free from network defects. Therefore it can be concluded that the stiffening effect also found in T_2 -relaxation measurements is resulting from additional junction points. Furthermore, the relative content of defects was quantified using the pre-factor B_n of the tri-exponential fit (see **Equation 4.8**). The results are depicted in **Figure 4.23** (left) and reveal a decreasing content of defects for higher DC .

The reduced relative amount of defects could be explained by the higher number of cross-links in the network. These limit the relative content of dangling ends in each growing chain, since many cross-links are present per chain.

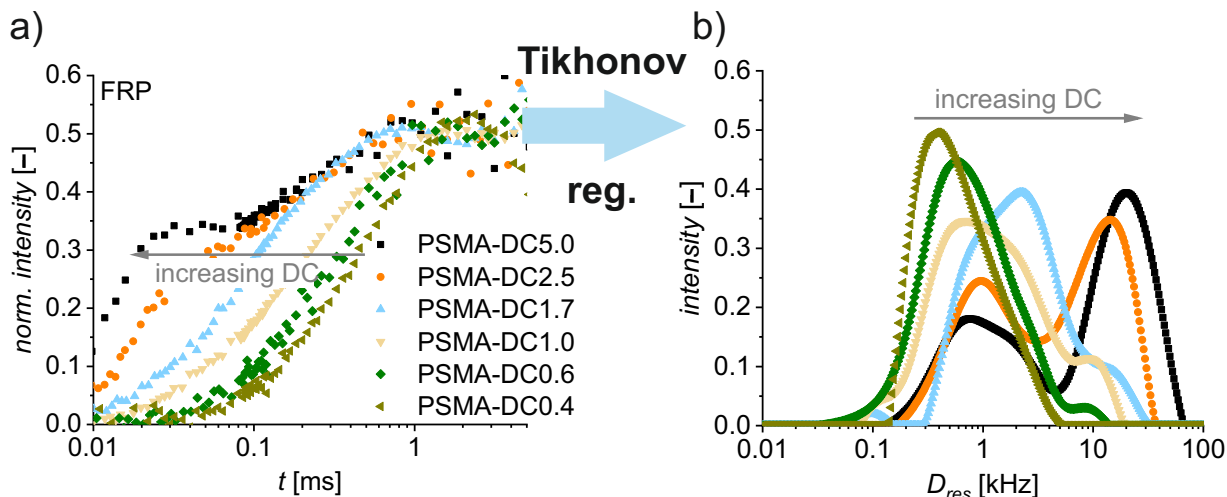


Figure 4.20: a) Depiction of the double quantum build-up curves of a set of free radical polymerized (FRP) PSMA samples with varying degree of cross-linking DC , as labeled in the legend. (1024 scans, 1/6 (g/g) polymer/ D_2O , RT, low-field NMR, pulse sequence see **Appendix B.3.3, p. 141**) b) The corresponding D_{res} distributions, which are obtained by the Tikhonov regularization, are depicted.

In case of the PSMA samples, the obtained distributions proved to be too broad to be described by the fit based on the assumption of a Gaussian distribution. Fits based on bimodal Gaussian distributions could also not be applied to PSMA networks. While fitting the curves well, they often yielded physically non-meaningful values of \bar{D}_{res} and σ , such as $\bar{D}_{res} \approx 0$ kHz for hard coupling materials. Therefore, this approach was not further considered for PSMA samples.

The heterogeneity of the PSMA samples was evaluated using the standard deviation of the D_{res} distributions. These are extracted from the distribution in the same way as for the T_2 -relaxation measurements according to **Equation 4.6**. A increasing heterogeneity was obtained for higher DC as depicted in **Figure 4.23** on the right. The two effects, reduced content of network defects and increasing standard deviation of the D_{res} distribution of the networks along DC , are counteracting each other in terms of heterogeneity. By the T_2 -relaxation experiments, which provide the overall sum of both influences (compare **Figure 4.10**), a increase in the heterogeneity is found. This could imply that the latter

is the dominating factor. However, the differences in mobility of the chain segments along a chain also have to be considered. Unfortunately, the samples above 5.0 mol% were experimentally not accessible since these could answer the question, where the obtained decrease in heterogeneity in T_2 is originating from.

Anionic single step

The samples provided by direct anionic co-polymerization of monomer and linker in a single polymerization step provided small changes between the build-up curves. A weak dependency of the DC is found, which implies a similar network mobility and thus size of the effective meshes of the network, i.e. chain length between two cross-links. The parameter B_n , as displayed in **Figure 4.23**, shows that the amount is decreasing from 58 to 31 %. However, a greater 10 % higher content of defects is determined compared to the FRP samples. This high content of defects explains the obtained lower apparent cross-link density (rigidity) of these samples. It could be explained by a higher contribution of dangling ends and loops. In case of the anionic polymerized samples, the growing chains repel each other due to electrostatic repulsion. Therefore, in the initial stage, each chain is growing individually and more likely attacks double bonds in the same chain rather than from another, which would lead to loop formation.

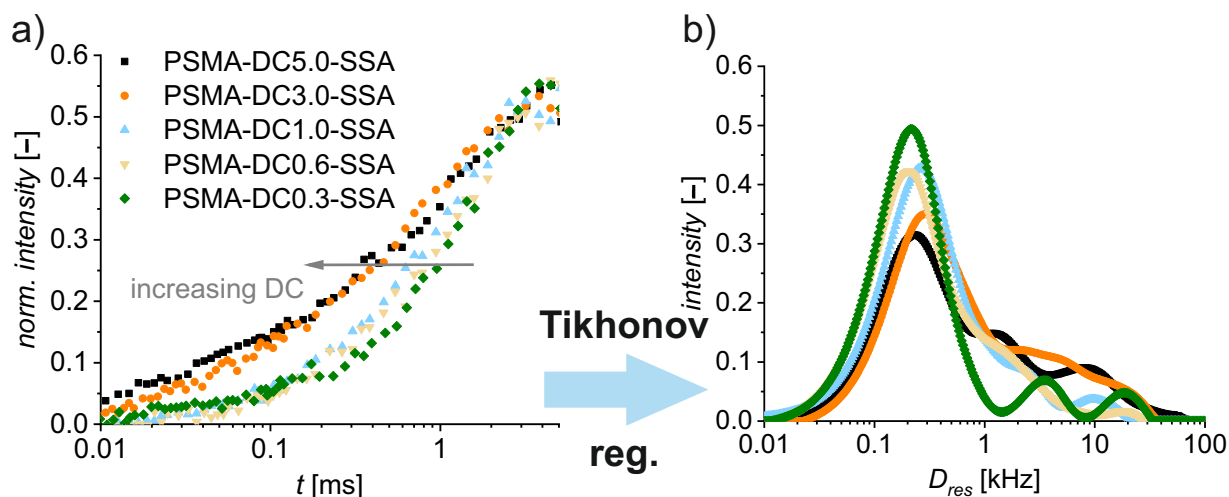


Figure 4.21: a) Poly(sodium methacrylate) samples with degree of cross-linking (DC) ranging from 0.3 to 5.0 mol%, obtained by anionic polymerization in a single reaction step (SSA), provided the depicted double quantum build-up curves b) and D_{res} distributions (1024 scans, 1/6 (g/g) polymer/ D_2O , RT, low-field NMR, pulse sequence see **Appendix B.3.3**, p. 141).

In a later stage these nanogels start to interconnect the network as they grow larger and the repulsive forces are not strong enough any more to prevent the cross-linking. In case of FRP these repulsive forces are missing and therefore the chain can more easily react with each other. In addition, it is known from the polymerization of linear chains that the concentration of the initiator defines the achievable chain length. The employed amount of initiator would have yielded in average a theoretical length of 100 monomer units per chain. By statistics, the expected number of cross-linker molecules per chain would be rather small, especially for low cross-linked networks. Conversely, the relative content of dangling chains would be large, if few junction points per chain are present. Even more dangling ends are to be expected, if it is considered that a full conversion of all cross-linker molecules is unlikely.

Furthermore, the heterogeneity arising from the network microstructure was analyzed, as displayed in **Figure 4.23 b**). These showed similar standard deviations of the D_{res} distributions for FRP and the samples obtained by anionic polymerization. Thus, it can be concluded that the chain length between two junction points is equally large. The cross-linking efficiencies are similar, however, due to the limited number of cross-linker molecules per chain more defects are formed in the anionic case.

Quasi-model networks

Next, the samples obtained by sequential polymerization were characterized, where first the polymer chain is built and subsequently the chains are cross-linked. These suffered from the same problems, as the highly rigid FRP samples with $DC > 5$ mol%. The build-up of the DQ signal of the quasi-model hydrogels with $DC \geq 1$ mol% was too fast to be experimentally accessible. Therefore, the results will not be discussed any further.

Model Networks

In case of the polymer networks, which were cross-linked by azide-alkyne Huisgen ligation, the build-up curves overlapped and no significant differences could be found (**Figure 4.22**, left). This implies that the polymer networks exhibit the same mobilities and have likely equally large meshes. The relative amount of defects (B_n) was higher than for the FRP samples, which should be mainly caused by the approx. 30 % of unreacted azide end-groups, which contribute as dangling ends to the network defects. If these network defects are neglected, the resulting D_{res} distributions are equally heterogeneous as shown in **Figure 4.23** on the right.

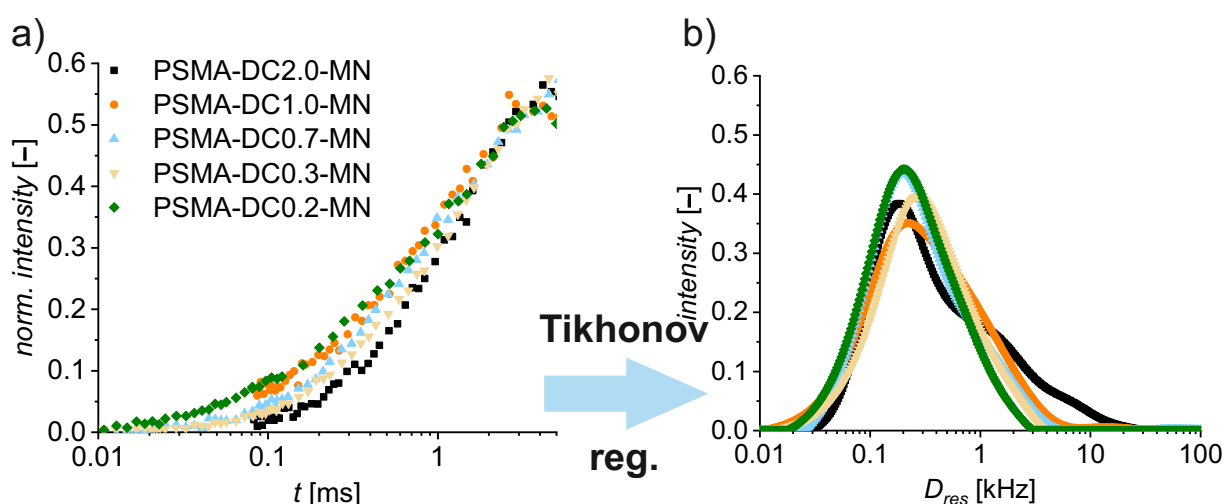


Figure 4.22: a) PSMA model hydrogels with DC ranging from 0.2 to 2.0 mol%, obtained by anionic polymerization of telechelic polymers with subsequent coupling by azide-alkyne ligation into the respective networks. The double quantum build-up curves are depicted b) and the resulting D_{res} distributions from the Tikhonov regularization (1024 scans, 1/6 (g/g) polymer/ D_2O , RT, low-field NMR, pulse sequence see **Appendix B.3.3**, p. 141).

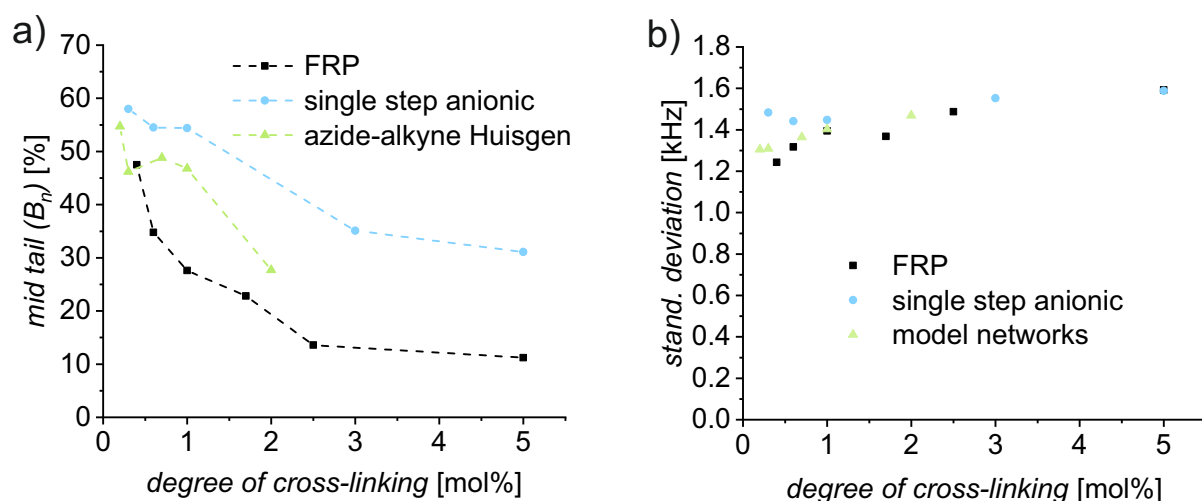


Figure 4.23: a) Relative contribution of the mid-tail (B_n , see **Equation 4.8**, p. 84) to the overall relaxation of the PSMA samples representing the amount of mobile network defects. b) The standard deviation of the D_{res} distributions as measure for the heterogeneity of the PSMA hydrogels. The FRP samples, the anionic single step and the model hydrogels are evaluated.

4.2.2.2 Double Quantum Coherence Measurements of Poly(Sodium Acrylate)

Free radical polymerized

Here, the FRP poly(sodium acrylate) (PSA) networks with varying DC of 0.6 to 5.0 mol% were analyzed. The samples with increasing cross-link density revealed that the build-up of the double quantum coherence is accelerated, which is an indication for the increased rigidity of the polymer structures, as depicted in **Figure 4.24**. The amount of mobile fractions B_n increases with decreasing DC , as shown in **Figure 4.27**, which can be explained by a lower relative amount of dangling chains resulting from the high average cross-link density.

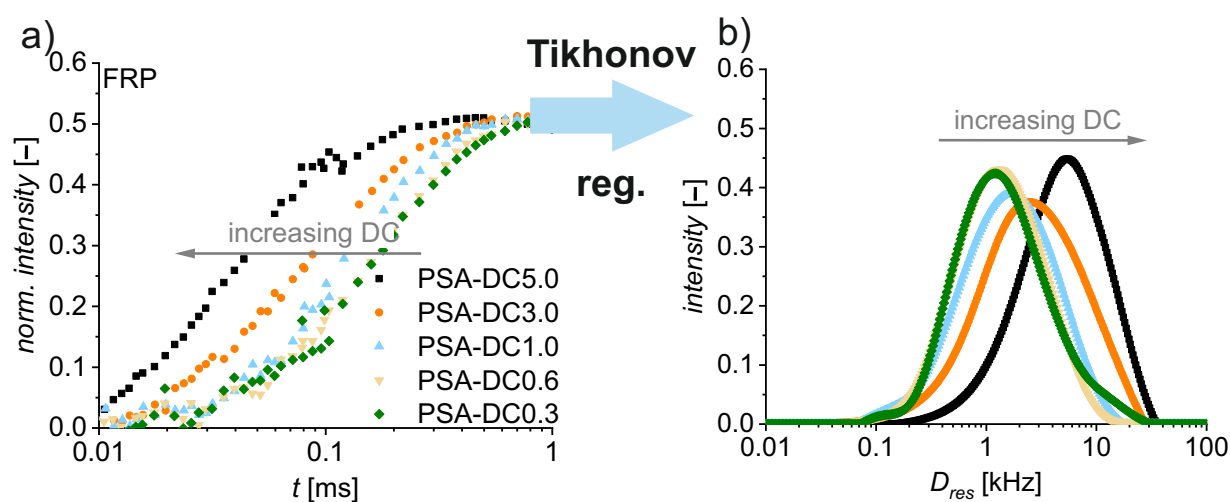


Figure 4.24: a) Depiction of the DQ build-up curves of the PSA samples obtained by FRP b) and the respective D_{res} distributions. (1024 scans, 1/6 (g/g) polymer/ D_2O , RT, low-field NMR, pulse sequence see **Appendix B.3.3, p. 141**)

RAFT content

In the next set of samples, 0.25 mol% of RAFT agent were added during the polymerization. The resulting networks showed a slower DQ build-up, and thus a more flexible network microstructure, compared to the FRP (compare **Figure 4.25** and **4.24**). This could suggest that the RAFT samples have larger mesh sizes than their FRP counterparts. Another explanation could be that the FRP samples have more physical entanglements, which act as additional cross-links. Additionally, it was observed that if the RAFT content is raised, the content of the mobile fraction B_n increases indicating a higher amount of network defects, such as dangling ends and loops (see **Figure 4.27**).

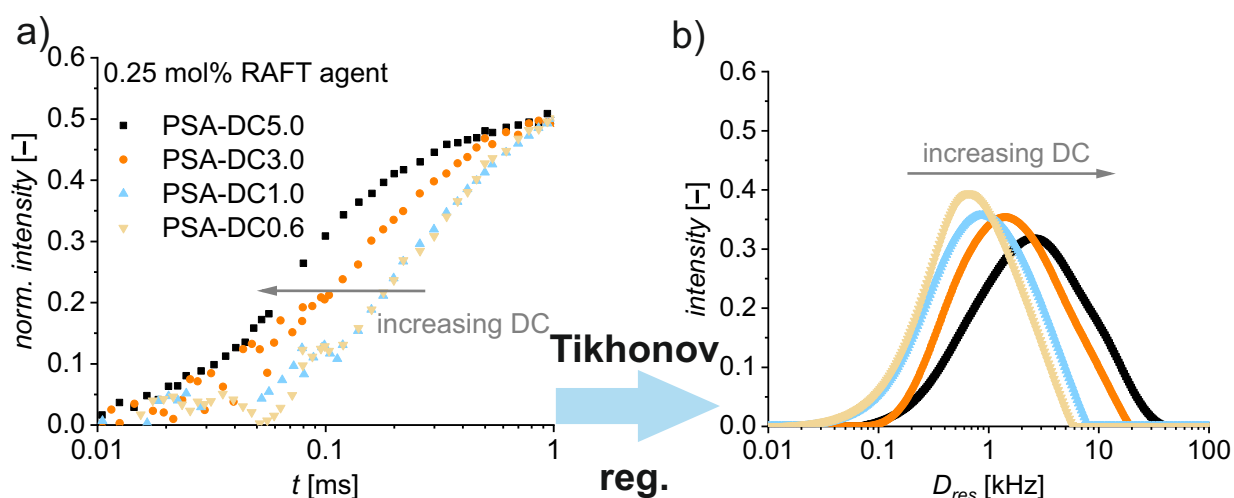


Figure 4.25: a) The DQ build-up curves for PSA samples with 0.25 mol% of RAFT agent and a varying DC (in mol%). The employed RAFT agent concentrations during polymerization are labeled in the legend (in mol%). (1024 scans, 1/6 (g/g) polymer/ D_2O , RT, low-field NMR, pulse sequence see **Appendix B.3.3**, p. 141) b) The corresponding distribution of the residual dipolar coupling constants D_{res} obtained by the Tikhonov regularization.

The build-up curves of PSA network with $DC = 1$ mol% with different amount of RAFT agent were measured. The changes in the mobility among the RAFT based samples could not be resolved, since the curves overlapped, as shown in **Figure 4.26**, which could indicate equally large mesh sizes.

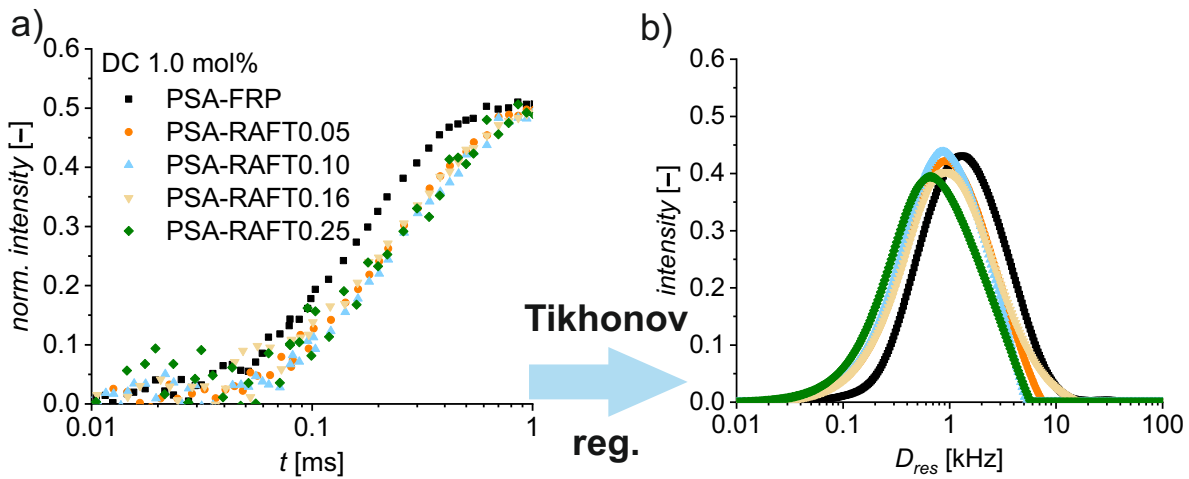


Figure 4.26: Results of double quantum experiments of PSA gel samples with different RAFT agent contents and $DC = 1$ mol%. a) The renormalized DQ build-up curves are shown. (1024 scans, 1/6 (g/g) polymer/ D_2O , RT, low-field NMR, pulse sequence see **Appendix B.3.3**, p. 141) b) The obtained D_{res} distributions from the Tikhonov regularization are displayed. No dependency of the DQ build-up curve on the RAFT agent content was found, which indicates that the underlying network structures free from defects are similar.

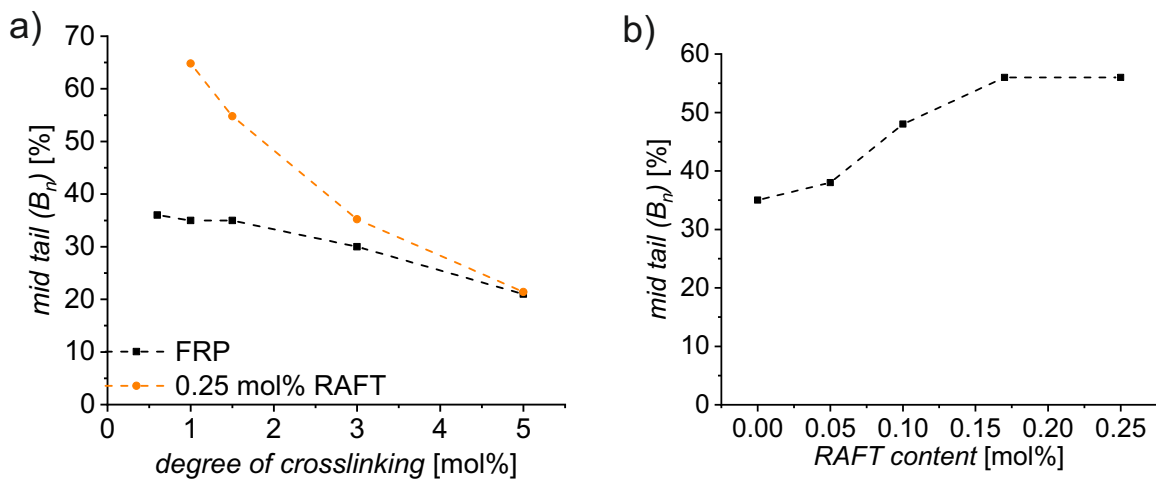


Figure 4.27: a) Depiction of the relative content of defects (B_n , see **Equation 4.8**, p. 84) of the PSA hydrogel samples with varying DC and two different concentrations of RAFT agent. b) Content of defects, as quantified by the mid-tail of the DQ signal, of PSA samples with $DC = 1$ mol% and varying RAFT agent contents.

Comparison of the mobility heterogeneity The Tikhonov-regularization and the analytical fit function (**Equation 4.9**) were applied to extract the inherent distributions of the residual dipolar coupling constants. Contrary to the PSMA networks, the PSA samples could be plotted using a single parameter method due to the monomodal narrower distributions of D_{res} , e.g. compare **Figure 4.25 and 4.20**. The distributions obtained by the Tikhonov-regularization are depicted in **Figure 4.28**. It was found for both applied methods, the Gaussian approach and the Tikhonov regularization that the standard deviations of the distributions remain independent of the cross-link density and the RAFT agent content. The standard deviations of the 3 and 5 mol% cross-linked sample synthesized using 0.25 mol% of RAFT agent, obtained by the Gaussian approach, were not considered as the measured $\bar{D}_{res} \approx 0$ lead to a singularity.

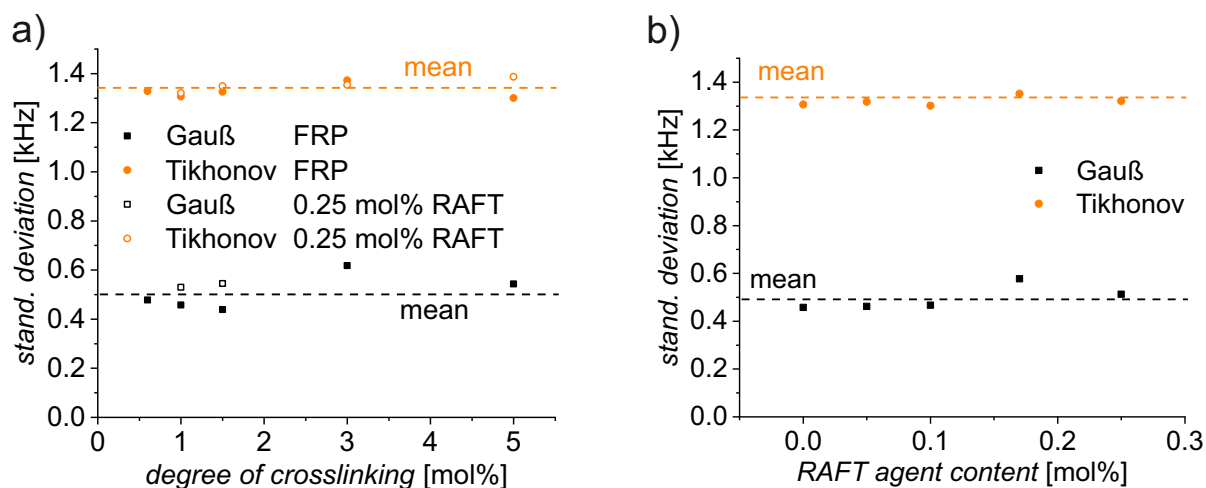
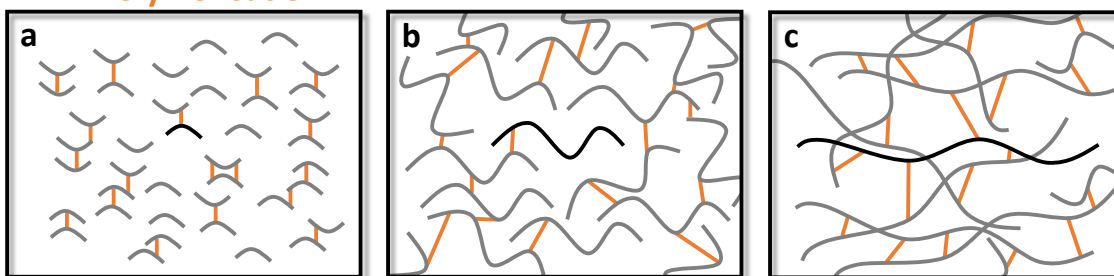


Figure 4.28: a) The calculated standard deviation of the D_{res} distributions of the build-up curves at varying DC illustrate the dependency of the heterogeneity of the network dynamics on the DC with a RAFT agent content of 0 (full symbols), and 0.25 mol% (empty symbols) of RAFT agent b) and on the RAFT agent content at $DC = 1$ mol%.

The results suggest that the mesh size distributions are equally heterogeneous for both FRP and RAFT polymerization. Consequently, the heterogeneity in mobility arises from non-elastic defects, such as dangling ends and loops. Based on the findings in the DQ and T_2 -relaxation section, a new picture of the RAFT based network formation mechanism is proposed, compare **Figure 3.12, p. 57**. It is known from literature, [161] that a higher RAFT agent content leads to shorter polymer chains with, on average, fewer cross-linking units per chain. Thus, the formed junction points are distributed over more chains leading

to a higher number of dangling ends. In an extreme case only one cross-link per chain is obtained, as shown in **Figure 4.29 a**, where no network formation is observed. If the RAFT agent content is reduced, the cross-link density per chain increases, **Figure 4.29 b**. In this case, network formation is achieved, but the network still contains many mobile parts, i.e. dangling ends. At a small amount of RAFT agent the length of the elastic chain is comparable to the one obtained in the FRP and the contribution of the mobile content is negligible, indicating fewer network defects, as reported in **Figure 4.29 c**.

RAFT Polymerisation



RAFT content

chain length /
crosslinks per chain

Figure 4.29: Representation of the proposed theoretical description of PSA network synthesized via RAFT mediated polymerization. a) High RAFT content lead to a not sufficient number of cross-linking points per chain for the achievement of network formation. b) increasing the amount of RAFT agent yields to networks with high content of dangling ends and c) at low amounts of RAFT agent the chains are bound multiple times to the network, limiting the amount of dangling ends, i.e. network defects. Adapted from [119]

4.3 Inverse Size-Exclusion Chromatography

4.3.1 Introduction

In the following section, an introduction to the basic principles of the inverse size exclusion chromatography (iSEC) and to the underlying molecular-statistical theory will be given. After providing the theoretical background, the results obtained by inverse SEC will be discussed in detail and compared to the results recorded in the NMR relaxation measurements.

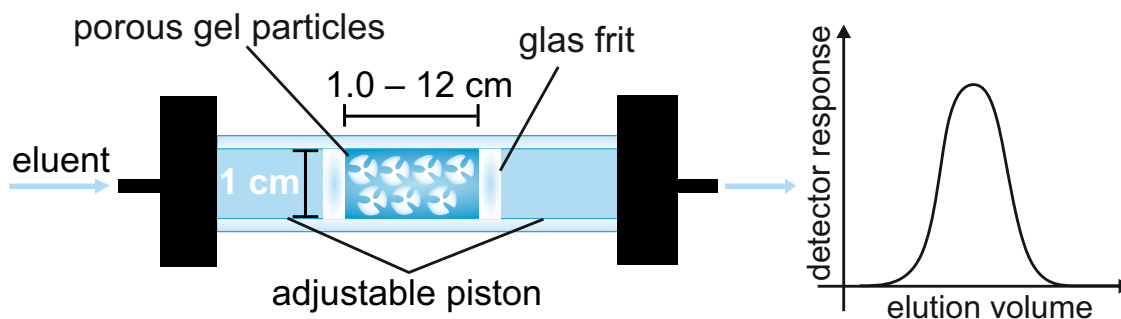


Figure 4.30: Schematic representation of the iSEC column. The inner chamber is adjusted by the movable pistons to the filling height of the analyzed porous gel. Each piston is equipped with a glass frit with $10 \mu\text{m}$ pore size to prevent the sample from leaving the chamber. The exiting glass frit is additionally protected by a layer of filter paper.

Inverse SEC is a method to access the pore size distribution (PSD) in the nanometer range of a porous material. It shares similarities with SEC from which it was developed. Both methods rely on a dissolved polymer, which is sent through a porous material that is packed into a column. In each case the retention time is recorded. Nevertheless, while in SEC the unknown component is the diffusing polymer and the stationary phase in the column is known, in inverse SEC it is *vice versa*. A known polymer standard is applied to the unknown porous material packed into the column, while the determined retention times allow back-calculations of the pore structure.

The mathematical calculations are based on the molecular-statistical theory, which describes the partitioning of flexible-chain macromolecules between the mobile phase and the porous stationary phase. [162] Here, the molar mass dependency of the distribution

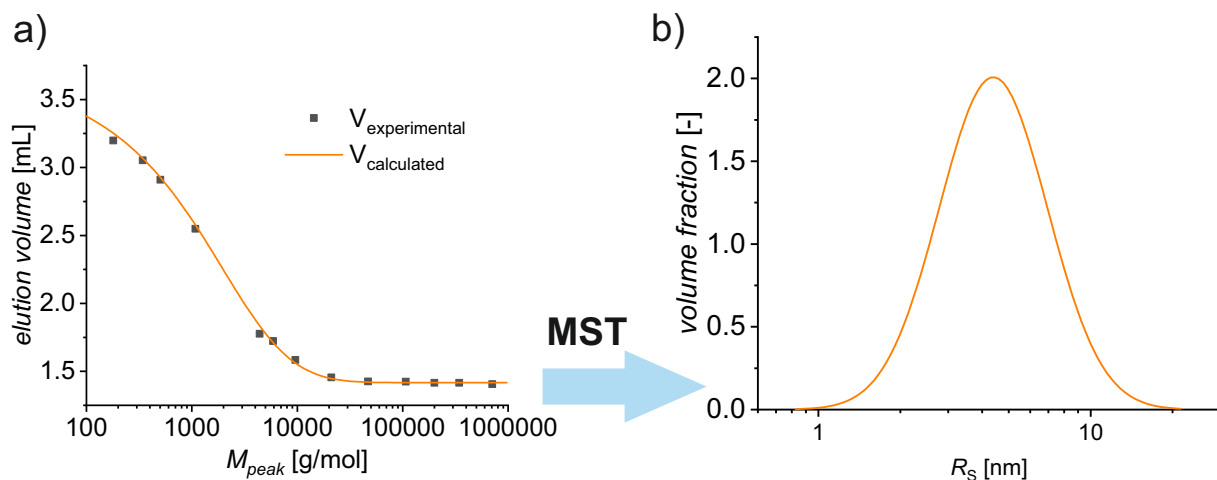


Figure 4.31: a) Example for a iSEC measurement of the sample PSMA-DC2.5-FRP with the resulting fit from the Porocheck software (PSS, Mainz, Germany). The elution volumes of the pullulan standards having the molecular weight (M_{peak} at the maximum) are given. b) The elugram is converted by the Porocheck software, based on the molecular-statistical theory (MST), into the respective pore size distributions.

coefficient K of defined test macromolecules is determined under the conditions of size-exclusion chromatography (see Chapter 2.7) according to [163, 164]

$$K = \frac{V_{el} - V_0}{V_p} \quad (4.10)$$

where V_p is the total volume of all pores, V_0 the void volume and V_{el} the elution volume of the respective polymer.

The pores are described by the parameter R , which is defined as

$$R \equiv 2 \frac{V}{S} \quad (4.11)$$

with V and S as the theoretical volume and surface area of a pore. Under the side condition of geometrical regular pores R denotes

$$R = \begin{array}{ll} \text{width} & \text{(slit-like model)} \\ \text{radius} & \text{(cylindrical model)} \\ 2/3 \text{ radius} & \text{(spherical model)} \end{array}$$

The attractiveness of **Equation 4.10** is that it is model independent and remains meaningful even for irregular shaped pores. The inhomogeneity of the pores is characterized

by the PSD function, $\Phi(R)$. By definition $\Phi_V(R)$ is the volume fraction of pores of size from R to $R + dR$. The surface-based PSD function $\Phi_S(R)$ is introduced similarly. Both functions are normalized to unity by

$$\int \Phi(R) = 1 \quad (4.12)$$

The volume-based average pore dimension parameter R_V is given by the following

$$\langle R_V \rangle = \int R \Phi_V(R) dR \quad (4.13)$$

The integration limits R_{min} and R_{max} corresponding to the minimum and maximum pore size are set to zero and infinity for the calculations.

The separation of macromolecules under SEC conditions in inhomogeneous porous media is governed by the surface-based pore dimension parameter, $\langle R_S \rangle \equiv \langle R \rangle$. [162] The average surface-based pore dimension is defined by [162]

$$\langle R_S \rangle = \int R \Phi_S(R) dR = \left[\int R^{-1} \Phi_V(R) dR \right] \quad (4.14)$$

The parameter $\langle R_S \rangle$ can also be expressed in the simple form of [162]

$$\langle R_S \rangle \equiv 2 \frac{V_p}{S_p} \quad (4.15)$$

where V_p and S_p are the total volume and the total surface area of all pores.

An important parameter for the description of the width of the PSD function is the standard width of the distribution, σ , with σ^2 being the dispersion, also called second central moment of the PSD function. Since σ usually increases with growing pore size distribution, it is convenient to express the extent of the pore size inhomogeneity by a relative width of the pore size distribution $w_{norm} = \sigma/\langle R \rangle$. Alternatively, the inhomogeneity can be expressed by the parameter U in terms of $U = \langle R_V \rangle/\langle R_S \rangle = 1 + \gamma^2$, in analogy to the \mathcal{D} of a polymer size distribution.

In a next step, the distribution coefficient K_{PSD} can be obtained from the volume-based PSD function $\phi_V(R)$ and the distribution coefficient $K_0(r/R)$ of a macromolecule of radius of gyration r in a pore of a transverse dimension R by

$$K(r) = K_{PSD}(r) = \int K_0(r/R) \Phi_V(R) dR \quad (4.16)$$

The form of the kernel function $K_0(r/R)$ is dependent on both the polymer molecule and pore model. To reduce complexity of the system, only pores of regular geometry are considered, i.e. slit-like and cylindrical pores. The polymer molecules consist of flexible chains, which change their motion behavior depending on the available space. Without

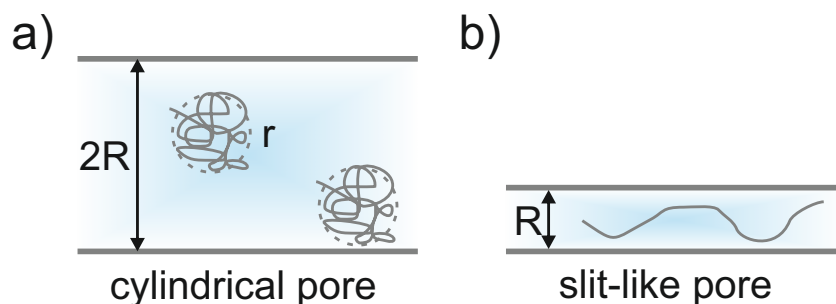


Figure 4.32: Typical conformations of polymer molecules in a) wide and b) narrow pores. In wide pores polymer coils behave similar to solid balls of equivalent radius r . In narrow, slit-like pores the long flexible chains unfold and penetrate by reptation.

spatial restriction, i.e. in large pores and free solution, polymers fold and can be treated as diffusing solid spheres with the radius of gyration r , as displayed in **Figure 4.32 a**. The case of large pores is consequently described best by cylindrical pores. In case of confined environments, such as slit-like pores, the chains unfold and penetrate even small pores by reptation, as shown in **Figure 4.32 b**. The formula for $K_0(r/R)$ for the model of an ideal flexible-chain macromolecule and pores of regular geometry have been developed by Casassa et al. [165] Here, the expression for the distribution coefficient of a polymer molecule in a cylindrical pore of radius R is given by

$$K_0(r/R) = \sum_{m=1}^{\infty} \frac{4}{\beta_m^2} \exp\left(-\beta_m \frac{r}{R}\right)^2 \quad (4.17)$$

where β_m is the m^{th} root of the Bessel function $J_0(\beta)$. In case of slit-like pores the distribution coefficient $K_0(r/R)$ with the slit width R can be derived from [163, 164]

$$K_0(r/R) = \sum_{m=1}^{\infty} \frac{8}{(\pi m)^2} \exp\left(-\pi m \frac{r}{R}\right)^2 \quad (4.18)$$

The radius of gyration of macromolecules r can be calculated from the molar mass M by **Equation 2.76** see Chapter 2.7, while the parameters, Q_M and α are known for many polymer-solvent systems and can be taken from literature. [84]

The unknown PSD function $\Phi_V(R)$ could be basically determined utilizing the experimentally obtained function $K_{PSD}(R)$ and the kernel function $K_0(r/R)$. However, using **Equation 4.16** to find an unknown $\Phi_V(R)$ function is classed among "ill-posed" mathematical problems providing infinite possible solutions, compare inverse Laplace transformation (**Chapter 4.2 p. 67**). Thus, minor errors in the experimental data and side conditions

would have a considerable effect on the calculation results. [162] Therefore, instead of computing the true shape of the PSD function a logarithmically normal distribution is postulated with the two fit parameters $\langle R \rangle$ and σ .

The distribution coefficient K can be approximated at small r by the following expression [163, 164]

$$K \approx 1 - \frac{4r}{\sqrt{\pi}} \langle R_S \rangle^{-1} = 1 - \frac{2r}{\sqrt{\pi}} \Sigma \quad (4.19)$$

with $\Sigma = S_p/V_p = 2/\langle R_S \rangle$. It has been proven, that the **Equation 4.19** stays valid for both homogeneous and inhomogeneous PSD, [162] as well as for pores of slit-like, cylindrical and spherical shape. [163–165] Consequently, the iSEC can be seen as an absolute method for the determination of $\langle R_S \rangle$. At high r the approximation of the theoretical model with pores of different geometry does not match universal dependence, but the difference remains small. As a consequence, the problem of an unknown shape of the pores can be avoided by expressing the results in terms of the the model independent parameter R .

4.3.2 Results of the Inverse Size-Exclusion Chromatography

The iSEC measurements were conducted employing the free radical polymerized (FRP) methacrylate samples as an example to establish the correlation of amount of cross-linker during synthesis to the achieved pore size distribution (PSD). Unfortunately, few literature could be found regarding the application of iSEC to hydrogel particles [44, 132] and therefore, first, a test procedure was developed in cooperation with the supplier of the analysis program and columns, Polymer Standards Service GmbH (PSS, Mainz, Germany). The practical process was modeled starting from the conditions of conventional SEC, i.e. flow rates of 1 ml/min, maximum fillings of the column and pure water as eluent, doped with sodium azide for the prevention of algae growth. Here, the cross-linked polymer particles were swollen to equilibrium overnight to avoid any changes, which might arise from insufficient swelling times. The flow rate was applied for approx. 1 h to settle the beads in the column, to remove interstitial air bubbles and to wash-out any traces of soluble impurities. After a constant pressure and stable base-line was achieved, the injections of the polymer standards were started – in case of water based systems, pullulan standards were used. Pretests with porous silica showed neither a dependency of the average pore size $\langle R_S \rangle$ on the bed length, with $\langle R_S \rangle = 3.9$ nm (1.8 cm) and 3.97 nm (8.2 cm), nor on the used flow rate, with $\langle R_S \rangle = 3.9$ nm (1.0 ml/min), 4.02 nm (0.5 ml/min), and 3.82 nm (0.25 ml/min)), respectively. Therefore, these parameters could be chosen freely for the development of the experimental procedure. Furthermore, the average pore size

of the aluminum oxide of 5.8 nm, which was provided by the manufacturer, matched the measured 5.4 nm of the iSEC. Yet, a longer bed length generated a better separation of the polymer and the system peak, which facilitated the identification of the required peak maxima. Consequently, longer bed lengths were preferentially used, usually 5 – 10 cm depending on the disposable amount of sample. Originally, the iSEC was developed for the analysis of solid porous materials, such as highly cross-linked polymer beads for SEC column fillings, [132] silica particles for HPLC, [166, 167] or porous alumina oxide and zeolites for catalytic purposes. [168] The polymer gels, especially the low cross-linked ones, proved to be too soft to be applicable. During the conventional SEC approach, the gel particles were deformed by the applied flow and squeezed into the exiting frit of the column leading to pressure overshoots up to the complete self-sealing of the column by gel-blocking. Thus, a thoughtful adaption of the utilized conditions had to be made and the flow rate was lowered to 0.2 mL/min. The addition of 1 wt% of sodium chloride (NaCl) lead to a lower swelling ratio with a higher efficient content of cross-links per volume and consequently more durable gels. In addition, the exiting glass frit with a pore size of ca. 10 μm was protected from penetrating polymer particles by addition of a layer of filter paper. With these changes, the measurement of hydrogels down to degree of cross-linkings (DC) of ≈ 0.6 mol% were enabled. Although, the adjustment of the movable pistons on the sides of the column to the sample filling height had to be handled with care, since the samples could be squeezed lowering the apparent pore size. This was demonstrated at the example of the sample PSMA-DC0.6-FRP, where the column filling was squeezed from a bed length of 8.2 cm to 4.4 cm lowering the apparent average pore size from 6.7 to 3.0 nm. The sodium chloride solution was later exchanged for an aqueous phosphate buffer solution, which provided a better resilience against possible pH differences between the samples that might influence the polymer separation beside the lower water uptake.

For each data point six measurements of the same batch were averaged. The column was packed three times and two measurements were recorded of each packing. Unfortunately, the reproducibility was uneven from sample-to-sample as indicated by the large error bars in **Figure 4.33 b**). With a lower degree of cross-linking a higher average pore size was found, as displayed in **Figure 4.33 a**). An empirical power law with a scaling exponent of -0.52 could be fitted to the data. The power dependency of about 0.5 of the degree of cross-linking could be explained by the distance of two cross-linked points in a polymer network l . As shown by **Equation 2.2** in **Chapter 2** the end-to-end distance of a Gaussian polymer chain is proportional to the square root of the number of monomer units n it consists of. Under the assumption that the average gap between two junction points can be described by a random folded chain of length n and that full conversion of the cross-linker is achieved, the distance l is inversely proportional to the cross-link

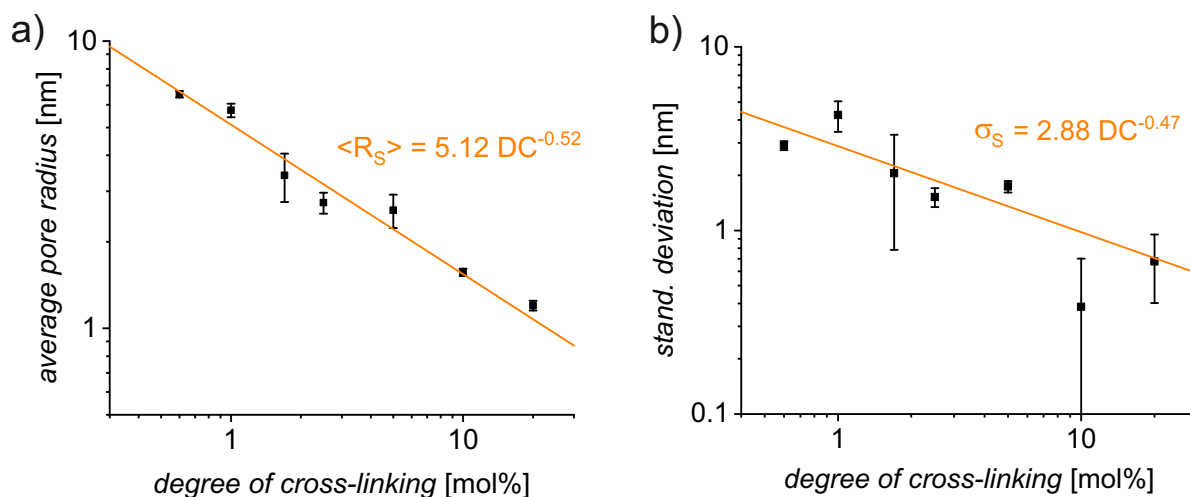


Figure 4.33: a) Dependency of the average pore size and b) the standard deviation of the obtained pore size distributions on the degree of cross-linking. For each data point, three different column packing were measured twice. A flow rate of 0.2 mL/min, a bed length of 5 – 10 cm and a 0.1 M solution of disodium phosphate with 0.05 M sodium azide as eluent were utilized, see also **Figure 4.31**, p. 96.

density DC with $l \sim n^{0.5} \sim DC^{-0.5}$. It has been mathematically proven that the radius of a circle R inside a regular polygon can be calculated by [163]

$$R = 2 \frac{S_A}{P_A} \quad (4.20)$$

where S_A is the area of the polygon and P_A its perimeter complemented by a third dimension, the depth, compare **Equation 4.11**, p. 96 in the previous section. With $S_A \sim l^2$ and the perimeter being a multitude of the side lengths l , follows $R \sim l \sim DC^{-0.5}$ and thus, a theoretical power dependency of -0.5 of the DC can be found as confirmed by the measurements. These considerations rely on the accuracy of the presumption of a folded Gaussian chain for the distance between two junction points. Especially in the examined case of high charged polymer backbones and stretched chains in fully swollen gels the assumptions should be rather invalid, nevertheless still provide good agreement with the experimental data. The same power dependency of the standard deviation of ca. -0.5 of the PSD is obtained, as shown in **Figure 4.33 b)**. The same power correlation implies in return that with growing average pore size a broader distribution is obtained.

In a next step, the obtained pore size distributions from the iSEC were compared to the relaxation rate distributions resulting from the T_2 -measurements. As described in Chapter 4.2, the transverse relaxation in NMR-relaxometry is related to the autocorrelation

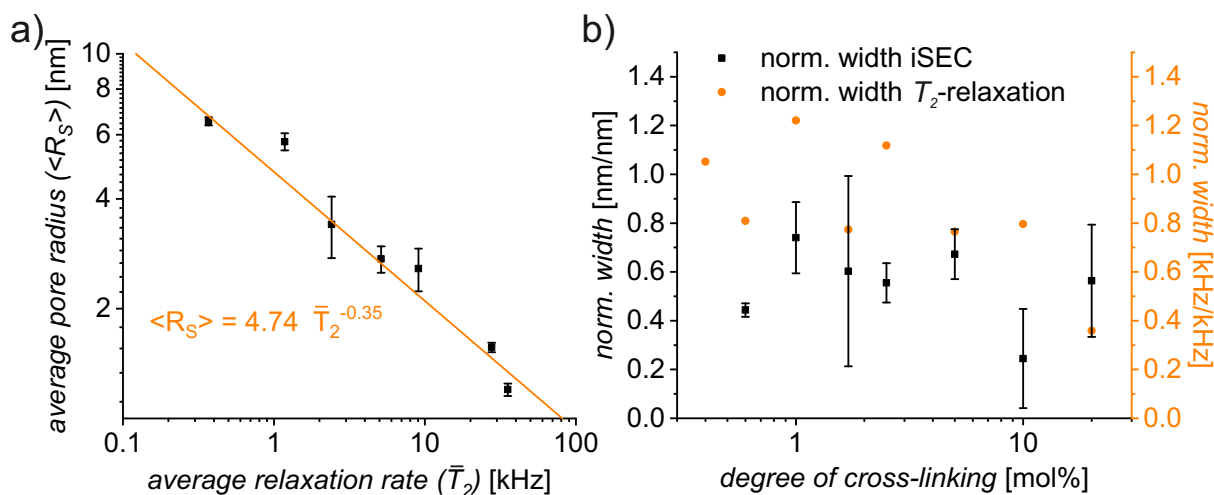


Figure 4.34: a) A correlation of the average relaxation rate as obtained by T_2 -NMR to the average pore radius is shown for the free radical polymerized poly(sodium methacrylate) with varying degree of cross-linking of 0.4 – 20 mol%. Please note that the samples in T_2 -NMR are swollen in a 1/6 g/g ratio polymer to D_2O and the iSEC hydrogels are swollen to the equilibrium in 0.1 M Na_2HPO_4 , which limits the obtained relationship between $\langle R_S \rangle$ and \bar{T}_2 to this specific case. b) The normalized width of the PSD and the relaxation rate distribution, as a measure of the heterogeneity of the respective distributions, are given.

function of the motion of the chain, which enables the connection of the molecular dynamics to the network topology. That the resulting mobility distribution truly resembles the underlying pore distribution is a likely conclusion but has sparsely been proven. [169] In most cases, the content of cross-linker during synthesis is equalized the number of effectively formed junction points. [41] In contrast to the NMR measurements, the iSEC does not rely on the interpretation of mobilities but provides access to the structure of the network via the open accessible voids. On the one hand, it could be shown that a lower cross-link density is leading to the expected network with more open voids **Figure 4.33**. On the other hand, an empirical power dependency of -0.35 was found between the average relaxation rate and the average pore radius. Thus, it is demonstrated that the average relaxation rate, as a measure for the average chain mobility, is directly correlated to the average pore size in a network, as displayed in **Figure 4.34 a)**, confirming earlier assumptions.

Finally, the heterogeneity of the PSD distribution is determined. Here, the second moment of the distribution, the standard deviation σ_S , is divided by the first moment of the

distribution, the average $\langle R_S \rangle$, to yield the relative width w_{norm} , which is a dimensionless number that is characteristic for the disparity of the distribution, as given by

$$w_{norm} = \frac{\sigma_S}{\langle R_S \rangle} \quad (4.21)$$

This dimensionless number w_{norm} enables the direct comparison of physically different distributions, such as the PSD and the T_2 -relaxation rate distributions. Therefore, w_{norm} is also calculated for the T_2 -relaxation rate distributions according to

$$w_{norm} = \frac{\sigma_{log}}{\bar{T}_2} \quad (4.22)$$

where σ_{log} is the standard deviation of the T_2 -relaxation rate distributions and \bar{T}_2 its average. The values of w_{norm} are shown in **Figure 4.34 b)** and reveal more heterogeneous distributions for the T_2 -measurements than for the iSEC measurements. These differences could arise from the limitation to logarithmic Gaussian distributions for the calculations of the PSD. The T_2 -relaxation data are transferred via inverse Laplace transformation into the relaxation rate distributions. This process enables the coverage of more inhomogeneous distributions, which should be less sensitive to underestimations. [150, 151]

4.4 Dielectric Spectroscopy

Poly(methacrylic acid) based hydrogels obtained by different synthetic strategies with a varying degree of cross-linking were analyzed by dielectric spectroscopy to evaluate the impact of these parameters on the conductivity of samples. The conductivity can be related to the mobility and amount of ions within the networks. The results were compared to diffusivity data obtained by NMR relaxometry measurements of Na^+ . First, a brief introduction to dielectric spectroscopy will be provided and in the subsequent section the measured results compared.

4.4.1 Introduction to Dielectric Spectroscopy

The interaction of electromagnetic fields with matter is described by the Maxwell's equations [170]

$$\text{curl} \vec{E} = -\frac{d\vec{B}}{dt} \quad (4.23)$$

$$\text{curl} \vec{H} = \vec{j} + \frac{d\vec{D}}{dt} \quad (4.24)$$

$$\text{div} \vec{D} = \rho_e \quad (4.25)$$

$$\text{div}\vec{B} = 0 \quad (4.26)$$

where \vec{E} and \vec{H} represent the vectors of the electric and magnetic fields respectively, \vec{D} denote the dielectric displacement, \vec{B} is the magnetic induction, \vec{j} the current density and ρ_e is the density of charges. In the linear response regime the magnetic induction \vec{B} and the dielectric displacement \vec{D} are described by the following [171]

$$\vec{B} = \mu^* \mu_0 \vec{H} \quad (4.27)$$

and [171]

$$\vec{D} = \epsilon^* \epsilon_0 \vec{E} \quad (4.28)$$

with $\mu^* = \mu' - i\mu''$ as the complex magnetic permittivity. μ' and μ'' represent the corresponding real and loss part of the magnetic permittivity. μ_0 is the magnetic permittivity of vacuum with $1.25 \cdot 10^{-6} \text{VsA}^{-1}\text{m}^{-1}$. [170] The magnetic permittivity μ_0 and the electric permittivity of vacuum ϵ_0 are related by [170]

$$\epsilon_0 \mu_0 = 1/c^2 \quad (4.29)$$

where c is the velocity of light in vacuum. The parameter ϵ^* is the complex dielectric permittivity of the material. For a periodical, sinusoidal electrical field $\vec{E}(t) = E_0 \exp(-i\omega t)$, with ω denoting the radial frequency, the complex dielectric function ϵ^* can be expressed by [170]

$$\epsilon^*(\omega) = \epsilon'(\omega) - i\epsilon''(\omega) \quad (4.30)$$

Equation 4.31, also called Ohm's law, describes the relationship between the electric field \vec{E} and current density \vec{j} as [171]

$$\vec{j} = \sigma^* \vec{E} \quad (4.31)$$

with $\sigma^*(\omega) = \sigma'(\omega) + i\sigma''(\omega)$ representing the complex electric conductivity function, where σ' and σ'' are the real and imaginary parts, respectively.

The complex conductivity and complex dielectric functions are consequently related by

$$\sigma^* = i\omega\epsilon_0\epsilon^* \quad (4.32)$$

For studying the underlying charge transport mechanisms and electrode polarization in disordered materials, both complex quantities σ^* and ϵ^* are of central importance, if a wide frequency and temperature range is measured, [170] as shown in **Figure 4.35 a**.

The main mechanism of charge transport in disordered systems is the hopping conduction, see **Figure 4.35 b**). [171, 172] Here, it is assumed that the charge carriers are

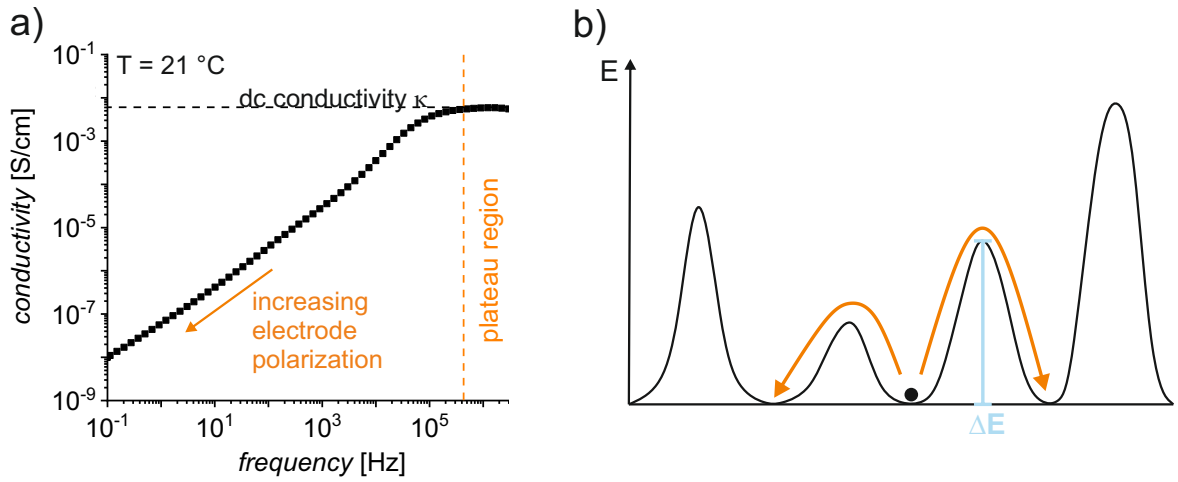


Figure 4.35: a) Dielectric spectrum of the sample PSMA-DC1.0-FRP revealing the plateau region and the initial noise region resulting from instrumental error. b) One dimensional scheme of the energy landscape as defined by the random barrier model. The minima provide the allowed particle positions. By definition all minima have equal energy, implying that all positions are equally likely, adapted from [171].

subjected to a series of spatial varying three-dimensional potentials. These potentials are random in nature and are derived from the network structure of the disordered system. Thus, the charge transport process is governed by the ability of the charge carriers to overcome the barriers, i.e. to 'hop' from local minimum to local minimum in the potential landscape. Hereby, the minima exhibit an equal energy potential and are consequently equally likely. The onset of the conductivity is mainly defined by the highest barrier, which has to be passed to achieve an infinite cluster of hopping sites. [173] The conductivity in bulk $\sigma(\omega)$ is given by [174]

$$\sigma(\omega) = \sigma_0 \left(\frac{i\omega}{\ln(1 + i\omega\tau_e)} \right) \quad (4.33)$$

where τ_e denotes the characteristic time corresponding to the rate $\omega_c = \tau_e^{-1}$ to overcome the highest barrier determining the onset conductivity, σ_0 . If the Taylor expansion of the natural logarithm is interrupted after the first term **Equation 4.33** becomes independent of the excitation frequency and is simplified to $\sigma \approx \sigma_0\omega_c$. According to Einstein and Smoluchowski, the microscopic description of the diffusion enables the evaluation of the diffusion coefficient from the dielectric spectra. [175] Thus, the characteristic hopping rate ω_c can be employed to calculate the diffusion coefficient D_{ion} of the charge carriers within

the network by [175]

$$D_{ion} = (\lambda_{ion}^2 \omega_c / 2) \quad (4.34)$$

where λ_{ion} represents the mean ion jump length in the timescale of ω_c . Combining **Equation 4.33** and **Equation 4.34** it can be concluded that the diffusion coefficient of the ions D_{ion} is proportional to the conductivity in bulk $\sigma(\omega)$.

4.4.2 Determination of the Direct Current Conductivity

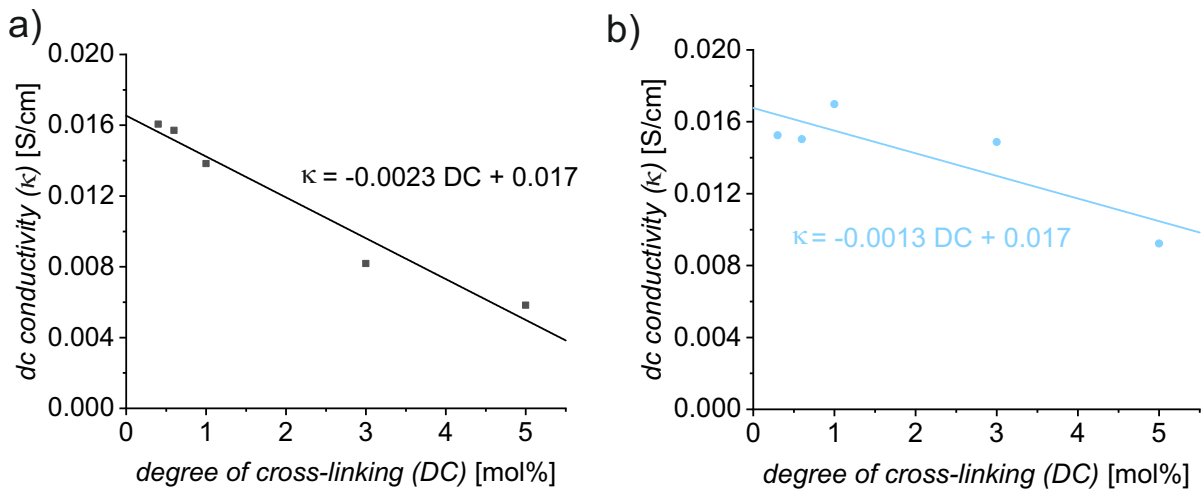


Figure 4.36: Dependency of the conductivity of poly(sodium methacrylate) networks of the degree of cross-linking. a) Samples obtained by free radical polymerization and b) samples obtained by single-step anionic co-polymerization are displayed (1/6 g/g polymer/water, 21 °C).

The conductivity of the hydrogels was determined in order to illustrate the influence of the different network structures on the mobility of the ions within this confined environment. Hereby, important information can be gained to improve network structures for processes, where the diffusion of ions into swollen polyelectrolytes plays a role. Possible fields of applications include desalination, [13] waste water treatment, or ion exchangers. [176]

For the measurements, the dry network particles were swollen to the same extent in deionized water. Subsequently, the particles were pressed into disc shaped specimen to reduce inter-particle resistance as well as the contribution of air bubbles, which would additionally reduce the apparent conductivity. A custom-build dielectric set-up was utilized with an accessible excitation frequency range of 0.1 to 10 MHz. The plateau of the measured frequency independent conductivity was taken as direct current (dc) conductivity of the

gel (κ), as displayed in **Figure 4.35 a)**. At frequencies below the plateau region the electrical polarization of the electrode reduces the measured conductivity by formation of adsorbed ion layers on the electrodes reducing the effective voltage. For the detailed measurement procedure the reader is referred to the experimental section.

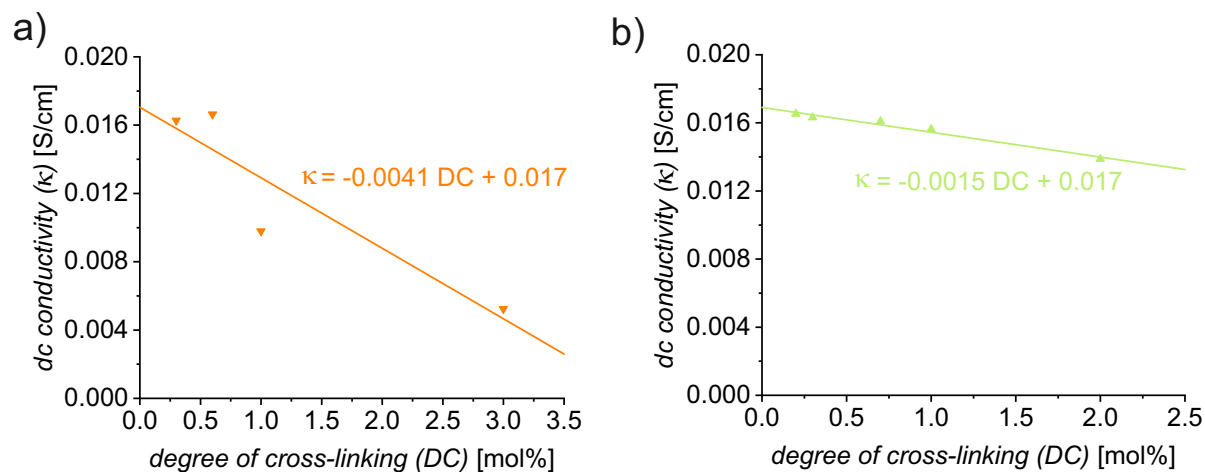


Figure 4.37: Display of the dependency of the direct current (dc) conductivity of poly(sodium methacrylate) hydrogels on the degree of cross-linking. The results of a) the quasi-model systems and b) the model networks are presented (1/6 g/g polymer/water, 21 °C).

As shown in **Figure 4.36** and **Figure 4.37**, the dc conductivity is linearly dependent of the degree of cross-linking. The quasi-model polymers revealed with a pre-factor of 42 mS/cm a stronger dependency on the degree of cross-linking than the other samples with 15 – 23 mS/cm. The quasi-model polymer networks are produced by connecting telechelic polymers via highly cross-linked micelles of ethylene glycol dimethacrylate, see **Chapter 3.1.4, p. 47**. These have a hydrophobic nature and can consequently not be passed by the moving ions. Thus, they form additional barriers in the structure, which could explain the reduction of the effective charge conduction.

Linear extrapolation of the experimental data towards zero gave in each case the same offset of about 0.017 S/cm. For a first comparison, the conductivity of a solution of sodium ions was calculated, undisturbed of interactions with a polymer matrix. It was assumed, that the concentration of the H_3O^+ and OH^- -ions, which is resulting from the weak alkalinity of the polymer and the self-disproportionation of water, can be neglected and thus, also their contribution to the ion conduction. In addition, it is presumed that

the charge conduction of the polymer network is small, since the negative charges are fixed to the backbone. The last assumption is that the polymer is a strong electrolyte, which dissociated completely in solution. Consequently, the conductivity of the sodium ions without the network κ_{Na^+} can be estimated from the polymer concentration by

$$\kappa_{Na^+} = \Lambda_{Na^+} c(Na^+) = \frac{\Lambda_{Na^+} m_p \rho_{water}}{M_{mon} m_{water}} \approx 0.052 \frac{S}{cm} \quad (4.35)$$

where Λ_{Na^+} is the molar conductivity of sodium ions in solution, while m_p and M_{mon} are the mass of the polymer and the molar mass of the monomer, respectively. The employed mass of the water is given by m_{water} , whereas its density is provided by ρ_{water} . The alkalinity of the PSMA backbone is with a pKa value of 9.54 weakly pronounced [177] and the charge density is with a concentration of ~ 1.5 mol/L rather concentrated, which makes the assumption of a purely sodium-ion dominated conduction justifiable. A reduction of the conductivity to 33 % of its theoretical value can be seen (0.017 vs. 0.052 S/cm). Since the conductivity of ions in hydrogels is proportional to its diffusivity, compare **Equation 4.33** and **Equation 4.34**, their relative reduction can be directly compared to each other. Guo et al. conducted NMR measurements of the mobility of sodium ions in hydrogel networks. The obtained reduction to 33 % in conductivity is in perfect agreement with the reduction to 33 % in diffusivity of sodium ions in polymethacrylic gels, which were found by the NMR measurements. [178] However, the source of the reduction cannot be conclusively be determined. If the number of mobile ions is reduced, e.g. by Manning condensation with the backbone, and thus a reduced diffusivity is obtained. Or, if ions are constrained by the network in their motion cannot be distinguished, since both effects would lead to the same decrease in diffusivity/conductivity. Since both effects are equally plausible computational calculations are necessary to trace back the reduction to one of the effects, or a combination of both.

4.5 Salt Rejection

In the course of this thesis, various polyelectrolyte networks with different network structure were synthesized. Desalination of seawater was taken as potential field of application for the testing of the polyelectrolyte networks. [13, 15, 179] In this desalination process, the ions in salt water are partially repelled during the swelling process of dry particles leading to a lower salinity of the water inside the gel. Subsequently, the supernatant phase enriched in salt is removed and the hydrogel is squeezed out to free the water with the reduced salinity. The gel particles can now be utilized in a second desalination cycle. By this process, a salt reduction of up to 30 % per cycle can be achieved. [14] The initial salt repulsion during the swelling is one of the two crucial steps for the efficiency of the desalination cycle, [81] the other being the energy consumption of the squeezing

process. [15] Since the salt repulsion can be tested using small amounts of sample of ≤ 1 g, in comparison to the required ≥ 30 g for the full cycle, [14, 81] it was chosen as test method of choice. Furthermore, it was reported that the salt repulsion represents the efficiency of the overall process well. [81]

The salt repulsion can be measured by swelling of the dry networks in a model salt solution of 1 wt% sodium chloride in water (10 g/L). The amount of polymer was adjusted that half of the solution remained in the supernatant and half entered the gel, which corresponds to a relative degree of swelling $Q_{rel} = Q/Q_{eq} = (m_{water} - m_{polymer})/(m_{polymer}Q_{eq})$ of 2, see **Chapter 4.1, p. 61**. The salt concentration of the supernatant phase was determined using a conductivity meter and the resulting salt rejection S_R in % was calculated utilizing [14]

$$S_R = \frac{\kappa - \kappa_0}{\kappa_0} \quad (4.36)$$

where κ and κ_0 are the conductivity of the supernatant and the initial conductivity respectively. The resulting salt rejection is shown in **Figure 4.38** in comparison to the theoretical calculations resulting from the Donnan theory as described in **Equation 4.37, 4.38 and 4.39**. [179] Here, the salt concentration of mobile anions in the gel phase c_{in} is provided under the assumption of an infinite surrounding salt bath by [179]

$$c_{in} = \sqrt{\left(\frac{DNc_p}{2}\right)^2 + c_{out}^2} - \frac{DNc_p}{2} \quad (4.37)$$

where c_0 is the initial salt concentration of the bath with 10 g/L = 0.17 mol/L (NaCl). The parameter c_p is the polymer concentration in the swollen hydrogel in mol/L, which is estimated using the density of water ρ_{water} , the molar mass of the monomer unit M_{mon} and the degree of swelling at the equilibrium Q_{eq} by $c_p = \rho_{water}M_{mon}^{-1}Q_{eq}^{-1}$. From the mass balance of added NaCl, the salt concentration in the supernatant phase c_{out} is computed, employing [179]

$$c_{out} = \frac{Q_{rel}c_0 - c_{in}}{Q_{rel} - 1} \quad (4.38)$$

where $Q_{rel} = 2$ is the relative degree of swelling. The salt rejection S_R is finally given in relation to the initial salt concentration by [179]

$$S_R = 100wt\% \left(\frac{c_{out} - c_0}{c_0} \right) \quad (4.39)$$

The experimental data, as displayed in **Figure 4.38**, reveal that a lower degree of swelling Q_{eq} leads to a higher salt rejection. The dependency of the Q_{eq} can be explained by the fact that a lower water absorbency leads to more charges per volume in the swollen state. Consequently, these repel more ions from the external solution by Coulomb and entropic

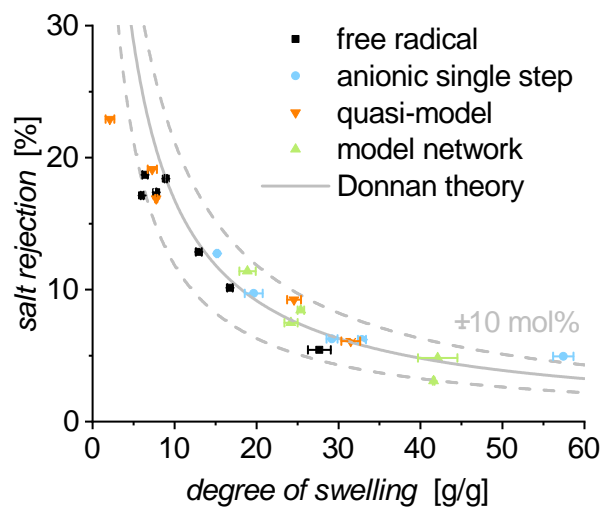


Figure 4.38: The salt rejection of all synthesized PSMA samples as a function of the degree of swelling at a fixed Q_{rel} of 2. The theoretical salt rejection is additionally displayed using the Donnan equilibrium with a degree of neutralization of 30 ± 10 mol%, respectively.

effects leading to the observed trend. The trend can be qualitatively described by the Donnan theory, although the experimental data demonstrate that the Donnan theory, see **Chapter 2.5.1, p. 26** overestimates the salt repulsion. The theory is expected to fail at high ionic strength, since concentrations are directly employed in **Equation 4.37** instead of the concentration dependent activities. In addition, condensation of opposite charges occurs, the so-called Manning condensation, which is not included. Here, ions of opposite charge form semi-stable complexes, which interact to the surrounding according to the sum of the contributing charges and thus reduce the effective charge density within the network. Manning condensation typically starts beyond a degree of neutralization of 30 mol%. However, even if these effects are taken into account, the Donnan prediction still overrates the salt repulsion and only with the assumption of a very small DN of around 7 mol% a good agreement between theory and experiment could be achieved. However, in case of highly cross-linked samples a smaller salt repulsion than predicted by the Donnan theory was obtained. This could be explained by the high content of non-charged components, like the cross-linker ethylene glycol dimethacrylate, which lead to a reduction of the swelling without increasing the number of charges. Thus, the salt rejection decreases. The overestimation of the Donnan theory was also found in previous work, [14, 81] where the authors could additionally show that the deviations are increasing with higher degree of neutralization.

Furthermore, the data showed no correlation of the salt rejection on the structure of the networks, which implies that the distribution of the fixed charges inside the polymer network does not significantly influence the salt partitioning. Thus, not the distribution of charges or the structure of the network affect the salt repulsion, but only the total number of charges throughout the whole network, as qualitatively predicted by the Donnan theory. These finding confirms recently published results based on acrylic acid hydrogels. [35,81]

Chapter 5

Conclusion and Outlook

Summary

The results presented in the current thesis provide a step towards the developments of advanced techniques for the synthesis and characterization of polymer networks. A variety of potential pathways for the synthesis of more defined networks were applied to (meth)acrylic acid based hydrogels and in-depth characterized. The anionic polymerization of a monomer and a bifunctional linker has been employed, as well as the utilization of efficient cross-linking procedures for the ligation of pre-formed telechelic polymers. The ligation techniques included the subsequent addition of a bifunctional monomer and the azide-alkyne Huisgen ligation. Besides the anionic polymerization, reversible addition-fragmentation transfer (RAFT) polymerization was investigated as a complementary living polymerization procedure. In this way, a large variety of different network architectures was synthesized, as shown in Chapter 3. Afterwards, the influence of the topology of the polymer networks on macroscopic properties were examined, such as the absorbency of sodium chloride solutions, the repulsion of salt during the swelling process and the mobility of ions within the network structure. In addition, $^1\text{H-NMR}$ relaxometry, double quantum $^1\text{H-NMR}$ and inverse size exclusion chromatography (iSEC) were employed to quantify the network architecture in a more sophisticated way.

Polymer Synthesis

Different synthetic methods and strategies were used to accomplish the various network topologies. Poly(sodium acrylate) (PSA) and poly(sodium methacrylate) (PSMA) hydrogels with a varying degree of crosslinking (DC) were synthesized via free radical polymerization (FRP). This method is often used in industry and those hydrogels were utilized as standards for the comparison of the more elaborated polymerization techniques. In case of the PSMA hydrogels, the degree of cross-linking DC was alternated in the range of 0.3 to 20 mol%, while for the PSA samples the DC varied between 0.6 and 5.0 mol%.

The water absorbency of the PSA and PSMA hydrogels were studied as one of their most important macroscopic quantities. An higher DC led to more constraints with decreasing water absorbency. Typical degrees of swelling in 1 wt% sodium chloride solution for the fully neutralized hydrogels were in the range of 6 to 42 g/g, when DC was varied between 20 and 0.3 mol%.

As a second approach for randomly cross-linked polymers, anionic polymerization was employed with DC ranging from 0.3 to 5.0 mol%. Due to the living character of the chain propagation no termination, disproportion, or back-biting reactions occurs, which would lead to more defects in the network structure. Swelling experiments confirmed higher swelling ratios compared to their FRP counterparts, which indicate a more loose cross-linked network structure.

Apart from the randomly cross-linked polymers, several other polymer architectures were realized in this thesis. The quasi-model networks were produced with a defined elastic chain length ($\bar{D} = 1.08 - 1.30$) via anionic polymerization of poly(tert-butyl methacrylate) (PtBMA), followed by hydrolysis and neutralization to PSMA. The meshes were cross-linked by addition of ethylene glycol dimethacrylate (EGDMA) to the living polymer chains under formation of highly cross-linked micelles. These networks exhibited a stronger dependency of the degree of swelling on the DC than the FRP counterparts resulting from the hydrophobic nature of the micelles.

The model networks were achieved by the anionic polymerization of symmetrical polymers, which bear on each end the same functional group. The control over the production process was confirmed by low dispersities of 1.07 – 1.30 and high conversion rates of $\geq 92\%$ towards the desired azide end group. The telechelic polymers were cross-linked into the networks via the azide-alkyne Huisgen ligation. $^1\text{H-NMR}$ analysis of the final networks revealed conversions of 58 to 79 % of the azides into the respective triazol, which could not be improved further. Non-stoichiometric conversion of the azide-alkyne Huisgen ligation during hydrogel formation were also found by Neffe et al. and are likely arising from the immobilization of the chains during gelation. [118]

In addition, random co-polymerization of acrylic acid and N,N'-methylene bisacrylamide via RAFT polymerization was performed with a resulting DC of 0.6 to 5.0 mol%. The main target was the determination of the influence of the RAFT agent of the final network properties and topology. The swelling experiments affirmed a higher swellability of the RAFT samples in comparison to FRP hydrogels, which implies a less dense connected polymer network.

NMR Relaxometry

The mobility of the local chain segments could be accessed by $^1\text{H-NMR}$ relaxometry to examine the local dynamics in swollen hydrogels. Namely, the T_2 -relaxation and the dou-

ble quantum (DQ) coherence could be used to gain insight into the network architecture. This is of great interest as other techniques cannot directly study the network architecture, but only measure macroscopic properties resulting from their average structure. The relaxometry experiments disclosed a large heterogeneity in the polymer mobility with T_2 and D_{res} distributions covering several decades with a typical range of 0.1 – 30 kHz. These experiments provide the possibility to discriminate the obtained hydrogels regarding their homogeneity and thus, the polymerization methods they originate from.

More constraints in the polymer network by higher DC led to a lower mobility and thus, to higher D_{res} constants and T_2 -relaxation rates, which is in good agreement with previous work. [41] The PSMA hydrogels exhibited similar standard deviations of the T_2 rate distributions regardless of the polymerization technique, which implies equally heterogeneous network topologies. The quasi-model systems with a fixed elastic chain length were the only exception. The cross-linking micelles in these hydrogels were immobile leading to very fast, physically not meaningful, relaxation rates of approximately 100 kHz and the distributions could not be resolved. Furthermore, the PSA hydrogels revealed increasing heterogeneities for higher RAFT agent contents, which could indicate a less dense network architecture.

The examination of the DQ coherence of the PSMA samples showed a that the obtained heterogeneity is a combination of two contradicting influences. The network structure itself is becoming more heterogeneous with higher DC with changes of the standard deviation of the D_{res} distribution σ_{log} from 1.2 to 1.6 kHz, while the content of defects is strongly decreasing from 48 to 11 %.

The DQ measurements revealed that the increase in mobility and in the swelling ability can be assigned to a higher amount of defects, such as dangling ends, rather than to a less homogeneous mesh size distribution. After subtraction of defects, the mobility distribution was found to be independent from the employed synthetic approach. The higher amount of dangling ends is likely due to the limitation of the chain length due to the presence of the RAFT agent, which leads to fewer cross-linker molecules per chain. Therefore, the RAFT agent concentration should be chosen low enough that the chain lengths are similar for the techniques that are being compared. Equal chain lengths are an important precondition to ensure that the findings are exclusively assignable to the influence of the RAFT agent on the cross-linking process.

The main conclusion of the time domain (TD) NMR experiments is that the FRP leads to equally or even less heterogeneous network structures than their controlled counterparts and that the TD NMR is a appropriate technique to examine the network structure of hydrogels and to validate if synthetic procedures increase the network heterogeneity.

Inverse Size Exclusion Chromatography

The inverse size exclusion chromatography is usually employed for the characterization of solid porous catalyst supports, or chromatography materials and was adapted for the usage on hydrogels in the course of this thesis. The method is based on the different accessibility of pores in the material for eluting polymer standard with varying extensions. The resulting different retention times of the standards can be utilized to back-calculate the underlying pore-size distributions in the substrate. FRP PSMA samples with a broad range of DC of 0.6 – 20 mol% were characterized. An increase in pore size with decreasing DC was found, with pore radii of 1.2 nm ($DC = 20$ mol%) to 6.5 nm ($DC = 0.6$ mol%). Furthermore, the average pore sizes could be correlated to the relaxation rates confirming that the mobility distributions truly represent the network structure. Here, an empirical power law dependency of the average pore radius $\langle R_S \rangle$ on the average relaxation rate \bar{T}_2 with $\langle R_S \rangle = 4.7 \bar{T}_2^{-0.35}$ was found.

Outlook

A wide range of polyelectrolyte network topologies were compared in this thesis. Light induced coupling methods based on the decomposition of tetrazoles, could provide another dimension for optimization. [128] This reactions is self-reporting due to the formed fluorescent cross-link, which allows for a easier quantification of the conversion. Further improvements could be obtained by usage of a reversible ligation technique, such as the Diels-Alder ring formation. [113] Here, the coupled chains can be cleaved and reconnected by changes of the temperature. This could lead to healing of defects in the network and ensure higher conversions due to the better mobility after gelation.

The network structure could be better assigned, especially the changes in mobility of the chain segments along a mesh, by employing isotope labeled block-copolymers. Here, deuterium labeled monomers mask different sections of the chain in $^1\text{H-NMR}$, i.e. either the mobile middle of the chain or its rigid ends close to the junction point. The NMR-relaxometry experiments, i.e. T_2 -relaxation and DQ coherence, could then distinguish between effects coming from the network structure and influences arising from mobility changes along a chain. Purposely heterogeneous network architectures upon insertion of additional dangling ends would lead to a better quantification of their contribution to the relaxation behavior. Sakai et al. already demonstrated the coupling of two different four-armed poly(ethylene oxide) for the generation of loop-free hydrogel networks. [25] This method could be adapted to polyelectrolytes to better understand their impact on the mobility distributions.

The dielectric measurements could be expanded to more polymer-ion combinations to confirm, if the reduction in diffusivity as found by NMR, is equally affecting the conductivity. [178] Also different polyelectrolytes should be tested to validate, if the obtained

reduction is a universal behavior of polymer networks. The comparison to equimolar solutions of these polyelectrolytes could provide the answer, if the ion-polymer dissociation is the dominating factor in the hindered mobility found in the networks, or the hindrance by the chain structure.

The iSEC should be adapted to low cross-linked organogels to expand the field of application. Here, a change to polystyrene/tetrahydrofuran is required and the limiting lower cross-link density have to be determined. An independent calculation tool for the pore size distribution based on the literature [38, 163–165], e.g. in form of a MATLAB script, is necessary to overcome the existing disadvantages of the commercial software like pre-set fit conditions, limitation to Gaussian distributions, and few available polymer-solvent combinations. A thorough study of more polymer samples should be conducted to proof the universality of the employed characterization technique.

Bibliography

- [1] L. J. Suggs, S. A. Moore, A. G. Mikos, *Physical Properties of Polymers Handbook*, Springer, New York, **2007**.
- [2] J. C. Hernández-Ortiz, E. Vivaldo-Lima, *Handbook of Polymer Synthesis, Characterization, and Processing*, Wiley, New York, **2013**.
- [3] P. J. Flory, J. Rehner, *J. Chem. Phys.* **1943**, *11*, 512.
- [4] P. J. Flory, *Principles of Polymer Chemistry*, Cornell University Press, Ithaca, **1953**.
- [5] F. Ganji, S. Vasheghani-Farahani, E. Vasheghani-Farahani, *Iran. Polym. J.* **2010**, *19*, 375.
- [6] S. J. Buwalda, K. W. Boere, P. J. Dijkstra, J. Feijen, T. Vermonden, W. E. Hennink, *J. Control. Release* **2014**, *190*, 254.
- [7] H. H. Hooper, J. P. Baker, H. W. Blanch, J. M. Prausnitz, *Macromolecules* **1990**, *23*, 1096.
- [8] W. Oppermann, *Swelling Behavior and Elastic Properties of Ionic Hydrogels*, American Chemical Society, Washington DC, **1992**.
- [9] F. L. Buchholz, A. T. Graham, *Modern Superabsorbent Polymer Technology*, Wiley-VCH, New York, **1998**.
- [10] F. Masuda, *Superabsorbent Polymers*, American Chemical Society, Washington DC, **1994**.
- [11] K. S. Kazanskii, S. A. Dubrovskii, *Chemistry and Physics of "Agricultural" Hydrogels*, Springer, Berlin, **1992**.
- [12] F. Fu, Q. Wang, *J. Environ. Manage.* **2011**, *92*, 407.
- [13] J. Höpfner, C. Klein, M. Wilhelm, *Macromol. Rapid Comm.* **2010**, *31*, 1337.

- [14] J. Höpfner, „A New Method of Seawater Desalination via Acrylic Acid Based Hydrogels: Synthesis, Characterization, and Experimental Realisation“, **dissertation, KIT, Karlsruhe, 2013.**
- [15] L. Arens, J. B. Albrecht, J. Höpfner, K. Schlag, A. Habicht, S. Seiffert, M. Wilhelm, *Macromol. Chem. Phys.* **2017**, *218*, 1.
- [16] L. Arens, F. Weißenfeld, C. O. Klein, K. Schlag, M. Wilhelm, *Adv. Sci.* **2017**, *4*, 1700112.
- [17] K. Ohmura, „An Update on the Global Superabsorbent Polymer Producers“, https://www.nonwovens-industry.com/issues/2015-11-01/view_far-east-report/an-update-on-the-global-superabsorbent-polymer-producers/, **2015**, accessed September 2019.
- [18] K. Pulidindi, S. Chakraborty, „Global Market Insight Polymer and Advanced Materials“, <https://www.gminsights.com/industry-analysis/superabsorbent-polymers-sap-market>, **2018**, accessed September 2019.
- [19] P. Nesvadba, *Radical Polymerization in Industry*, Wiley, New York, **2012.**
- [20] Y. Gu, J. Zhao, J. A. Johnson, *Trends in Chemistry* **2019**, *1*, 318.
- [21] J. Wang, T. S. Lin, Y. Gu, R. Wang, B. D. Olsen, J. A. Johnson, *ACS Macro. Lett.* **2018**, *7*, 244.
- [22] M. Zhong, R. Wang, K. Kawamoto, B. D. Olsen, J. A. Johnson, *Science* **2016**, *353*, 1264.
- [23] E. Mendes, P. Lindner, M. Buzier, F. Boué, J. Bastide, *Phys. Rev. Lett.* **1991**, *66*, 1595.
- [24] S. Seiffert, *Polym. Chem.* **2017**, *8*, 4472.
- [25] T. Sakai, U.-I. Chung, T. Matsunaga, M. Shibayama, Y. Yamamoto, C. Ito, R. Yoshida, S. Suzuki, N. Sasaki, *Macromolecules* **2008**, *41*, 5379.
- [26] Y. Gu, K. Kawamoto, M. Zhong, M. Chen, M. J. Hore, A. M. Jordan, L. S. T. Korley, B. D. Olsen, J. A. Johnson, *PNAS* **2017**, *114*, 4875.
- [27] G. Hild, *Progr. Polym. Sci.* **1998**, *23*, 1019.
- [28] N. Ide, T. Fukuda, *Macromolecules* **1997**, *30*, 4268.
- [29] N. Ide, T. Fukuda, *Macromolecules* **1999**, *32*, 95.

- [30] R. Henkel, P. Vana, *Macromol. Chem. Phys.* **2014**, *215*, 182.
- [31] Q. Yu, Y. Zhu, Y. Ding, S. Zhu, *Macromol. Chem. Phys.* **2008**, *209*, 551.
- [32] N. Hadjichristidis, A. Hirao, *Anionic Polymerization*, Springer, Tokyo, **2015**.
- [33] G. Carrot, B. Schmitt, P. Lutz, *Polym. Bull.* **1998**, *40*, 181.
- [34] C. Tsitsilianis, I. Iliopoulos, G. Ducouret, *Macromolecules* **2000**, *33*, 2936.
- [35] L. Arens, M. Wilhelm, *Macromol. Chem. Phys.* **2019**, *220*, 1.
- [36] A. J. Scott, A. Nabifar, A. Penlidis, *Macromol. React. Eng.* **2014**, *8*, 639.
- [37] A. R. Kannurpatti, K. J. Anderson, J. W. Anseth, C. N. Bowman, *J. Polym. Sci. Pol. Phys.* **1997**, *35*, 2297.
- [38] F. Lange, K. Schwenke, M. Kurakazu, Y. Akagi, U. I. Chung, M. Lang, J. U. Sommer, T. Sakai, K. Saalwächter, *Macromolecules* **2011**, *44*, 9666.
- [39] H. Zhou, J. Woo, A. M. Cok, M. Wang, B. D. Olsen, J. A. Johnson, *PNAS* **2012**, *109*, 19119.
- [40] F. Di Lorenzo, S. Seiffert, *Polym. Chem.* **2015**, *6*, 5515.
- [41] J. Höpfner, G. Guthausen, K. Saalwächter, M. Wilhelm, *Macromolecules* **2014**, *47*, 4251.
- [42] K. Saalwächter, J. U. Sommer, *Macromol. Rapid Comm.* **2007**, *28*, 1455.
- [43] G. Webb, *Modern Magnetic Resonance*, Springer, Cham, **2018**.
- [44] P. DePhillips, A. M. Lenhoff, *J. Chromatogr. A* **2000**, *883*, 39.
- [45] M. D. Lechner, K. Gehrke, E. H. Nordmeier, *Makromolekulare Chemie*, Springer, Berlin, **2014**.
- [46] B. Tieke, *Makromolekulare Chemie: eine Einführung*, Wiley-VCH, Weinheim, **2014**.
- [47] R. J. Young, P. A. Lovell, *Introduction to Polymers*, CRC Press, Boca Raton, **2011**.
- [48] P. M. Visakh, *Polyelectrolytes: Thermodynamics and Rheology*, Springer, Cham, **2014**.
- [49] F. L. Buchholz, *J. Chem. Educ.* **1996**, *73*, 512.
- [50] D. A. Mortimer, *Polymer* **1991**, *25*, 29.

- [51] C. Schröfl, D. Snoeck, V. Mechtcherine, *Mater. Struct.* **2017**, *50*, 1.
- [52] M. J. Zohuriaan-Mehr, H. Omidian, S. Doroudiani, K. Kabiri, *J. Mater. Sci.* **2010**, *45*, 5711.
- [53] H. J. Zhang, T. L. Sun, A. K. Zhang, Y. Ikura, T. Nakajima, T. Nonoyama, T. Kurokawa, O. Ito, H. Ishitobi, J. P. Gong, *Adv. Mater.* **2016**, *28*, 4884.
- [54] D. L. Taylor, M. in het Panhuis, *Adv. Mater.* **2016**, *28*, 9060.
- [55] S. W. Lv, Y. Liu, M. Xie, J. Wang, X. W. Yan, Z. Li, W. G. Dong, W. H. Huang, *ACS Nano* **2016**, *10*, 6201.
- [56] T. Kureha, D. Aoki, S. Hiroshige, K. Iijima, D. Aoki, T. Takata, D. Suzuki, *Angew. Chem. Int. Edit.* **2017**, *56*, 15393.
- [57] R. H. Kollarigowda, A. S. Mathews, S. Abraham, *ACS Appl. Bio Mater.* **2019**, *2*, 277.
- [58] M. E. Roth-Konforti, M. Comune, M. Halperin-Sternfeld, I. Grigoriants, D. Shabat, L. Adler-Abramovich, *Macromol. Rapid Comm.* **2018**, *39*, 1.
- [59] H. Yuk, S. Lin, C. Ma, M. Takaffoli, N. X. Fang, X. Zhao, *Nat. Commun.* **2017**, *8*, 14230.
- [60] A. K. Yetisen, H. Butt, L. R. Volpatti, I. Pavlichenko, M. Humar, S. J. Kwok, H. Koo, K. S. Kim, I. Naydenova, A. Khademhosseini, S. K. Hahn, S. H. Yun, *Biotechnol. Adv.* **2016**, *34*, 250.
- [61] U. W. Gedde, *Polymer Physics*, Chapman & Hall, London, **1995**.
- [62] G. R. Strobl, *The Physics of Polymers: Concepts for Understanding Their Structures and Behavior*, Springer, Berlin, **1997**.
- [63] P. J. Flory, *Principles of Polymer Chemistry*, Cornell University Press, Ithaca, **1953**.
- [64] M. L. Huggins, *J. Chem. Phys.* **1941**, *9*, 440.
- [65] W. Göpel, H.-D. Wiemhöfer, *Statistische Thermodynamik*, Spektrum, Akademischer Verlag, Heidelberg, **2000**.
- [66] T. L. Hill, *Statistical Thermodynamics*, Dover Publications, New York, **1986**.
- [67] J.-P. Cohen Addad, *Physical Properties of Polymeric Gels*, Wiley, Chichester, **1996**.

- [68] H. M. James, *J. Chem. Phys.* **1947**, *15*, 651.
- [69] M. Rubinstein, S. Panyukov, *Macromolecules* **2002**, *35*, 6670.
- [70] P. J. Flory, J. Rehner, *J. Chem. Phys.* **1943**, *11*, 521.
- [71] W. Schmickler, *Grundlagen der Elektrochemie*, Vieweg, Braunschweig, **1996**.
- [72] G. S. Manning, *J. Phys. Chem.* **1981**, *85*, 1506.
- [73] P. W. Atkins, J. De Paula, *Physikalische Chemie*, Wiley-VCH, Weinheim, **2002**.
- [74] X. Li, W. Wu, J. Wang, Y. Duan, *Carbohydr. Polym.* **2006**, *66*, 473–479.
- [75] E. M. Purcell, H. C. Torrey, R. V. Pound, *Phys. Rev.* **1946**, *69*, 37.
- [76] A. Abragam, *The Principles of Nuclear Magnetism*, Clarendon Press, Oxford, **1961**.
- [77] A. E. Derome, *Modern NMR Techniques for Chemistry Research*, Pergamon Press, Oxford, **1987**.
- [78] F. A. Bovey, L. Jelinski, P. A. Mirau, *Nuclear Magnetic Resonance Spectroscopy*, Academic Press, San Diego, **1988**.
- [79] K. Schmidt-Rohr, H. W. Spiess, *Multidimensional Solid-State NMR and Polymers*, Academic Press, New York, **1994**.
- [80] B. Blümlich, *NMR Imaging of Materials*, Clarendon Press, Oxford, **2000**.
- [81] L. Arens, „Polyelectrolyte Hydrogels with Various Network Architectures : Synthesis, Characterization and Use in Membrane-Free Desalination“, **dissertation, KIT, Karlsruhe, 2013**.
- [82] C.-S. Wu, *Handbook Of Size Exclusion Chromatography And Related Techniques*, Marcel Dekker, New York, **2003**.
- [83] H. Pasch, B. Trathnigg, *Multidimensional HPLC of Polymers*, Springer, Berlin, **2013**.
- [84] E. Nordmeier, *J. Phys. Chem.* **1993**, *97*, 5770.
- [85] T. F. Beskers, T. Hofe, M. Wilhelm, *Macromol. Rapid Comm.* **2012**, *33*, 1747.
- [86] T. F. Beskers, T. Hofe, M. Wilhelm, *Polym. Chem.* **2015**, *6*, 128.
- [87] S. Morlock, J. M. Kübel, T. F. Beskers, B. Lendl, M. Wilhelm, *Macromol. Rapid Comm.* **2018**, *39*, 1.

- [88] J. M. Kübel, C. Botha, A. Bucka, J. Höpfner, H. Zimmermann, M. Godejohann, M. Wilhelm, *Macromol. Rapid Comm.* **2019**, *40*, 1.
- [89] F. Di Lorenzo, S. Seiffert, *Macromolecules* **2013**, *46*, 1962.
- [90] J. Brandrup, *Polymer Handbook*, Wiley, New York, **1999**.
- [91] T. Malavasic, U. Osredkar, I. Anzur, I. Vizovisek, *J. Macromol. Sci. Chem.* **1986**, *23*, 853.
- [92] A. Leon, B. Vincent, N. Cawdery, *Colloid Polym. Sci.* **1994**, *272*, 427.
- [93] E. Čadová, J. Dybal, J. Kříž, P. Vlček, M. Janata, L. Toman, *Macromol. Chem. Phys.* **2008**, *209*, 1657.
- [94] D. Baskaran, A. H. Müller, *Progr. Polym. Sci.* **2007**, *32*, 173.
- [95] M. Szwarc, *Nature* **1956**, *178*, 1168.
- [96] S. K. Varshney, J. P. Hautekeer, R. Fayt, R. Jerdme, P. Teyssie, *Macromolecules* **1990**, *23*, 2618.
- [97] C. S. Patrickios, *Macromol. Symp.* **2010**, *291*, 1.
- [98] A. I. Triftaridou, D. Kafouris, M. Vamvakaki, T. K. Georgiou, T. C. Krasia, E. Themistou, N. Hadjiantoniou, C. S. Patrickios, *Polym. Bull.* **2007**, *58*, 185.
- [99] T. Annable, R. Buscall, R. Ettelaie, D. Whittlestone, *J. Rheol.* **1993**, *37*, 695.
- [100] K. C. Tam, R. D. Jenkins, M. A. Winnik, D. R. Bassett, *Macromolecules* **1998**, *31*, 4149.
- [101] V. Kadam, T. Nicolai, E. Nicol, L. Benyahia, *Macromolecules* **2011**, *44*, 8225.
- [102] C. Tsitsilianis, I. Iliopoulos, *Macromolecules* **2002**, *35*, 3662.
- [103] A. J. Ryan, C. J. Crook, J. R. Howse, P. Topham, R. A. Jones, M. Geoghegan, A. J. Parnell, L. Ruiz-Pérez, S. J. Martin, A. Cadby, A. Menelle, J. R. Webster, A. J. Gleeson, W. Bras, *Faraday Discuss.* **2005**, *128*, 55.
- [104] M. Guvendiren, K. R. Shull, *Soft Matter* **2007**, *3*, 619.
- [105] K. J. Henderson, T. C. Zhou, K. J. Otim, K. R. Shull, *Macromolecules* **2010**, *43*, 6193.
- [106] P. Rempp, J. E. Herz, *Angew. Makromol. Chem.* **1979**, *76*, 373.

- [107] T. K. Georgiou, C. S. Patrickios, *Macromolecules* **2006**, *39*, 1560.
- [108] F. Jachimowicz, H. C. Wang, G. Levin, M. Szwarc, *J. Phys. Chem.* **1978**, *82*, 1371.
- [109] M. Malkoch, R. Vestberg, N. Gupta, L. Mespouille, P. Dubois, A. F. Mason, J. L. Hedrick, Q. Liao, C. W. Frank, K. Kingsbury, C. J. Hawker, *Chem. Commun.* **2006**, 2774.
- [110] A. Shefer, A. J. Grodzinsky, K. L. Prime, J. P. Busnel, *Macromolecules* **1993**, *26*, 5009.
- [111] C. Mengel, W. H. Meyer, G. Wegner, *Macromol. Chem. Phys.* **2001**, *202*, 1138–.
- [112] C. C. Lin, A. Raza, H. Shih, *Biomaterials* **2011**, *32*, 9685.
- [113] K. C. Koehler, K. S. Anseth, C. N. Bowman, *Biomacromolecules* **2013**, *14*, 538.
- [114] V. V. Rostovtsev, L. G. Green, V. V. Fokin, K. B. Sharpless, *Angew. Chem. Int. Edit.* **2002**, *41*, 2596.
- [115] G. K. Such, A. P. Johnston, K. Liang, F. Caruso, *Progr. Polym. Sci.* **2012**, *37*, 985.
- [116] H. B. Tinmaz, I. Arslan, M. A. Tasdelen, *J. Polym. Sci. A1* **2015**, *53*, 1687.
- [117] E. Jabbari, *Polymer* **2002**, *13*, 4873.
- [118] S. Piluso, R. Vukićević, U. Nöchel, S. Braune, A. Lendlein, A. T. Neffe, *Eur. Polym. J.* **2018**, *100*, 77.
- [119] F. Cavalli, C. Pfeifer, L. Arens, L. Barner, M. Wilhelm, *Macromol. Chem. Phys.* **2020**, *221*, 1.
- [120] N. D. Truong, J. C. Galin, J. François, Q. T. Pham, *Polymer* **1986**, *27*, 467.
- [121] Q. Ma, M. Chen, H. R. Yin, Z. G. Shi, Y. Q. Feng, *J. Chromatogr. A* **2008**, *1212*, 61.
- [122] T. Norisuye, T. Morinaga, Q. Tran-Cong-Miyata, A. Goto, T. Fukuda, M. Shibayama, *Polymer* **2005**, *46*, 1982.
- [123] K. Saalwächter, S. Seiffert, *Soft Matter* **2018**, *14*, 1976.
- [124] S. Seiffert, *Progr. Polym. Sci.* **2017**, *66*, 1.
- [125] D. C. Tuncaboylu, M. Sahin, A. Argun, W. Oppermann, O. Okay, *Macromolecules* **2012**, *45*, 1991.

- [126] K. Urayama, T. Kawamura, S. Kohjiya, *Polymer* **2009**, *50*, 347.
- [127] K. Nishi, H. Asai, K. Fujii, Y. S. Han, T. H. Kim, T. Sakai, M. Shibayama, *Macromolecules* **2014**, *47*, 1801.
- [128] D. Estupiñán, C. Barner-Kowollik, L. Barner, *Angew. Chem. Int. Edit.* **2018**, *57*, 5925.
- [129] F. Cavalli, H. Mutlu, S. O. Steinmueller, L. Barner, *Polym. Chem.* **2017**, *8*, 3778.
- [130] M. Hess, E. Roeben, A. Habicht, S. Seiffert, A. M. Schmidt, *Soft Matter* **2019**, *15*, 842.
- [131] E. Roeben, L. Roeder, S. Teusch, M. Effertz, U. K. Deiters, A. M. Schmidt, *Colloid Polym. Sci.* **2014**, *292*, 2013.
- [132] L. Hagel, M. Östberg, T. Andersson, *J. Chromatogr. A* **1996**, *743*, 33.
- [133] L. Brannon-Peppas, R. S. Harland, *Absorbent Polymer Technology*, Elsevier, Amsterdam, **1990**.
- [134] R. S. Harland, R. K. Prud'homme, *Polyelectrolyte gels: Properties, preparation, and applications*, American Chemical Society, Washington DC, **1992**.
- [135] J. Chen, H. Park, K. Park, *J. Biomed. Mater. Res.* **1999**, *44*, 53.
- [136] J. C. Kasper, W. Friess, *Eur. J. Pharm. Biopharm.* **2011**, *78*, 248.
- [137] G. Moad, E. Rizzardo, *Macromolecules* **1995**, *28*, 8722.
- [138] V. J. Triacca, P. E. Gloor, S. Zhu, A. N. Hrymak, A. E. Hamielec, *Polym. Eng. Sci.* **1993**, *33*, 445.
- [139] A. M. Wasserman, L. L. Yasina, I. I. Aliev, V. Doseva, V. Y. Baranovsky, *Colloid Polym. Sci.* **2004**, *282*, 402.
- [140] F. Kramer, M. V. Deshmukh, H. Kessler, S. J. Glaser, *Concept. Magn. Reson. A* **2004**, *21*, 10.
- [141] N. Bloembergen, E. M. Purcell, R. V. Pound, *Phys. Rev.* **1948**, *73*, 679.
- [142] E. L. Hahn, *Phys. Rev.* **1950**, *80*, 580.
- [143] A. Maus, C. Hertlein, K. Saalwächter, *Macromol. Chem. Phys.* **2006**, *207*, 1150.
- [144] T. Gullion, S. Louis, D. B. Baker, *J. Magn. Reson.* **1990**, *89*, 479.

- [145] A. Guthausen, G. Zimmer, P. Blümmler, B. Blümich, *J. Magn. Reson.* **1998**, *130*, 1.
- [146] H. Y. Carr, E. M. Purcell, *Phys. Rev.* **1954**, *94*, 630.
- [147] J. G. Powles, J. H. Strange, *P. Phys. Soc.* **1963**, *82*, 6.
- [148] R. Böhmer, K. L. Ngai, C. A. Angell, D. J. Plazek, *J. Chem. Phys.* **1993**, *99*, 4201.
- [149] P. K. Dixon, *Phys. Rev. B* **1990**, *42*, 8179.
- [150] G. C. Borgia, R. J. Brown, P. Fantazzini, *J. Magn. Reson.* **1998**, *132*, 65.
- [151] S. W. Provencher, *Comput. Phys. Commun.* **1982**, *27*, 213.
- [152] P. T. Callaghan, S. Godefroy, B. N. Ryland, *Magn. Reson. Imaging* **2003**, *21*, 243.
- [153] P. T. Callaghan, S. Godefroy, B. N. Ryland, *J. Magn. Reson.* **2003**, *162*, 320.
- [154] K. Saalwächter, *Rubber Chem. Technol.* **2012**, *85*, 350.
- [155] S. Ulrich, A. Laguecir, S. Stoll, *Macromolecules* **2005**, *38*, 8939.
- [156] K. Saalwächter, *Prog. Nucl. Mag. Res. Sp.* **2007**, *51*, 1.
- [157] J. L. Valentín, D. López, R. Hernández, C. Mijangos, K. Saalwächter, *Macromolecules* **2009**, *42*, 263.
- [158] K. Saalwächter, F. Kleinschmidt, J. U. Sommer, *Macromolecules* **2004**, *37*, 8556.
- [159] W. Chassé, J. L. Valentín, G. D. Genesky, C. Cohen, K. Saalwächter, *J. Chem. Phys.* **2011**, *134*, 044907.
- [160] X. Guo, S. Theissen, J. Claussen, V. Hildebrand, J. Kamphus, M. Wilhelm, B. Luy, G. Guthausen, *Macromol. Chem. Phys.* **2018**, *219*, 1.
- [161] C. Barner-Kowollik, *Handbook of RAFT polymerization*, Wiley-VCH, Weinheim, **2008**.
- [162] A. A. Gorbunov, L. Y. Solovyova, V. A. Pasechnik, *J. Chromatogr.* **1988**, *448*, 307.
- [163] E. F. Casassa, *J. Polym. Sci. Pol. Lett.* **1967**, *5*, 773.
- [164] E. F. Casassa, Y. Tagami, *Macromolecules* **1969**, *2*, 14.
- [165] E. F. Casassa, *Macromolecules* **1976**, *9*, 182.
- [166] K. Jerabek, A. Revillon, E. Puccilli, *Chromatographia* **1993**, *36*, 259.

- [167] J. H. Knox, H. J. Ritchie, *J. Chromatogr. A* **1987**, *387*, 65.
- [168] L. Z. Vilenchik, J. Asrar, R. C. Ayotte, L. Ternorutsky, C. J. Hardiman, *J. Chromatogr. A* **1993**, *648*, 9.
- [169] Y. Q. Song, *J. Magn. Res.* **2013**, *229*, 12.
- [170] F. Kremer, *Broadband Dielectric Spectroscopy*, Springer, Berlin, **2003**.
- [171] R. Richert, *Nonlinear Dielectric Spectroscopy*, Springer, Cham, **2018**.
- [172] K. S. Schweizer, E. J. Saltzman, *J. Phys. Chem. B* **2004**, *108*, 19729.
- [173] H. Böttger, V. V. Bryksin, *Phys. Status Solidi B* **1976**, *78*, 9.
- [174] J. C. Dyre, *Phys. Rev. B* **1988**, *37*, 10143.
- [175] J. R. Sangoro, F. Kremer, *Accounts Chem. Res.* **2012**, *45*, 525.
- [176] P. M. Visakh, B. Oguz, A. P. Guillermo, *Polyelectrolytes*, Springer, Cham, **2014**.
- [177] A. Rojas-Hernández, E. L. Ibarra-Montaño, N. Rodríguez-Laguna, A. Aníbal Sánchez-Hernández, *J. Appl. Sol. Chem. Model.* **2015**, *4*, 7.
- [178] X. Guo, C. Pfeifer, M. Wilhelm, B. Luy, G. Guthausen, *Macromol. Chem. Phys.* **2019**, *220*, 1.
- [179] J. Höpfner, T. Richter, P. Košovan, C. Holm, M. Wilhelm, „Seawater Desalination via Hydrogels: Practical Realisation and First Coarse Grained Simulations“, Springer, Heidelberg, **2013**.
- [180] B. J. Suh, F. Borsa, D. R. Torgeson, *J. Magn. Reson. Ser. A* **1994**, *110*, 58.
- [181] A. J. Shaka, S. P. Rucker, A. Pines, *J. Magn. Reson.* **1988**, *77*, 606.

Appendix A

Experimental

A.1 Materials

The following chemicals, 1,4-dioxane ($\geq 99.8\%$, Fisher Chemical), tetrahydrofuran (THF, $\geq 99.5\%$, Carl Roth), sodium hydroxide (NaOH, extra pure, Acros Organics), calcium hydride (CaH_2 , 92 %, Alfa Aesar), n-butyllithium (n-BuLi, 1.6M in cyclohexane, Acros Organics), sec-butyllithium (sec-BuLi, 1.4M in cyclohexane, Acros Organics), methanol (MeOH, $\geq 99.9\%$, Fisher Chemicals), hydrochloric acid (HCl, 35 wt%, Merck), lithium (Li, $\geq 99.0\%$, Merck), N,N-dimethylformamide (DMF, $\geq 99\%$, Sigma-Aldrich), sodium azide (NaN_3 , $\geq 99.0\%$), pentaerythritol ($\geq 98\%$, Alfa Aesar), potassium hydroxide (KOH, $\geq 85\%$, Riedel-de Haën), propargyl bromide (80 %, Alfa Aesar), ethyl acetate ($> 99\%$, Acros Organics), cyclohexane ($\geq 99\%$, Fisher Chemicals), N,N,N',N'',N''-pentamethyldiethylenetriamine (PMDETA, $\geq 99\%$, Sigma-Aldrich), copper(I)bromide (CuBr , $\geq 98.0\%$, Sigma-Aldrich), 4,4'-azobis(4-cyanovaleric acid) (V-501, 98 % Alfa Aesar), N,N'-methylenebisacrylamide (MBA, $\geq 99.5\%$, Sigma Aldrich), sodium hydrogen carbonate (NaHCO_3 , $\geq 99.5\%$, Roth) and sodium chloride (NaCl, 99.9 %, VWR) were used as received.

Deionized water was taken from the house supply with a conductivity of $\leq 8\ \mu\text{S}/\text{cm}$.

The monomers methacrylic acid (MAA, $\geq 99\%$, Merck), acrylic acid (AA, 99 %, Sigma Aldrich) and ethylene glycol dimethacrylate (EGDMA, $\geq 97.5\%$, Merck) were distilled prior to usage to remove the inhibitor. Azobis(isobutylnitril) (AIBN, 98 %, Merck) was recrystallized for purification.

Deuterium oxide (D_2O , 99.9 % isotope purity, Acros Organic), deuterated chloroform (CDCl_3 , 99.8 % isotope purity, Sigma-Aldrich) and 2d-tetrachloro ethane (99.5 % isotope

purity, Armar Chemicals) were employed as solvents for the $^1\text{H-NMR}$ experiments.

A.2 Free Radical Polymerization of Methacrylic Acid

1,4-Dioxane (39 mL) was placed in a three-neck round bottom flask and the amount was adjusted to ensure a final 20 wt% ratio between polymer and solvent. Methacrylic acid (MAA, 10 g, 0.12 mol) as monomer, and ethylene glycol dimethacrylate as cross-linker were added (exact weighting see **Table A.1**). The solution was stirred to establish a homogeneous mixture. Afterwards, nitrogen gas was lead through the solution for 20 min to establish an inert atmosphere. Azobisisobutyronitrile (AIBN, 0.038 mg, $2.3 \cdot 10^{-4}$ mol) was added and the reaction was started by heating the mixture to 70 °C. After 8 hours, the reaction was quenched by cooling to ambient temperature. The resulting networks were extracted three times by consecutive mixing with an excess of tetrahydrofuran (THF) and subsequent removal of the supernatant solution by filtration. The remaining THF within the network was removed by mixing with water and the collapsed networks were taken up in diluted sodium hydroxide solution (0.1 M, 1.1 eq.). The amount of necessary sodium hydroxide solution V_{NaOH} was estimated according to the following equation

$$V_{\text{NaOH}} = 1.1 \frac{m_{\text{dry}}}{M_{\text{MAA}}[\text{NaOH}]_0} \quad (\text{A.1})$$

with m_{dry} as the mass of the dry network, M_{MAA} as the molecular weight of methacrylic acid and $[\text{NaOH}]_0$ as the concentration of sodium hydroxide. The neutralization was conducted overnight and subsequently, the networks were extracted multiple times with deionized water to remove the excess of ions from the network until the supernatant phase exhibited a conductivity of $\leq 50 \mu\text{S/cm}$. Drying under reduced pressure in the freeze-dryer yielded the product as an white soft powder.

sample	amount of EDGMA [g]	sample	amount of EDGMA [g]
PSMA-DC20-FRP	4.60	PSMA-DC1.7-FRP	0.39
PSMA-DC10-FRP	2.30	PSMA-DC1.0-FRP	0.23
PSMA-DC5.0-FRP	1.15	PSMA-DC0.6-FRP	0.14
PSMA-DC3.0-FRP	0.69	PSMA-DC0.4-FRP	0.092
PSMA-DC2.5-FRP	0.58		

Table A.1: Table of the synthesized poly(sodium acrylate) (PSMA) samples obtained by free radical polymerization (FRP). The respective degree of cross-linking DC and degree of neutralization DN are provided, as well as the employed amount of the linker ethylene glycol dimethacrylate (EDGMA).

A.3 Anionic Polymerization of Poly(Sodium Acrylate)

The anionic polymerization is very sensitive to impurities, such as water, oxygen and carbon dioxide. Small traces of these components will terminate the reaction under formation of stable side product making a living polymerization impossible. Consequently, the anionic polymerization was performed under an argon atmosphere and the chemicals utilized in this work, were purified by the following procedures:

The employed monomers tert-butyl methacrylate (*t*BMA, 98 %, Sigma-Aldrich) and ethylene glycol dimethacrylate (EGDMA, ≥ 97.5 %, Merck), as well as 1,4-dibromobutane (≥ 98 %, Alfa Aesar) were dried over calcium hydride (CaH_2 , 92 %, Alfa Aesar) overnight, degassed by three consecutive freeze-pump-thaw cycles and subsequently distilled under reduced pressure. Afterwards, the reactants were stored under an argon atmosphere at -20 °C in a freezer and used within one week.

The solvent tetrahydrofuran (THF, ≥ 99.5 %, Carl Roth) was stirred overnight with CaH_2 , distilled over elemental sodium (Na , ≥ 99 %, Merck) with benzophenone (99 %, Acros Organics) as indicator. After formation of a dark violet color, the pure THF was distilled into the reaction flask.

The co-initiator 1,1-diphenylethylene (DPE, 98 %, Alfa Aesar) was titrated with *n*-butyllithium until the formation of a persistent red color. In the following, cyclohexane was removed under reduced pressure and the DPE purified by distillation. Afterwards, pure tetrahydrofuran was condensed into the flask and the solution was kept under an argon atmosphere at -20 °C in a freezer.

Lithium chloride (LiCl , ≥ 98 %, Sigma-Aldrich) was stored at 120 °C to prevent water uptake.

A.3.1 Anionic Polymerization of Polymethacrylate Networks in a Single Step

First, a round bottom Schlenk flask was armed with a magnetic stirring bar and 100 mg of lithium chloride (2.4 mmol), baked-out utilizing a heat gun at 650 °C and evacuated under high vacuum until the pressure reached $\leq 10^{-3}$ mbar. Subsequently, the flask was flushed with dry argon and the procedure was repeated three times. After the preparation of the flask, 170 mL of purified THF were introduced under counterflow of argon as well as 34.3 mL of tert-butyl methacrylate (30 g, 0.21 mol) as monomer and the cross-linker ethylene glycol dimethacrylate (EDGMA). The required amount of EDGMA is displayed in **Table A.2**. The content of THF was adjusted to a 20 wt% ratio between polymer and solvent. The flask was cooled to -80 °C using liquid nitrogen/acetone. Afterwards, the reaction was initialized employing a mixture of 0.2 mL of a 1.4M *sec*-butyllithium solution ($2.8 \cdot 10^{-4}$ mol) and 55.5 mg 1,1-dipenylethylene ($3.0 \cdot 10^{-4}$ mol). The polymerization was

quenched after 3 hours by adding 1 mL of pure methanol. Soluble side products were removed from the network by threefold extraction with THF. The tert-butyl protecting group was cleaved off under reflux utilizing a 50 vol% solution of concentrated (35 wt%) hydrochloric acid in dioxane. The cleavage was finished after 8 hours and the hydrochloric acid removed by rinsing with deionized water until the washing water exhibited a pH of 7. The resulting carboxylic groups were neutralized overnight with 1.1 eq. of a 0.1 M sodium hydroxid solution, which was estimated according to **Equation A.1**. Afterwards, the gel was repeatedly washed with deionized water until the conductivity of the supernatant phase dropped below 50 $\mu\text{S}/\text{cm}$. The final product was achieved after freeze-drying in vacuo.

sample	amount of EDGMA [g]	amount of THF [mL]
PSMA-DC5.0-SSA	1.15	50
PSMA-DC3.0-SSA	0.69	48
PSMA-DC1.0-SSA	0.23	46
PSMA-DC0.6-SSA	0.14	46
PSMA-DC0.3-SSA	0.069	46

Table A.2: Table of the synthesized poly(sodium acrylate) (PSMA) samples obtained by anionic copolymerization. The respective degree of cross-linking DC and degree of neutralization DN are provided, as well as the employed amount of THF and the linker ethylene glycol dimethacrylate (EDGMA).

A.3.2 Anionic Polymerization of Quasi-Model Polymer Networks

Here, the Schlenk flask was filled with 100 mg lithium chloride (2.4 mmol) and dried in a similar fashion as described in the previous section. In the following, pure THF (120 mL) was distilled into the flask as solvent ensuring a final 20 wt% ratio of polymer to solvent. Afterwards, 0.1 g of elemental lithium (0.1 g, 0.014 mol) were added and the mixture vigorously stirred for one hour activating the lithium surface. Subsequently, 0.3 M diphenyl ethylene solution (DPE, see **Table A.3**) was introduced as co-initiator and the stirring continued overnight. The unreacted lithium was removed and the dark red mixture cooled to $-80\text{ }^\circ\text{C}$. When reaching the final temperature, 34.3 mL of the monomer tert-butyl methacrylate (30 g, 0.21 mol) was injected rapidly and the reaction performed over the course of 2-3 hours in a temperature range between -30 to $-40\text{ }^\circ\text{C}$ (THF/liquid nitrogen). Afterwards, the polymer solution was cooled again to $-80\text{ }^\circ\text{C}$ and the cross-linker ethyleneglycol dimethacrylate was added. The cross-linking reaction was quenched

after one hour with methanol. The achieved polymer networks were subjected to the deprotection and working-up procedure described in the previous section giving the final polymethacrylate network as a white powder after freeze-drying in vacuo.

sample	EDGMA [g]	THF [mL]	DPE solution [mL]	M_n (SEC) [kg/mol]	\bar{D}
PSMA-DC5.0-QM	33.4	210	70.3	3.1	1.28
PSMA-DC3.0-QM	20.1	185	42.2	5.1	1.14
PSMA-DC1.0-QM	6.7	150	14.1	18.5	1.11
PSMA-DC0.6-QM	4.0	145	8.4	26.7	1.08
PSMA-DC0.3-QM	2.0	140	4.2	46.3	1.09

Table A.3: Table of the synthesized poly(sodium arcylate) (PSMA) samples obtained by sequential anionic polymerization, where first the polymer chain is build by a difunctional initiator and then the chains are cross-linked to form a polymer network. The respective degree of cross-linking DC and degree of neutralization DN are provided, as well as the employed amount of THF, DPE solution and the linker ethylene glycol dimethacrylate (EDGMA).

A.3.3 Model Networks by Anionic Polymerization with subsequent Cross-linking by Azide-Alkyne Huisgen Ligation

Anionic Polymerization First, the polymer mesh in the network was synthesized by anionic polymerization. Here, the Schlenk flask was equipped with 100 mg of lithium chloride (0.034 eq., 2.4 mmol) and dried as described in the previous section. Afterwards, lithium (0.1 g, 0.014 mol), and 0.3 M diphenyl ethylene solution, respectively, were introduced. The respective volumes of the DPE solution are displayed in **Table A.4**. The total amount of THF was adjusted to 125 mL by condensing pure THF into the flask and the reaction mixture was vigorously stirred overnight. The mixture was cooled to -80 °C and 10 g of the monomer tert-butyl methacrylate (11.5 mL, 0.070 mol) added. The polymerization was performed for 2-3 hours at -30 to -40 °C. Subsequently, the mixture was cooled to -80 °C and the polymerization quenched by addition of an excess of 1,4-dibromo butane (4.0 mL, 33.5 mmol), which was injected rapidly. The stirring was continued for another hour and then the polymer was precipitated by pouring the THF solution into a 1:9 methanol:water mixture, filtrated and redissolved in THF. Afterwards, water was added dropwise to the THF solution until the polymer precipitated. The polymer was removed by filtration and redissolved in THF again. In the following, the first precipitation step was repeated and the polymer dried at 70 °C in vacuo. If necessary, the last precipitation

step was repeated until no traceable impurities of 1,4-dibromo butane remained.

Substitution of the Bromide End Group In the following, the polymer end group was changed from bromide to azide. The purified polymer (10 g) was dissolved in dimethyl formamide (DMF, 200 mL, 2.5 mol) and 500 mg of sodium azide (7.7 mmol) were added. The substitution was conducted overnight at room temperature and the polymer solution subjugated to the full three step precipitation process mentioned above in order to remove remaining sodium azide quantitatively. Eventually, the precipitated polymer was dried in the drying oven at 70 °C under high vacuum.

targeted sample	DPE solution [mL]	M_n (NMR) [kg/mol]	M_n (SEC) [kg/mol]	\mathcal{D}	end group $-\text{N}_3$ [%]
PSMA-DC2.0-MN	23.4	3.6	4.0	1.30	93
PSMA-DC1.0-MN	11.7	6.6	6.9	1.13	100
PSMA-DC0.7-MN	8.2	8.9	9.4	1.15	93
PSMA-DC0.3-MN	3.5	23.4	24.0	1.07	92
PSMA-DC0.2-MN	2.3	35.9	35.7	1.08	100

Table A.4: List of the synthesized linear poly(sodium acrylate) (PSMA) samples obtained by anionic polymerization end-capped with sodium azide. The required amount of diphenylethylene (DPE) solution are provided. The respective molecular weights M_n as given with their dispersity \mathcal{D} , as obtained by size exclusion chromatography (SEC), with poly(tert-butyl methacrylate) standards, and nuclear magnetic resonance spectroscopy (NMR), by comparison of the initiator to monomer content of the final polymer. The relative content of the desired azide end-group is also obtained by NMR analysis as described in the main text.

Synthesis of Tetrapropargyl Pentaerythritol as 4-Armed Linker 2.4 g of pentaerythritol (0.017 mol) was added into a solution of 15 g of potassium hydroxide (0.264 mol) in 60 mL of anhydrous DMF. After stirring at 50 °C for one hour, 20 g of propargyl bromide (15.0 mL, 7.7 mol) was introduced dropwise under strong gas development. The solution turned brown and the reaction was continued overnight at 40 °C. The reaction mixture was quenched by addition of water and the water phase extracted thrice with 100 mL of ethyl ether. The organic layers were combined, washed with brine and dried over sodium sulfate. The ethyl ether was removed by rotary evaporation and the adduct further purified by filtration over a silica gel column employing a 3:7 ethyl acetate:cyclohexane mixture as mobile phase. 1.62 g (5.6 mmol, yield 32 %) of a colorless liquid were obtained.

ESI-MS (M+Na): exp: 311.1257 m/z (theo: 311.1254 m/z), $^1\text{H-NMR}$ (CDCl_3 , ppm): 4.13 (8H, $-\text{O}-\text{CH}_2$), 3.55 (8H, $\text{C}-\text{CH}_2-\text{O}$), and 2.43 (4H, $\text{C}\equiv\text{CH}$).

Cross-linking of the Polymers by Azide-alkyne Huisgen Ligation For the network formation, 10 g of polymer, pentamethyl ethylene diamine (PMDTA, 0.5 mL, 2.4 mmol) as base and a 0.1 M solution of tetrapropargyl pentaerythritol in THF as 4-armed cross-linker were placed in a flask. The required amount of linker solution V_{linker} was calculated following

$$V_{linker} = \frac{m_{polymer}}{M_n c_{linker}} \quad (\text{A.2})$$

with the concentration of the linker c_{linker} , the molar mass of the polymer M_n from the SEC measurements, and the employed mass of the polymer $m_{polymer}$, see **Table A.5**. The volume of THF was adjusted to a total of 56.2 mL, which equals a 20 wt% ratio of the final polymer to the solvent. The solution was purged with argon for 20 min and 5.0 mg of copper(I)bromide ($3.5 \cdot 10^{-5}$ mol) as catalyst was added. After gelation the stirring was stopped and the flask left at room temperature for ~ 2 weeks. The reaction was quenched by exposure to air and the formed network extracted thrice with THF. The tert-butyl ester protecting group was cleaved off under reflux using a 50 vol% solution of concentrated (35 wt%) hydrochloric acid in dioxane. The network was rinsed with deionized water until the pH of the washing water was neutral. Sodium hydroxide was added in a 10 % excess to convert the acid to the carboxylate. After reaction at room temperature overnight, the gel was repeatedly washed with deionized water until the conductivity of the supernatant phase is $\leq 50 \mu\text{S}/\text{cm}$.

sample	linker solution [mL]	defects [%]
PSMA-DC2.0-MN	33.4	26
PSMA-DC1.0-MN	20.1	22
PSMA-DC0.7-MN	6.7	26
PSMA-DC0.3-MN	4.0	33
PSMA-DC0.2-MN	2.0	42

Table A.5: Table of the synthesized poly(sodium acrylate) (PSMA) polymer networks produced by azide-alkyne Huisgen ligation. The resulting number of defects, in terms of unreacted azide and wrong end-group, were determined by $^1\text{H-NMR}$ spectroscopy as described in the main text **Chapter 3.1.5, p. 49**.

A.4 Free Radical Polymerization of Acrylic acid

4,4'-Azobis(4-cyanovaleric acid) (V-501) as initiator and N,N'-metylenbisacrylamide (MBA) as cross-linking agent were dissolved in the desired volume of monomer acrylic acid (AA). Afterwards, water in a 20:80 weight ratio monomer to solvent was added to the mixture and the vial was deoxygenated for 15 min by purging with argon. The reaction was started by heating to 70 °C and quenched after 16 hours by cooling to room temperature. Subsequently, extractables were removed by consecutively washing the networks three times with an excess of deionized water. Finally, the solvent was removed by lyophilization. The exact weightings are provided in **Table A.6**.

From polymer to polyelectrolytes Similar to the methacrylic acid samples, each of the PAA network synthesized was neutralized in order to achieve polyelectrolyte gels, which could be employed in e.g. desalination. The neutralization was performed by mixing a known amount of dry polymer with an excess of 0.1 M sodium hydrocarbonate, which was calculated following

$$V_{NaHCO_3} = 1.1 \frac{m_{dry}}{M_{AA} [NaHCO_3]_0} \quad (\text{A.3})$$

where V is the required volume of $NaHCO_3$ having the concentration $[NaHCO_3]$ for a given mass of dry network m_{dry} . M_{AA} is the molecular weight of acrylic acid. The network was left in basic solution overnight. Afterwards, the polymer was washed with distilled water until the pH reached 7. Eventually, the network was dried via lyophilization.

A.5 Reversible Addition Fragmentation Transfer Polymerization of Acrylic acid

Here, acrylic acid (AA) was used as monomer, N,N'-metylenebisacrylamide (MBA) as cross-linker, and S,S-bis(α,α' -dimethyl- α'' -acetic acid)trithiocarbonate (TRITT) as RAFT agent. In analogy to the FRP, the reaction was performed in distilled water (20 wt%) and V-501 was employed as initiator. The molar ratio of V-501 to TRITT was set to 0.15:1, while the employed amounts of AA, MBA and TRITT are specified in **Table A.6**. The polymerization was started by heating the solution to 70 °C and was performed overnight. Afterwards, the sol content was removed by washing the network extensively thrice with an excess of deionized water. Subsequently, the network was neutralized overnight using a 1.1 molar excess of 0.1 M $NaHCO_3$ solution. Ultimately, the water inside the hydrogel was removed via lyophilization.

sample	acrylic acid [g]	TRITT [mg]	MBA [mg]	V-501 [mg]	water [g]
PSA-DC0.6-FRP	1.0	–	12.8	0.6	4.0
PSA-DC0.6-RAFT0.10	1.0	3.9	12.8	0.6	4.0
PSA-DC1.0-FRP	1.0	–	21.4	0.6	4.0
PSA-DC1.0-RAFT0.05	1.0	2.0	21.4	0.3	4.0
PSA-DC1.0-RAFT0.10	1.0	3.9	21.4	0.6	4.0
PSA-DC1.0-RAFT0.17	1.0	6.7	21.4	1.0	4.0
PSA-DC1.0-RAFT0.25	1.0	9.8	21.4	1.5	4.0
PSA-DC1.5-FRP	1.0	–	32.1	0.6	4.0
PSA-DC1.5-RAFT0.10	1.0	3.9	32.1	0.6	4.0
PSA-DC1.5-RAFT0.25	1.0	9.8	32.1	1.5	4.0
PSA-DC3.0-FRP	1.0	–	64.2	0.6	4.0
PSA-DC3.0-RAFT0.10	1.0	3.9	64.2	0.6	4.0
PSA-DC3.0-RAFT0.25	1.0	9.8	64.2	1.5	4.0
PSA-DC5.0-FRP	1.0	–	107.0	0.6	4.0
PSA-DC5.0-RAFT0.10	1.0	3.9	107.0	0.6	4.0
PSA-DC5.0-RAFT0.25	1.0	9.8	107.0	1.5	4.0

Table A.6: Summary of the poly(sodium acrylate) (PSA) networks synthesized either via conventional free radical polymerization (FRP) or RAFT polymerization. The exact masses of all substances are given.

Appendix B

Experimental Characterization Procedures

B.1 Swelling experiments

In a typical swelling experiment, 10 mg of dry polymer (m_p) was placed on a metal sieve (m_{sieve}) on a metal rack. The metal rack was immersed in a closed Petri dish to prevent evaporation and a large excess of 1 wt% sodium chloride solution was added. The height of the solution was adjusted that the contact between the dry polymer and the solution occurred exclusively through the sieve. After equilibrating overnight at room temperature, the sieve and the polymer were gently pressed onto a paper towel for one minute to remove the interstitial water and subsequently weighed ($m_{swollen}$). The degree of swelling (Q_{eq}) was calculated according to **Equation B.1**.

$$Q_{eq} = \frac{m_{water}}{m_p} = \frac{m_{swollen} - m_{sieve} - m_p}{m_p} \quad (\text{B.1})$$

where m_{water} is the amount of water, which was taken up. The data reported in the main text are the mean value and the standard deviation of the results were obtained in three independent measurements.

B.2 Fourier-Transform Infrared Spectroscopy

FT-IR spectra of the dried and ground polymer particles were recorded in attenuated total reflection (ATR) utilizing a Vertex 70 spectrometer equipped with a liquid nitrogen cooled MCT detector (Bruker, Ettlingen, Germany). 64 scans were employed over a range of 600 - 4000 cm^{-1} with a resolution of 4 cm^{-1} .

B.3 Nuclear Magnetic Resonance Spectroscopy

B.3.1 High-Field NMR-Spectroscopy

The ^1H -NMR spectra were measured using an Avance III Microbay 400 MHz spectrometer (Bruker, Karlsruhe, Germany) employing 1024 scans. The samples were prepared by dissolving 10 - 20 mg in 0.6 - 0.7 mL of CDCl_3 in case of hydrophobic or D_2O in case of hydrophilic samples. If cross-linked networks were analyzed, 10 - 20 mg of sample were dispersed in 0.6 - 0.7 mL of solvent and then swollen to equilibrium overnight at room temperature.

B.3.2 ^1H -NMR T_2 -relaxation

For the ^1H -NMR T_2 -relaxation measurements 40-50 mg of sample was mixed in a 1 to 6 weight ratio with D_2O and subsequently dried overnight at 70 °C under reduced pressure to reduce residual H_2O . Afterwards, the sample was placed in a sealed 10 mm NMR tube, mixed again in a 1 to 6 weight ratio with D_2O and equilibrated for 2 days. The filling and placing of the sample were adjusted to ensure that it is in the region of the highest homogeneity of the magnet field. Usually, the sample height did not exceed 8 mm and the position was adjusted accordingly.

The experiments were conducted on a bench-top 20 MHz minispec NF (Bruker, Karlsruhe, Germany) and the sample temperature was kept at 30 °C using a BVT3000 unit (Bruker, Karlsruhe, Germany). For all measurements, the receiver gain was set to 90 - 92 dB, which corresponds to a maximum intensity of 70 - 90 %. The pulse attenuation is probe specific and was not changed (setting 0 dB) and the magnitude acquisition mode was used unless otherwise denoted. Before each measurement, the resonance frequency and the field offset of the magnet of the spectrometer were adjusted in order that the NMR signal was on-resonance. In addition, the magnetic field was matched and the pulse lengths were determined performing a nutation measurement. Here, a series of the maxima of free induction decays with varying pulse length were acquired. A sine function was fitted to the data, while the first maximum gave the 90° pulse length and the first minimum the 180° pulse length. Typical values for the pulse lengths were found to be in the range of 2.7, and 5.0 μs respectively.

The T_2 -relaxation process covers several orders of magnitude between 10 μs and 4 s. Consequently, it is not possible to measure the full decay in one experiment and the relaxation curve was obtained combining a set of pulse sequences. A magic sandwich echo (MSE) pulse sequence and 4-5 Carr-Purcell-Meiboom-Gill (CPMG) based pulse sequences were recorded individually. [41] Since a simple CPMG experiment with its phase $(y)^n$, which is displayed in **Figure B.1**, would lead to spin-locking effects [180] more sophisticated

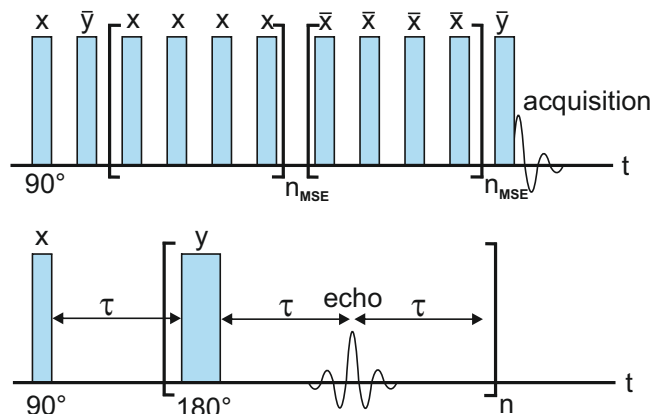


Figure B.1: Schematic representation of the pulse sequences for the measurement of spin-spin relaxation times: MSE-sequence on the top and the CPMG-sequence at the bottom.

XX4 ($y\bar{y}\bar{y}y$)ⁿ [181] and XY16 ($y\bar{x}y\bar{x}\bar{x}y\bar{x}y\bar{y}\bar{x}y\bar{x}x\bar{y}x\bar{y}$)ⁿ [144] phase cycling schemes were used instead. During each measurement, 100 data points were collected and 1024 scans averaged. The MSE was measured in conjunction with the XX4 in a joint pulse program. The MSE was recorded for 50 μs , while the following XX4 sequence used a pulse separation of $\tau = 50 \mu\text{s}$ and a echo separation of 2τ . To cover the long tailing of the relaxation curve, three XY16 pulse sequences were employed subsequently with pulse separations of $\tau = 0.04, 0.1, \text{ and } 1 \text{ ms}$. In case of step decays at short relaxation times, an additional XX4 sequence with $\tau = 5 \mu\text{s}$ was measured to increase the point density in the crucial time frame. Recycle delays of 1 s and no dummy scans were utilized. Of the XX4 pulse sequence all cycles were recorded, while of the XY16 sequence every 8th cycle was traced. The data from all measurements of one sample were collected in a single data file. Subsequently, the solvent signal was subtracted using a single exponential decay fitted to the data above 100 ms, as shown in **Figure 4.4** in **Chapter 4.2** in the main text. [41]

B.3.3 Residual Dipolar Coupling Measurements

The double quantum (DQ) experiments were performed employing the same NMR equipment and sample conditions as described in the T_2 -relaxation experiments above. The measurement of the DQ coherences is accomplished by the complex Baum-Pines pulse sequence, which was further improved and implemented for the minispec by Saalwächter et al. [156, 159] The acquisition parameters, such as pulse length, phase angle, and resonance frequency are optimized for a maximum signal intensity for each measurement.

The imaginary part was matched to zero, to avoid loss of signal. In a typical DQ experiment, 40 data points were recorded of the DQ signal S_{DQ} and of the reference intensity S_{ref} with an initial spacing of 0.01 ms and an increment of 10 μs , which is doubled after each 8 points. Due to the length of the excitation and reconversion pulse trains, the first point could be measured only after 80 μs , which proved to be insufficient to cover the full build-up curve of higher cross-linked samples. Consequently, an adapted version of the pulse program was used, [159] which enabled earlier acquisition of 30 data points between 10 and 100 μs with an initial spacing of 1 μs , while the spacing was doubled after every 8 data points. Hereby, the excitation and reconversion pulse train was shortened to 3 pulses.

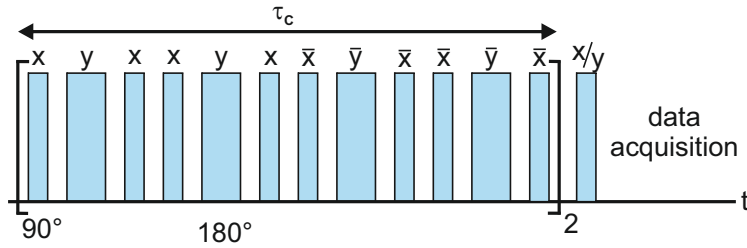


Figure B.2: Schematic representation of the modified Baum-Pines pulse sequence for the measurement of the double quantum coherence build-up.

A normalization of the double quantum intensity is required to recover the build-up curve undistorted by relaxation effects. The normalization is performed by a stepwise subtraction of the long tail of the double quantum curve with two single exponential functions. The following fits and window sizes have been found to be beneficial for the application on methacrylate hydrogels. First, a single exponential function $[A \exp(-t/\tau_A)]$ is fitted to the sum of the double quantum intensity I_{DQ} and the reference signal I_{ref} above 20 ms and subsequently subtracted giving the reduced intensity I_{red} , as displayed in **Figure B.3**. In the second step, another exponential fit $[B \exp(-t/\tau_B)]$ is applied to I_{red} between 2 and 20 ms. The so-called build-up curve of the double quantum signal I_{norm} , which consists purely of the network contribution, is calculated according to [159]

$$I_{norm} = \frac{I_{DQ}}{I_{DQ} + I_{ref} - A \exp(-t/\tau_A) - B \exp(-t/\tau_B)} \quad (\text{B.2})$$

The resulting build up curve is shown in **Figure B.3**

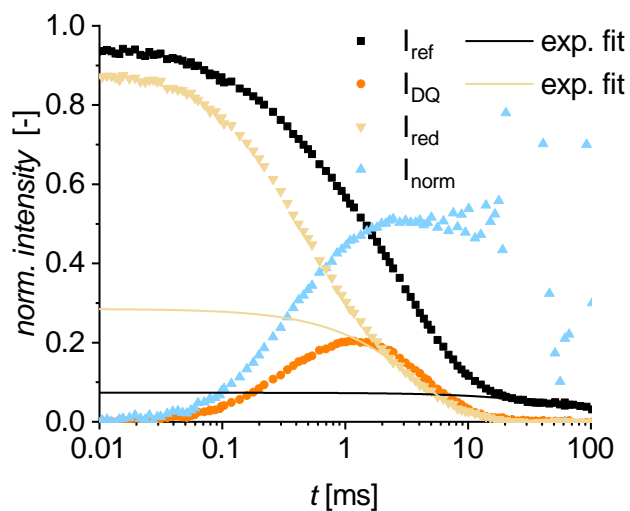


Figure B.3: Evaluation of double quantum build-up data by removal of single exponential tails from the raw data to compensate for relaxation processes. The tails are removed in two steps: the first fit is made to I_{ref} after 20 ms. Subtraction of the fit from I_{ref} yields I_{red} . The second fit is on I_{red} between 2 – 20 ms. The renormalized DQ build-up resulting from **Equation B.2** is displayed with blue symbols.

B.4 Size-Exclusion Chromatography

B.4.1 Conventional Size-Exclusion Chromatography (SEC)

For the SEC measurements, the polymers were dissolved in HPLC-grade THF with a concentration of about 1 g/L at room temperature. The molecular weight and the molecular weight distribution were determined employing a Agilent 1100 series SEC equipped with an Agilent 1200 differential refractive index (DRI) detector (Agilent, Santa Clara, United States) at 35 °C. Two SDV Lux 300mm x 8mm columns (1,000 and 10,000 Å pore size, PSS, Mainz, Germany) were used. THF was utilized as mobile phase with a flow rate of 1 mL/min. Usually, 100 μ L of the analyte solution were injected on the column if not specified otherwise. The columns were calibrated using tert-butyl methacrylate standards (PSS, Mainz, Germany) ranging from 1 to 900 kg/mol.

B.4.2 Coupled Fourier-Transform Infrared Spectroscopy Size-Exclusion Chromatography

In case of the FTIR-SEC measurements, an Agilent 1260 infinity pump was used for the determination of the molecular weight and the molecular weight distribution in combination with a Agilent 1200 DRI detector (Agilent, Santa Clara, United States) and a 70 Vertex FTIR-spectrometer (Bruker, Ettlingen, Germany). Here, 500 μL of a 4 g/L solution of the analyte dissolved in HPLC-grade THF were injected manually. The linear M SDV semi-prep column (PSS, Mainz, Germany) was employed to enable higher concentration during separation to enhance the signal intensity of the FTIR. A custom-built flow-cell with multiple reflections was inserted in the FTIR-spectrometer and the measurement was conducted in attenuated total reflection (ATR). [85,86] The liquid nitrogen cooled MCT detector was used for an improved signal to noise ratio. Usually, the measurement took 90 min, while 32 scans of the FTIR were averaged for a single data point. A range of 600 - 4000 cm^{-1} was covered in each spectrum with a resolution of 4 cm^{-1} . The drift of the instrument over time was compensated using the TIMO software package employing a second order polynomial fit. [85,86]

B.5 Inverse Size-Exclusion Chromatography

The SEC installation for the inverse SEC measurements consisted of a 1260 Infinity pump (Agilent, Santa Clara, United States), a 1260 Infinity ALS autosampler (Agilent, Santa Clara, United States), a 1260 Infinity DRI detector (Agilent, Santa Clara, United States), and a degasser unit (PSS, Mainz, Germany). A buffer solution of 0.1 M Na_2HPO_4 in water (14.2 g/L), doped with 0.05M NaN_3 , was used as eluent for the hydrogels, while hydrophobic samples were measured with HPLC grade THF as eluent. Narrow molecular weight distributed polymers were utilized as standards for the measurements, i.e. pullulan (0.18 - 708 kg/mol, PSS, Mainz, Germany) as water soluble polymer. For each measurement, the sample has been swollen in the eluent overnight, until it reached the equilibrium. A 10 mm (inner diameter) glass column (PSS, Mainz, Germany) with adjustable pistons was packed with the swollen gel with a bed length of 4 - 8 cm. The glass frit in flow direction with 10 μm pore size was protected by a filter paper to avoid that gel was squeezed into the frit. A low flow rate of 0.2 mL/min was established to push out the remaining air between the particles. In case of a sharp pressure rise, the flow was stopped and the column re-packed. If a constant pressure of 3 - 6 bar was achieved, the measurement was continued. Hereby, 1 g/L of the polymer standard were dissolved in the eluent on the previous day and 50 μL of the solution were injected by the autosampler. The peak maxima of each polymer were recorded and the pore size distribution calculated

using the PoroCheck software package (PSS, Mainz, Germany).

B.6 Dielectric Spectroscopy

In case of dielectric spectroscopy measurements, the polyelectrolyte was swollen overnight in a 1:6 polymer to water ratio. About 50 mg of hydrogel were pressed into disc shaped specimen in a 8 mm cylindrical press setup utilizing ~ 10 bar. The specimen were placed in a Ares G2 rheometer (TA instruments, Eschborn, Germany) in a custom-built 8 mm plate-plate geometry for dielectric experiments. The height was adjusted until the normal force reached 0.1 N. Afterwards, the excess material was removed and the distance between the geometries determined. The dielectric measurements were conducted using an Alpha-AN-Analyzer (Novocontrol Technologies, Montabaur, Germany). The excitation frequencies were alternated from 0.1 to 10^7 Hz. The conductivity was determined by averaging 6 points of the initial plateau, as displayed in **Figure 4.35 of Chapter 4.4.1** in the main text body.

Appendix C

Figures

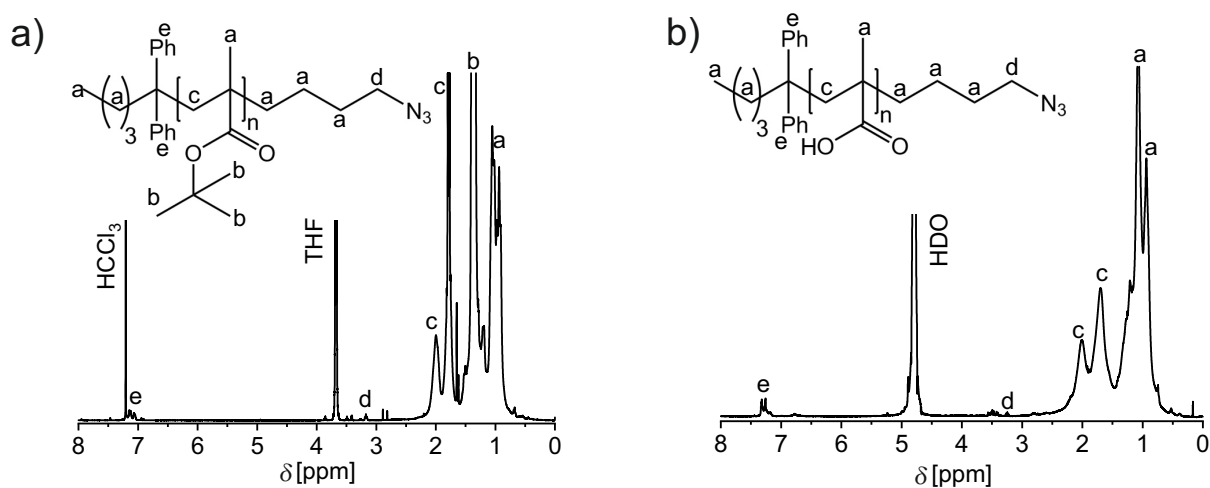


Figure C.1: a) ¹H-NMR spectrum of poly(tert-butyl methacrylate) in CDCl₃ with $M_n = 43.5$ kg/mol. b) ¹H-NMR spectrum of the same polymer in D₂O after the deprotection reaction under reflux with 50/50 vol% HCl/1,4-dioxane and purification by precipitation, see **Chapter A.3.3, p. 133**. It reveals the disappearance of the signal *b* at 1.54 ppm assignable to the tert-butyl protecting group confirming a successful deprotection. (1024 scans, RT)

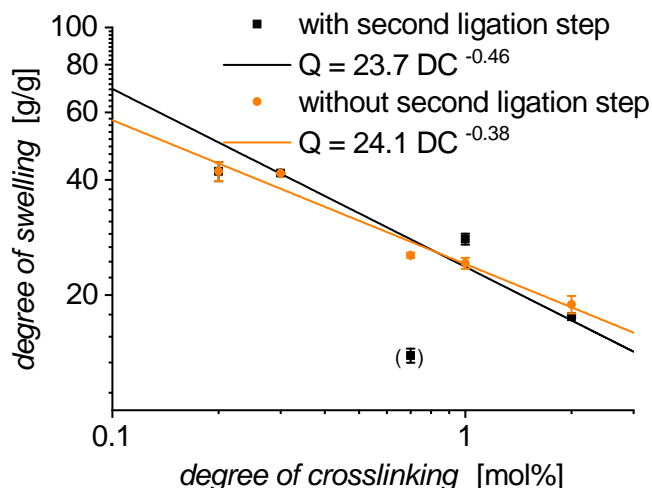


Figure C.2: Measurement of the degree of swelling (Q) of poly(sodium acrylate). The samples were obtained by anionic polymerization of telechelic poly(*tert*-butyl methacrylate) with azides as end groups, which are coupled into the network by azide-alkyne ligation and subsequently hydrolyzed. The cross-linking is performed in a single step (orange) after which $\sim 30\%$ of azide groups remained unreacted, despite an equimolar ratio of linker and azide functionalities. In a second batch the missing quantity of cross-linker was added after the first reaction cycle, which gave the black data points. The stronger deviations of Q from the expected power law indicate ill defined networks (black data points, point in brackets not used for fit). Thus, only the hydrogels resulting from the single cross-linking step were characterized further.

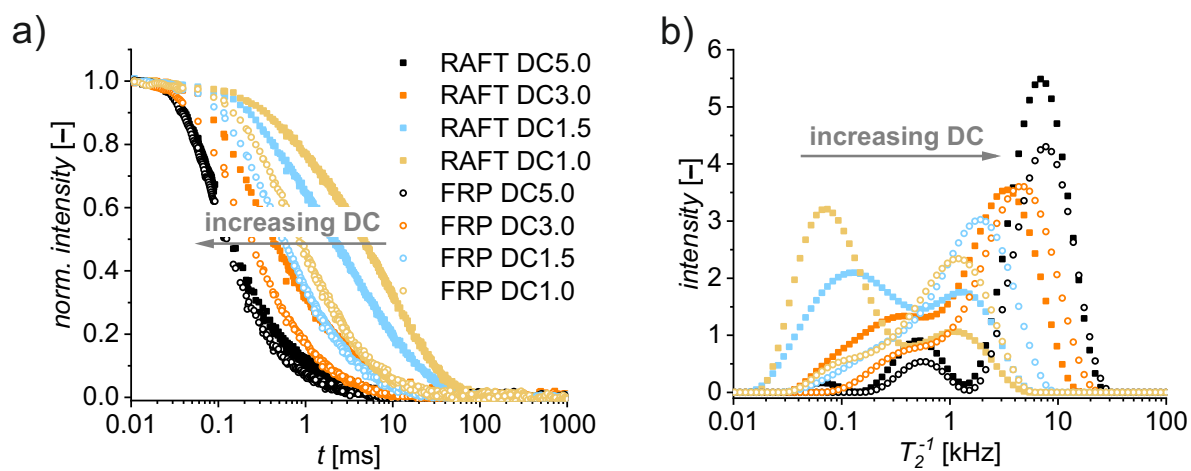


Figure C.3: a) ^1H -NMR T_2 -relaxation curves of poly(sodium acrylate) (PSA) hydrogels with a degree of cross-linking DC ranging from 0.6 to 5 mol% synthesized via FRP, empty symbols, or with 0.25 mol% RAFT agent, full symbols. (1024 scans, 1/9 (g/g) polymer/ D_2O , RT, low-field NMR, pulsesequence see **Appendix B.3.2**, p. 140) b) The respective relaxation rate distributions resulting from the inverse Laplace transformation (ILT).

Appendix D

List of Variables

A	free energy / area
α	smoothing parameter ILT
\vec{B}_0	magnetic field
β	inverted standard deviation / stretch factor
c	concentration
C	scaling constant of the entropy of conformation
d	diameter
D	dispersity
DC	degree of cross-linking, cross-link density
DN	degree of neutralization
D_{res}	residual dipolar coupling constant
δ	chemical shift
e	elementary charge
ΔE	Energy
$\epsilon(r)$	relative electric permittivity
ϵ_0	dielectric constant
g	osmotic coefficient / gravitational acceleration
G	free enthalpy
γ	gyromagnetic ratio
h	height
\hbar	Planck constant
\hat{H}	Hamilton operator
i	dissociation parameter
I	ionic strength
k_B	Boltzmann constant
K	equilibrium constant / distribution coefficient
κ	direct current conductivity

l	length
\mathcal{L}	Laplace operator
λ	extension ratio
λ_B	Bjerrum length
λ_D	Debye length
m	mass
m_i	Eigen values
M	number of sub-units per polymer chain / molecular weight
\vec{M}	net magnetization
M_C	molecular weight between two junction points
M_n	number average molar mass
M_w	weight average molar mass
μ	chemical potential
n	number
N	number of states / number of junctions per unit volume
N_A	Avogadro constant
ν	resonance frequency
ν_e	number of junctions / number of chains per unit volume
ω_l	larmor frequency
ω_{lin}	lin based
ω_{log}	log based
Ω	number of chain conformations
P	pressure
$P(r)$	probability
$P(x, y, z)$	probability
Π	osmotic pressure
ϕ	volume fraction
Φ	potential / pore size distribution
Q	degree of swelling
Q_{syn}	degree of swelling during the hydrogel formation
r	end-to-end distance
\vec{r}	end-to-end vector
R	ideal gas constant / pore dimension
R_h	radius of hydration
ρ	density
S	entropy / surface
σ	standard deviation / conductivity

t	time
T	temperature
T_1	longitudinal relaxation time in NMR
T_2	transverse relaxation time in NMR
T_g	glass transition temperature
τ	relaxation time
τ_e	time delay
θ	angle
U	internal energy
V	volume
V_0	standard volume
V_1/V_2	partial volume
V_{el}	elution volume
V_{void}	void volume
V_{pore}	pore volume
w_{norm}	normalized width
W	reversible work
x_1/x_2	mole fraction
χ	Flory-Huggins parameter
Y	conversion rate
z	charge
∇	nabla operator

List of Tables

3.1	Schematic representation of the polymer networks achievable by the different synthetic procedures including the presumed network heterogeneities.	40
A.1	Table of the synthesized poly(sodium acrylate) (PSMA) samples obtained by free radical polymerization (FRP). The respective degree of cross-linking DC and degree of neutralization DN are provided, as well as the employed amount of the linker ethylene glycol dimethacrylate (EDGMA).	130
A.2	Table of the synthesized poly(sodium acrylate) (PSMA) samples obtained by anionic copolymerization. The respective degree of cross-linking DC and degree of neutralization DN are provided, as well as the employed amount of THF and the linker ethylene glycol dimethacrylate (EDGMA).	132
A.3	Table of the synthesized poly(sodium acrylate) (PSMA) samples obtained by sequential anionic polymerization, where first the polymer chain is build by a difunctional initiator and then the chains are cross-linked to form a polymer network. The respective degree of cross-linking DC and degree of neutralization DN are provided, as well as the employed amount of THF, DPE solution and the linker ethylene glycol dimethacrylate (EDGMA).	133
A.4	List of the synthesized linear poly(sodium acrylate) (PSMA) samples obtained by anionic polymerization end-capped with sodium azide. The required amount of diphenylethylene (DPE) solution are provided. The respective molecular weights M_n as given with their dispersity \mathcal{D} , as obtained by size exclusion chromatography (SEC), with poly(tert-butyl methacrylate) standards, and nuclear magnetic resonance spectroscopy (NMR), by comparison of the initiator to monomer content of the final polymer. The relative content of the desired azide end-group is also obtained by NMR analysis as described in the main text.	134

A.5	Table of the synthesized poly(sodium acrylate) (PSMA) polymer networks produced by azide-alkyne Huisgen ligation. The resulting number of defects, in terms of unreacted azide and wrong end-group, were determined by $^1\text{H-NMR}$ spectroscopy as described in the main text Chapter 3.1.5, p. 49	135
A.6	Summary of the poly(sodium acrylate) (PSA) networks synthesized either via conventional free radical polymerization (FRP) or RAFT polymerization. The exact masses of all substances are given.	137

List of Figures

2.1	Schematic representation of different polymer topologies. The most prominent cases are linear, cyclic, and branched polymers, as well as polymers, which are coupled into networks via physical or chemical bonds, adapted from [47].	6
2.2	Comparison between an ideal network polymer (left) and a real network polymer (right), both with 9 junction points (ν_e). In addition, the unit volume V_0 and the functionality ζ of the cross-link are presented, i.e. the number of coupled chains per junction. The synthesized networks feature defects like (1) loops, (2) dangling ends, (3) entanglements, (4) multiple coupled and (5) unbound chains (sol).	7
2.3	Depiction of the general approaches for polymer network synthesis using an initiator (green) and the monomer (orange) yielding the polymer (black). 1) The network formation can be conducted in a single step by in situ copolymerization of a multifunctional linker (gray). 2) In the second approach, the polymer chain is formed first, which is cross-linked in a subsequent step.	8
2.4	Examples of (1) weak, e.g. poly(sodium acrylate) and (2) strong anionic polyelectrolytes, e.g. poly(sodium styrene sulfonate), as well as (3) weak, e.g. polyethylenimine (generates in aqueous solutions in-situ a polyelectrolyte by proton abstraction), and (4) strong cationic polyelectrolytes, e.g. poly(hexadimethrine bromide). The strong polyelectrolytes can be used under basic and acidic conditions, while weak acids, such as polyacrylic acid are limited to neutral or basic media. The weak basic polymers, like polyethylenimine, can be employed in neutral or acidic conditions to ensure dissociation into the ions.	9
2.5	Various examples of polymers commonly employed in superabsorbers, either directly or as co-polymers. (1) polymethacrylic acid, (2) polyacrylic acid, (3) polyacrylamide, (4) polyethylene oxide and (5) polyvinyl alcohol.	10

2.6 Illustration of the desalination procedure based on poly(sodium acrylate) hydrogels. (1) Mixing of dry polymer network with brine; (2) Removal of the supernatant phase enriched in salt; (3) Release of desalinated water from the gel interior via external pressure. The energy consumption of the process ΔE can be estimated by the required pressure P and the change in volume dV using $dE = P dV$ 11

2.7 Arithmetic example of distribution functions $P(x, y, z)$ and $P(r)$ calculated for a polymer chain with 10,000 repeating units and an efficient link length of 0.25 nm (\approx one monomer). 12

2.8 Difference in entropy of mixing of **a)** two low molecular species with the same size and **b)** of a polymer in a solvent. While **a)** provides $N = N_1 + N_2$ atom sites for each particle and therefore the same number N of states, **b)** has more parameters, since the polymer segments can move freely and adopt many conformations. The polymer chains exhibit the additional constrain of the connection between their sub-units, adapted from literature. [65] 13

2.9 Partial volume V_1 and V_2 and mixing volume $V_1 + V_2$ of a polymer solution, adapted from [65]. 14

2.10 Entropy of mixing ΔS_{mix} per monomer unit normalized to k_B as a function of the volume fraction of polymer ϕ_2 with the number of sub-units (\equiv monomers) in a polymer chain $M = 500$ and the total number of unit cells $N_0 = N_1 + M N_2$, adapted from [65]. Please note that at polymer chain lengths above $M = 500$ the mixing term becomes independent of M . [66] . 15

2.11 Schematic representation of a network deformation under affine conditions, i.e. the local displacement is proportional to the overall displacement. . . . 17

2.12 Schematic representation of the displacement of a cross-link in a polymer network from (x, y, z) to (x', y', z') under strain, adapted from [47]. . . . 18

2.13 Visualization of the mathematical approach for the description of the phantom model. The network is considered as a patchwork of consecutive layers of connected, e.g. tetrafunctional, cross-links (with functionality $\zeta = 4$) having a tree-like topology. The last tier of cross-links fixes the network on the surface of the volume element. The network is unimodal, symmetrically grown, adapted from [1]. 20

2.14 Polyelectrolyte particles in a salt solution partially repel ions from solution during swelling, whereby the surrounding solution is enriched in salt content. 25

2.15 Figure of swollen ionic gel in equilibrium with external electrolyte solution. Adapted from [4]. 27

-
- 2.16 Principle scheme of the NMR process. The spins precess after application of an external magnetic field \vec{B}_0 along the z-axis (left), displayed in a rotating frame around z. The population difference between the two separate energy states results in a net magnetization \vec{M} . A pulse B_1 perpendicular to the static field \vec{B}_0 causes the spins to flip. This results in saturation of the energy levels and the net magnetization rotates into the x'y'-plane (right). 30
- 2.17 After applying a 90° pulse the net magnetization \vec{M} is rotating in the x'y'-plane (middle). Two relaxation mechanisms lead \vec{M} back to its initial state at equilibrium: The longitudinal T_1 -relaxation along the z-axis (left), where the energy is transferred to the surrounding lattice and the spins drop to the ground state. In case of the transversal T_2 -relaxation (right) the spins are dephasing over time, which causes a loss of net magnetization in the x'y'-plane. 33
- 2.18 Scheme of a size exclusion chromatography set-up with – in flow direction [green] – the solvent reservoir, (optional: a degasser unit for increased baseline stability), the high-pressure pump, an injector with autosampler, the analytical column, the detector(s) and the solvent waste. (1) In the analytical column the polymers are separated according to their size in solution. Small polymer coils [gray] might enter the porous stationary phase, while large coils [orange] find no suitable pores to reside and thus, flow faster down the column. (2) This results in different elution volumes, which can be recorded by the detector(s). Adapted from [82] and [83]. 36
- 2.19 Typical SEC calibration curve: The logarithm of the molecular weight is plotted versus the elution volume revealing the upper exclusion limit (\equiv void volume of the column V_0), i.e. the polymer coils are too large for the pores, and the lower exclusion limit (\equiv total available volume $V_t = V_0 + V_{\text{pores}}$), i.e. the polymer is small enough that it fits in all pores. Adapted from [82]. 37
- 3.1 Representation of the cross-linking process via FRP polymerization between a mono- (orange) and a bifunctional (gray) monomer, in the presence of the initiator (green). The resulting polymer chains are displayed in black. The overlap between the polymer chains is considered as a junction point, independently of its origin (backbiting reaction, entanglement or cross-linking agent). The FRP polymerization yields high cross-linked nanogels, which are later loosely connected by bridging chains. Figure adapted from [30]. 41
-

-
- 3.2 The process of free radical polymerization (FRP) includes: 1. the initiation, which generates active radicals by decomposition of the initiator (I); 2. the propagation, where the (macro)radical grows by sequential addition of monomers (M), and 3. the termination ([1] radical recombination or [2] disproportionation) and transfer reactions, where the final polymer chain (P) is obtained. 42
- 3.3 Synthesis route for the free radical polymerization of poly(sodium methacrylate) (PSMA). The methacrylic acid (MAA) is co-polymerized with ethylene glycol dimethylacrylate (EGDMA) using azobisisobutyronitrile (AIBN) as initiator. Subsequently, the polymer is neutralized with 0.1 M sodium hydroxid (NaOH). 43
- 3.4 Typical side reactions in the anionic polymerization of (meth-)acrylates: 1) 1,2-addition of the initiator *Ini* (e.g. *s*-BuLi) onto the carbonyl function, which lowers the amount of growing chains. 2) Intramolecular backbiting reaction of the carbanion onto the carbonyl group, which ends the chain propagation. This attack can also occur intermolecularly resulting in the ligation of two chains. 45
- 3.5 Schematic display of the synthesis of poly(sodium methacrylate) in a single polymerization step. The monomer tert-butyl methacrylate (*t*BuMA) is co-polymerized with ethylene glycol dimethylacrylate (EGDMA) by anionic polymerization. Afterwards, the ester is cleaved off and the carboxylic group is transformed into the carboxylate by addition of 0.1 M sodium hydroxide (NaOH). 47
- 3.6 Synthesis route of poly(sodium methacrylate) by sequential anionic polymerization. In a first step, the elastic chain is build-up from tert-butyl methacrylate (*t*BuMA) and in a subsequent reaction the cross-linking takes place by addition of ethylene glycol dimethylacrylate (EGDMA). The micelles are resulting from the excess of EDGMA, which is required to ensure network formation. The tert-butyl protecting group is cleaved off with 50/50 vol% HCl/1,4-dioxane and subsequently the polymer neutralized by addition of 0.1 M sodium hydroxide (NaOH). 48
- 3.7 Synthesis of model hydrogels by anionic polymerization of the tert-butyl methacrylate (*t*BuMA). The chains are end-capped with bromide functionalities, which are transformed into the azide end groups by a S_N -reactions. Afterwards, the polymer network is formed by azide-alkyne Huisgen ligation and the protecting groups are removed to enable the neutralization with 0.1 M sodium hydroxide (NaOH). 50
-

3.8	Elugrams obtained by size-exclusion chromatography coupled with a Fourier-transform infrared spectrometer (SEC-FTIR). The intensities of the carbonyl vibration (1726 cm^{-1}) and the azide vibration (ca. 2100 cm^{-1}) are displayed. On the left, an example of a insufficient purified polymer is shown, which exhibits residual sodium azide as indicated by the azide signal eluting together with the system peak. On the right hand side, a polymer with an improved working-up procedure is displayed. Here, no dissolved sodium azide is affirmed but an azide signal eluting together with the polymer indicating a successful end-functionalization.	52
3.9	Synthesis of the four armed alkyne linker tetrapropargyl pentaerythritol from pentaerythritol and propargylbromide at elevated temperature in presence of potassium hydroxide.	53
3.10	End group analysis of the telechelic PSMA polymers by high field ^1H -NMR-spectroscopy. The transformation of the bromide to the azide end-group is shown on the left, while on the right the ^1H -NMR-spectrum of a swollen network (in D_2O) after the cross-linking is displayed. The integrals over the azide and the triazole peaks reveal an insufficient cross-linking, while 21 % of all azides remained unreacted. (1024 scans, RT)	53
3.11	Synthesis route of free radical polymerized poly(sodium acrylate) using acrylic acid (AA) and N,N'-methylene bisacrylamide (MBA) followed by a neutralization with 0.1 M sodium hydrogencarbonate (NaHCO_3).	56
3.12	Representation of the cross-linking process via RAFT polymerization between a monomer (orange) and a bifunctional linker (gray) using an radical initiator (green). The RAFT agent is depicted by a yellow circle, while the polymer is denoted by the black lines. The overlap between the polymer chains reveals the cross-linking points, which can originate from backbiting reactions, entanglements, or the cross-linking agent. In RAFT polymerization small linear chains are formed, which are cross-linked in a later stage of the polymerization process, compare also Figure 3.1 , p. 41. The figure is adapted from [30].	57
3.13	Synthesis route towards poly(sodium acrylated) hydrogels based on RAFT polymerization using acrylic acid (AA) as monomer, methylene bisacrylamide (MBA) as cross-linker, and S,S-di((2-methyl)propionic acid) trithiocarbonate (TRITT) as RAFT agent.	58
4.1	a) Determination of the degree of swelling of the FRP PSMA samples with different working-up procedures. b) Swellability of PSMA hydrogels arising from different synthetic procedures. (1 wt% NaCl, overnight)	62

-
- 4.2 a) Depiction of the swelling experiments of the quasi-model PSMA networks. b) The degree of swelling of poly(sodium acrylate) hydrogels with varying RAFT agent contents. (1 wt% NaCl, overnight) 63
- 4.3 Schematical representation of the main principle of the determination of the network structure by T_2 -NMR experiments. The relaxation process is caused by homonuclear dipolar couplings of protons. These are distance r and angular Θ dependent, see **Equation 4.3**. Rigid polymer chains (blue) reveal strong dipolar couplings, since the angle changes comparably slowly causing high residual dipolar couplings. Mobile chains (green) are changing the angle faster and thus, cause weak residual dipolar couplings. 65
- 4.4 (Left) Display of the whole T_2 -relaxation curve for a typical sample (PMA-DC01-FRP) by combining the CPMG/XY16 experiments with three different evolution times τ_e with the early points measured by MSE and XX4. In blue: The solvent subtracted data fitted with a single exponential function as described in the text. (Right) The distribution of relaxation rates T_2^{-1} obtained by the inverse Laplace transformation (ILT). [41] 66
- 4.5 a) The ^1H -NMR T_2 -relaxation curves and b) the corresponding relaxation rate (T_2^{-1}) distributions of free radical polymerized (FRP) poly(sodium methacrylate) (PSMA) samples with different degrees of cross-linking (DC in mol%) (1024 scans, 1/6 (g/g) polymer/ D_2O , RT, low-field NMR, pulse sequence see **Appendix B.3.2, p. 140**). 69
- 4.6 a) The ^1H -NMR T_2 -relaxation curves and b) the corresponding relaxation rate distributions of poly(sodium methacrylate) (PSMA) samples obtained by anionic co-polymerization in a single step with different degree of cross-linking (DC in mol%). (1024 scans, 1/6 (g/g) polymer/ D_2O , RT, low-field NMR, pulse sequence see **Appendix B.3.2, p. 140**) Please note that relaxation rates higher than 44 kHz are not physically meaningful, see **Equation 4.3, p. 64**. This can be seen as mathematical artifacts resulting from the ILT. 70
- 4.7 a) The ^1H -NMR T_2 -relaxation curves b) and the corresponding relaxation rate distributions of poly(sodium methacrylate) (PSMA) samples obtained through anionic polymerization with subsequent coupling. The respective degree of cross-linking (DC) is provided in the legend in mol%. Please note that relaxation rates faster than 44 kHz are not physically meaningful, see **Equation 4.3, p. 64** (1024 scans, 1/6 (g/g) polymer/ D_2O , RT, low-field NMR, pulse sequence see **Appendix B.3.2, p. 140**). 71
-

-
- 4.8 a) $^1\text{H-NMR}$ T_2 -relaxation curves and b) the corresponding relaxation rate distributions of poly(sodium methacrylate) (PSMA) samples obtained by anionic polymerization with subsequent cross-linking via azide-alkyne Huisgen ligation with different degree of cross-linking (DC) (1024 scans, 1/6 (g/g) polymer/ D_2O , RT, low-field NMR, pulse sequence see **Appendix B.3.2, p. 140**). 72
- 4.9 a) Comparison of the characteristic T_2 -relaxation times τ as obtained by the stretched exponential fit (**Equation 4.4, p. 67**). Each data set was fitted employing an empirical power law. The lower slopes and higher prefactors indicate a lower efficiency of the cross-linking process in case of the anionic single step hydrogels and the model networks. b) Schematic representation of the correlation between τ and the network structure. The quasi-model networks provide more rigid polymer network structure, due to the large hydrophobic micelles of EDGMA arising from the synthesis. 73
- 4.10 Heterogeneity of the mobility of the polymer networks produced with different methods as measured by the T_2 -relaxation behavior. a) Displayed are the width of the distribution, as measured by the stretched exponential fit (**Equation 4.4, p. 67**), b) and the standard deviation of the relaxation rate distributions (**Equation 4.6, p. 68**), as obtained by the inverse Laplace transformation. They reveal similar heterogeneities of the PSMA mobility distributions regardless of the synthetic procedure. 74
- 4.11 1) Schematic representation of the influence of the cross-link density on 2) the heterogeneity of the T_2 -relaxation rate distributions. Crossing chains denote junction points. With few cross-links the chains in the network are unrestricted in their motion leading to a narrow mobility distribution (T^{-1}_2). In case of many cross-links the short polymer chains are stiffened, which also causes narrow T_2 -relaxation rate distributions (at higher rates). If mobile chain segments and rigid junction points are equally represented in the network broad mobility distributions are obtained. 75
- 4.12 a) $^1\text{H-NMR}$ T_2 -relaxation curves of poly(sodiumacrylate) (PSA) hydrogels with a degree of cross-linking DC ranging from 0.6 to 5 mol% synthesized via FRP, empty symbols, or with 0.10 mol% RAFT agent, full symbols. (1024 scans, 1/6 (g/g) polymer/ D_2O , RT, low-field NMR, pulse sequence see **Appendix B.3.2, p. 140**) b) The respective relaxation rate distributions resulting from the inverse Laplace transformation (ILT). 76
-

4.13	a) The dependency of the characteristic relaxation time of the magnetization τ on the degree of cross-linking DC at different RAFT agent contents: 0 (black), 0.10 (orange) and 0.25 mol% (blue). b) The dependency of the heterogeneity on the DC as measured by β^{-1} obtained by fitting of the relaxation data. The respective RAFT agent concentrations in mol% are given in the legend.	77
4.14	a) Normalized decay of the transversal magnetization of poly(acrylic acid) hydrogel samples with a degree of cross-linking of 1.0 mol% and varying RAFT agent contents of 0.05 to 0.25 mol%, as depicted in the legend. b) Inverse Laplace transform of the relaxation decay, revealing the distribution of relaxation rates.	78
4.15	a) Depiction of the interconnection between the empirical time constant τ and the RAFT agent content. b) The dependency of the heterogeneity of poly(sodium acrylate) (PSA) networks on the RAFT agent content as measured by β^{-1} obtained by fitting of the relaxation data (Equation 4.4, p. 67). The degree of cross-linking DC was kept at 1.0 mol%.	79
4.16	a) Normalized decay of the transversal magnetization of poly(acrylic acid) hydrogel samples with varying degree of neutralization (DN) of 0 to 100 mol%, as depicted in the legend. (1024 scans, 1/6 (g/g) polymer/D ₂ O, RT, low-field NMR, pulse sequence see Appendix B.3.2, p. 140) b) Inverse Laplace transform of the relaxation decay, revealing the distribution of relaxation rates.	80
4.17	a) Depiction of the dependency of the empirical time constant τ on the degree of neutralization DN . b) The interconnection of the heterogeneity and the DN as measured by β^{-1} obtained by fitting of the relaxation data. The degree of cross-linking (DC) was kept at 1.0 mol%. The parameter β^{-1} reveals a plateau formation at $DN \geq 50$ mol%.	81
4.18	a) Width of the T_2 -relaxation rate distributions of poly(sodiumacrylate) with varying degree of cross-linking (DC) and b) RAFT agent contents as obtained by Equation 4.6, p. 68	82
4.19	Example for a double quantum build-up curve (I_{norm} , left) and the resulting D_{res} distribution from the Tikhonov regularization (right). The build-up curve free from contribution of defects is obtained from the reference signal (I_{ref}) and the double quantum signal (I_{DQ}) by stepwise subtraction of two exponential fits and subsequent normalization, detailed procedure see Chapter B.3.3, p. 141 . (1024 scans, 1/6 (g/g) polymer/D ₂ O, RT, low-field NMR, pulse sequence see Appendix B.3.3, p. 141)	83

-
- 4.20 a) Depiction of the double quantum build-up curves of a set of free radical polymerized (FRP) PSMA samples with varying degree of cross-linking DC , as labeled in the legend. (1024 scans, 1/6 (g/g) polymer/D₂O, RT, low-field NMR, pulse sequence see **Appendix B.3.3, p. 141**) b) The corresponding D_{res} distributions, which are obtained by the Tikhonov regularization, are depicted. 86
- 4.21 a) Poly(sodium methacrylate) samples with degree of cross-linking (DC) ranging from 0.3 to 5.0 mol%, obtained by anionic polymerization in a single reaction step (SSA), provided the depicted double quantum build-up curves b) and D_{res} distributions (1024 scans, 1/6 (g/g) polymer/D₂O, RT, low-field NMR, pulse sequence see **Appendix B.3.3, p. 141**). 87
- 4.22 a) PSMA model hydrogels with DC ranging from 0.2 to 2.0 mol%, obtained by anionic polymerization of telechelic polymers with subsequent coupling by azide-alkyne ligation into the respective networks. The double quantum build-up curves are depicted b) and the resulting D_{res} distributions from the Tikhonov regularization (1024 scans, 1/6 (g/g) polymer/D₂O, RT, low-field NMR, pulse sequence see **Appendix B.3.3, p. 141**). 89
- 4.23 a) Relative contribution of the mid-tail (B_n , see **Equation 4.8, p. 84**) to the overall relaxation of the PSMA samples representing the amount of mobile network defects. b) The standard deviation of the D_{res} distributions as measure for the heterogeneity of the PSMA hydrogels. The FRP samples, the anionic single step and the model hydrogels are evaluated. 89
- 4.24 a) Depiction of the DQ build-up curves of the PSA samples obtained by FRP b) and the respective D_{res} distributions. (1024 scans, 1/6 (g/g) polymer/D₂O, RT, low-field NMR, pulse sequence see **Appendix B.3.3, p. 141**) 90
- 4.25 a) The DQ build-up curves for PSA samples with 0.25 mol% of RAFT agent and a varying DC (in mol%). The employed RAFT agent concentrations during polymerization are labeled in the legend (in mol%). (1024 scans, 1/6 (g/g) polymer/D₂O, RT, low-field NMR, pulse sequence see **Appendix B.3.3, p. 141**) b) The corresponding distribution of the residual dipolar coupling constants D_{res} obtained by the Tikhonov regularization. 91
-

-
- 4.26 Results of double quantum experiments of PSA gel samples with different RAFT agent contents and $DC = 1$ mol%. a) The renormalized DQ build-up curves are shown. (1024 scans, 1/6 (g/g) polymer/D₂O, RT, low-field NMR, pulse sequence see **Appendix B.3.3, p. 141**) b) The obtained D_{res} distributions from the Tikhonov regularization are displayed. No dependency of the DQ build-up curve on the RAFT agent content was found, which indicates that the underlying network structures free from defects are similar. 92
- 4.27 a) Depiction of the relative content of defects (B_n , see **Equation 4.8, p. 84**) of the PSA hydrogel samples with varying DC and two different concentrations of RAFT agent. b) Content of defects, as quantified by the mid-tail of the DQ signal, of PSA samples with $DC = 1$ mol% and varying RAFT agent contents. 92
- 4.28 a) The calculated standard deviation of the D_{res} distributions of the build-up curves at varying DC illustrate the dependency of the heterogeneity of the network dynamics on the DC with a RAFT agent content of 0 (full symbols), and 0.25 mol% (empty symbols) of RAFT agent b) and on the RAFT agent content at $DC = 1$ mol%. 93
- 4.29 Representation of the proposed theoretical description of PSA network synthesized via RAFT mediated polymerization. a) High RAFT content lead to a not sufficient number of cross-linking points per chain for the achievement of network formation. b) increasing the amount of RAFT agent yields to networks with high content of dangling ends and c) at low amounts of RAFT agent the chains are bound multiple times to the network, limiting the amount of dangling ends, i.e. network defects. Adapted from [119] . . . 94
- 4.30 Schematic representation of the iSEC column. The inner chamber is adjusted by the movable pistons to the filling height of the analyzed porous gel. Each piston is equipped with a glass frit with 10 μm pore size to prevent the sample from leaving the chamber. The exiting glass frit is additionally protected by a layer of filter paper. 95
- 4.31 a) Example for a iSEC measurement of the sample PSMA-DC2.5-FRP with the resulting fit from the Porocheck software (PSS, Mainz, Germany). The elution volumes of the pullulan standards having the molecular weight (M_{peak} at the maximum) are given. b) The elugram is converted by the Porocheck software, based on the molecular-statistical theory (MST), into the respective pore size distributions. 96
-

-
- 4.32 Typical conformations of polymer molecules in a) wide and b) narrow pores. In wide pores polymer coils behave similar to solid balls of equivalent radius r . In narrow, slit-like pores the long flexible chains unfold and penetrate by reptation. 98
- 4.33 a) Dependency of the average pore size and b) the standard deviation of the obtained pore size distributions on the degree of cross-linking. For each data point, three different column packing were measured twice. A flow rate of 0.2 mL/min, a bed length of 5 – 10 cm and a 0.1 M solution of disodium phosphate with 0.05 M sodium azide as eluent were utilized, see also **Figure 4.31, p. 96**. 101
- 4.34 a) A correlation of the average relaxation rate as obtained by T_2 -NMR to the average pore radius is shown for the free radical polymerized poly(sodium methacrylate) with varying degree of cross-linking of 0.4 – 20 mol%. Please note that the samples in T_2 -NMR are swollen in a 1/6 g/g ratio polymer to D_2O and the iSEC hydrogels are swollen to the equilibrium in 0.1 M Na_2HPO_4 , which limits the obtained relationship between $\langle R_S \rangle$ and \bar{T}_2 to this specific case. b) The normalized width of the PSD and the relaxation rate distribution, as a measure of the heterogeneity of the respective distributions, are given. 102
- 4.35 a) Dielectric spectrum of the sample PSMA-DC1.0-FRP revealing the plateau region and the initial noise region resulting from instrumental error. b) One dimensional scheme of the energy landscape as defined by the random barrier model. The minima provide the allowed particle positions. By definition all minima have equal energy, implying that all positions are equally likely, adapted from [171]. 105
- 4.36 Dependency of the conductivity of poly(sodium methacrylate) networks of the degree of cross-linking. a) Samples obtained by free radical polymerization and b) samples obtained by single-step anionic co-polymerization are displayed (1/6 g/g polymer/water, 21 °C). 106
- 4.37 Display of the dependency of the direct current (dc) conductivity of poly(sodium methacrylate) hydrogels on the degree of cross-linking. The results of a) the quasi-model systems and b) the model networks are presented (1/6 g/g polymer/water, 21 °C). 107
- 4.38 The salt rejection of all synthesized PSMA samples as a function of the degree of swelling at a fixed Q_{rel} of 2. The theoretical salt rejection is additionally displayed using the Donnan equilibrium with a degree of neutralization of 30 ± 10 mol%, respectively. 110
-

B.1	Schematic representation of the pulse sequences for the measurement of spin-spin relaxation times: MSE-sequence on the top and the CPMG-sequence at the bottom.	141
B.2	Schematic representation of the modified Baum-Pines pulse sequence for the measurement of the double quantum coherence build-up.	142
B.3	Evaluation of double quantum build-up data by removal of single exponential tails from the raw data to compensate for relaxation processes. The tails are removed in two steps: the first fit is made to I_{ref} after 20 ms. Subtraction of the fit from I_{ref} yields I_{red} . The second fit is on I_{red} between 2 – 20 ms. The renormalized DQ build-up resulting from Equation B.2 is displayed with blue symbols.	143
C.1	a) ^1H -NMR spectrum of poly(tert-butyl methacrylate) in CDCl_3 with $M_n = 43.5$ kg/mol. b) ^1H -NMR spectrum of the same polymer in D_2O after the deprotection reaction under reflux with 50/50 vol% $\text{HCl}/1,4$ -dioxane and purification by precipitation, see Chapter A.3.3, p. 133 . It reveals the disappearance of the signal b at 1.54 ppm assignable to the tert-butyl protecting group confirming a successful deprotection. (1024 scans, RT)	146
C.2	Measurement of the degree of swelling (Q) of poly(sodium acrylate). The samples were obtained by anionic polymerization of telechelic poly(tert-butyl methacrylate) with azides as end groups, which are coupled into the network by azide-alkyne ligation and subsequently hydrolyzed. The cross-linking is performed in a single step (orange) after which ~ 30 % of azide groups remained unreacted, despite an equimolar ratio of linker and azide functionalities. In a second batch the missing quantity of cross-linker was added after the first reaction cycle, which gave the black data points. The stronger deviations of Q from the expected power law indicate ill defined networks (black data points, point in brackets not used for fit). Thus, only the hydrogels resulting from the single cross-linking step were characterized further.	147
C.3	a) ^1H -NMR T_2 -relaxation curves of poly(sodium acrylate) (PSA) hydrogels with a degree of cross-linking DC ranging from 0.6 to 5 mol% synthesized via FRP, empty symbols, or with 0.25 mol% RAFT agent, full symbols. (1024 scans, 1/9 (g/g) polymer/ D_2O , RT, low-field NMR, pulssequence see Appendix B.3.2, p. 140) b) The respective relaxation rate distributions resulting from the inverse Laplace transformation (ILT).	148

Appendix E

Acknowledgment

This thesis would not exist without the contribution of many people. Especially I want to highlight the following people:

· Prof. Dr. Manfred Wilhelm

My special thanks I would like to express to the person without whom this work would never have been accomplished. His suggestions have always been constructive and have always encouraged me to implement my ideas and tread new ways. Although the results were desperate on some days, he never doubted my person and thus offered me a secure backing. His opportunities to make my stay in Chile possible, his contacts to South Africa (to name just a few) will have a decisive influence on my future life.

· The Deutsche Forschungsgemeinschaft (DFG)

Without the financial support of the DFG through the SFB1176, many attempts would not have been possible, many seminars, many conference contributions would not have been.

· Prof. Bernabé Rivas

Bernabé Rivas for the possibility to conduct a research stay in his group in Concepción, Chile. It was a wonderful experience and a heartily welcome, which I always love to recall. And...you truly found the best seafood restaurant of South America.

· Prof. Leonie Barner

Leonie Barner for the helpful discussions during our meetings and the beneficial cooperation. Although Australia is on the other side of the world, your suggestions fertilized my papers in many ways.

· Dr. Federica Cavalli for the fruitful cooperation. You shared with me the word of polymer networks and contributed in many ways to our joint efforts.

· Jonas Keller and Dr. Lukas Arens for the scientific discussion on NMR and polymerization techniques, as well as the support in the laboratory.

· Birgit Huber

Her tireless and helpful way of accommodating my often tedious attempts in her compact workload, has added decisive aspects to my iSEC results.

· The whole working group for the meaty barbecues and many cakes, a plenty of discussions about science and more, the vinous tours to Freiburg, and of course the nice working atmosphere. Without your proof-reading and many comments this thesis would not exist.

· My family and especially Christian gave me the necessary support outside of chemistry. Thank you for the selfless and tireless support and the many “kitchen talks” in the recent years.

· Many thanks to all the unnamed.

Please forgive me for not being able to name everyone, who has given me your help in many different ways and has contributed to the success.